

From hot melts to cool dies:

MRI mapping of anisotropic structure formation during high-moisture extrusion of plant proteins

Sam Kuijpers



Propositions:

1. Macroscopic lamellar phase separation is directed by micronscale alignment. (this thesis)
2. Flow-MRI enables parametrising current *in silico* models of high-moisture extrusion. (this thesis)
3. Adoption of MRI techniques by industry requires high-resolution yet low-field solutions.
4. Industrial investment in mimicking animal meat with plant-based alternatives is a waste of resources.
5. Promoting inter-department research projects by universities facilitates research with higher impact
6. Including fruit-bearing trees in public spaces after infrastructure revisions increases social cohesion.
7. Musicianship is a vital but overlooked opportunity for learning in Dutch schools.

Propositions belonging to the thesis, entitled
From hot melts to cool dies: MRI mapping of anisotropic structure formation during high-moisture extrusion of plant proteins
Sam A Kuijpers
Wageningen, 13 November 2026

From hot melts to cool dies:
MRI mapping of anisotropic structure formation during high-moisture extrusion of plant proteins

Sam A. Kuijpers

Thesis Committee

Promotor:
Prof. Dr J. P. M. van Duynhoven
Professor, Magnetic Resonance in Relation to Food
Wageningen University & Research

Co-promotor:
Dr C. Terenzi
Associate professor, Laboratory in Biophysics
Wageningen University & Research

Other Members:
Prof. V. Fogliano, Wageningen University & Research
Prof. Dr D. Topgaard, University of Lund, Sweden
Dr K. E. Anderssen, Nofima, Norway
Dr L. M. C. Sagis, Wageningen University & Research

This research was conducted under the auspices of VLAG Graduate School (Biobased, Biomolecular, Chemical, Food, and Nutrition Sciences)

From hot melts to cool dies:
MRI mapping of anisotropic structure formation during high-moisture extrusion of plant proteins

Sam A. Kuijpers

Thesis

submitted in fulfilment of the requirements for the degree of doctor
at Wageningen University
by the authority of the Rector Magnificus,
Prof. Dr C. Kroeze,
in the presence of the
Thesis Committee appointed by the Academic Board
to be defended in public
on Friday 13 November 2026
at 3:30 p.m. in the Omnia Auditorium.

Sam A. Kuijpers
From hot melts to cool dies: MRI mapping of anisotropic structure formation during high-moisture extrusion of plant proteins
242 pages.

PhD thesis, Wageningen University, Wageningen, the Netherlands (2026)
With references, with summary in English
DOI 10.18174/681956

Contents

	Page
Chapter 1	
Introduction	7
Chapter 2	
Quantification of phase separation in high-moisture soy protein extrudates by NMR and MRI	37
Chapter 3	
Underpinning hierarchical anisotropic structure formation in soy protein high-moisture extrudates by magnetic resonance imaging	69
Chapter 4	
Mapping anisotropic structure formation of soy protein during high-moisture extrusion	107
Chapter 5	
Impact of pH-shifting on multiscale structural anisotropy of high-moisture extrudates of soy proteins	149
Chapter 6	
MRI velocimetry during high-moisture extrusion: probing wall-slip and yield stress of soy protein concentrate	179
Chapter 7	
General discussion	207
Chapter 8	
Summary	229
List of publications, Authorship statement, Acknowledgements	233
Colophon	242

Chapter

1

Introduction

1.1 The protein transition

The world population is projected to grow to 10 billion people by 2050 and, to feed this population, a 70% increase in global food production is required, as estimated by the Food and Agricultural Organisation in 2009 [1]. Proteins are a key part of our diet and can be consumed via multiple sources [2]. An increase in welfare and income generally result in diets containing more animal-based products, yet the large-scale production of such products has profound impact on the environment and human wellbeing [2]. Intensive livestock farming majorly contributes to emission of strong greenhouse gasses, such as ammonia [3], and it is estimated that around one third of all arable land is used to grow feed crops, resulting in a strong loss of biodiversity [4]. Additionally, the consumption of large quantities of red and/or processed meat has been related to a number of diseases such as coronary heart disease and colorectal cancer [5]. Furthermore, large-scale farming poses an increased risk for zoonosis, where animal-borne diseases, such as bird-flu or Q-fever, are transmitted to humans [6], alongside a growing concern for the animal welfare [7].

As a result, in most western countries, a transition away from the consumption of animal-based protein towards a more plant-based diet is observed [2]. While partially or completely altering food choice might appear simple, there is actually a large psychological factor involved, such as past experiences, habit and hedonic appreciation, [8] and many consumers are not ready to make this transition [9]. Meat is often still seen as a luxury product with better sensorial attributes, price and availability compared to plant-based alternative products [10–12]. Thus, the resemblance to meat has been identified as a key factor affecting consumer acceptance of plant-based meat alternatives [12]. To aid in facilitating the transition towards a more plant-based diet, alternative protein products are aimed at mimicking animal-based products. This strategy allows consumers to change their diet without having to change their eating habits. Yet, consumer acceptance remains a barrier in the wide-spread adoption of such meat alternatives [10, 13].

Animal meat is inherently hierarchically structured with nm-scale actin and myosin proteins that bundle together to form sarcomeres at length scales around 1-3 µm. These sarcomeres stack to form myofibrils which span the length of the muscle fibre. Bundles of myofibrils form the muscle fibres at the 10 to 100 µm-scale which make up the muscle tissues at the mm-scale [14]. This structure is not trivial to mimic using plant proteins which generally possess a globular shape and do not naturally align in fibrils.

1.2 Plant-based meat alternatives

The concept of substituting meat with plant-based alternatives can be traced back more than 2000 years with the production of tofu in East Asia [15]. Other historical plant-based meat alternatives are tempeh [16] and seitan [13]. However, what is currently often seen as the first generation of plant-based meat alternatives originated in the 1960s with the introduction of single-screw extrusion to create low-moisture textured vegetable products (TVPs) from plant-protein materials [13]. These products were designed to be more meat-like than their historical counterparts with the goal to convince meat-eating consumers to reduce their meat intake [10, 13]. With the development of high-moisture extrusion (HME) equipment in the late 1980s, plant-protein products with textural properties closer to animal meat could be produced [17]. In the late 2000s, a Couette shear-cell based approach was developed, by which fibrous texture similar to animal meat could be achieved. This method, however, is batch-based, and has longer processing times [18]. Thus, HME remains the industry standard for producing fibrous plant-based meat alternatives due to the continuous and scalable nature of the technique. The remainder of this section will focus on the use of HME, and the different aspects involved in creating a plant-based meat alternative product as outlined by the diagram in Fig 1.1.

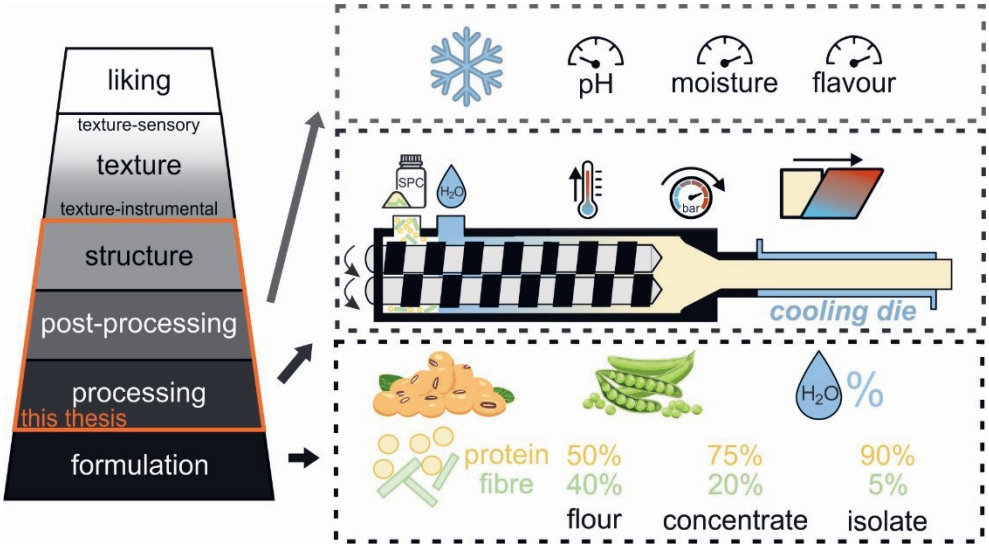

Fig. 1.1: *Diagram of the main steps involved in the production of meat alternatives. A more detailed schematic of the aspects involved in formulation, processing and post-processing is shown on the right.*

1.2.1 Formulation of HME extrudates

The choice of ingredients used during processing has a significant influence on the type of product that can be made. This includes aspects like the botanical source of the protein, such as plant species and cultivar or growth climate. Legume proteins are most commonly used for manufacturing plant-based meat alternatives, with soy and pea being the most important sources [19]. Additionally, other proteins such as wheat gluten [20, 21] can be added in smaller quantities as structuring agents to enhance fibrous texture. In recent times, the large-scale production of soy protein has received criticism due to the link to deforestation of rainforests and presence of antinutritional factors. Yet, soy protein is a byproduct of the soybean oil production and shows a balanced amino acid composition, wide availability, and specific protein functional properties such as good gelling and water holding capacity [22]. As such, soy protein is a dominant industrial ingredient for meat alternatives manufactured by HME and was therefore studied in this thesis.

Apart from the botanical source of the legume protein, the type of industrial separation process is relevant. Legume proteins are generally available as three types, namely as defatted flours, concentrates or isolates, each respectively with more processing steps to enrich protein content [23, 24]. In the case of soy protein, defatted flour is produced by dehulling and milling the whole plant seeds and subsequently extracting the oil using mechanical pressing or solvents such as hexane. The defatted protein flour contains roughly 50 wt% protein and 40 wt% carbohydrate fibres, as well as some residual oil. The defatted flour can be further processed by aqueous solvent extraction of the soluble fibres. This results in a protein concentrate, typically containing 65-75 wt% protein and roughly 20 wt% of insoluble carbohydrate fibres. Soy protein concentrate (SPC) can be further processed by first solubilising the protein in alkaline solution, removing the water-insoluble carbohydrate fibre fraction, and subsequently extracting the remaining protein using acid precipitation. The dried soy protein isolate (SPI) typically has a concentration above 90 wt% protein with residual fibres, comprising up to 5 wt% of dry matter [25]. It is important to note that these processing steps have an effect on the denaturation degree of the protein [26]. Due to variation in soy cultivars, cultivation region and industrial separation processes, commercial SPCs show a wide range in protein and fibre composition as well as denaturation degree, which combined can impact on structuring capacity during HME [25–27].

1.2.2 Processing and post-processing

As schematically depicted in Fig. 1.1, a HME system typically consists of a long barrel, typically around 50 cm at lab-scale to more than a meter at pilot-plant or production-scale, and is divided into individually heated sections, allowing for custom temperature profiles. Inside the barrel, two co-rotating screws are situated that serve to push the material forward as well as to mix and knead it. At the barrel exit, a cooling die is connected [28]. During HME of plant-proteins, protein and water are added at the start of the barrel where the mixing

screws facilitate the hydration of the protein into a dough. Typically, HME moisture contents range between 40–80%, but most commonly values in the range of 50–60% are used [29]. In the subsequent heated kneading section, the thermo-mechanical conversion from a protein dough to a hot protein melt takes place. The temperature is ramped up to about 140–160 °C depending on the type of protein used [30–32]. At the end of the barrel section, in the exit die, the hot protein melt is forced through a narrower opening into the cooling die. Here pressures are in the range of 10–20 bar and high tensile and shear forces are experienced by the protein melt [33]. Subsequently, the protein melt is cooled in the cooling die under shear, which promotes fibrous structure formation and facilitates phase separation [29]. The material exiting the cooling die is called an extrudate. Typically, these extrudates require further post-processing steps, such as marination and freezing, to become a consumable meat alternative product.

Marination is an effective way to add flavour compounds and colourants, as well as to alter the pH and prevent microbial spoilage. Impregnation of such components through diffusive or osmotic absorption, however, is a slow process. Therefore, directly after extrusion, the material is often cut or torn to decrease the sizes of the extruded pieces and increase the overall available surface area for impregnation with a marinade [29]. The pH and ionic strength of marinades can additionally be used to alter the water holding capacity of meat alternative products which has been linked to the perception of juiciness [34]. The primary function of freezing is to increase the shelf-life of the product. However, freezing can also induce further structural changes to the extrudate, increasing the fibrousness of the structure [29, 35].

1.2.3 The structure-texture and texture-liking relations

For meat alternatives, taste, flavour, colour and texture are main drivers of liking by consumers [19]. While taste, flavour, and colour can be modified by formulation [22], texture is for a major part also determined by the underlying structure, which in turn is determined by HME processing and post-processing conditions. To quantify textural attributes, such as mouthfeel and visual appearance, trained expert sensory panels are required [36, 37]. Such panels, however, are expensive and time-consuming. Therefore, the industry is in need of instrumental surrogate methods regarding mouthfeel textural attributes. These methods infer information on the macroscopic mechanical behaviour of extrudates with properties such as hardness, brittleness, elasticity or stiffness [36] Examples of such methods are: (i) the Warner-Bratzler shear force test, with a single blade used to cut the surface of a product [38]; (ii) the Kramer-cell shear force test, with five to ten dull parallel blades used to indent the surface [39], also employed in the present thesis; the (iii) texture profile analysis, where a number of different probes are used to press down on or cut through a sample [20]; and (iv) tensile tests, where samples are cut into dogbone shapes either parallel or perpendicular to the extrusion direction and placed under tension [40]. By

assessing the sample both parallel and perpendicular to the extruder flow direction, information about the anisotropy of the underlying structure can be obtained. In this work, when texture is discussed, the structure-texture relation is referred. However, study of this relation is not the main goal of this thesis.

Both the processing and post-processing steps contribute to structure and, ultimately, texture of a meat alternative product. To achieve a fibrous texture similar to that of meat, plant proteins have to be structured at multiple length scales [29]. The different structuring mechanisms involved in the HME processing of soy protein, and their respective length scales, are discussed in depth in section 1.3.

1.3 Structuring processes during HME of soy protein

There are multiple hypotheses concerning the multiscale structure formation mechanisms that lead to a meat-like anisotropic fibrous texture [29]. Figure 1.2 schematically depicts the structuring events involved in creating SPC extrudates including their relative location in the extruder (bottom), as well as the corresponding length scale of structural elements (right). This section elaborates on these structure formation hypotheses, and the open research questions (RQ) addressed in this thesis are highlighted after the corresponding sections.

After initial mixing of the protein and water, a hydrated protein dough is formed where water is absorbed and distributed throughout the mixture of partially denatured protein and carbohydrate fibre [41]. Due to the relatively low temperatures in the mixing section, required to be between 20–80 °C for the liquid feed, no significant conformational changes of the protein take place yet [42]. Subsequently, the hydrated protein dough enters the heated barrel sections where, due to the increased temperature and mechanical energy supplied by the barrel screws, the protein further denatures. Due to the plasticising nature of water, the temperature of denaturation is moisture-dependent [43].

Above the denaturation temperature, non-covalent bonds become dissociated enabling liquefaction of the protein dough into a cohesive protein melt [28]. Due to the high shear forces at these temperatures, also covalent disulphide bonds become destabilised. This enables the exchange between sulfhydryl and disulphide groups promoting the formation of intermolecular crosslinks [44–46]. Essentially, a transient crosslinked protein network forms, where a balance between the temperature- and shear-induced formation and rearrangement of molecular bonds is present [29, 47]. It has been shown that, in the kneading section, the first structuring process occurs at the nm-scale where, due to the strongly sheared flow, proteins aggregate. These aggregates align along the rotational direction of the screw enabling nm-to-µm scale fibril formation whose size is controlled by a balance between the thermal and mechanical energy [29, 47, 48].

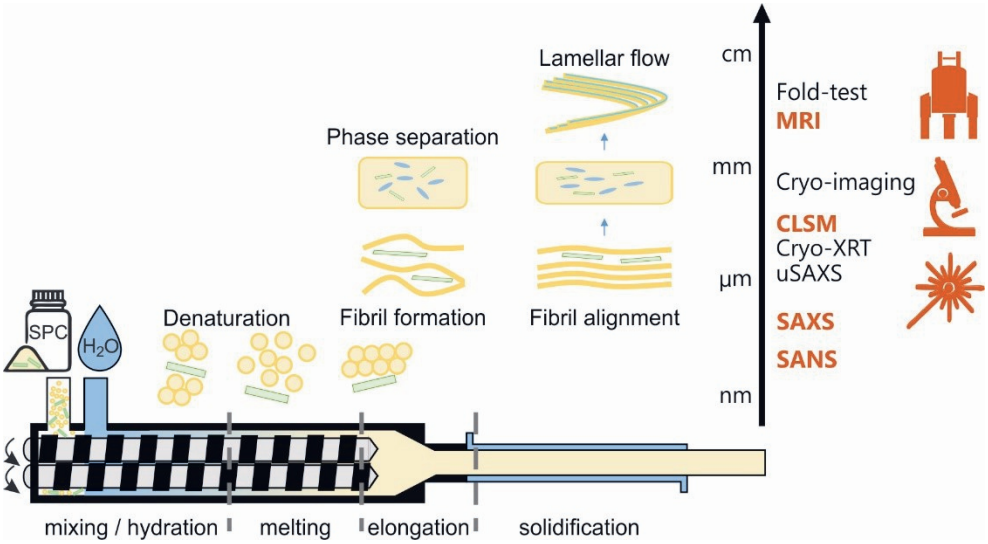

Fig. 1.2: *Diagram of the HME process. Below the extruder, the primary process occurring within each section is listed. Above the extruder, displayed in increasing structuring length scale, are the hypothesised structuring mechanisms. On the right side, multiscale structure measurement techniques are listed. The techniques marked in orange are used in the present thesis, with a focus on MRI-based techniques.*

RQ 1: Where inside the extruder, and at what length scales, does anisotropic structure formation occur during extrusion?

Both covalent and non-covalent bonds are involved in protein fibril formation. Covalent S-S bonds destabilise and rearrange during the extrusion process through SS/SH interchange reactions [31, 49, 50]. Non-covalent bonds have an important role in forming and maintaining protein secondary and tertiary structures. Here, hydrogen bonds play a crucial role in protein secondary structure formation, while hydrophobic regions in proteins are normally folded into the protein core [51, 52]. Due to the unfolding of protein molecules during extrusion, these regions become exposed and can associate with similar regions of neighbouring proteins, promoting aggregation [52]. However, differential solubility assay results could only find a minor role of hydrogen bonds and hydrophobic interactions on the fibrous structure formation during extrusion [49]. Another type of non-covalent bond is formed via inter- and intramolecular electrostatic interactions, which can form between two oppositely charged amino acids [34, 51, 53]. Protein surface charge has been proposed as a general mechanism involved in fibrillar protein aggregation [54, 55], yet the effect of surface charge during extrusion has not been studied in detail. As such, there is no conclusive evidence which of the proposed underlying mechanisms, namely covalent S-S bonds or non-covalent electrostatic interactions, dominate in the formation of protein fibrils during extrusion.

RQ 2: What is the role of electrostatic protein interactions on the multiscale structure formation during extrusion?

Irrespective of the exact nature of protein fibril formation, these fibrils can form a network. During this process, separation of the protein melt into a continuous protein phase and a dispersed polysaccharide phase occurs [29]. The mechanism behind this separation has been described using the theory of thermodynamic incompatibility of the biopolymers, namely protein and carbohydrates, [56, 57] as well as viscoelastic phase separation [58] which is the result of asymmetry between different components in a mixture, such as differing glass transition temperatures or molecular sizes. In both cases, at the µm-scale, the formation of a dispersed phase is thought to enable clustering of protein fibrils, forming a transient network due to the alignment and deformation of the dispersed phase [18, 29, 59]. Additionally, the alignment of the fibres is thought to be the result of elongation of the dispersed phase [57, 60] which is hypothesised to be strongest in the transition zone due to the combination of shear and tensile forces [33].

In the final part of the extrusion process, the protein melt is pushed through the cooling die. Due to the external cooling of the melt, the transient protein network becomes solidified there [29] because the rate of bond formation and breakage shifts from a balanced state to mostly the formation of bonds due to the lower thermal energy. An increase in the viscosity and elastic modulus of the protein melt is observed as a result [61, 62]. Concomitantly, the protein network contracts driving the expulsion of water from the matrix and syneresis at the mm-scale [29] resulting in the characteristic lamellar water-rich and protein-rich phases [63]. This process has been shown to occur in the absence of a second biopolymeric phase, such as in SPI, [32, 63]. Yet, the addition of a second biopolymeric phase is thought to aid structure formation by fracturing the protein network, up to an optimum of around 20–25 wt% dry matter [63, 64].

RQ 3: Does lamellar phase separation occur at µm- and/or mm-scale in extrudates?

Along the extrusion direction, phase separation of such extrudates results in a V-shaped lamellar structure [33]. This is thought to occur due to the constant shear during cooling [29, 33]. However, it is challenging to characterise the structure formation occurring within the cooling die *in situ* during extrusion with currently adopted measurement techniques. By using a dead-stop operation, where the extruder is stopped and rapidly cooled leaving the content of the cooling die intact, information on the development of this V-shape has been acquired [33]. This showed an increase in lamellar structure definition as the melt passes through the cooling die. Since the extrusion process is halted, no information on the

formation of this lamellar structure can be assessed. Hence, to this goal, modelling efforts to describe the cooling die flow *in silico* are of key importance. From these models, it has been suggested that solidification of the protein melt takes places once the combination of stresses during flow have dropped below the yield stress of the melt [65]. Due to the established temperature gradient in the melt, perpendicular to the flow direction, solidification is spatially non-uniform [29]. It is hypothesised that the V-shape is dependent on the shape of this temperature profile [66]. First modelling studies have indicated that flow behaviour of the protein melt in the cooling can only be explained when wall-slip occurs [67, 68]. Direct experimental quantification of wall-slip has been attempted but turned out to be challenging [69].

RQ 4: What is the contribution of wall-slip to the flow behaviour of the hot protein melt inside the cooling die?

1.4 Structural characterisation of HME extrudates

1.4.1 Multiscale structure quantification

At the macroscopic scale, *i.e.* the mm-to-cm scale, the lamellar phase-separated structure of extrudates can be investigated. A simple and fast method, usable *at line*, is the fold or fracture test [30, 64]. Here the extrudate is folded and torn directly after extrusion to visually assess the layered structure that has formed. By means of image analysis, this technique allows for semi-quantitative comparison of structures obtained by different processing conditions [70]. A more sophisticated approach is the use of cryo-imaging, where thin slices are cut from a frozen extrudate and subsequently imaged using a digital camera. Here, phase separation at the mm-scale can be visualised [71]. The use of cryogenic X-ray tomography (XRT) enables the three-dimensional (3D) measurement of intact frozen extrudate samples with spatial resolutions down to tens of µm [63]. XRT proved capable of differentiating the lamellar structure of SPC and SPI materials resulting from different processing; yet, the sample freezing step, required to achieve sufficient contrast between phase-separated water-rich and protein-rich regions, makes the technique unsuited to study microstructural effects due to post-processing.

RQ 5: What is the effect of post-processing, such as freezing and swelling, on the phase-separated extrudate structure?

At the microscopic scale, the presence, orientation and alignment of the fibrous structure is evaluated. A common approach is to use conventional microscopy techniques, such as Confocal Laser Scanning Microscopy (CLSM), which are able to image extrudate microstructure at (sub-)µm resolution [64, 72]. CLSM requires the use of dyes, usually

Rhodamine B, to stain proteins. Additionally, dyes that stain carbohydrate can be used to simultaneously measure the dispersed carbohydrate phase [64, 73]. CLSM imaging, however, requires the extrudate sample to be cut in thin slices, because the imaging penetration depth is limited to tens of µm due to the optical opacity of extrudate samples. Furthermore, upon dye absorption the material swells slightly, which in turn can alter the microstructure of the protein fibre network. Alternatively, diffuse laser light reflectance (DR) is used as a fast method to assess the degree of fibre alignment with the potential for application *at line*. The method involves an incident laser beam, which creates a reflectance spot on the material that is captured by a digital camera [74, 75]. The light scatters on structures larger than its wavelength and propagates through the material through a continuous time random-walk principle [76]. In an anisotropic medium, a larger number of photons will scatter along the direction of anisotropy relative to scattering perpendicular to this direction. As a result, the degree of anisotropy in the microstructure can be elucidated by comparing the length and width of the reflectance spot at the surface of the extrudate. The length of these axes is used to calculate an anisotropy index (AI(DR)). In an isotropic sample, this shape will be circular with an AI(DR) close to 0 whilst, in an anisotropic sample, this shape will become elliptical with an AI(DR) between 0 and 1. Another method to study the µm-scale anisotropy in extrudates is polarised fluorescence spectroscopy. This method uses different wavelengths of polarised light to illuminate naturally occurring fluorophores, such as the amino acid tryptophan, in protein extrudates [77]. The fluorescence is measured with polarisers either parallel or perpendicular to each other and the intensity difference is used to define an anisotropy index. Additionally, by probing the entire range of excitation and emission wavelengths, molecular level information can be gained from various intrinsic fluorophores emitting at different wavelengths, although assessment of their relation to structure is not straightforward [77]. While the probed length scale in DR and polarised fluorescence spectroscopy is likely at a µm-scale, in AI(DR) structural anisotropy is averaged over a volume of roughly 5 mm in width and 5 mm in depth, due to the penetration of the laser.

Nanometre-scale measurement techniques are required to elucidate how the protein aggregates build up the microstructural protein network. Whilst electron microscopy and atomic force microscopy can technically reach a resolution down to 10 nm, they require extensive sample preparation and/or only probe the surface of a sample. Small angle scattering (SAS) techniques, using neutrons (SANS) or X-rays (SAXS), are an effective method to elucidate the internal nm-to-µm scale structure of extrudates [78, 79] and their combined use has been demonstrated for SPC extrudates [48]. Neutrons and X-rays both have wavelengths significantly smaller than visible light, respectively 0.18 nm and roughly 0.1 nm, which is comparable to atomic sizes and inter-distance spacings [80, 81]. Neutrons interact with the sample through nuclear interactions which can result in the scattering of the incident neutron beam. The scattering pattern can be used to acquire nm-to-µm scale

information on structure and anisotropy [81]. X-rays interact with the sample through electromagnetic interactions with the electron clouds of atoms in the sample [80] and scattering can be used in a similar manner to neutrons. However, due to their different nature, SANS is more suited for low electron density compounds than SAXS [81]. As a result, SANS and SAXS probe protein and carbohydrates differently in SPC extrudates [48]. SANS can give information of protein aggregate size [78], distance between scattering inhomogeneities [48], and the 13–125 nm-scale anisotropy of structures formed by these protein aggregates, including their angle [48, 78]. SAXS measurements can quantify anisotropic structures in the range of 100 nm to 1 µm [78]. This makes SANS and SAXS powerful techniques to elucidate the smallest structural components of the multiscale extrudate structure.

Finally, **at the molecular scale**, information about types of inter- and intra-molecular bonds is inferred. Fourier transform infra-red (FTIR) spectroscopy can be used to acquire insights into the secondary protein structure, such as relative abundance of α-helix and β-sheets [82]; yet freeze-drying and subsequent powdering of the sample is required. To gain information on relative differences in inter-molecular covalent and non-covalent bond formation, dissolution assays are used. The method dissolves protein in buffers of varying degrees of denaturing strength and subsequently analyses these using combustion methods [49] or high-pressure liquid chromatography [83].

As outlined in this section, an arsenal of measuring techniques is present that enable structure characterisation at different separate length scales. However, many of these techniques are invasive, risk damaging of the structure, are limited to surface regions only, operate at a single length scale, lack spatial and/or molecular-level information or are difficult to translate to *in situ* conditions. This motivates the use of Nuclear Magnetic Resonance (NMR)-based techniques, including MRI, which can provide structural information at multiple length scales in a non-invasive and spatially-resolved manner.

1.4.2 Magnetic Resonance Imaging (MRI)

Time-domain (TD-)NMR and MRI have been applied to study several types of soft, porous materials such as food systems [84–86]. Hitherto, characterisation of plant-protein high-moisture extrudates has been performed using low-field TD-NMR or imaging to respectively determine the fraction of freezable/non-freezable water [87] or spatial distribution of water [88–91]. However, these imaging results achieved little contrast between water-rich and protein-rich regions as visualised by XRT [63]. For the first time, in the present work, TD-NMR and MRI methods are applied to quantitatively determine structural anisotropy in high-moisture extrudates of soy protein at multiple length scales. The use of high magnetic field strengths and strong magnetic field gradients for imaging has the potential to increase both the sensitivity and the spatial resolution achievable in the NMR/MRI measurements.

Principles of NMR

Atomic and subatomic particles, such as nuclei, protons, neutrons and electrons, intrinsically possess a spin angular momentum and magnetic dipole moment. When a nucleus has a non-null magnetic moment, it can interact with an externally applied magnetic field [92]. The most straightforward example, and also the main nuclei of interest in this thesis, is the hydrogen atom, ^{1}H, because it is highly abundant in most materials and has relatively simple NMR properties.

NMR-active nuclei with non-zero spin are randomly oriented in the absence of an external magnetic field. When an external magnetic field called B_0 is applied, they tend to align with this field. As a result, there is a non-null net magnetisation arising from the sum of all nuclear magnetic moments within the sample. The population distribution of nuclear spins between energy levels in a magnetic field, B_0, is determined by the Boltzmann equation: $\frac{N_{upper}}{N_{lower}} = e^{\frac{\gamma\hbar B_0}{k_b T}}$, where the ratio between the spin in a high-energy state (N_{upper}) and low-energy state (N_{lower}) is dependent on the nucleus-specific gyromagnetic ratio, $\gamma = 267.5 \cdot 10^6$ rad $s^{-1}T^{-1}$ for ^{1}H, the reduced Planck's constant, $\hbar$, the external magnetic field, B_0, Boltzmann constant, k_B and temperature, T. Because there is a finite thermal energy in the system, scaling with temperature according to k_BT, it is only slightly more favourable for spins to be in an orientation with low magnetic energy. The Boltzmann distribution determines the NMR signal intensity and is only $\sim 1 \cdot 10^{-5}$ for ^{1}H-nuclei at room temperature in an external magnetic field of 14 T, showing that NMR is a low-sensitivity technique.

Due to their spin angular momentum, nuclei precess around the B_0 axis at a frequency called the Larmor frequency, namely $\omega_0 = \gamma B_0$. The transition between nuclear spin states, thus, occurs with an energy, $\Delta E = \gamma\hbar B_0$, dependent on the nuclear resonance frequency [92].

In NMR, the net nuclear magnetisation, called M_0, is manipulated using radio frequency (r.f.) pulses that apply a temporary oscillating magnetic field at the Larmor frequency, called B_1. Due to this short perturbation of the B_0 field, the magnetisation is tilted from the B_0 axis, commonly the z-axis, by 90° ($\pi/2$ radians) towards the xy-plane. The extent of this perturbation of the net magnetisation depends on the r.f. pulse strength and duration. The xy-component of the precession around the z-axis of the net magnetisation induces an oscillating current in the r.f. coil which in turn gives rise to a voltage. This voltage is the measured NMR signal, called the free-induction decay (FID), and is time-dependent due to the return of the magnetisation to thermal equilibrium. Since each ^{1}H in a molecule has its own microscopic magnetic field, spins may locally experience small fluctuations in the total magnetic field strength. As a result, the spins do not precess all at the same frequency. Additionally, differences in the local electron density around the nuclei as well as imperfections in the B_0 field contribute to this effect. The former is the basis of NMR

spectroscopy, where these small differences in frequency, called the chemical shift, are used to characterise molecular groups in a sample. [92, 93].

Relaxation of the NMR signal and time-domain NMR

As the term free-induction decay suggests, the measured NMR signal in the xy-plane does not continue indefinitely. The signal decay arises from two relaxation mechanisms: the longitudinal and transverse spin relaxation. Longitudinal relaxation refers to the return of the spins to their thermal equilibrium, along the B_0 field. This form of relaxation involves the transfer energy exchange between the nuclear spin system and the surrounding molecules. To re-establish thermal equilibrium, the local magnetic fields must fluctuate at frequences near the Larmor frequency [93]. The time constant by which this process occurs is the T_1 relaxation time. Transverse relaxation refers to the loss of phase coherence of the spins precessing in the xy-plane. Differently from T_1, T_2 is sensitive to all *local* field fluctuations, including low-frequency, "quasi-static", fields originating from neighbouring nuclei. Such fields cause individual spins to experience slightly different local magnetic fields, making them precess at slightly different frequencies, thus leading to rapid dephasing. Consequently, the magnetisation in the xy-plane decreases to zero. The time constant by which this process occurs is the T_2 relaxation time. As a result, transverse relaxation can occur faster than longitudinal relaxation.

The molecular origin of relaxation and the associated relaxation time, or the inverse called relaxation rate, depends on the rotational motion of the molecules around their own axis, called the rotational correlation time, τ_c. This molecular parameter is affected by the size of the molecule, the temperature of the sample and the viscosity of the medium. Thus, the relaxation behaviour of nuclei can give information on the local molecular environment of the molecule these nuclei reside on. Generally, T_1 and T_2 values are long for small rapidly tumbling molecules such as water because the frequency of tumbling is far away from the Larmor frequency and interactions of the magnetic dipoles of the molecules are fleeting. As schematically shown in Fig. 1.3, when the tumbling rate is close to the Larmor frequency, the transfer of energy between spins is optimal and the associated T_1 value is smallest and close to value for T_2. When molecular tumbling becomes slower than the Larmor frequency, which is the case for large molecules or solids, the T_1 value increases with τ_c. However, the value for T_2 decreases almost linearly. As the tumbling rate falls below the Larmor frequency, local fields created by each spin fluctuate less and less and assume an increasingly static character, effectively dephasing the spins in this environment.

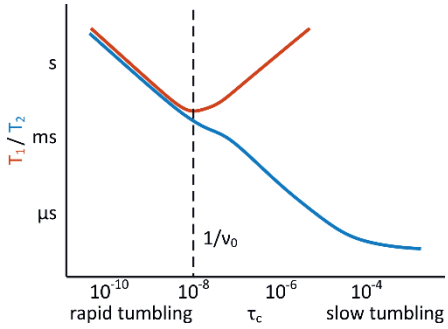

Fig. 1.3: *Schematic of the relation between the T_1/T_2 and correlation time τ_c. The dashed line indicates $1/\nu_0$.*

To measure T_1 values, a so-called Inversion Recovery (IR) experiment can be performed. First a 180° (π radians) pulse is given to the system, rotating the spins from their equilibrium position to the -z axis, along which longitudinal relaxation occurs. This is required because transverse relaxation occurs as soon as there is non-null magnetisation in the xy-plane. To measure the signal, however, a 90° pulse to rotate the magnetisation to the xy-plane is required. By varying the delay between the initial 180° and subsequent 90° pulse, a different amount of longitudinal relaxation can take place. As a result, a different magnitude of the net magnetisation in the xy-plane will be measured during acquisition of the FID. The following relation can be used to find a value for T_1 [94]:

$$M_z(t) = M_0\left(1 - ke^{-\frac{t}{T_1}}\right). \qquad \text{Eq. 1.1}$$

Here, k = 2 when using the IR pulse sequence. When applying a 90° pulse to a spin system in equilibrium, the magnetisation shifts to the xy-plane. The FID that is measured directly after the 90° pulse, however, includes the effect of static inhomogeneities of the B_0 field on top of the molecular dynamics affecting T_2. This faster decay rate is called the T_2^* and can be corrected for by using the so-called spin-echo. By applying a 180° pulse in the xy-plane at fixed intervals after the 90° pulse, the spin system rotates around the x or y axis. Effectively, the net magnetisation has reversed direction whereas the individual precession frequencies remain unaffected. As a result, the 'faster' and 'slower' spins rephase into an echo, instead of dephasing further, as schematically shown in Fig 1.4. The signal intensity of this echo only decreases due to the loss of coherence by irreversible dephasing from molecular origin. By applying a number, n, of subsequent 180° pulses, spaced by the echo time, T_E, a so-call Carr Purcell Meiboom Gill (CPMG) sequence [95], a complete T_2 decay can be measured which can be fitted to extract the T_2 relaxation time using the following relation [94]:

$$M_{xy}(t) = M_0 e^{-nT_E/T_2}. \qquad \text{Eq. 1.2}$$

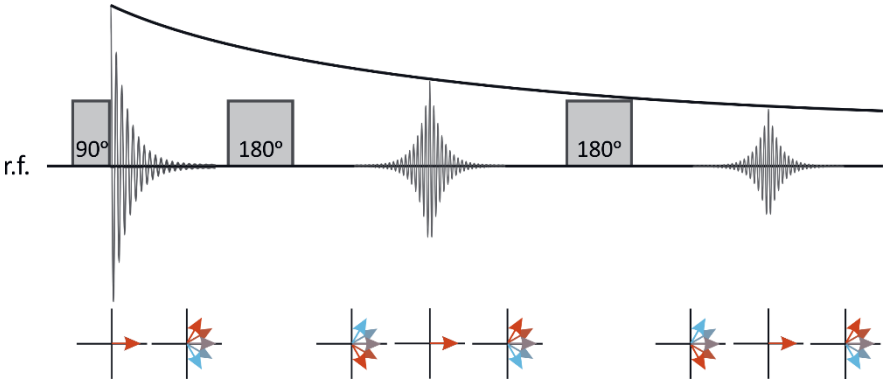

Fig. 1.4: *Schematic representation of the spin-echo pulse sequence (top) and the effect on the spin phase ensemble. The 'slower' precessing spins are displayed in red, the 'faster' precessing spins in blue.*

Spatial dependence and magnetic resonance imaging

To create a spatially dependant signal, magnetic field gradients, which are wire coils wound in a specific way, are used. When a current is passed through these coils, a second magnet field is applied which alters the resonance frequency of the spins as a function of position according to:

$$\omega(x) = \gamma B(x) = \gamma(B_0 + xG_x), \qquad \text{Eq. 1.3}$$

with the spatially-dependent precession frequency, ω(x), which depends on the gyromagnetic ratio, γ, and the spatially-dependent magnetic field, B(x). The spatially-dependent magnetic field is a combination of the static B_0 field and the applied gradient, G_x in T/m as a function of place, x. In an MRI system, usually three such gradients are present, one for each orthogonal cartesian direction. By linearly combining these three gradients, spatial dependence in any cartesian direction can be achieved. Because of this, imaging gradients are usually not referred to as x, y and z gradients, but as read, phase and slice-selective gradients, based on their purpose in the pulse sequence. Figure 1.5 shows a schematic diagram of such pulse sequence using a spin-echo.

The first imaging dimension is acquired by using the so-called slice gradient during application of the 90° and 180° pulses (G_{slice} in Fig. 1.5). Because the gradient locally alters the Larmor frequency and the 90° pulse only excites spins when it is in resonance with the Larmor frequency, a specific region can be selectively rotated to the xy-plane without affecting spins in the rest of the sample. When the same gradient and r.f. frequency is applied for the 180° pulse of a spin echo, again only this region is affected.

The second imaging dimension can be achieved by keeping one gradient, the read gradient also called the frequency-encoding gradient (G_{read} in Fig. 1.5), continuously on during

acquisition of the data. The acquired data will thus contain multiple frequences which can be decoded to spatial positions based on the used gradient strength and combination of the cartesian magnetic field gradient coils. To ensure that the peak of the signal echo, when no net phase dispersion from the use of gradients is present, is in the centre of the readout window, a dephasing gradient is used before signal acquisition of half the strength or duration of the read gradient. Note that the chemical shift information in such imaging scheme is lost.

The third imaging dimension is acquired by pulsing a gradient perpendicular to the read gradient, during the preparation period before acquisition of the data, called the phase-encoding gradient (G_{phase} in Fig. 1.5). The effect is a net accumulation of phase while the gradient is on which is retained when the gradient is switched off. The phase difference of the acquired signal relative to a reference signal, for example acquired without phase-encoding, can then be used to decode the spatial location of the signals. This gradient is ramped between different acquisitions to sample the entire range of spatial frequencies required for a 2D image. Thus, this imaging dimension requires significantly longer to sample than the read gradient dimension.

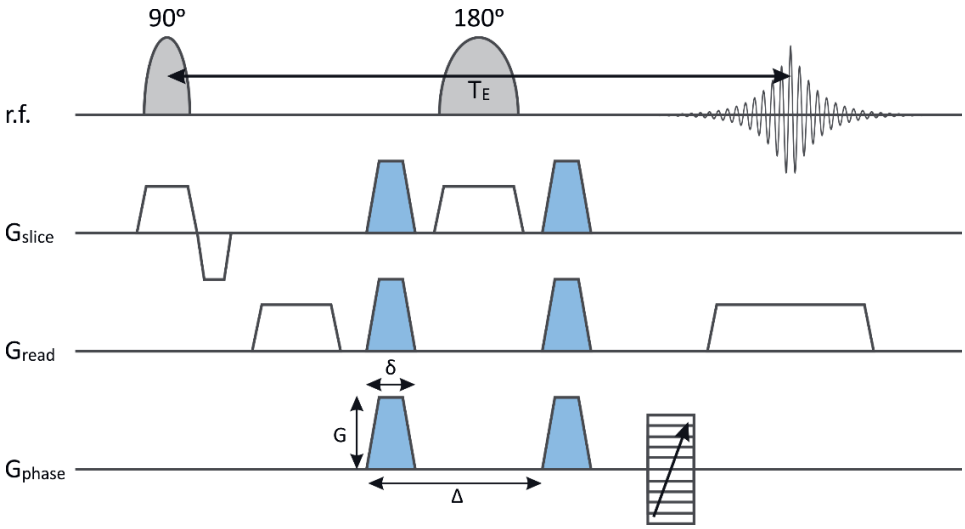

Fig. 1.5: *Diagram of a spin-echo MRI pulse sequence including the soft r.f. pulses and data acquisition in grey, trapezoidal imaging gradients in white and trapezoidal motion encoding gradients in blue. The motion encoding gradients are arbitrarily chosen, but in this example would point diagonally out of plane from the xy-plane of the image. The echo time, T_E, between the 90° pulse and the centre of the echo is marked. Additionally, the gradient strength, G, the gradient duration, δ, and the gradient spacing, Δ, are shown. The slice-selective gradient, G_{slice}, is used during the soft r.f. pulse and includes a rephasing lobe just after the 90° pulse to correct for accumulation of phase dispersion during the soft pulse. The read gradient, G_{read}, is used during readout of the signal. The dephasing lobe can be situated with positive polarity before the 180° as shown, or directly before the readout itself with negative polarity. The ramped phase-encoding gradient, G_{phase}, is pulsed for a short duration to accumulate a phase shift. Repeat acquisitions are required to use each of the displayed ramp intensities, indicated by an arrow.*

By combining all three gradients in an MRI pulse sequence, a 2D image can be constructed where each pixel in the image represents intensity data, weighted for T_1 and/or T_2, coming from a small 3D volume (voxel) in the sample. The molecular dynamics of the ^{1}H atoms in these voxels will influence the longitudinal and transverse relaxation and thus the relative intensity of the acquired signal. This, in combination with proton density itself, is the origin of the image intensity and contrast in MRI images [96].

Encoding of self-diffusive motion

The accumulated phase difference acquired by the spins during a short pulsed field gradient (PFG) can in principle be reversed if, at a later timepoint, the exact same PFG but with opposite polarity is applied. Alternatively, in a spin-echo, two identical PFG equidistant from the 180° pulse are used (blue gradients in Fig. 1.5 and 1.6). In the presence of thermally driven molecular motion, dependent on the size of the molecule and the viscosity of the liquid, called translational self-diffusion, a molecule can travel to a different location in the time period between the two PFG pulses. Consequently, as schematically depicted in Fig. 1.6, when the second PFG is applied, the dephasing of the spins by the first PFG and the rephasing by the second PFG is mismatched, resulting in signal attenuation due to a loss of phase coherence. This signal attenuation as a function of the gradient strength or the time between gradients can be used to probe the self-diffusional dynamics of the ^{1}H nuclei. The additional term in the signal intensity decay, apart from attenuation of the signal due to relaxation, is:

$$S(t) = S_0 e^{-bD}, \qquad \text{with } b = \gamma^2 G^2 \delta^2 (\Delta - \delta/3). \qquad \text{Eq. 1.4}$$

Here, D is the apparent ^{1}H self-diffusion coefficient and b is the factor that reflects the strength and timing of the gradients used to encode for diffusion, which depends on the gyromagnetic ratio, γ, gradient strength, G, the gradient duration, δ, and the time between PFGs, called the diffusion time, Δ [97]. By acquiring multiple images at different gradient strengths or Δ, a decay curve can be constructed from which the diffusion coefficient can be fitted [98]. This method assumes free isotropic self-diffusion of the molecules. However, if the translational molecular motion is restricted by the environment, for example water in a dense protein matrix, the acquired diffusion coefficient might appear smaller than is the case.

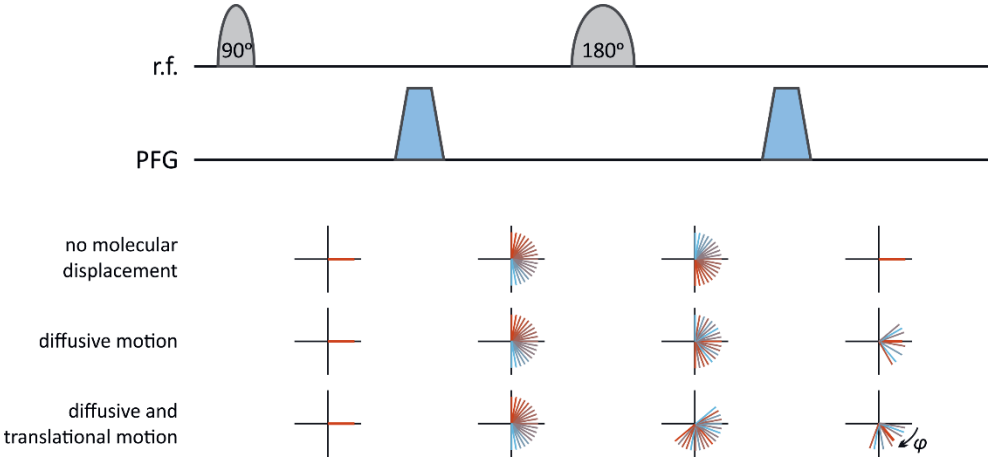

Fig. 1.6: *Schematic diagram of the effect of diffusion and translational motion, such as flow, on the phase of the spin ensemble. The 'slower' precessing spins are displayed in red, the 'faster' precessing spins in blue. In the presence of translational motion, a phase shift is accumulated. For simplicity, the effect of T_2 on the phase coherence is ignored in the diagram.*

Diffusion Tensor (DT-)MRI

If such restriction of the molecular self-diffusion by the matrix is non-uniform, for example water diffusing between the aligned fibres in muscle tissue, the measured apparent self-diffusion coefficient cannot adequately describe the diffusion behaviour in the system. The gradient direction used for self-diffusion encoding is the direction in which the measurement is sensitive to the effect of self-diffusive motion. This property can be used to acquire information about the anisotropy of diffusion by repeating the same acquisition using different combinations of multiple PFG directions. In the simplest form, read, phase and slice-selective magnetic field gradients can be applied to obtain three orthogonal diffusion-weighted images. If three diagonal directions, namely read-phase, read-slice and phase-slice are also encoded, a so-called self-diffusion tensor can be constructed (See Fig. 1.7). The self-diffusion tensor holds information about the magnitude and direction of molecular self- diffusion in three dimensions, which can be extracted by calculating the self-diffusion eigenvalues ($\lambda_{1,2,3}$) of the tensor and their associated eigenvectors ($\varepsilon_{1,2,3}$) by applying: $\boldsymbol{D}\varepsilon_i = \lambda_i\varepsilon_i = \lambda_i\boldsymbol{I}\varepsilon_i$ [99]. The eigenvalues and associated eigenvectors (See Fig 1.7) are commonly sorted according to their magnitude, *i.e.* fastest, intermediate and slowest self-diffusion coefficient, such that: $\lambda_1 > \lambda_2 > \lambda_3$. From these, properties such as the fractional anisotropy (FA) and the Principal Diffusion Direction (PDD) can be calculated. The former gives a measure for how anisotropic the self-diffusion within a voxel is by using the following linear combination of the self-diffusion eigenvalues and the average diffusion coefficient, D_{av} [100]:

$$FA = \sqrt{\frac{3[(\lambda_1 - D_{av})^2 + (\lambda_2 - D_{av})^2 + (\lambda_3 - D_{av})^2]}{2[\lambda_1^2 + \lambda_2^2 + \lambda_3^2]}}. \quad \text{Eq. 1.5}$$

The PDD provides the orientation of each eigenvalue in 3D space. By creating maps of these eigenvectors, where the x, y, and z-orientation are encoded in the three colour channels, Red, Green and Blue (RGB), detailed information about the self-diffusion anisotropy can be acquired [101]. By increasing the number of self-diffusion encoding directions beyond the initial six tensor elements, the self-diffusion anisotropy can be calculated more accurately at the cost of additional measurement time [100, 102]. Generally, not the entire self-diffusion decay is measured for each orientation. Instead, multiple images (~8) are acquired with minimal self-diffusion encoding, i.e. b ~ 0 s/mm^2 and a larger amount (~30–60) of acquisitions using different PFG directions, e.g. at b = 1000 s/mm^2 [102].

$$\boldsymbol{D} = \begin{bmatrix} D_{xx} & D_{xy} & D_{xz} \\ D_{yx} & D_{yy} & D_{yz} \\ D_{zx} & D_{zy} & D_{zz} \end{bmatrix}$$

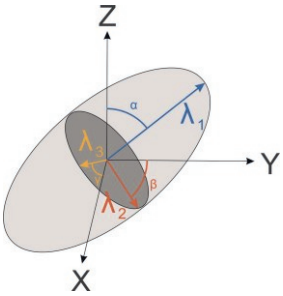

Fig. 1.7: *Self-diffusion tensor and schematic representation of the diffusion ellipsoid that can be drawn using the eigenvalues (magnitude) and eigenvectors (orientation) of the tensor.*

MRI flow velocimetry

Using the same principle as diffusion encoding, the bulk molecular motions of molecules can be measured as schematically depicted in Fig. 1.6. Since the velocities associated with flow are generally much higher than the random diffusion of a molecule through Brownian motion, gradient amplitudes are smaller for flow measurements. In the case of a spin-echo, a PFG is placed before and after the 180° pulse and the direction of these PFGs should be parallel to the flow of the medium. In a static sample, the net dephasing accumulated by the PFGs during this time is zero since the second PFG refocuses the dephasing applied by the first PFG (see Fig. 1.6). However, when the sample is locally displaced as a result of flow, during the time, Δ, by a distance vΔ, the second PFG cannot refocus the dephasing from the first PFG, and thus a phase shift, φ, is accumulated. The magnitude of this phase shift is be given by: $\varphi = \gamma G \delta v \Delta$. The phase shift is, thus, directly proportional to the velocity for phase shifts defined between -π and π. Phase shifts outside this range may appear as motion in the reverse direction [103].

1.5 Thesis Outline

The main aim of this thesis is two-fold. Firstly, the need for MRI-based techniques to quantitatively analyse the processing-structure relation is addressed. Secondly, these techniques are used together with other measuring modalities operating at smaller length scales, such as CLSM or SAS techniques, to investigate the mechanisms driving the multiscale structure formation during the HME processing of soy protein. These complementary measurement techniques will be used to address **RQ1–5**. In Fig. 1.8, a diagram is presented of each chapter in the present thesis. Chapters in green (**2**, **3** and **6**) focus on MRI method development for quantitative analysis of extrudate structure. Additionally, chapter 2 investigates the post-processing-structure relation. Chapters in yellow (**3**, **4** and **5**) focus on characterising the processing-structure relation of HME.

In **Chapter 2**, MRI is presented as a non-invasive method to study the phase-separated structure, into protein-rich and water-rich phases, of high-moisture extrudates at the sub-mm scale. Extrudates are produced using SPC as well as SPI. A comparison is made between spatially-resolved time domain (TD-)MRI and bulk TD-NMR results to provide a comprehensive assessment of the material. This shows the feasibility of the latter, industrially more accessible, system to quantify phase separation. Furthermore, **(RQ 5)** is addressed by studying the effect of post-processing on MRI contrast between the protein-rich and water-rich phases.

Chapter 3 builds on the results from the previous chapter and investigates the capability of DT-MRI as an MRI-based technique to assess phase-separated structure in SPC extrudates down to the µm-scale. Here, DT-MRI utilises the orientation dependence of the self-diffusion coefficient of water molecules as a molecular probe of structural anisotropy. For this purpose, SPC extrudates produced at three different pH values are investigated. T_2-weighted MRI images, showing the sub-mm scale structure, are quantified using the Rotational Fourier Transform (RFT) algorithm [104]. Thereafter, a comparison is made with the µm-scale structure as observed by CLSM. The combined use of DT-MRI and T_2-weighted MRI enables characterising at what length scales, from µm-to-mm scale, phase-separation into lamellar structures occurs and addresses **(RQ 3)**. The applicability of the adopted (DT-)MRI method to other structured protein products, particularly mozzarella, is discussed.

In **Chapter 4,** a multiscale mapping of structure formation in the complete HME process at pilot-scale is performed to address **(RQ 1)**. Material is taken from the barrel sections, transition zone and cooling die after performing a dead-stop operation and characterised using complementary measurement techniques. At the nm-to-µm scale, SANS and SAXS are used to study protein aggregation and fibril formation [48]. The µm-to-mm scale is characterised by 2D DR as well as by T_2-weigthed MRI images analysed using RFT. The effect of a breaker plate is also briefly discussed.

In **Chapter 5**, pH-shifting is investigated as a processing aid to direct structure formation during HME. To address **(RQ 2)** and unravel the dominant multiscale structuring mechanism, including protein fibril formation and phase separation into PR and WR regions, a comprehensive study is performed on extrudate samples shifted to pH values between 4.2 and 9.9. These samples are assessed at multiple length scales: at the molecular scale using protein solubility, at the nm-scale using SANS, at the µm-scale using SAXS and AI(DR), and at the sub-mm scale by MRI. Results are compared to texture measurements. Additionally, the effect of pH-shifting in relation to extrusion scale is discussed.

In **Chapter 6**, the use of MRI to *in situ* study protein melt flow through the cooling die is explored. A custom MRI-transparent cooling die, able to run through a benchtop MRI magnet, is designed and implemented. This cooling die is used to extrude SPC at three different pH values and the flow of the protein melt inside the cooling die is measured by MRI velocimetry. This enables direct measurement of the effect of wall-slip and enables addressing **(RQ 4)**. The resulting flow velocity profiles are fitted using an adapted Herschel-Bulkley model, which includes the effect of the temperature gradient in the melt.

The general discussion, in **Chapter 7**, consists of three parts. Firstly, the main findings and answers to the RQs in this thesis are compiled and related to their broader context. Secondly, the hierarchical structure of high-moisture extrudates is discussed and future topics of research are presented. Finally, the use of MRI to study HME cooling die flow *in situ* is discussed as well as ways to improve the flow-MRI platform discussed in this thesis.

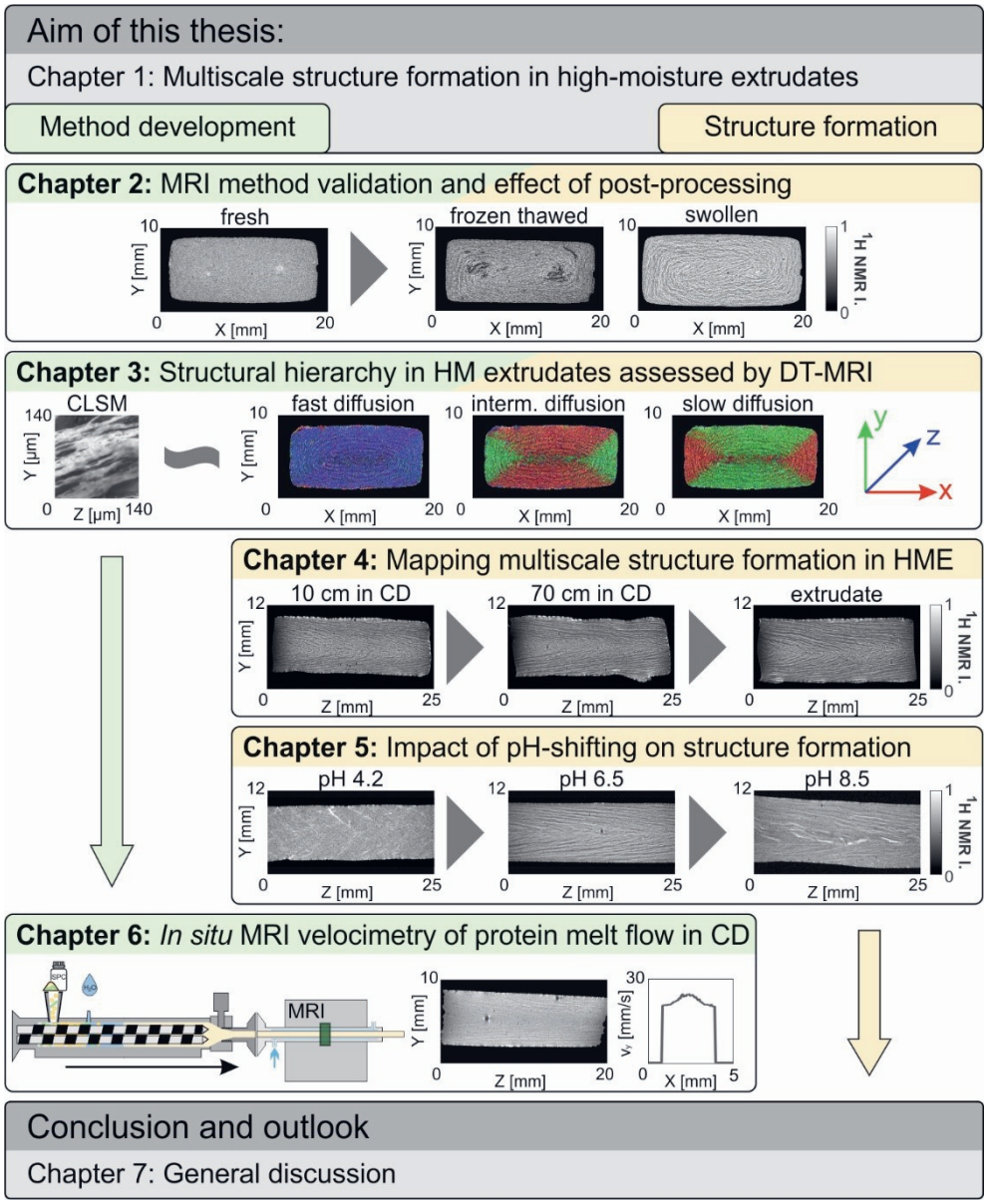

Fig. 1.8: *Graphical outline of this thesis, showing the main objective discussed in each chapter.* ***Chapters 2*** *and* ***3*** *describe the capability of MRI to ex situ characterise the development of phase-separated lamellar regions within the structure of high-moisture extrudates of soy protein. In* ***Chapters 4*** *and* ***5*** *these methods are used to ex situ characterise the multiscale structure formation during HME of SPC, respectively by dead-stop operation and pH-shifting. In* ***Chapter 6****, the development and application of a flow-MRI platform is described for spatially resolving flow properties in situ inside the cooling die, during HME. Such in situ velocimetry data were used to parametrise current in silico models of HME.*

References

[1] P. R. Ehrlich and A. H. Ehrlich, "Can a collapse of global civilization be avoided?," *Proc. R. Soc. B Biol. Sci.*, vol. 280, no. 1754, 2013, doi: 10.1098/rspb.2012.2845.

[2] H. Aiking and J. de Boer, "The next protein transition," *Trends Food Sci. Technol.*, vol. 105, no. July 2018, pp. 515–522, 2020, doi: 10.1016/j.tifs.2018.07.008.

[3] J. Webb *et al.*, "Managing ammonia emissions from livestock production in Europe," *Environ. Pollut.*, vol. 135, no. 3 SPEC. ISS., pp. 399–406, 2005, doi: 10.1016/j.envpol.2004.11.013.

[4] H. H. E. van Zanten, H. Mollenhorst, C. W. Klootwijk, C. E. van Middelaar, and I. J. M. de Boer, "Global food supply: land use efficiency of livestock systems," *Int. J. Life Cycle Assess.*, vol. 21, no. 5, pp. 747–758, 2016, doi: 10.1007/s11367-015-0944-1.

[5] C. Bonnet, Z. Bouamra-Mechemache, V. Réquillart, and N. Treich, "Viewpoint: Regulating meat consumption to improve health, the environment and animal welfare," *Food Policy*, vol. 97, no. February, p. 101847, 2020, doi: 10.1016/j.foodpol.2020.101847.

[6] B. A. Jones *et al.*, "Zoonosis emergence linked to agricultural intensification and environmental change," *Proc. Natl. Acad. Sci. U. S. A.*, vol. 110, no. 21, pp. 8399–8404, 2013, doi: 10.1073/pnas.1208059110.

[7] H. C. J. Godfray *et al.*, "Meat consumption, health, and the environment," *Science*, vol. 361, no. 6399, 2018, doi: 10.1126/science.aam5324.

[8] E. P. Köster, "Diversity in the determinants of food choice: A psychological perspective," *Food Qual. Prefer.*, vol. 20, no. 2, pp. 70–82, 2009, doi: 10.1016/j.foodqual.2007.11.002.

[9] C. Hartmann and M. Siegrist, "Consumer perception and behaviour regarding sustainable protein consumption: A systematic review," *Trends Food Sci. Technol.*, vol. 61, pp. 11–25, 2017, doi: 10.1016/j.tifs.2016.12.006.

[10] A. C. Hoek, P. A. Luning, P. Weijzen, W. Engels, F. J. Kok, and C. de Graaf, "Replacement of meat by meat substitutes. A survey on person- and product-related factors in consumer acceptance," *Appetite*, vol. 56, no. 3, pp. 662–673, 2011, doi: 10.1016/j.appet.2011.02.001.

[11] A. C. Hoek, S. Malekpour, R. Raven, E. Court, and E. Byrne, "'Towards environmentally sustainable food systems: decision-making factors in sustainable food production and consumption,'" *Sustain. Prod. Consum.*, vol. 26, pp. 610–626, 2021, doi: 10.1016/j.spc.2020.12.009.

[12] E. S. Collier *et al.*, "Identifying barriers to decreasing meat consumption and increasing acceptance of meat substitutes among Swedish consumers," *Appetite*, vol. 167, no. August, p. 105643, 2021, doi: 10.1016/j.appet.2021.105643.

[13] J. He, N. M. Evans, H. Liu, and S. Shao, "A review of research on plant-based meat alternatives: Driving forces, history, manufacturing, and consumer attitudes," *Compr. Rev. Food Sci. Food Saf.*, vol. 19, no. 5, pp. 2639–2656, 2020, doi: 10.1111/1541-4337.12610.

[14] A. Loumeaud, P. Pouletaut, S. F. Bensamoun, D. George, and S. Chatelin, "Multiscale Mechanical Modeling of Skeletal Muscle: A Systemic Review of the Literature," *J. Med. Biol. Eng.*, vol. 44, no. 3, pp. 337–356, 2024, doi: 10.1007/s40846-024-00879-3.

[15] K. Chang and H. J. Hou, "Science and technology of tofu making," in *Handbook of fruits and vegetable processing*, 1st ed., Y. H. Hui, S. Ghazala, D. M. Graham, K. D. Murrell, and W. K. Nip, Eds. CRC Press, 2003, pp. 443–478. doi: https://doi.org/10.1201/9780203912911.

[16] P. Dinesh Babu, R. Bhakyaraj, and R. Vidhyalakshmi, "A Low Cost Nutritious Food 'Tempeh'-A Review," *World J. Dairy Food Sci.*, vol. 4, no. 1, pp. 22–27, 2009.

[17] H. Akdogan, "Pressure, torque, and energy responses of a twin screw extruder at high moisture contents," *Food Res. Int.*, vol. 29, no. 5–6, pp. 423–429, 1996, doi: 10.1016/s0963-9969(96)00036-1.

[18] B. L. Dekkers, R. M. Boom, and A. J. van der Goot, "Structuring processes for meat analogues," *Trends Food Sci. Technol.*, vol. 81, no. May, pp. 25–36, 2018, doi: 10.1016/j.tifs.2018.08.011.

[19] K. Kyriakopoulou, B. Dekkers, and A. J. van der Goot, *Plant-Based Meat Analogues*. Elsevier Inc., 2019. doi: 10.1016/B978-0-12-814874-7.00006-7.

[20] J. H. Chiang, S. M. Loveday, A. K. Hardacre, and M. E. Parker, "Effects of soy protein to wheat gluten ratio on the physicochemical properties of extruded meat analogues," *Food Struct.*, vol. 19, no. September 2018, p. 100102, 2019, doi: 10.1016/j.foostr.2018.11.002.

[21] X. Zhang, Y. Zhao, T. Zhang, Y. Zhang, L. Jiang, and X. Sui, "High moisture extrusion of soy protein and wheat gluten blend: An underlying mechanism for the formation of fibrous structures," *Lwt*, vol. 163, no. May, p. 113561, 2022, doi: 10.1016/j.lwt.2022.113561.

[22] K. Kyriakopoulou, J. K. Keppler, and A. J. van der Goot, "Functionality of ingredients and additives in plant-based meat analogues," *Foods*, vol. 10, no. 3, 2021, doi: 10.3390/foods10030600.

[23] Y. Wang *et al.*, "The development process of plant-based meat alternatives: Raw material formulations and processing strategies," *Food Res. Int.*, vol. 167, no. February, p. 112689, 2023, doi: 10.1016/j.foodres.2023.112689.

[24] K. E. Preece, N. Hooshyar, and N. J. Zuidam, "Whole soybean protein extraction processes: A review," *Innov. Food Sci. Emerg. Technol.*, vol. 43, no. July, pp. 163–172, 2017, doi: 10.1016/j.ifset.2017.07.024.

[25] N. A. Deak, L. A. Johnson, E. W. Lusas, and K. C. Rhee, "Soy Protein Products, Processing, and Utilization," *Soybeans Chem. Prod. Process. Util.*, pp. 661–724, 2008, doi: 10.1016/B978-1-893997-64-6.50022-6.

[26] K. H. Lee, H. S. Ryu, and K. C. Rhee, "Protein solubility characteristics of commercial soy protein products," *JAOCS, J. Am. Oil Chem. Soc.*, vol. 80, no. 1, pp. 85–90, 2003, doi: 10.1007/s11746-003-0656-6.

[27] J. Li *et al.*, "Varying precipitation conditions allow directing the composition and physical properties of soy protein concentrates," *J. Food Sci.*, vol. 89, no. 2, pp. 925–940, 2024, doi: 10.1111/1750-3841.16907.

[28] H. Akdogan, "High moisture food extrusion," *Int. J. Food Sci. Technol.*, vol. 34, no. 3, pp. 195–207, 1999, doi: 10.1046/j.1365-2621.1999.00256.x.

[29] R. G. M. Van der Sman and A. J. Van der Goot, "Hypotheses concerning structuring of extruded meat analogs," *Curr. Res. Food Sci.*, vol. 6, no. May, p. 100510, 2023, doi: 10.1016/j.crfs.2023.100510.

[30] V. L. Pietsch, J. M. Bühler, H. P. Karbstein, and M. A. Emin, "High moisture extrusion of soy protein concentrate: Influence of thermomechanical treatment on protein-protein interactions and rheological properties," *J. Food Eng.*, vol. 251, pp. 11–18, Jun. 2019, doi: 10.1016/j.jfoodeng.2019.01.001.

[31] A. Nisov, M. Nikinmaa, E. Nordlund, and N. Sozer, "Effect of pH and temperature on fibrous structure formation of plant proteins during high-moisture extrusion processing," *Food Res. Int.*, vol. 156, p. 111089, Jun. 2022, doi: 10.1016/j.foodres.2022.111089.

[32] P. Wittek, H. P. Karbstein, M. Azad Emin, M. José, and B. Apesteguía, "Blending Proteins in High Moisture Extrusion to Design Meat Analogues: Rheological Properties, Morphology Development and Product Properties," *Foods*, vol. 10, no. 07, p. 1509, 2021, doi: 10.3390/foods.

[33] P. Wittek, F. Ellwanger, H. P. Karbstein, and M. A. Emin, "Morphology development and flow characteristics during high moisture extrusion of a plant-based meat analogue," *Foods*, vol. 10, no. 8, Aug. 2021, doi: 10.3390/foods10081753.

[34] S. H. V Cornet, S. J. E. Snel, J. Lesschen, A. Jan, V. Der Goot, and R. G. M. Van Der Sman, "Enhancing the water holding capacity of model meat analogues through marinade composition," *J. Food Eng.*, vol. 290, p. 110283, 2021, doi: 10.1016/j.jfoodeng.2020.110283.

[35] O. Yuliarti, T. J. Kiat Kovis, and N. J. Yi, "Structuring the meat analogue by using plant-based derived composites," *J. Food Eng.*, vol. 288, no. January 2020, p. 110138, 2021, doi: 10.1016/j.jfoodeng.2020.110138.

[36] M. Peleg, "On fundamental issues in texture evaluation and texturization - A view," *Food Hydrocoll.*, vol. 20, no. 4, pp. 405–414, 2006, doi: 10.1016/j.foodhyd.2005.10.008.

[37] M. Schlangen, I. van der Doef, A. J. van der Goot, M. P. Clausen, and T. E. Kodger, "Meat analogues: The relationship between mechanical anisotropy, macrostructure, and microstructure," *Curr. Res. Food Sci.*, vol. 10, no. December 2024, p. 100980, 2025, doi: 10.1016/j.crfs.2025.100980.

[38] R. Osen, S. Toelstede, F. Wild, P. Eisner, and U. Schweiggert-Weisz, "High moisture extrusion cooking of

pea protein isolates: Raw material characteristics, extruder responses, and texture properties," *J. Food Eng.*, vol. 127, pp. 67–74, 2014, doi: 10.1016/j.jfoodeng.2013.11.023.

[39] M. Immonen, A. Chandrakusuma, J. Sibakov, M. Poikelispää, and T. Sontag-Strohm, "Texturization of a Blend of Pea and Destarched Oat Protein Using High-Moisture Extrusion," *Foods*, vol. 10, no. 7, p. 1517, 2021, doi: https://doi.org/10.3390/foods10071517.

[40] V. L. Pietsch, R. Werner, H. P. Karbstein, and M. A. Emin, "High moisture extrusion of wheat gluten: Relationship between process parameters, protein polymerization, and final product characteristics," *J. Food Eng.*, vol. 259, no. September 2018, pp. 3–11, 2019, doi: 10.1016/j.jfoodeng.2019.04.006.

[41] S. H. V. Cornet, S. J. E. Snel, F. K. G. Schreuders, R. G. M. van der Sman, M. Beyrer, and A. J. van der Goot, "Thermo-mechanical processing of plant proteins using shear cell and high-moisture extrusion cooking," *Crit. Rev. Food Sci. Nutr.*, vol. 62, no. 12, pp. 3264–3280, 2022, doi: 10.1080/10408398.2020.1864618.

[42] J. Zhang, L. Liu, H. Liu, A. Yoon, S. S. H. Rizvi, and Q. Wang, "Changes in conformation and quality of vegetable protein during texturization process by extrusion," *Critical Reviews in Food Science and Nutrition*, vol. 59, no. 20. Taylor and Francis Inc., pp. 3267–3280, Nov. 13, 2019. doi: 10.1080/10408398.2018.1487383.

[43] L. A. De Graaf, "Denaturation of proteins from a non-food perspective," *J. Biotechnol.*, vol. 79, no. 3, pp. 299–306, 2000, doi: 10.1016/S0168-1656(00)00245-5.

[44] M. Pommet, A. Redl, M. H. Morel, S. Domenek, and S. Guilbert, "Thermoplastic processing of protein-based bioplastics: Chemical engineering aspects of mixing, extrusion and hot molding," *Macromol. Symp.*, vol. 197, pp. 207–218, 2003, doi: 10.1002/masy.200350719.

[45] R. Osen, S. Toelstede, P. Eisner, and U. Schweiggert-Weisz, "Effect of high moisture extrusion cooking on protein-protein interactions of pea (Pisum sativum L.) protein isolates," *Int. J. Food Sci. Technol.*, vol. 50, no. 6, pp. 1390–1396, 2015, doi: 10.1111/ijfs.12783.

[46] J. Ubbink and B. J. Muhialdin, "Protein physical state in meat analogue processing," *Curr. Opin. Food Sci.*, vol. 45, p. 100822, Jun. 2022, doi: 10.1016/j.cofs.2022.100822.

[47] C. J. R. Verbeek and L. E. Van Den Berg, "Extrusion processing and properties of protein-based thermoplastics," *Macromol. Mater. Eng.*, vol. 295, no. 1, pp. 10–21, 2010, doi: 10.1002/mame.200900167.

[48] E. D. Garina *et al.*, "SANS and SAXS : A Love Story to unravel structural evolution of soy proteins and polysaccharide fibres during high moisture extrusion for meat alternatives," *Food Hydrocoll.*, vol. 155, no. January, p. 110121, 2024, doi: 10.1016/j.foodhyd.2024.110121.

[49] K. S. Liu and F. H. Hsieh, "Protein-protein interactions during high-moisture extrusion for fibrous meat analogues and comparison of protein solubility methods using different solvent systems," *J. Agric. Food Chem.*, vol. 56, no. 8, pp. 2681–2687, 2008, doi: 10.1021/jf073343q.

[50] F. J. Monahan, J. B. German, and J. E. Kinsella, "Effect of pH and Temperature on Protein Unfolding and Thiol/ Disulfide Interchange Reactions during Heat-Induced Gelation of Whey Proteins," *J. Agric. Food Chem.*, vol. 43, no. 1, pp. 46–52, 1995, doi: 10.1021/jf00049a010.

[51] W. Wang, S. Nema, and D. Teagarden, "Protein aggregation-Pathways and influencing factors," *Int. J. Pharm.*, vol. 390, no. 2, pp. 89–99, 2010, doi: 10.1016/j.ijpharm.2010.02.025.

[52] J. A. J. Housmans, G. Wu, J. Schymkowitz, and F. Rousseau, "A guide to studying protein aggregation," *FEBS J.*, vol. 290, no. 3, pp. 554–583, 2023, doi: 10.1111/febs.16312.

[53] L. Grossmann and D. J. McClements, "Current insights into protein solubility: A review of its importance for alternative proteins," *Food Hydrocoll.*, vol. 137, no. December 2022, p. 108416, 2023, doi: 10.1016/j.foodhyd.2022.108416.

[54] M. R. H. Krebs, K. R. Domike, and A. M. Donald, "Protein aggregation: More than just fibrils," *Biochem. Soc. Trans.*, vol. 37, no. 4, pp. 682–686, 2009, doi: 10.1042/BST0370682.

[55] E. van der Linden and P. Venema, "Self-assembly and aggregation of proteins," *Curr. Opin. Colloid Interface Sci.*, vol. 12, no. 4–5, pp. 158–165, 2007, doi: 10.1016/j.cocis.2007.07.010.

[56] V. B. Tolstoguzov, "Some physico-chemical aspects of protein processing into foodstuffs," *Topics in*

Catalysis, vol. 2, no. 5. pp. 339–370, 1988. doi: 10.1016/S0268-005X(88)80001-8.

[57] V. B. Tolstoguzov, "Thermoplastic extrusion-the mechanism of the formation of extrudate structure and properties," *J. Am. Oil Chem. Soc.*, vol. 70, no. 4, pp. 417–424, 1993, doi: 10.1007/BF02552717.

[58] H. Tanaka, "Viscoelastic phase separation in soft matter and foods," *Faraday Discuss.*, vol. 158, pp. 371–406, 2012, doi: 10.1039/c2fd20028g.

[59] T. Koyama and H. Tanaka, "Volume-shrinking kinetics of transient gels as a consequence of dynamic interplay between phase separation and mechanical relaxation," *Phys. Rev. E*, vol. 98, no. 6, pp. 4–6, 2018, doi: 10.1103/PhysRevE.98.062617.

[60] B. L. Dekkers, R. Hamoen, R. M. Boom, and A. J. van der Goot, "Understanding fiber formation in a concentrated soy protein isolate - Pectin blend," *J. Food Eng.*, vol. 222, pp. 84–92, 2018, doi: 10.1016/j.jfoodeng.2017.11.014.

[61] R. G. M. van der Sman and L. J. Mauer, "Starch gelatinization temperature in sugar and polyol solutions explained by hydrogen bond density," *Food Hydrocoll.*, vol. 94, no. March, pp. 371–380, 2019, doi: 10.1016/j.foodhyd.2019.03.034.

[62] T. Purcell, G. Delaplace, A. Riaublanc, M. Demême, A. Derensy, and G. Della Valle, "A general viscosity model for high moisture extrudates of pea protein isolates / gluten blend," *Phys. Fluids*, vol. 37, no. 3, 2025, doi: https://doi.org/10.1063/5.0256835.

[63] M. Nieuwland, W. Heijnis, A. J. van der Goot, and R. Hamoen, "XRT for visualizing microstructure of extruded meat replacers," *Curr. Res. Food Sci.*, vol. 6, p. 100457, 2023, doi: 10.1016/j.crfs.2023.100457.

[64] Q. Deng *et al.*, "High-moisture extrusion of soy protein: Effects of insoluble dietary fiber on anisotropic extrudates," *Food Hydrocoll.*, vol. 141, no. March, p. 108688, 2023, doi: 10.1016/j.foodhyd.2023.108688.

[65] E. Högg, T. Horneber, and C. Rauh, "Experimental and numerical analyses of the texturisation process of a viscoelastic protein matrix in a cooling die after high moisture extrusion cooking," *Proc. der 26. GALA-Fachtagung "Experimentelle Strömungsmechanik,"* no. September, pp. 45.1-45.8, 2017.

[66] J. L. Sandoval Murillo, R. Osen, S. Hiermaier, and G. Ganzenmüller, "Towards understanding the mechanism of fibrous texture formation during high-moisture extrusion of meat substitutes," *J. Food Eng.*, vol. 242, pp. 8–20, Feb. 2019, doi: 10.1016/j.jfoodeng.2018.08.009.

[67] E. Högg, T. Horneber, and C. Rauh, "Modeling and experimental analysis of protein matrix solidification in cooling dies during high-moisture extrusion," *Front. Food Sci. Technol.*, vol. 5, no. February, pp. 1–19, 2025, doi: 10.3389/frfst.2025.1443376.

[68] E. Kaunisto, C. Ohgren, N. Lor, and M. Stading, "A mean-field phase separation model enabling the coupling of non-isothermal flow phenomena with fibre formation in high-moisture extrusion of meat analogues," *J. Food Eng.*, vol. 412, p. 112972, 2026, doi: 10.1016/j.jfoodeng.2026.112972.

[69] E. Kaunisto, B. Tsegaye, R. Kotzé, J. Wiklund, R. Kádár, and M. Stading, "Towards in-line rheology measurement of protein melts during high moisture extrusion by pulsed ultrasound velocimetry," *J. Food Eng.*, vol. 1, p. 112461, 2025, doi: https://doi.org/10.1016/j.jfoodeng.2024.112461.

[70] Y. Ma, M. Schlangen, J. Potappel, L. Zhang, and A. J. van der Goot, "Quantitative characterizations of visual fibrousness in meat analogues using automated image analysis," *J. Texture Stud.*, vol. 55, no. 1, pp. 1–12, 2024, doi: 10.1111/jtxs.12806.

[71] P. Wittek, N. Zeiler, H. P. Karbstein, and M. A. Emin, "High moisture extrusion of soy protein: Investigations on the formation of anisotropic product structure," *Foods*, vol. 10, no. 1, Jan. 2021, doi: 10.3390/foods10010102.

[72] J. Li *et al.*, "The interplay between soy proteins and dietary fiber in determining the structure and texture of high moisture extrudates," *Food Hydrocoll.*, vol. 156, no. February, p. 110256, 2024, doi: 10.1016/j.foodhyd.2024.110256.

[73] K. J. Grabowska, S. Zhu, B. L. Dekkers, N. C. A. De Ruijter, J. Gieteling, and A. J. Van Der Goot, "Shear-induced structuring as a tool to make anisotropic materials using soy protein concentrate," *J. Food Eng.*, vol. 188, pp. 77–86, 2016, doi: 10.1016/j.jfoodeng.2016.05.010.

[74] J. Ranasinghesagara, F. Hsieh, and G. Yao, "A photon migration method for characterizing fiber

formation in meat analogs," *J. Food Sci.*, vol. 71, no. 5, 2006, doi: 10.1111/j.1750-3841.2006.00038.x.

[75] R. Van Beers, B. Aernouts, M. M. Reis, and W. Saeys, "Anisotropic light propagation in bovine muscle tissue depends on the initial fiber orientation, muscle type and wavelength," *Opt. Express*, vol. 25, no. 18, p. 22082, 2017, doi: 10.1364/oe.25.022082.

[76] G. H. Weiss, J. M. Porrà, and J. Masoliver, "The continuous-time random walk description of photon motion in an isotropic medium," *Opt. Commun.*, vol. 146, no. 1–6, pp. 268–276, 1998, doi: 10.1016/S0030-4018(97)00475-6.

[77] H. Patel, C. Barnés-Calle, Å. Rinnan, S. B. Engelsen, and F. W. J. van den Berg, "Characterization of the anisotropy in proteinaceous semi-solid food matrices through polarized fluorescence spectroscopy," *J. Food Compos. Anal.*, vol. 140, no. September 2024, 2025, doi: 10.1016/j.jfca.2025.107237.

[78] B. Tian *et al.*, "Small angle neutron scattering quantifies the hierarchical structure in fibrous calcium caseinate," *Food Hydrocoll.*, vol. 106, no. March, p. 105912, 2020, doi: 10.1016/j.foodhyd.2020.105912.

[79] J. I. Zink *et al.*, "Structural and mechanical anisotropy in plant-based meat analogues," *Food Res. Int.*, vol. 179, no. December 2023, p. 113968, 2024, doi: 10.1016/j.foodres.2024.113968.

[80] B. Hammouda, "Probing nanoscale structures - the SANS toolbox," 2008.

[81] P. S. Singh, *Small-Angle Scattering Techniques (SAXS/SANS)*. Elsevier B.V., 2017. doi: 10.1016/B978-0-444-63776-5.00006-1.

[82] M. Palanisamy, S. Töpfl, R. G. Berger, and C. Hertel, "Physico-chemical and nutritional properties of meat analogues based on Spirulina/lupin protein mixtures," *Eur. Food Res. Technol.*, vol. 245, no. 9, pp. 1889–1898, 2019, doi: 10.1007/s00217-019-03298-w.

[83] D. Verfaillie, F. Janssen, G. Van Royen, and A. G. B. Wouters, "A systematic study of the impact of the isoelectric precipitation process on the physical properties and protein composition of soy protein isolates," *Food Res. Int.*, vol. 163, no. November 2022, p. 112177, 2023, doi: 10.1016/j.foodres.2022.112177.

[84] H. Van As and J. Van Duynhoven, "MRI of plants and foods," *J. Magn. Reson.*, vol. 229, pp. 25–34, 2013, doi: 10.1016/j.jmr.2012.12.019.

[85] J. van Duynhoven, A. Voda, M. Witek, and H. Van As, *Time-domain NMR applied to food products*, 1st ed., vol. 69, no. C. Elsevier Ltd., 2010. doi: 10.1016/S0066-4103(10)69003-5.

[86] M. R. Serial, C. Terenzi, J. Van Duynhoven, and H. Van As, "MRI of Transport and Flow in Plants and Foods," *Magn. Reson. Microsc. Instrum. Appl. Eng. Life Sci. Energy Res.*, pp. 237–261, 2022, doi: 10.1002/9783527827244.ch11.

[87] F. L. Chen, Y. M. Wei, and B. Zhang, "Characterization of water state and distribution in textured soybean protein using DSC and NMR," *J. Food Eng.*, vol. 100, no. 3, pp. 522–526, 2010, doi: 10.1016/j.jfoodeng.2010.04.040.

[88] A. Hu, T. Li, H. Zhou, F. Guo, Q. Wang, and J. Zhang, "Water binding ability changes of different proteins during high-moisture extrusion," *Food Hydrocoll.*, no. [pre-print], 2024.

[89] Y. Sun, M. Dong, J. Bai, X. Liu, X. Yang, and X. Duan, "Preparation and properties of high-soluble wheat gluten protein-based meat analogues," *J. Sci. Food Agric.*, no. March, 2023, doi: 10.1002/jsfa.12922.

[90] T. Tian *et al.*, "High moisture extrusion of soybean-wheat co-precipitation protein : Mechanism of fibrosis based on different extrusion energy regulation," *Food Hydrocoll.*, vol. 144, no. June, p. 108950, 2023, doi: 10.1016/j.foodhyd.2023.108950.

[91] L. Wang, J. Xu, M. Zhang, H. Zheng, and L. Li, "Preservation of soy protein-based meat analogues by using PLA/PBAT antimicrobial packaging film," *Food Chem.*, vol. 380, no. December 2021, 2022, doi: 10.1016/j.foodchem.2021.132022.

[92] M. H. Levitt, *Spin dynamics: Basics of nuclear magnetic resonance, 2nd edition.*, vol. 34A, no. 1. 2009. doi: 10.1002/cmr.a.20130.

[93] J. H. Keeler, "Understanding NMR spectroscopy," *Choice Rev. Online*, vol. 43, no. 10, pp. 43-5896-43–5896, 2006, doi: 10.5860/choice.43-5896.

[94] F. Bloch, "Nuclear induction," *Physical Review*, vol. 70, no. 7. pp. 460–474, 1946. doi: 10.1016/0031-8914(51)90068-7.

[95] S. Meiboom and D. Gill, “Modified spin-echo method for measuring nuclear relaxation times,” *Rev. Sci. Instrum.*, vol. 29, no. 8, pp. 688–691, 1958, doi: 10.1063/1.1716296.

[96] E. M. Haacke, R. W. Brown, M. R. Thompson, and R. Venkatesan, *Magnetic Resonance Imaging - Physical principles and sequence design*, 1st Editio. Wiley-Liss, 1999.

[97] E. O. Stejskal and J. E. Tanner, “Spin diffusion measurements: Spin echoes in the presence of a time-dependent field gradient,” *J. Chem. Phys.*, vol. 42, no. 1, pp. 288–292, 1965, doi: 10.1063/1.1695690.

[98] P. T. Callaghan, “Translational Dynamics and Magnetic Resonance: Principles of Pulsed Gradient Spin Echo NMR.” Oxford University Press, Sep. 15, 2011. doi: 10.1093/acprof:oso/9780199556984.001.0001.

[99] P. B. Kingsley, “Introduction to diffusion tensor imaging mathematics: Part I. Tensors, rotations, and eigenvectors,” *Concepts Magn. Reson. Part A Bridg. Educ. Res.*, vol. 28, no. 2, pp. 101–122, 2006, doi: 10.1002/cmr.a.20048.

[100] P. B. Kingsley, “Introduction to diffusion tensor imaging mathematics: Part II. Anisotropy, diffusion-weighting factors, and gradient encoding schemes,” *Concepts Magn. Reson. Part A Bridg. Educ. Res.*, vol. 28, no. 2, pp. 123–154, 2006, doi: 10.1002/cmr.a.20049.

[101] P. J. Basser, J. Mattiello, and D. LeBihan, “MR diffusion tensor spectroscopy and imaging,” *Biophys. J.*, vol. 66, no. 1, pp. 259–267, 1994, doi: 10.1016/S0006-3495(94)80775-1.

[102] P. B. Kingsley, “Introduction to diffusion tensor imaging mathematics: Part III. Tensor calculation, noise, simulations, and optimization,” *Concepts Magn. Reson. Part A Bridg. Educ. Res.*, vol. 28, no. 2, pp. 155–179, 2006, doi: 10.1002/cmr.a.20050.

[103] D. J. Bryant, J. A. Payne, D. N. Firmin, and D. B. Longmore, “Measurement of flow with nmr imaging using a gradient pulse and phase difference technique,” *Journal of Computer Assisted Tomography*, vol. 8, no. 4. pp. 588–593, 1984. doi: 10.1097/00004728-198408000-00002.

[104] M. I. Gobes, S. A. Kuijpers, C. Terenzi, R. G. M. van der Smaan, J. P. M. van Duynhoven, and J. Hohlbein, “Rotated Fourier transform (RFT) enables the quantification of anisotropic structure in high-moisture plant-protein extrudates,” *Food Struct.*, vol. 44, no. June, p. 100437, 2025, doi: 10.1016/j.foostr.2025.100437.

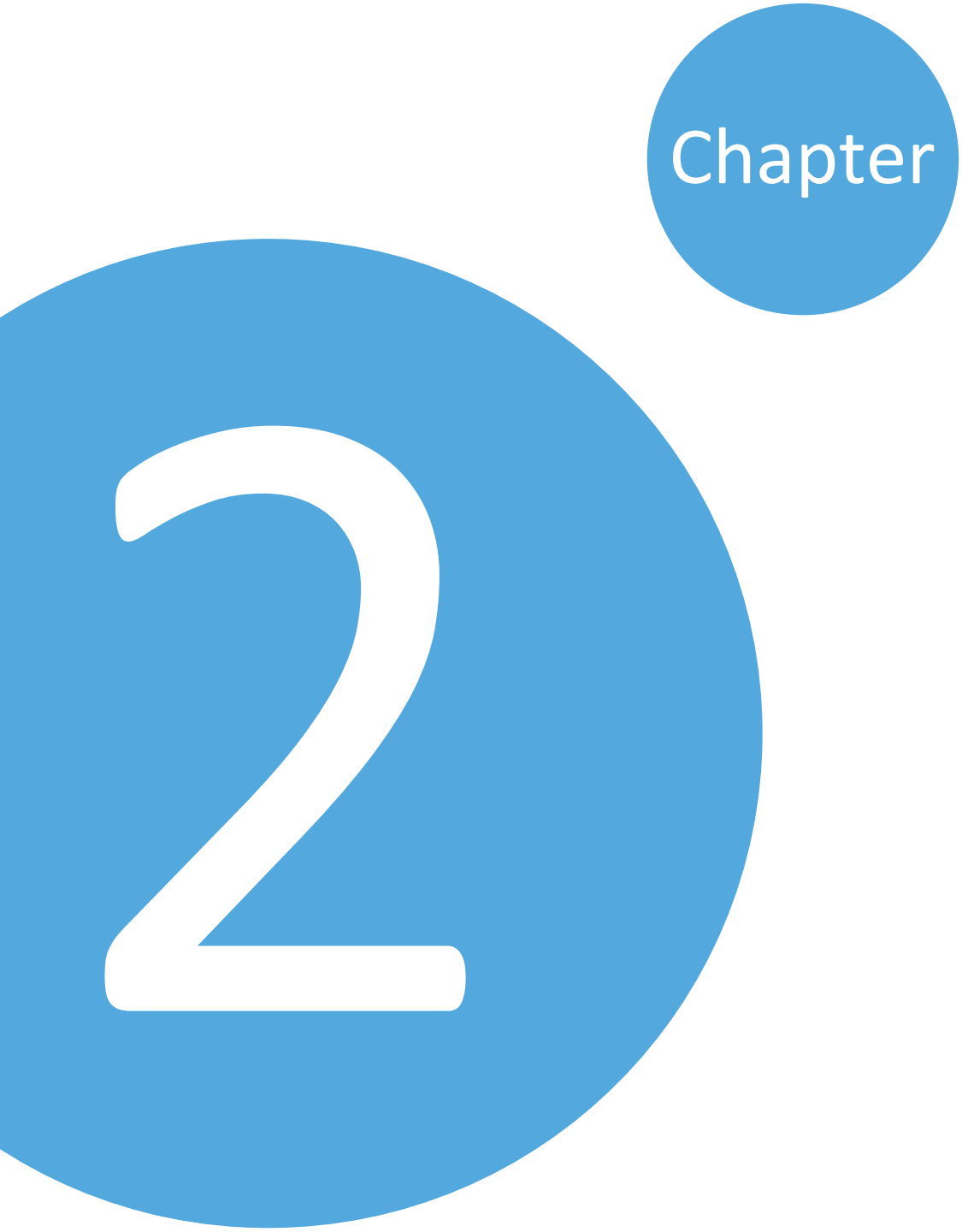
Chapter
2

Quantification of phase separation in high-moisture soy protein extrudates by NMR and MRI.

This chapter was published as:

Kuijpers, S.A.; Goudappel, G.-J.; Huppertz, T.; Van Duynhoven, J.P.M.; and Terenzi, C. Quantification of phase separation in high-moisture soy protein extrudates by NMR and MRI, *Food Res. Int.*, 2024, 197, 115225,

Abstract

High-moisture (HM) extrusion is the dominant industrial process to create structured plant-based protein products that can be used for animal-free meat alternatives. Yet, the underlying mechanisms, such as phase separation, that govern structure formation in plant-protein extrudates, are still poorly understood. Current hypotheses require experimental data in order to be verified, but measurement techniques able to quantify phase-separated anisotropic protein extrudates are lacking or have yet to be validated. In this study, Low-Field Time Domain (LF TD)-NMR and High-Field (HF) MRI techniques have been employed to unravel phase separation in HM extrudates of soy proteins. Results show that swelling with water enhances the ^{1}H NMR/MRI signal-to-noise ratio in the measurements and unveils the presence of lamellar regions, while freeze-thawing enhances phase separation due to freeze concentration. Phase separation could be quantified by the observation of two distinct populations by LF TD-NMR T_2 measurements. MRI images of dead-stop ribbon samples from HM extrusion revealed how the thickness of the aligned lamellar regions increases during passage of the protein melt through the cooling die. We conclude that TD-NMR can quantify phase separation, while spin-echo MRI can spatially resolve the lamellar structure conformation of HM extrudates. Thus, NMR and MRI are powerful techniques for non-invasively characterising *ex situ* structure formation during HM extrusion, and for validating hypotheses on shear- and temperature-induced phase separation.

2.1 Introduction

In many western countries, a transition from animal meat towards plant-based alternatives is occurring [1, 2]. Currently, high-moisture extrusion (HME) is the dominant, industrially-scalable, process to create fibrous texture from plant proteins [3, 4]. In HME, after mixing of water and plant protein, the resulting dough is transported to a heated extruder barrel, where proteins undergo denaturation [5, 6]. Under the strongly sheared flow in HME, these proteins aggregate and align at the nm-scale along the flow direction [6, 7]. Above the denaturation temperature, non-covalent bonds rearrange [6] and extensive exchange between sulfhydryl (SH) and disulphide (SS) groups takes place, which in turn promotes the formation of inter-molecular cross-links [6, 8, 9]. Upon cooling of the protein melt, concomitant solidification and phase separation into protein- and water-rich domains occurs [6]. By shearing the protein melt during cooling, phase separation is further promoted, and dispersed phases within the material become elongated, forming an anisotropic lamellar structure at the sub-mm scale [10, 11]. Additionally, the structure of high-moisture extrudates can be further altered by freeze-structuring, or by swelling in a marinade [12, 13]. These HME post-processing steps can have further impact on phase separation and, thus, on the fibrous texture of the final product.

The multiscale structure of the high-moisture extrudates has been identified as essential for understanding process-texture relationships, and an arsenal of spectroscopic and microscopic techniques has been introduced for this purpose [14]. However, each measurement technique focuses on a limited range of structural length scales and, thus, the formation of multiscale, phase-separated, lamellar features is generally not well described. So far, only cryo-imaging [4] and cryo- X-Ray Tomography (XRT) [12] have been used for studying lamellar phase separation in plant-protein extrudates. Yet, under the cryogenic imaging conditions required for such measurements, structural changes induced by freeze-thawing or swelling cannot be investigated [6]. The present work focusses on assessing the capability of ^{1}H Nuclear Magnetic Resonance (NMR) and Magnetic Resonance Imaging (MRI) relaxation measurements, which are non-invasive and require no prior cryo-fixation, to detect and quantify phase separation in plant-protein extrudates. These techniques are able to respectively probe the molecular mobility and the spatial distribution of water, in several types of soft porous materials, including food systems [15–17]. However, these NMR and MRI methods have only scarcely been exploited for assessing the impact of HME on the multiscale structure of plant-protein extrudates. In literature, two mobile water populations have been identified using Time Domain (TD-) NMR in both textured soy protein [18] and soy protein extrudates [19] at a Low Field (LF) magnetic field strength of 0.5 T. These works identified a dominant water population with T_2 values in the order to tens of ms, ascribed to water confined in a protein matrix. Additionally, LF MRI measurements were conducted at 0.5 T to describe the spatial distribution of water in plant-protein extrudates [19–22]. In

such studies, MRI data showed limited ^{1}H intensity contrast, and macroscopic fibrous structures, commonly visible in plant-protein extrudates [4, 23], were hardly noticeable. Likely, both sample preparation and MRI measurement conditions were not specifically optimised for assessing phase-separated structures.

In the present work, we combined High-Field (HF) MRI and LF TD-NMR techniques to quantitatively assign spatial structural features to motionally-distinct water states within high-moisture extrudates of a soy protein concentrate (SPC) and a soy protein isolate (SPI). By ^{1}H HF MRI, we first studied the effect of freeze-thawing and swelling in water on the phase-separated structure, and the related ^{1}H MRI contrast, for soy protein extrudates. TD-MRI was used to acquire spatially-resolved T_1 and T_2 maps. With the aim to detect fast-relaxing ^{1}H NMR signal components, shorter T_E values than in HF MRI were required, invoking the use of LF NMR instrumentation, with correspondingly shorter dead times, and of an FID-CPMG pulse sequence [24–26]. For this scope, LF conditions are particularly favourable as T_2 tends to become longer, thus making it possible to detect even the fastest-decaying T_2 signal components [27]; Concurrently, T_1 tends to be shorter and, thus, measurements can become faster. By combining spatially-resolved and bulk measurements of T_1 and T_2, relaxation properties of water could be associated with the observed lamellar phase-separated features. These insights were exploited for *ex situ* characterisation of phase-separated lamellar structure formation, due to cooling and shear, during passage of the hot protein melt through the cooling die.

2.2 Materials and Methods

2.2.1 High-moisture extrusion

Alpha8 SPC and Supro 500E IP SPI were purchased from Solae (St. Louis, MO, USA) and ARCON SJ SPC from ADM (Europoort, The Netherlands). A lab-scale twin-screw extruder (XTS19, Xtrutech LTD, United Kingdom) with a length:diameter ratio, L/D, of 47:1.8 cm was employed to process SPC and SPI powders. SPC or SPI powder was fed to the extruder using a volumetric feeder (Brabender Technologie, Utrecht, Netherlands). During extrusion, water was pumped into the extruder (Masterflex L/S Easy Load II, USA) yielding a MC of 54% (Alpha 8, dead-stop samples), 56% (Alpha 8, Supro 500E; samples used for NMR relaxometry) and 63% (Arcon SJ, samples used for assessment of impact of freeze-thawing). At a screw speed of 350 RPM, the powder and water ratio was adjusted to keep the extrudate throughput at 5 kg/h. The extrusion temperature profile was respectively set to 75, 120, 160, 135 °C (SPC) or 75, 120, 130, 135 °C (SPI) for barrel zones 1 to 4. The cooling die was cooled with water of 65 °C. A rectangular cooling die geometry was employed with the dimensions 19x7x300 mm^3 (WxHxL). When the extruder was running in steady-state, extrudate samples of 30 cm were taken and immediately transferred to watertight zip-lock bags. The extrudates were cooled using ice water, and subsequently frozen for prolonged

storage. To study the effect of freezing, one batch of extrudate was, instead, stored in the fridge and measured within 24 hours of production. While the extruder was running in steady-state, barrel sections and cooling die were rapidly cooled, and a dead-stop operation was performed. Samples were taken from the barrel sections and cooling die, transferred to a watertight zip-lock bag, cooled using ice water, and then frozen for prolonged storage.

2.2.2 Sample preparation

^{1}H HF MRI: SPC or SPI samples, of approximately 3 cm in length along the extruder flow direction, were cut from either a frozen or chilled extrudate. Frozen samples were thawed overnight in a fridge at 4 °C and directly used either as non-swollen (NS) sample or as sample swollen (S) in demineralised water at 4 °C in a 50 mL tube, using a water:sample weight ratio of 15:1. After swelling, excess moisture was removed from the outer surface of the extrudate using a paper towel. The sample was placed in a 25 mm NMR tube and sealed with parafilm to prevent water evaporation.

^{1}H LF TD-NMR: SPC or SPI samples, of approximately 3 mm in length along the extruder flow direction, were cut from thawed extrudate and weighed. Samples were either directly transferred to a 10 mm NMR tube and sealed using a rubber cap to prevent water evaporation or first swollen by placing the sample in demineralised water at 4 °C in a 50 mL tube at a water:sample weight ratio of 15:1. After swelling, excess moisture was removed from the outer surface of the extrudate using filter paper and the sample was weighed again. The sample was placed in a 10 mm NMR tube and sealed using a rubber cap to prevent water evaporation.

2.2.3 NMR and MRI techniques

HF MRI

A 600 MHz (14 T) wide-bore spectrometer (Ascend 600WB Avance NEO, Bruker, Germany) equipped with a 1.5 T/m imaging gradient system (Micro 2.5, Bruker, Germany) and a 25 mm diameter quadrature ^{1}H probe (MicWB40/025 QTR, Bruker, Germany) was used. The duration of the radio frequency (r.f.) 90° excitation and 180° refocusing pulses was set to 2.1 ms at 0.4 W and 1.7 ms at 4.8 W, respectively, for all MRI measurements and was calculated by the software, Paravision 360 version 3.3.

^{1}H T_1- and T_2-weighted MRI: Extrudates were measured using the Rapid Acquisition with Relaxation Enhancement (RARE) sequence [28]. This sequence employs multiple spin echoes to consecutively acquire multiple lines of k-space with a single excitation, accelerating the acquisition without significantly impacting image quality. Acquisition parameters were set as follows: echo time, T_E= 10.5 ms; repetition time, T_R= 1 s; RARE-factor of 2; a total of 2 averages, to perform a two-step phase cycle; field-of-view (FOV) of 25x10

mm^2 or of 25x20 mm^2, respectively for axial or sagittal images (see Fig. S2.1 in SI); voxel volume of 39x39x500 μm^3 in both orientations. The measurement duration, respectively for recording 8 axial or sagittal imaging slices per acquisition, was 4.3 and 8.6 min.

T_1 mapping: The RARE Variable Repetition Time (RAREVTR) sequence was used to acquire MRI images at 16 different T_R values, geometrically spaced from 100 ms to 10 s. Per-voxel data fitting, applying a saturation-recovery exponential build-up function [29, 30] was performed to extract the T_1 maps. The smallest accessible value for T_E, namely 5.4 ms for SPC and 6.0 ms for SPI, was used for acquiring a single slice at a voxel volume of 78x78x500 μm^3 in order to minimise T_2-weighing. The FOV was set to 25x25 mm^2 and 30x25 mm^2, respectively for SPC and SPI, and the corresponding measurement duration was 94 min and 112 min.

T_2 mapping: The Multi-Slice Multi-Echo (MSME) sequence was applied to acquire MRI images using a total of 48 echoes with T_E of 5.4 ms or a total of 64 echoes with T_E of 6.0 ms, respectively for SPC and SPI. The MSME sequence employed a two-step 180° phase-cycle to limit contributions from spurious echoes. Per-voxel exponential fitting of measured data [29, 30] was performed to extract the T_2 maps. To reduce T_1-weighing, T_R was set to 5 *s* for SPC and to 10 s for SPI for a single slice. Voxel volume and FOV were set as for the T_1 mapping data, yielding a total measurement duration of 27 min and 64 min for SPC and SPI, respectively. The T_2-maps were corrected for self-diffusion effects originating from the imaging and spoiler magnetic field gradients, as described by Oakden *et al.* (2014) [31], and the read magnetic field gradient applied during acquisition was corrected for as described by Edzes *et al.* (1998) [32]. An average water apparent diffusion coefficient of $9.5 \cdot 10^{-10}$ m^2/s was used for both correction methods (see Fig. S2.10 in SI).

LF TD-NMR

For spatially unresolved LF ^{1}H TD-NMR measurements, a 20 MHz (0.5 T) benchtop NMR spectrometer was employed (Minispec mq20, Bruker, Germany) using quadrature detection. The duration of the 90° and 180° r.f. pulses were 2.3 µs and 4.6 µs, respectively.

T_1 relaxation: The Inversion Recovery (IR) sequence, namely $\left[\left(T_R - 180^o_{\pm y} - \tau_{inv} - 90^o_{\pm x} - t_{delay} - t_{acq}\right)_n\right]_N$, was adopted acquiring a total of n = 4 averages with a four-steps phase-cycle. Acquisition parameters were set to: T_R = 2 *s*; t_{delay}= 50 µs; acquisition time, t_{acq} = 20 µs; dwell time, t_{DW}= 0.4 µs. A total of N= 48 values of the inversion time, τ_{inv}, were chosen as geometrically spaced in the range 10-2000 ms, yielding a total measurement duration of 11 min. Data was fitted by a bi-exponential build-up function [29] to extract the T_1 relaxation times.

T_2 relaxation: The Carr-Purcell-Meiboom-Gill (CPMG) pulse sequence [25], preceded by the acquisition of the Free-Induction-Decay (FID) signal after the first 90° pulse, namely the FID-CPMG sequence, $\left[T_R - 90^o_{\pm x} - t^{FID}_{acq} - \left(180^o_{\pm y} - \tau - t^{CPMG}_{acq} - \tau\right)_N\right]_n$, and was adopted to measure the NMR T_2 signal decay over a dynamic range including the fast-decaying components that cannot be measured with the sole CPMG sequence [15, 33]. The acquisition parameters were: t_{DW} = 0.4 µs; t^{FID}_{acq} = τ = 0.1 ms; t^{CPMG}_{acq} = 4 µs; N = 4000 echoes; n = 4 scans; T_R = 5 s; using a four-step 90° phase-cycle measured in complex mode and yielding a total measurement duration of 1 min. Data was corrected for background signal using a measurement on an empty sample tube. CPMG data was exponentially reduced to 3000 datapoints before fitting the FID-CPMG decay curves using a three-component exponential decay function over the CPMG decay and a Gaussian function [34] over the first 50 datapoints of the FID.

2.2.4 Data analysis

^{1}H MRI data processing and image analysis was carried out in MATLAB R2022b. To read the measured MRI data from Paravision 360 version 3.3, the pvmatlab package by Bruker was used. In house scripts for automated data processing were written using MATLAB functions available by default or provided by the Image Processing Toolbox version 11.6 and Curve Fitting Toolbox version 3.8 from MATLAB. By default, background signal in the MRI images was masked. For processing LF-NMR data, the LF NMR Toolbox version 3.0.1 [35] was used. The T_1-T_2 correlated 2D relaxation data was analysed using a 2D Inverse Laplace Transform (ILT). The regularisation factor, α, was determined according to the method described by Song *et al.* (2002) by finding the heel of the graph when plotting fit residuals χ against α [36]. Lamellae thickness measurements on MRI images and fibre bundle thickness measurements on CLSM images were done using the measurement tool in ImageJ 2.15. Individual lamellae were identified from two adjacent regions with high (~80%) and low (~30%) ^{1}H NMR intensities. Dead-stop ribbon MRI images were quantified using MATLAB and the following steps were used to determine the width of the lamellar phase region, $W_{exterior}$: (i) the image region without sample and sample regions with voids were masked; (ii) the image was subdivided into 30 vertical strips of 7 voxels thick, along the extruder flow direction.; (iii) the mean ^{1}H NMR intensity for each strip was taken along the 7 voxels in the horizontal direction; (iv) the mean intensity difference, ΔI, was calculated for each Δy, *i.e.* the spatial derivative, and was plotted against its y-position; (v) A threshold value of 20% above the baseline was set to distinguish regions with high or low spatial variation in signal intensity, respectively corresponding to lamellar phase separation (>20%) and interior (<20%) regions. The reported $W_{exterior}$ values and related standard deviations were calculated from the number of voxels, with signal intensity above the threshold, converted to mm, for each of the 30 strips.

2.3 Results and discussion

2.3.1 ^{1}H MRI contrast induced by swelling or freeze-thawing

Fig. 2.1A-B shows MRI results respectively for fresh, or frozen and thawed, extrudates, in non-swollen (NS, top) or swollen (S, bottom) state after 17 hours of swelling. A higher ^{1}H NMR intensity, by a factor of about two, is observed for the equilibrium S sample with respect to its NS state, for both the fresh and frozen-thawed extrudates, due to the correspondingly increased water content (30wt%, see Table S2.1 in SI) and concomitant increased molecular mobility of water elongating transverse relaxation times. Monitoring the volume increase of an SPC extrudate sample, by MRI, *during* water uptake showed that swelling occurs predominantly isotropic (see Fig. S2.3 in SI) and is consistent with the corresponding gravimetric data (see Table S2.1 in SI). The MRI images for the S frozen-thawed SPC sample shown in Fig. 2.1B exhibit distinct lamellar structure resulting from phase separation, identifiable from the presence of consecutive regions of high and low ^{1}H NMR intensity (see Section 2.4) with an in-plane thickness of 300 ± 40 µm. The lamellae run parallel to the extrusion direction and are predominantly present towards the outer edges of the SPC extrudate, closer to the walls of the cooling die. The NS frozen-thawed sample exhibits lamellae with a lower in-plane thickness, of 220 ± 40 µm, compared to the S sample. The increase in lamellar phase thickness upon swelling with water, of about 36%, is in agreement with the corresponding increase in sample volume of about 33% (see Fig. S2.3 in SI). The lamellar structure observed by MRI is consistent with evidence, reported in the literature for frozen and thawed samples, obtained by cryo-imaging [4] or by cryo-XRT measurements [12]. For the fresh sample, the lamellar phase-separated regions are visible in both the S and NS state, with respective thicknesses of about 100 ± 40 µm and 80 ± 40 µm. These values are closer to the adopted MRI resolution of 39 µm and, thus, the phase-separated lamellae are less well resolved than in the frozen-thawed samples. The more pronounced phase separation effect after freezing and thawing is likely caused by freeze concentration [6]. The lower ^{1}H MRI signal intensity of frozen-thawed sample, globally of about 20% in NS, compared to the fresh sample, measured using the same T_E and, thus, exhibiting the same T_2-weighting, is likely due to the denser protein network in the former sample, in turn causing a decrease in the molecular mobility of the water after freeze concentration. In the S sample, the ^{1}H MRI signal intensity is about 12% lower for the frozen-thawed sample, this is in line with the roughly 10wt% increased swelling observed in the fresh sample (data not shown).

In the axial and sagittal MRI images of NS and S fresh extrudate in Fig. 2.1A arrows point to regions with higher intensity, indicating higher water content. In the images of NS and S frozen-thawed extrudate (Fig. 2.1B) voids are present at these locations. These regions correspond to the locations where the double screws were present in the extruder barrel sections. This indicates that the water present in the melt at the high-shear zones near the

screw walls partially separates out of the protein network after the abrupt pressure transition at the breaker plate. Upon freezing, ice crystallisation and expansion takes place, and upon thawing water is re-absorbed, leaving voids in the matrix (Fig. 2.1B, NS sample). Subsequent swelling fills these voids, and high intensity regions reappear (Fig. 2.1B, S sample). Unless mentioned otherwise, in the next sections NMR and MRI experiments were performed on frozen and thawed extrudates.

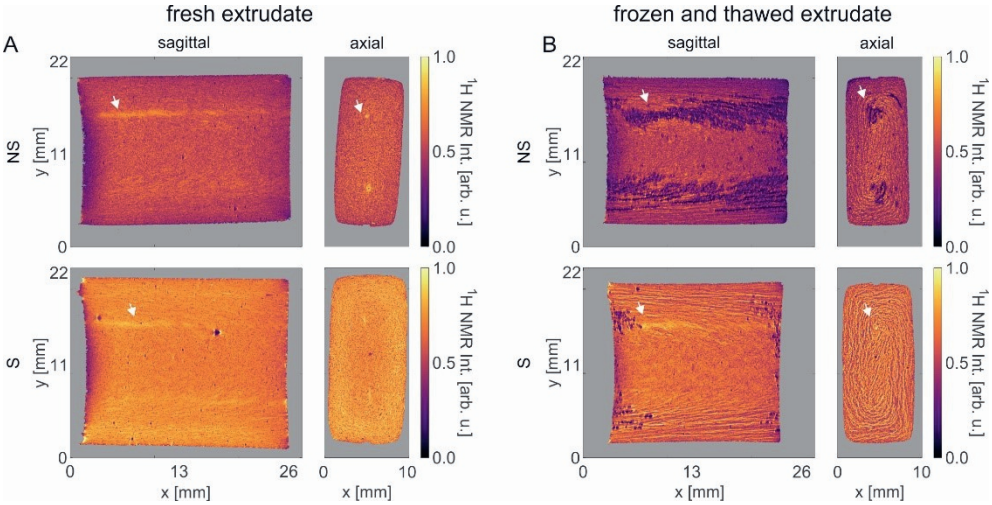

Fig. 2.1: *For fresh extrudate (A) and frozen and thawed extrudate (B) without (NS sample, top) or with (S sample, bottom) water swelling: T_1- and T_2-weighted sagittal (left) and axial (right) ^{1}H MRI images for four 63% MC SPC samples extruded at a barrel temperature of 160°C. In each axial or sagittal image, the signal intensity is normalised to the maximum intensity of the respective image for the fresh S sample (A, bottom). The voxel volume of 39x39x500 µm^3. The direction of extrusion is from left to right. The region occupied by the sample is masked, and the imaging voxels outside this mask are displayed in grey.*

2.3.2 Unveiling water phases by HF TD-MRI and by spatially-unresolved LF TD-NMR

^{1}H MRI can be combined with spin relaxation measurements to gain spatially-resolved information about water mobility at the sub-µm-scale [30, 37]. Figure 2.2 shows a T_2-weighted image (A, D), a T_1 map (B, E) and a T_2 map (C, F) for both SPC (A-C) and SPI (D-F) water swollen extrudates. Compared to the denser multi-layered structure seen in SPC, extrudates manufactured using SPI show a coarser phase separation, in agreement with previous visual macroscopic assessments [10], cryo-imaging [4] and cryo-XRT observations [12].

Both T_1 (B, E) and pulsed field gradient corrected T_2 (C, F) maps in Fig. 2.2 point to a direct correlation between long relaxation times and high-intensity regions in the respective T_2-

weighted images (A, D). For SPI (Fig. 2.2, right panel), the highest- or lowest- intensity regions have, respectively, the longest ([1800 ms, 140 ms]) or shortest ([900 ms, 25 ms]) set of [T_1,T_2] values. The longest T_1 value found for SPI is close to the T_1 value, ∼2100 ms, measured at 14 T for the excess bulk water after extrudate swelling (data not shown). This indicates that a water-rich (WR) domain is present in the SPI extrudate, with molecular mobility close to that of free water. The water fraction with $T_1 \sim$ 900 ms has a comparably lower mobility, and is assigned to water within a protein-rich (PR) domain. We note that magnetic susceptibility differences between WR and PR regions in our SPC sample, potentially affecting our MRI results, are estimated to yield respective differences in chemical shift below about 1 ppm [38, 39]. This limited effect is mostly due to the fact that the mass magnetic susceptibility of water ($\sim -9.04 \cdot 10^{-6}$ L/Kg) is much larger than that of proteins ($\sim -0.675 \cdot 10^{-6}$ L/Kg), as obtained by estimating the protein density around 1.3 Kg/L [40]. We thus consider such susceptibility-induced effect to be comparable to the effect due to differences in chemical environments, and not to appreciably affect the relaxation times measured at high field. For SPC (Fig. 2.2, left panel) the highest- or lowest-intensity regions correspond to [T_1,T_2] values of [1000 ms, 60 ms] or [400 ms, 8 ms], respectively. Compared to SPI, SPC is expected to exhibit an overall denser protein structure, as also revealed by the T_2-weighted MRI data (Fig. 2.2A): this explains the comparably shorter water relaxation times. The water fraction with $T_1 \sim$ 1000 ms is assigned, in analogy to data discussion for SPI, to a WR domain with high mobility, while that with $T_1 \sim$ 400 ms is assigned to a PR region. It is to notice that the low ^{1}H MRI intensity towards the outer regions of the sample, especially visible in Fig. 2.2D for SPI, arises from spatial inhomogeneities in the r.f. excitation field, as the larger volume of the SPI sample approaches the boundaries of the sensitive volume of the r.f. coil.

The scaling factor between the relaxation times of the water fractions in the WR and PR domains is about 2 and 5, respectively for T_1 and T_2. Hence, under the same imaging resolution, T_2 mapping is more sensitive to differences in water mobility than T_1 mapping. However, water in the PR domains of SPC exhibits $T_2 \sim$ 8 ms, in the order of the T_E value, of 5.4 ms, adopted for T_2 mapping. Hence, the shortest T_2 values for SPC are likely poorly sampled in MRI measurements. It is to notice that partial-volume effects are likely present in both T_1 and T_2 maps, particularly for SPC with thinner lamellar structures, *i.e.* the imaging voxels in such maps, of size set to 78x78x500 μm^3, likely contain signal of both WR and PR phases as the slice thickness is about 6 times larger than the in-plane resolution and the macrostructure is not necessarily oriented along the slice gradient direction.

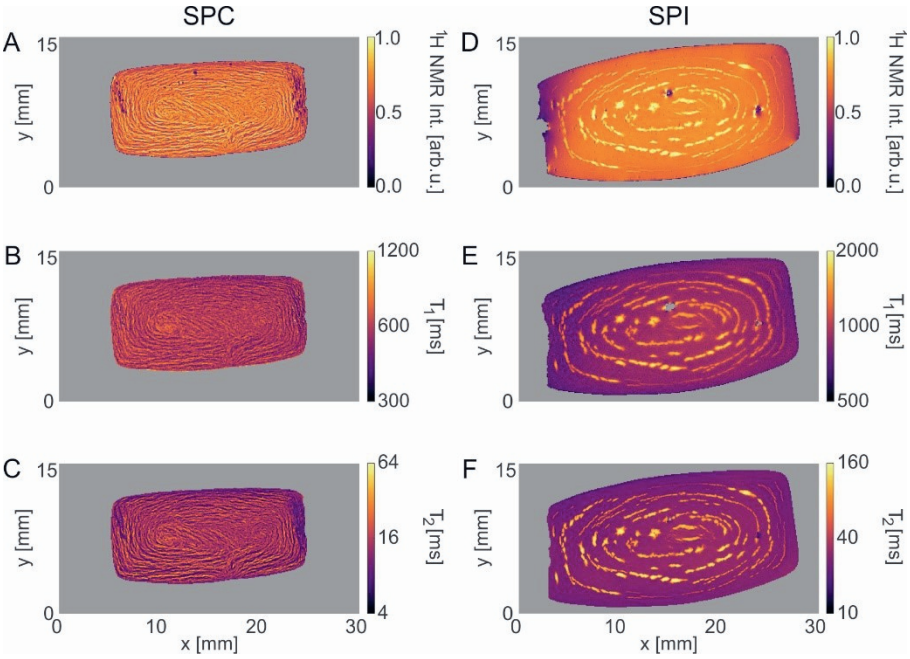

Fig. 2.2: *Axial TD-MRI results for water swollen SPC (A-C) and SPI (D-F) samples extruded with MC of 56% and at 160°C and 140°C, respectively. For each sample, a T_2-weighted image (A, D), T_1-map (B, E) and T_2-map (C, F) are displayed. Time-domain colour bars are in logarithmic scale using a ratio of 2 (T_1-map) or 4 (T_2-map). T_2-maps are corrected for diffusion effects by the imaging gradients. The sample volume is masked and voxels outside this mask are set to grey.*

Fig. 2.3 displays the different T_1 (A-B) and T_2 (C-E) values for SPC extrudate obtained by fitting LF TD-NMR data (see Fig. S2.4 in SI for the corresponding fitting results for SPI extrudate). Results show that, for the NS SPC sample, in order of increasing molecular mobility, two T_1 components, namely: (35 ± 1) ms and (76 ± 2) ms, and four T_2 components, namely: (0.014 ± 0.001) ms, (0.12 ± 0.01) ms, (10.4 ± 0.1) ms and (30 ± 1) ms could be identified. For the swollen SPC sample, the T_1 values of such components respectively became: (57 ± 1) ms and (148 ± 5) ms; The T_2 values of such components respectively became: (0.015 ± 0.001) ms, (0.16 ± 0.01) ms, (18.5 ± 0.2) ms and (75 ± 2) ms. The two fast-relaxing sub-ms components remain, within the experimental error, unaltered upon swelling of the sample. The fastest-relaxing ^{1}H population has T_2 in the order of tens of µs, and is thus associated with a macromolecular ^{1}H population, hereby referred to as the "immobile" (IM) phase [34, 41, 42], that does not interact with taken up water. We assign the latter component to ^{1}H within semi-crystalline cellulose in the fibre phase of the extrudate and/or ^{1}H within proteins that partially retained their secondary structure. The second fastest-relaxing component has T_2 in the order of hundreds of µs, and could originate from macromolecular ^{1}H within amorphous fibres and gelled proteins exchanging hydrogens with surface-adsorbed water; we here refer to the latter population as the

"gelled polymer" (GP) phase. The two slowest-relaxing components that could be discerned in both T_1 and T_2 TD-NMR measurements, have relaxation times in the order of several tens of ms that respectively increase by a factor of about 1.8-2.5 upon swelling of the SPC extrudate in water. Such components could also be detected by HF TD-MRI.

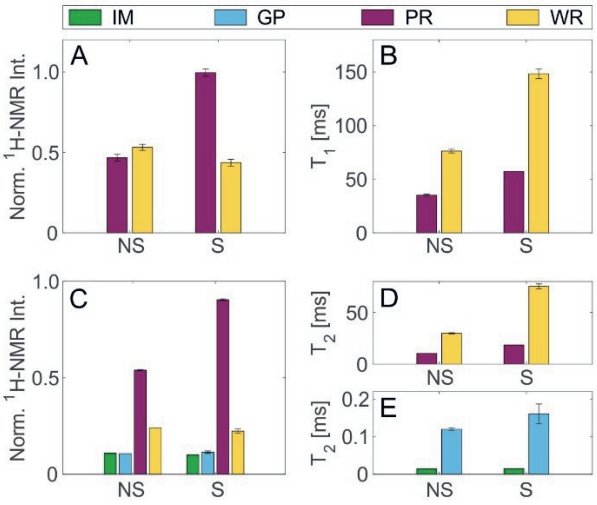

Fig. 2.3: *Relative ^{1}H populations (A and C) and corresponding T_1 (B) and T_2 (D) values obtained by LF TD-NMR relaxometry (respectively IR and FID-CPMG, see Section 2.3) of non-swollen (NS) and swollen (S) SPC extrudates obtained at MC = 56% and peak barrel temperature of 160°C. The ^{1}H NMR signal intensity is normalised to that of NS sample and corrected for the sample weight before swelling. Error bars represent the standard deviation for triplicate samples and are shown only when exceeding the histogram bar contour line. IM = immobile hydrogens; GP = gelled polymer; PR = protein-rich phase; WR = water-rich phase.*

Fig. 2.4 shows the comparison and good mutual agreement between the relative signal intensity fractions of the two T_1 components (top panel), and two most mobile, T_2 components (bottom panel) in LF TD-NMR measurements of the S extrudate and the respective relative ^{1}H signal intensity of the phase-separated regions as revealed by HF TD-MRI. The latter was determined by locally masking the image regions according to the T_2 values therein, by using Bradley's method [43]. We note that, while relative ^{1}H signal intensities observed by LF TD-NMR at 0.5 T and by HF TD-MRI at 14 T can be mutually compared, the respective T_1 and T_2 values cannot be quantitatively compared, because of their inherent field-strength dependence.

^{1}H T_1-T_2 correlation measurements were carried out at 0.5 T to validate that the two populations found at LF are from water inside the PR and WR regions. Data were processed in MATLAB by using an ILT algorithm as described in Section 2.4 [36]. The two mobile water populations measured at LF (Fig. 2.3) have $T_1/T_2 \sim 2$–3 (see Fig. S2.6 in SI). Within the

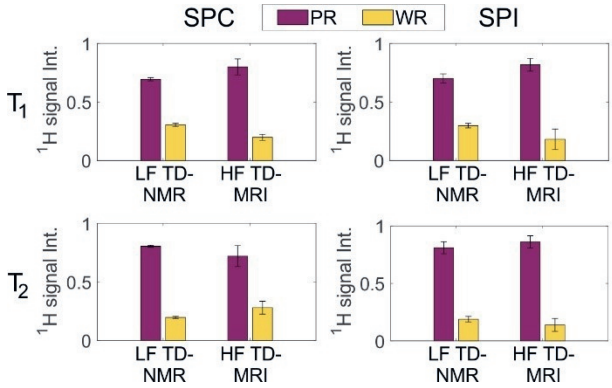

Fig. 2.4: *For swollen SPC and SPI extrudate samples: qualitative comparison between spatially-unresolved LF TD-NMR data (Fig. 2.3) and spatially-resolved HF TD-MRI data (Fig. 2.2). LF TD-NMR signal intensity populations have been normalised to the total fraction of mobile water phases in the swollen sample to reflect contributing components seen in HF TD-MRI. Error bars correspond to the error of triplicate samples (LF TD-NMR) or fit error (HF TD-MRI) and are shown only when exceeding the histogram bar contour line.*

two water populations, proton exchange rate and water self-diffusion scale in a similar manner and, thus, T_1/T_2 ratios are the same. We remark that the T_1 and T_2 values obtained from the respective HF MRI maps yielded higher and non-uniform T_1/T_2 ratio values (Fig. 2.2) than LF data. We attribute this observation to the differences in magnetic field strength and extent of B_1 inhomogeneities, as well as, in the case of HF MRI T_2 maps, to additional effects from water self-diffusion in the presence of MRI imaging gradients even during the shortest adopted T_E value of 5 ms. Notably, in the LF T_1-T_2 correlation plots, these water populations span just a decade on both relaxation time axes and are not well resolved by the ILT algorithm due to smoothing of the calculated signal density distribution. We note that this may also have precluded the observation of these two populations in previous TD-NMR studies of HME samples [19, 21, 44]. The MRI images of the SPC extrudate, however, clearly show the presence of two, motionally-distinct, water populations: per-voxel single-exponential fitting (Fig. 2.2) could unravel such populations (Fig. 2.4). These discrete fitting results show that the T_1 values of the NS sample for both the WR and PR phases increase similarly upon swelling. However, this is not reflected in the population sizes of these phases, nor can this be observed for the T_2 values. The discrepancy between the relative fractions of the NS and S samples in T_1 relaxation recovery and similarly between the relative fractions of the protein-rich phase for both samples in the T_1 and T_2 relaxation, are due to the different sensitivities of the IR (T_1) and FID-CPMG (T_2) measurements to molecular mobility. Figure S2.8 in SI shows how the relative fractions and relaxation times found for NS SPC by the T_1 IR experiment are largely impacted by the sampling of the datapoints. A CPMG-based T_2 measurement can achieve a more complete sampling and, with the additional acquisition of the FID, can resolve components over multiple relaxation time decades without increasing the total measurement duration appreciably. Thus,

measurements of T_2 relaxation decays by FID-CPMG are the preferred approach to investigate phase separation.

2.3.3 Self-diffusional averaging effect on ^{1}H T_2 relaxation NMR

Within the SPC extrudates, both proteins and insoluble cellulose fibres are present; a schematic picture of the resulting multiscale structure for SPC extrudates is depicted in Fig. 2.5. The lamellar phase-separated structures at mm-scale observed by cryo-imaging [4] are sketched in Fig. 2.5A. The sub-mm lamellar structure as observed by MRI and cryo-XRT [12] is shown in Fig. 2.5B. At the µm-scale (schematic picture in Fig. 2.5C), insoluble fibres are dispersed in the continuous cross-linked protein phase, as shown by CLSM images of SPC extrudates (see Fig. S2.9 in SI) and sheared SPC gels [45]. Fast diffusional exchange of water between compartments (see Fig. 2.5) that have distinct ^{1}H T_2 values can cause signal averaging effects and make the underlying T_2 values undistinguishable. In the SPC extrudates studied here, water self-diffusive exchange can take place between the PR and WR domains as well as between fibre (F) and protein (P) sub-environments of the PR domains, respectively with shorter or longer T_2 values. These two diffusive exchange mechanisms take place, respectively, at the sub-mm scale or at the µm-scale. We note that, at the larger length scale, diffusional averaging appears to be slow, as distinct T_2 values for the PR and WR domains could be identified both by TD-NMR and HF MRI (see Fig. 2.2 and 2.3). Regarding the diffusional exchange at the µm-scale, we expect it to be in the fast regime, given that only one population could be experimentally observed for the PR domain. We hereby set out to verify that these observations, in relation to the provided phase assignments, are in accordance with theoretical predictions. As a criterion for effective, fast, diffusional averaging we consider [46]:

$$2\sqrt{2\frac{a^2\Delta R_2}{\pi^2 D}} \ll 1, \qquad \text{Eq. 2.1}$$

where $2a$ is the one-dimensional compartment size, ΔR_2 is the difference in transverse relaxation rates for water between the two diffusionally exchanging compartments, while D is the corresponding water self-diffusion coefficient of water over these ^{1}H domains. The compartment size, $2a$, can be estimated by MRI (Fig. 2.1) and cryo-XRT [12] at the sub-mm scale, or by CLSM (Fig. S2.9 in SI) at the µm-scale. We note that the criterion for diffusional averaging described assumes that the dimensions and water self-diffusion coefficients of both compartments are identical. However, the SPC extrudates examined in the present work are spatially heterogeneous systems. Thus, upper and lower values were extracted from Eq. 2.1, thus reflecting the diffusional averaging ranges due to this structural heterogeneity. Figure 2.5D shows the results of the diffusional averaging estimates for the length scales depicted in Fig. 2.5B and C.

We first estimated the self-diffusive exchange at the sub-mm scale, for which ΔR_2 was calculated from the T_2 values for the lamellar phase-separated PR and WR domains of both NS and S SPC samples in Fig. 2.3. The D value was, $7 \cdot 10^{-10}$ m^2/s for the PR phase, assuming isotropic diffusion, as obtained by Diffusion Tensor MRI (DT-MRI) measurements (see Fig. S2.10 in SI). For a domain size of 300 ± 100 µm and the ΔR_2 for NS SPC, Eq. 2.1 yields the range 20-60. This theoretical prediction agrees with the experimentally observed absence of diffusional averaging, as two separate water T_2 populations are observed.

After the above validation of the adopted theoretical prediction in Eq. 2.1 for our spatially heterogeneous sample, we performed the same calculation for the µm-scale diffusionally exchanging domains. At such length scale, where water within the PR domain is associated with either the continuous protein matrix P or the dispersed fibre phase F, only one T_2 component is experimentally observed. The expected result for such case is that the diffusional averaging estimate of Eq. 2.1 should yield ≪1. For domain sizes of 15 ± 5 µm, we can infer a relaxation rate difference between the F and P phases $\Delta R_2 \ll 90$ s^{-1}, which we deem plausible.

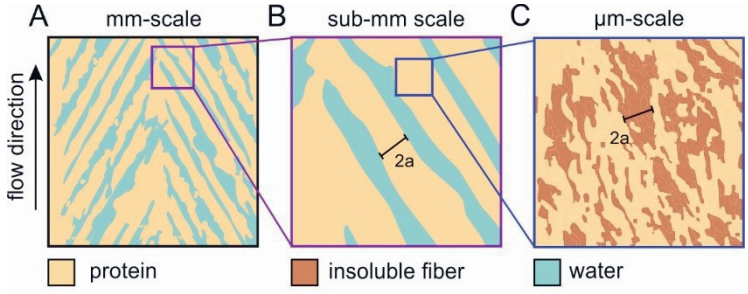

D

diffusional averaging

	sub-mm scale
I. ΔR_2 [s^{-1}]	63 ± 2
II. D [$m^2/s \cdot 10^{10}$]	7 ± 3
III. $2a$ [µm]	150 ± 50
IV. $2\sqrt{2\frac{a^2 \Delta R_2}{\pi^2 D}}$	20 – 40

	µm-scale
I. $2\sqrt{2\frac{a^2 \Delta R_2}{\pi^2 D}}$	<< 1
II. $2a$ [µm]	15 ± 5
III. D [$m^2/s \cdot 10^{10}$]	7 ± 3
IV. ΔR_2 [s^{-1}]	<< 90

Fig. 2.5: *Schematic depiction of the µm-to-mm scale structure of SPC extrudates. (A-B) Lamellar protein- and water-rich domains at mm-scale. (C) Insoluble fibres dispersed in a continuous protein phase (µm-scale). (D) Diffusional averaging calculation for the two length scales outlined in panel B and C. At the sub-mm scale, the relaxation rate difference, ΔR_2, are based on Fig. 2.3. The compartment size 2a is estimated from MRI (Fig. 2.1B). The resulting diffusional averaging regime is indicated by a range of dimensionless values. At the µm-scale, a result of 0.1 in the Belton-Hills criterion is assumed to exhibit significant diffusional averaging. 2a is estimated using CLSM data (Fig. S2.9 in SI). The resulting ΔR_2 is an upper estimate of the relaxation rate difference for diffusional averaging to occur. The extrusion direction is the same for A-C.*

2.3.4 Dead-stop HME SPC samples from the cooling die

A HME dead-stop experiment was performed and ^{1}H MRI images were acquired (see Fig. 2.6A-C) for SPC samples collected at different positions inside the cooling die, to capture the effect of lamellar structure development. The sample taken from the first section of the cooling die shows a homogeneous interior region, while further along the cooling die a larger phase-separated region becomes visible at the outer edges of the sample, close to the cooling die wall. This effect is even more pronounced for the extrudate collected after leaving the cooling die. The spatial dependence of the width of this anisotropic lamellar exterior region, namely $W_{exterior}$, is presented in Fig. 2.6D. We find that, as the protein melt progresses through the cooling die and, thus, experiences cooling and sheared flow for a prolonged time, $W_{exterior}$ increases.

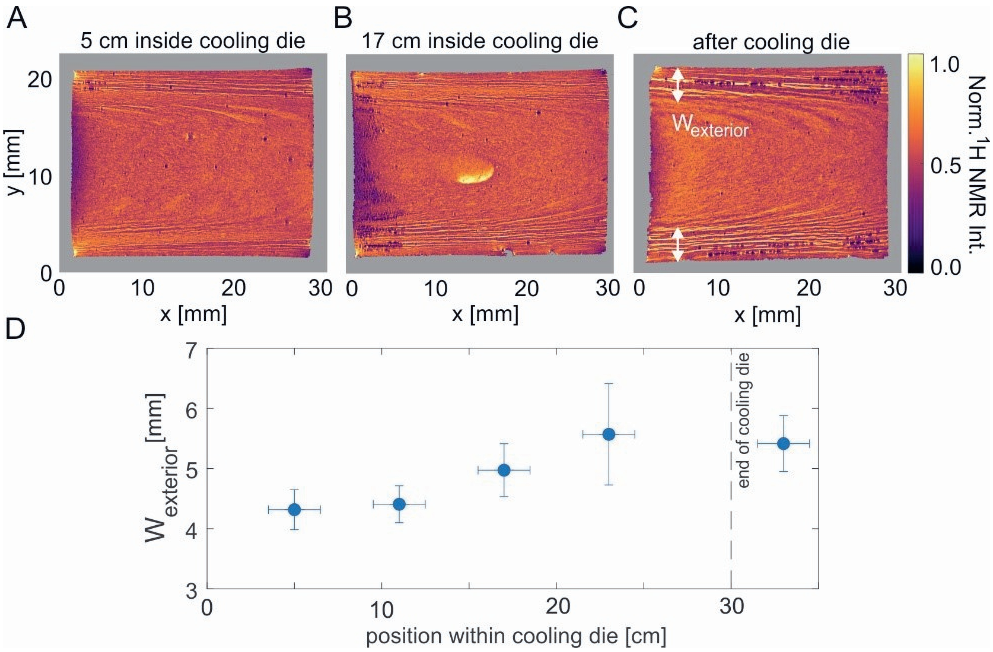

Fig. 2.6: *Sagittal T_2-weighted MRI images for dead-stop SPC samples extruded at 160°C with a MC of 54% and collected at (A) 5 cm inside the cooling die, (B) 11 cm inside the cooling die, or (C) after passage through the whole cooling die. The extrusion direction is from left to right (D): Increase in the width of lamellar phase-separated exterior region, $W_{exterior}$, calculated from the MRI images in (A-C) by comparing the variation in intensity between voxels, displayed as function of the position within the cooling die. The vertical error bars represent the standard deviation from sampling $W_{exterior}$ 30 times within one MRI image. The horizontal error bar represents the uncertainty in the cooling die position from using dead-stop samples of approximately 3 cm long in the extruder flow direction.*

2.4 General discussion

2.4.1 Performance of NMR and MRI methods for assessing phase separation of soy protein extrudates

Fig. 2.2 showed how both swelling with water or freeze-thawing can be used to enhance the imaging contrast for ^{1}H MRI measurements of soy protein extrudates. As visible in Fig. 2.1A, swelling has comparatively little effect on the lamellar structure of the fresh SPC extrudate. The ^{1}H MRI signal intensity and imaging contrast between phase-separated regions increases upon swelling due to the corresponding increase in sample volume and in the T_2 values for mobile water confined within the matrix. The other mechanism, namely freeze-thawing, leads to freeze concentration in the PR phase, and to growth of ice crystals in the WR phase. The latter also leads to mechanical separation of these two phases [6]. Upon water-induced swelling of a frozen-thawed extrudate, both the PR and WR phase take up water, which yields a more clearly discernible effect of phase separation as shown in Fig. 2.1B, Fig. 2.2A and Fig. 2.6A. Thus, in agreement with cryo-XRT [12], MRI has shown that the formation of lamellar phase-separated regions in the SPC extrudates is enhanced by freeze-thawing of the samples. Swelling of frozen-thawed extrudates yields similar results to the swelling of fresh extrudates, where imaging contrast is enhanced, while the lamellar structure appears unaltered.

Both MRI (see Fig. S2.3 in SI) and gravimetric measurements (see Table S2.1 in SI) indicate that the degree of water-induced swelling for SPI extrudates is about three times that of SPC extrudates. This is consistent with water absorption results in literature [47]. Correspondingly, also the T_1 and T_2 values measured at HF for S SPI extrudates, respectively within 500-2000 ms and 15-150 ms, are longer than those found for SPC, namely 500-1000 ms and 8-60 ms, as shown in Fig. 2.3. Both data point to a higher intermolecular crosslink density for SPC as compared to SPI. Establishing unequivocal relationships between T_1 and T_2 relaxation behaviour and intermolecular crosslink density was however out of the scopes of this work. To quantify the degree of intermolecular crosslinking in these samples, either covalent, or non-covalent, we envisage the use of reducing and denaturing solvents [48] and, where feasible, solid-state NMR methods [49, 50].

2.4.2 Ex situ observation of lamellar phase-separated structure formation along the cooling die

MRI is able to characterise the structure formation processes during passage of a hot protein melt through the cooling die, and this can be exploited to investigate how HME process parameters, like barrel temperature throughput and cooling die temperature, affect the formation and development of the desired anisotropic lamellar structure in extrudates. Figure 2.6 shows how, during passage of the hot protein melt through the

cooling die, the width of the lamellar phase-separated region increased as a function of the travelled distance within the cooling die. This is the effect of cooling and shearing on the hot protein melt formed within the preceding extruder barrel sections [51, 52]. It is generally recognised that phase separation predominantly takes place within the cooling die and several attempts have been made to quantitatively described effects of gradients in temperature and shear. Currently, the underlying mechanisms causing phase separation, either spinodal decomposition [53, 54], or viscoelastic contraction of crosslinked proteins [6], are still under debate. A bottleneck in settling this debate is the lack of experimental data that could quantitatively verify the different proposed mechanistic models. A recent publication by Zink *et al.* (2024) showed how the flow profile of SPC extrudate depends on the protein concentration, resulting in a parabolic flow profile with "core"-flow behaviour at higher protein concentration, namely, 40wt% [52]. Imaging data presented thus far, such as cryo-imaging measurements on frozen slices of dead-stop materials from the cooling die as well as from the barrel section in HME, only provide a qualitative view. These data indicate that phase separation possibly starts before the cooling die in the preceding barrel section [51, 55]. This is in line with our work where significant lamellar structure was observed already at 5 cm inside the cooling die (Fig. 2.6).

The presented TD-NMR and MRI measurements of SPC extrudates and dead-stop samples provide a quantitative assessment of phase separation up to the sub-mm scale (Fig. 2.3 and Fig. 2.6). The phase-separated lamellar region grows from the wall of the cooling die to the centre of the protein melt, in agreement with the parabolic flow profiles observed in literature and predicted by mechanistic models [51–53]. At the cooling die wall, the protein melt will solidify and show slip and/or plug flow behaviour. Within the interior regions, the protein melt solidifies later and continues flowing, resulting in parabolic phase-separated lamellae [6, 52, 53]. Quantitative *ex situ* assessment of phase separation by LF TD-NMR and HF MRI may be used to verify spatio-temporal models constructed on the bases of the two aforementioned hypotheses. We foresee that future *in situ* LF MRI methods based on velocimetry measurements, already employed in the study of food dispersions [56, 57], will enable mapping flow and temperature profiles *during* passage of the cooling die of benchtop extruders, to inform respective constitutive models of anisotropic microstructure formation.

2.5 Conclusions

HF ^{1}H MRI and LF TD-NMR relaxation measurements have shown that HME of SPC and SPI materials results in extrudates with a lamellar phase-separated structure, which manifests itself in the existence of two water populations with distinct T_1 and T_2 properties. For both types of soy protein extrudates, the HF ^{1}H MRI contrast between the lamellar phases can be enhanced by swelling with water, or by freeze-thawing. Both post-processing steps enhance the SNR and emphasise the existing lamellar structure without altering the relative fraction of water within either of the two phases, as shown by the respective T_2 data acquired with a CPMG sequence. In SPC extrudates, the fast diffusional exchange between water molecules associated, on a µm-scale, with the continuous protein phase and the dispersed fibre phase causes efficient averaging of the respective relaxation times and, thus, they cannot be resolved as two distinct water populations. The transverse relaxation decay for ^{1}H NMR populations from immobile semi-crystalline and gelled polymer regions, expected to be insensitive to phase separation, swelling or freeze-thawing, could be detected via the initial acquisition of the FID within a combined FID-CPMG pulse sequence, making the latter approach sensitive to a wider dynamic range, as compared to T_1 measurements, for ^{1}H NMR populations within high-moisture extrudates than. HF MRI can be used to unveil the development of the lamellar structure during passage of the protein melt through the cooling die. We conclude that both LF TD-NMR and HF MRI can contribute to the existing arsenal of experimental techniques adopted for structural characterisation of high moisture extrudates, providing a non-invasive and quantitative measurement route to assessing phase separation over a wide range of length scales, from µm to mm.

Authorship statement

Sam Kuijpers: Writing – original draft, Visualisation, Software, Methodology, Investigation, Formal analysis, Data curation. Gert-Jan Goudappel: Validation, Software, Methodology. Thom Huppertz: Writing – review & editing, Validation, Supervision, Conceptualisation. John P.M. van Duynhoven: Writing – review & editing, Validation, Supervision, Methodology, Funding acquisition, Conceptualisation. Camilla Terenzi: Writing – review & editing, Validation, Supervision, Project administration, Methodology, Funding acquisition, Conceptualisation.

Declaration of competing interest

JvD and GJG are employed by a company that manufactures and markets plant-based meat alternatives.

Acknowledgements

This project was supported by the uNMR-NL Grid: A distributed, state-of-the-art Magnetic Resonance facility for the Netherlands (NWO grant 184.035.002). This research is funded by the NWO OTP-TTW program and is part of the 'Measurement and Modelling of Multiscale Processed Protein Products' (MP3) project under project number 18744. We would like to thank the consortium partners for their input and fruitful discussions. We thank Martijn Gobes for providing us with CLSM images of SPC extrudate. Additionally, we thank Frank Vergeldt for the discussions on data analysis and Jo Janssen for his insights on modelling the swelling of polymer (hydro)gels.

References

[1] K. Kyriakopoulou, B. Dekkers, and A. J. van der Goot, *Plant-Based Meat Analogues*. Academic Press., 2019. doi: 10.1016/B978-0-12-814874-7.00006-7.

[2] H. Aiking and J. de Boer, "The next protein transition," *Trends Food Sci. Technol.*, vol. 105, pp. 515–522, 2020, doi: 10.1016/j.tifs.2018.07.008.

[3] S. H. V. Cornet, S. J. E. Snel, F. K. G. Schreuders, R. G. M. van der Sman, M. Beyrer, and A. J. van der Goot, "Thermo-mechanical processing of plant proteins using shear cell and high-moisture extrusion cooking," *Crit. Rev. Food Sci. Nutr.*, vol. 62, no. 12, pp. 3264–3280, 2022, doi: 10.1080/10408398.2020.1864618.

[4] P. Wittek, H. P. Karbstein, M. Azad Emin, M. José, and B. Apesteguía, "Blending Proteins in High Moisture Extrusion to Design Meat Analogues: Rheological Properties, Morphology Development and Product Properties," *Foods*, vol. 10, no. 07, p. 1509, 2021, doi: 10.3390/foods.

[5] C. J. R. Verbeek and L. E. Van Den Berg, "Extrusion processing and properties of protein-based thermoplastics," *Macromol. Mater. Eng.*, vol. 295, no. 1, pp. 10–21, 2010, doi: 10.1002/mame.200900167.

[6] R. G. M. Van der Sman and A. J. Van der Goot, "Hypotheses concerning structuring of extruded meat analogs," *Curr. Res. Food Sci.*, vol. 6, no. May, p. 100510, 2023, doi: 10.1016/j.crfs.2023.100510.

[7] H. Akdogan, "High moisture food extrusion," *Int. J. Food Sci. Technol.*, vol. 34, no. 3, pp. 195–207, 1999, doi: 10.1046/j.1365-2621.1999.00256.x.

[8] M. H. Morel, A. Redl, and S. Guilbert, "Mechanism of heat and shear mediated aggregation of wheat gluten protein upon mixing," *Biomacromolecules*, vol. 3, no. 3, pp. 488–497, 2002, doi: 10.1021/bm015639p.

[9] R. Osen, S. Toelstede, P. Eisner, and U. Schweiggert-Weisz, "Effect of high moisture extrusion cooking on protein-protein interactions of pea (Pisum sativum L.) protein isolates," *Int. J. Food Sci. Technol.*, vol. 50, no. 6, pp. 1390–1396, 2015, doi: 10.1111/ijfs.12783.

[10] V. L. Pietsch, J. M. Bühler, H. P. Karbstein, and M. A. Emin, "High moisture extrusion of soy protein concentrate: Influence of thermomechanical treatment on protein-protein interactions and rheological properties," *J. Food Eng.*, vol. 251, pp. 11–18, Jun. 2019, doi: 10.1016/j.jfoodeng.2019.01.001.

[11] B. L. Dekkers, R. Hamoen, R. M. Boom, and A. J. van der Goot, "Understanding fiber formation in a concentrated soy protein isolate - Pectin blend," *J. Food Eng.*, vol. 222, pp. 84–92, 2018, doi: 10.1016/j.jfoodeng.2017.11.014.

[12] M. Nieuwland, W. Heijnis, A. J. van der Goot, and R. Hamoen, "XRT for visualizing microstructure of extruded meat replacers," *Curr. Res. Food Sci.*, vol. 6, p. 100457, 2023, doi: 10.1016/j.crfs.2023.100457.

[13] S. H. V Cornet, S. J. E. Snel, J. Lesschen, A. Jan, V. Der Goot, and R. G. M. Van Der Sman, "Enhancing the water holding capacity of model meat analogues through marinade composition," *J. Food Eng.*, vol. 290, p. 110283, 2021, doi: 10.1016/j.jfoodeng.2020.110283.

[14] F. K. G. Schreuders, M. Schlangen, K. Kyriakopoulou, R. M. Boom, and A. J. van der Goot, "Texture methods for evaluating meat and meat analogue structures: A review," *Food Control*, vol. 127. 2021. doi: 10.1016/j.foodcont.2021.108103.

[15] J. van Duynhoven, A. Voda, M. Witek, and H. Van As, *Time-domain NMR applied to food products*, 1st ed., vol. 69. Academic Press., 2010. doi: 10.1016/S0066-4103(10)69003-5.

[16] H. Van As and J. Van Duynhoven, "MRI of plants and foods," *J. Magn. Reson.*, vol. 229, pp. 25–34, 2013, doi: 10.1016/j.jmr.2012.12.019.

[17] I. V. Koptyug, "MRI of mass transport in porous media: Drying and sorption processes," *Prog. Nucl. Magn. Reson. Spectrosc.*, vol. 65, pp. 1–65, 2012, doi: 10.1016/j.pnmrs.2011.12.001.

[18] F. L. Chen, Y. M. Wei, and B. Zhang, "Characterization of water state and distribution in textured soybean protein using DSC and NMR," *J. Food Eng.*, vol. 100, no. 3, pp. 522–526, 2010, doi: 10.1016/j.jfoodeng.2010.04.040.

[19] A. Hu, T. Li, H. Zhou, F. Guo, Q. Wang, and J. Zhang, "Water binding ability changes of different proteins during high-moisture extrusion," *Food Hydrocoll.*, vol. 152, p. 109935, 2024.

[20] L. Wang, J. Xu, M. Zhang, H. Zheng, and L. Li, "Preservation of soy protein-based meat analogues by using PLA/PBAT antimicrobial packaging film," *Food Chem.*, vol. 380, no. December 2021, 2022, doi: 10.1016/j.foodchem.2021.132022.

[21] T. Tian *et al.*, "High moisture extrusion of soybean-wheat co-precipitation protein : Mechanism of fibrosis based on different extrusion energy regulation," *Food Hydrocoll.*, vol. 144, no. June, p. 108950, 2023, doi: 10.1016/j.foodhyd.2023.108950.

[22] Y. Sun, M. Dong, J. Bai, X. Liu, X. Yang, and X. Duan, “Preparation and properties of high-soluble wheat gluten protein-based meat analogues,” *J. Sci. Food Agric.*, no. March, 2023, doi: 10.1002/jsfa.12922.

[23] S. Xia *et al.*, “Effects of moisture content and processing temperature on the strength and orientation regulation of fibrous structures in meat analogues,” *Food Hydrocoll.*, vol. 145, no. May, 2023, doi: 10.1016/j.foodhyd.2023.109113.

[24] E. Trezza, A. M. Haiduc, G. J. W. Goudappel, and J. P. M. Duynhoven, “Rapid phase-compositional assessment of lipid-based food products by time domain NMR,” *Magn. Reson. Chem.*, vol. 44, pp. 1023–1030, 2006, doi: 10.1002/mrc.1893.

[25] S. Meiboom and D. Gill, “Modified spin-echo method for measuring nuclear relaxation times,” *Rev. Sci. Instrum.*, vol. 29, no. 8, pp. 688–691, 1958, doi: 10.1063/1.1716296.

[26] H. Y. Carr and E. M. Purcell, “Effects of diffusion on free precession in nuclear magnetic resonance experiments,” *Phys. Rev.*, vol. 94, no. 3, pp. 630–638, 1954, doi: 10.1103/PhysRev.94.630.

[27] M. H. Levitt, *Spin dynamics: Basics of nuclear magnetic resonance*, 2nd editio. John Wiley and Sons Ltd, 2007.

[28] J. Hennig, A. Nauerth, and H. Friedburg, “RARE imaging: A fast imaging method for clinical MR,” *Magn. Reson. Med.*, vol. 3, no. 6, pp. 823–833, 1986, doi: 10.1002/mrm.1910030602.

[29] F. Bloch, “Nuclear induction,” *Physical Review*, vol. 70, no. 7. pp. 460–474, 1946. doi: 10.1016/0031-8914(51)90068-7.

[30] E. M. Haacke, R. W. Brown, M. R. Thompson, and R. Venkatesan, *Magnetic Resonance Imaging - Physical principles and sequence design*, 1st Editio. Wiley-Liss, 1999.

[31] W. Oakden and G. J. Stanisz, “Effects of diffusion on high-resolution quantitative T2 MRI,” *NMR Biomed.*, vol. 27, no. 6, pp. 672–680, 2014, doi: 10.1002/nbm.3104.

[32] H. T. Edzes, D. Van Dusschoten, and H. Van As, “Quantitative T2 imaging of plant tissues by means of multi-echo MRI microscopy,” *Magn. Reson. Imaging*, vol. 16, no. 2, pp. 185–196, 1998, doi: 10.1016/S0730-725X(97)00274-9.

[33] K. Van Putte and J. Van Den Enden, “Fully automated determination of solid fat content by pulsed NMR,” *J. Am. Oil Chem. Soc.*, vol. 51, no. 7, pp. 316–320, Jul. 1974, doi: https://doi.org/10.1007/BF02633005.

[34] J. Van Duynhoven, I. Dubourg, G. J. Goudappel, and E. Roijers, “Determination of MG and TG phase composition by time-domain NMR,” *JAOCS, J. Am. Oil Chem. Soc.*, vol. 79, no. 4, pp. 383–388, 2002, doi: 10.1007/s11746-002-0493-7.

[35] H. T. Pedersen, R. Bro, and S. B. Engelsen, “Towards rapid and unique curve resolution of low-field NMR relaxation data: trilinear SLICING versus two-dimensional curve fitting.,” *J. Magn. Reson.*, vol. 157, no. 1, pp. 141–155, 2002, doi: 10.1006/jmre.2002.2570.

[36] Y. Q. Song, L. Venkataramanan, M. D. Hürlimann, M. Flaum, P. Frulla, and C. Straley, “T1-T2 correlation spectra obtained using a fast two-dimensional Laplace inversion,” *J. Magn. Reson.*, vol. 154, no. 2, pp. 261–268, 2002, doi: 10.1006/jmre.2001.2474.

[37] P. T. Callaghan, “Translational Dynamics and Magnetic Resonance: Principles of Pulsed Gradient Spin Echo NMR.” Oxford University Press, Sep. 15, 2011. doi: 10.1093/acprof:oso/9780199556984.001.0001.

[38] J. Luo, X. He, D. A. d’Avignon, J. J. H. Ackerman, and D. A. Yablonskiy, “Protein-induced water 1H MR frequency shifts: Contributions from magnetic susceptibility and exchange effects,” *J. Magn. Reson.*, vol. 202, no. 1, pp. 102–108, 2010, doi: 10.1016/j.jmr.2009.10.005.

[39] M. Cerdonio, S. Morante, D. Torresani, S. Vitale, A. DeYoung, and R. W. Noble, “Reexamination of the evidence for paramagnetism in oxy- and carbonmonoxyhemoglobins,” *Proc. Natl. Acad. Sci. U. S. A.*, vol. 82, no. 1, pp. 102–103, 1985, doi: 10.1073/pnas.82.1.102.

[40] H. Fischer, I. Polikarpov, and A. F. Craievich, “Average protein density is a molecular-weight-dependent function,” *Protein Sci.*, vol. 13, no. 10, pp. 2825–2828, 2004, doi: 10.1110/ps.04688204.

[41] L. Grunin, M. Ivanova, V. Schiraya, and T. Grunina, “Time-Domain NMR Techniques in Cellulose Structure Analysis,” *Appl. Magn. Reson.*, vol. 54, no. 10, pp. 929–955, 2023, doi: 10.1007/s00723-023-01600-4.

[42] D. Radloff, C. Boeffel, and H. W. Spiess, “Cellulose and cellulose/poly(vinyl alcohol) blends. 2. Water organization revealed by solid-state NMR spectroscopy,” *Macromolecules*, vol. 29, no. 5, pp. 1528–1534, 1996, doi: 10.1021/ma950405h.

[43] D. Bradley and G. Roth, “Adaptive Thresholding using the Integral Image,” *J. Graph. Tools*, vol. 12, no. 2, pp. 13–21, 2007, doi: 10.1080/2151237x.2007.10129236.

[44] S. Xia *et al.*, “Physicochemical and structural properties of meat analogues from yeast and soy protein prepared via high-moisture extrusion,” *Food Chem.*, vol. 402, no. February 2022, 2023, doi:

10.1016/j.foodchem.2022.134265.
[45] K. J. Grabowska, S. Zhu, B. L. Dekkers, N. C. A. De Ruijter, J. Gieteling, and A. J. Van Der Goot, "Shear-induced structuring as a tool to make anisotropic materials using soy protein concentrate," *J. Food Eng.*, vol. 188, pp. 77–86, Nov. 2016, doi: 10.1016/j.jfoodeng.2016.05.010.
[46] P. S. Belton and B. P. Hills, "The effects of diffusive exchange in heterogeneous systems on N.M.R. line shapes and relaxation processes," *Mol. Phys.*, vol. 61, no. 4, pp. 999–1018, 1987.
[47] D. Webb, H. Dogan, Y. Li, and S. Alavi, "Physico-Chemical Properties and Texturization of Pea, Wheat and Soy Proteins Using Extrusion and Their Application in Plant-Based Meat," *Foods*, vol. 12, no. 8, 2023, doi: 10.3390/foods12081586.
[48] K. S. Liu and F. H. Hsieh, "Protein-protein interactions in high moisture-extruded meat analogs and heat-induced soy protein gels," *JAOCS, J. Am. Oil Chem. Soc.*, vol. 84, no. 8, pp. 741–748, Aug. 2007, doi: 10.1007/s11746-007-1095-8.
[49] J. Brus *et al.*, "Structure and Dynamics of Alginate Gels Cross-Linked by Polyvalent Ions Probed via Solid State NMR Spectroscopy," *Biomacromolecules*, vol. 18, no. 8, pp. 2478–2488, 2017, doi: 10.1021/acs.biomac.7b00627.
[50] T. Wang, P. Phyo, and M. Hong, "Multidimensional solid-state NMR spectroscopy of plant cell walls," *Solid State Nucl. Magn. Reson.*, vol. 78, pp. 56–63, 2016, doi: 10.1016/j.ssnmr.2016.08.001.
[51] P. Wittek, F. Ellwanger, H. P. Karbstein, and M. A. Emin, "Morphology development and flow characteristics during high moisture extrusion of a plant-based meat analogue," *Foods*, vol. 10, no. 8, Aug. 2021, doi: 10.3390/foods10081753.
[52] J. I. Zink, V. Lutz-bueno, S. Handschin, C. Dütsch, P. Fischer, and E. J. Windhab, "Structural and mechanical anisotropy in plant-based meat analogues," *Food Res. Int.*, p. 113968, 2024, doi: 10.1016/j.foodres.2024.113968.
[53] E. Kaunisto, S. Wassén, and M. Stading, "A thermodynamical finite element model of the fibre formation process during extrusion of high-moisture meat analogues," *J. Food Eng.*, vol. 362, no. 111760, 2024, doi: 10.1016/j.jfoodeng.2023.111760.
[54] J. L. Sandoval Murillo, R. Osen, S. Hiermaier, and G. Ganzenmüller, "Towards understanding the mechanism of fibrous texture formation during high-moisture extrusion of meat substitutes," *J. Food Eng.*, vol. 242, pp. 8–20, Feb. 2019, doi: 10.1016/j.jfoodeng.2018.08.009.
[55] E. D. Garina *et al.*, "SANS and SAXS : A Love Story to unravel structural evolution of soy proteins and polysaccharide fibres during high moisture extrusion for meat alternatives," *Food Hydrocoll.*, vol. 155, no. January, p. 110121, 2024, doi: 10.1016/j.foodhyd.2024.110121.
[56] E. C. Barnes, D. I. Wilson, and M. L. Johns, "Velocity profiling inside a ram extruder using magnetic resonance (MR) techniques," *Chem. Eng. Sci.*, vol. 61, no. 5, pp. 1357–1367, Mar. 2006, doi: 10.1016/j.ces.2005.08.032.
[57] M. R. Serial, T. Nikolaeva, F. J. Vergeldt, J. van Duynhoven, and H. van As, "Selective oil-phase rheo-MRI velocity profiles to monitor heterogeneous flow behavior of oil/water food emulsions," *Magn. Reson. Chem.*, vol. 57, no. 9, pp. 766–770, 2019, doi: 10.1002/mrc.4811.
[58] P. A. Rinck, *Magnetic Resonance in Medicine: A critical introduction*, 14th ed. TwinTree, 2024.
[59] S. Godefroy, J. P. Korb, M. Fleury, and R. G. Bryant, "Surface nuclear magnetic relaxation and dynamics of water and oil in macroporous media," *Phys. Rev. E - Stat. Physics, Plasmas, Fluids, Relat. Interdiscip. Top.*, vol. 64, no. 2, p. 13, 2001, doi: 10.1103/PhysRevE.64.021605.
[60] D. Weber, J. Mitchell, J. Mcgregor, and L. F. Gladden, "Comparing strengths of surface interactions for reactants and solvents in porous catalysts using Two-dimensional NMR relaxation correlations," *J. Phys. Chem. C*, vol. 113, no. 16, pp. 6610–6615, 2009, doi: 10.1021/jp811246j.
[61] B. P. Hills, "The proton exchange cross-relaxation model of water relaxation in biopolymer systems, II. The sol and gel states of gelatine," *Mol. Phys.*, vol. 76, no. 3, pp. 509–523, 1992.
[62] B. P. Hills, S. F. Takacs, and P. S. Belton, "The effects of proteins on the proton N.M.R. transverse relaxation time of water II. Protein aggregation," *Mol. Phys.*, vol. 67, no. 4, pp. 919–937, 1989, doi: 10.1080/00268978900101541.

2.6 Supplementary Information

2.6.1 MRI slice orientations

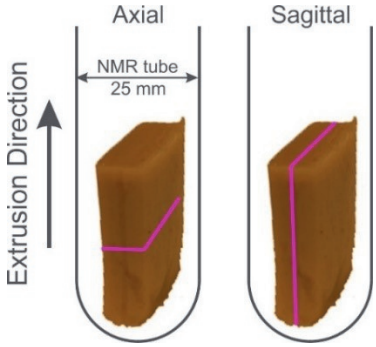

Fig. S2.1: *MRI slice orientation and nomenclature with respect to an extrudate sample and 25 mm NMR tube.*

2.6.2 Swelling of SPC and SPI extrudates in water

The MRI acquisition focused on shorter acquisition times to study swelling over time. A T_1-filter, consisting of an inversion 180° pulse followed by an inversion time, τ_{inv}, was added at the start of the RARE pulse sequence to selectively filter the ^{1}H signal from the swelling medium. The τ_{inv} values for SPC or SPI extrudates measurements were experimentally determined to be 1325 ms with a T_R of 5 s or 1525 ms with a T_R of 10 s, respectively (Fig. S.2). To ensure the water suppression has reached steady-state during acquisition, 4 dummy scans were applied. Other parameters were set as follows: T_E of 5.7 ms; T_R of 5 s (SPC) or 10 s (SPI), RARE-factor of 8; a single average and 3 slices recorded per image acquisition; the FOV was set to 25x25 mm^2 and 30x25 mm^2 respectively for SPC and SPI. The spatial resolution was 78x78x500 µm^3. The measurement duration, respectively for SPC or SPI extrudate image acquisitions was 3.3 min and 6.7 min.

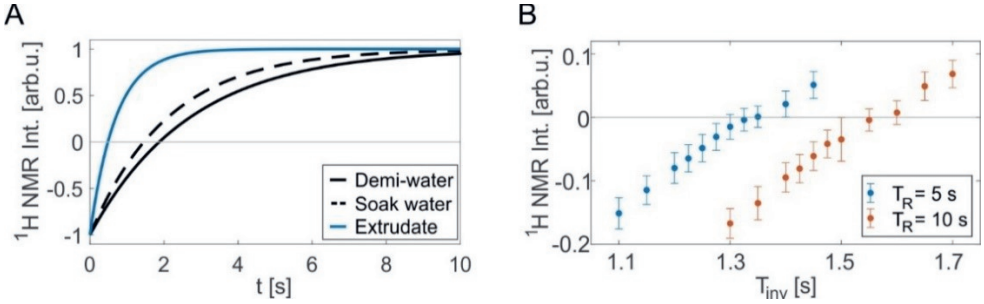

Fig. S2.2: *Inversion Recovery principle and experimental results. (A) Theoretical inversion recovery curve calculated using* $M_Z = M_0 \cdot (1 - 2e^{-\tau_{inv}/T_1} + e^{-t/T_R})$ [29, 58] *and* T_R *= 5 s (SPC).* T_1 *used are: 0.9 s (SPC), 2.1 s (swelling medium) and 2.7 s (demineralised water) measured using a bulk IR experiment (data not shown). (B) Experimental water signal* after *suppression by* T_1 *filter using various* τ_{inv} *to selectively suppress signal. Data has been corrected for background signal (air outside sample tube). The average water signal acquired reveals an optimal water suppression at a* τ_{inv} *of 1325 and 1525 ms, respectively for a* T_R *of 5 s (SPC) and 10 s (SPI).*

Fig. S2.3A shows the increase in normalised relative area, $\frac{A_S - A_{NS}}{A_{NS}}$, as function of the water swelling time, t_{swell}, of the detected sample region within the selected axial MRI slice. Both SPC and SPI, rapidly swell during the first 3 hours, before slowing down and reaching equilibrium after 15 hours. As a benchmark for isotropic swelling, the ratio between the length, L, and the width, W, of the axial MRI slice, as defined in Fig. S2.3C, was calculated (Fig. S2.3B): when swelling is isotropic, the L/W ratio should remain constant over time during swelling. Results initially show some experimental variation and after this initial stage, the L/W ratio stabilises. We conclude from Fig. S2.3 that predominantly isotropic swelling occurs and, hence, a limited degree of swelling-induced macrostructural deformations are present. In the remainder of this paper, MRI images of SPC and SPI extrudates will be shown that are acquired after 17 hours of water swelling at 4 °C.

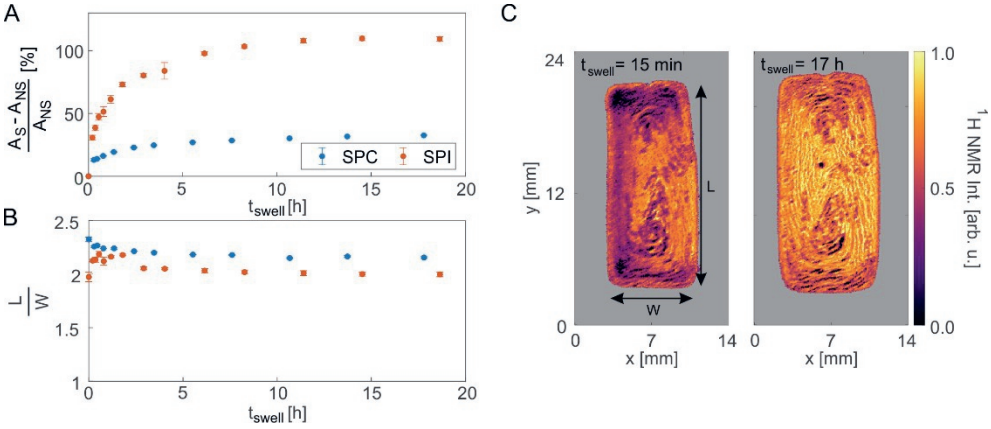

Fig. S2.3: *Swelling of SPC and SPI extrudate in water* in situ*. Samples extruded with initial MC of 56% at a peak extruder barrel temperature of 160°C and 130°C, respectively. (A) Relative swelling of extrudates, defined as the increase in axial (cross-sectional) area as function of swelling time, t_{swell} in hours. (B) Ratio of sample length (L) over sample width (W) as function of t_{swell} in hours. (C) T_1-filtered, T_2-weighted ^{1}H MRI of SPC sample at 15 min and 17h of swelling.*

2.6.3 Gravimetric swelling of soy protein extrudates

Swelling of SPC and SPI extrudates was gravimetrically determined for every experiment involving swollen samples. Table S2.1 shows the results for 3 mm thick slabs used in LF TD-NMR and 3 cm slabs used for MRI experiments. The 3 mm samples show a higher degree of swelling compared to the 3 cm samples.

Table S2.1: *Gravimetric swelling data of SPC and SPI extrudate after 17 hour swelling. 3 mm sample used for LF TD-NMR. 3 cm sample used for MRI. Errors represent standard deviation of triplicate measurement.*

swelling [wt%]	3 mm sample	3 cm sample
SPC	41 ± 0	32 ± 2
SPI	153 ± 8	106 ± 2

2.6.4 LF TD-NMR SPI fit analysis

Results show that for a swollen SPI sample, four components can be identified using an FID-CPMG pulse sequence at LF, compared to the two components found by HF TD-MRI (Fig. 2.2D-F). In order of increasing molecular mobility, two T_1 components could be identified, namely: (165 ± 1) ms and (353 ± 7) ms. In order of increasing molecular mobility, four T_2 components could be identified, namely: (0.016 ± 0.008) ms, (0.14 ± 0.01) ms, (56 ± 1) ms and (182 ± 11) ms. However, only one T_1 components, of (67 ± 1) ms and three T_2 components of (0.015± 0.010) ms, (0.14 ± 0.02) ms and (16.6 ± 0.1) ms, could be discerned in the NS sample. Similar to SPC, the two fastest decaying T_2 components show no significant change upon swelling of the sample.

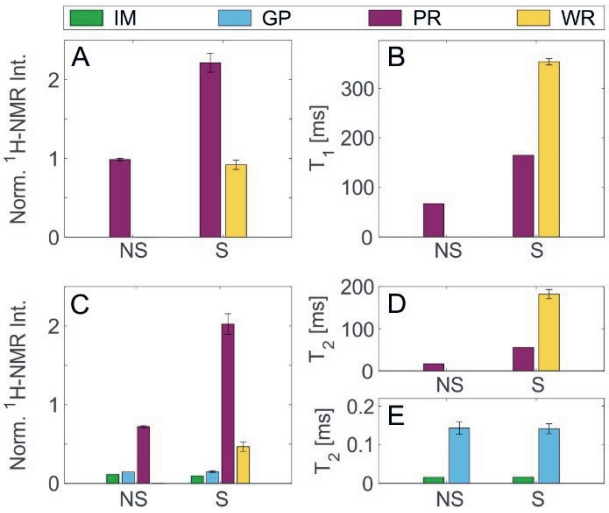

Fig. S2.4: *LF TD-NMR of NS and S frozen-thawed SPI extrudate. Extrusion at MC of 56% and peak barrel temperature of 140°C. A-B: magnitudes and relaxation times of inversion recovery data. C-E: magnitudes and relaxation times of FID-CPMG data. Shortest components (E) are fitted using the FID. Normalisation according to non-swollen weight of sample. Error bars represent the standard deviation for triplicate samples and are shown only when exceeding the histogram bar contour line. IM = immobile hydrogens; GP = gelled polymer; PR = protein-rich phase; WR = water-rich phase.*

In the swollen sample, the two T_1 components are expected to be from the PR and the WR phase similar to SPC. In non-swollen SPI, a single mobile water phase is seen. Figure S2.5 shows an MRI image of non-swollen SPC and SPI, thawed overnight at 4°C in a sealed container. Here, it can clearly be seen that the WR phase regions, as seen in Fig. 2, show no ^{1}H NMR intensity in SPI throughout the sample. Gravimetric swelling data in Table S2.1 shows that SPI is able to take up large amounts of water compared to SPC. Therefore, after freeze concentration and upon thawing of the sample, the SPI PR phase takes up the majority of the WR phase, leaving voids where the WR phase was.

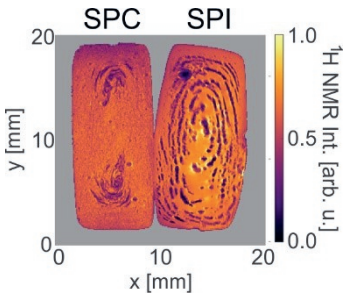

Fig. S2.5: *T_1- and T_2-weighted image of non-swollen, frozen- thawed SPC (left) and SPI (right) extruded at 160°C and 130°C respectively at a moisture content of 56%.*

2.6.5 T_1-T_2 correlation inverse Laplace transform

A T_1-T_2-correlated measurement was performed on a LF spectrometer with a swollen SPC sample, extruded at 60% MC and peak barrel temperature of 160°C, using the pulse sequence used in Song *et al.* (2002) [36]. The inter pulse delay, τ_1, for 50 acquisitions, was exponentially spaced between 0.1 ms and 2000 ms. The subsequent CPMG was acquired using a τ_2 = 0.1 ms, acquiring 2000 echoes, using a 4-phase encoding cycle and quadrature detection. Measurements were analysed using a 2D Inverse Laplace Transform (ILT). The regularisation factor, α, was determined according to the method described by Song *et al.* (2002) by finding the heel of the graph when plotting fit residuals χ against α and was equal to 117 [36]. Figure S2.6 shows the T_1-T_2-map and resulting ILT spectra for T_1 (vertical) and T_2 (horizontal). A single large component is revealed that spans one decade along both the T_1 and T_2 axes. The diagonal blue line represents $T_1 = T_2$ and the red dotted line, intersecting the main mobile components, represents $T_1 = 3 \cdot T_2$ and shows that similar relaxation exchange mechanisms are present in both T_1 and T_2 [59–62]. The two T_1 and T_2 populations found by discrete fit analysis (Fig. 2.3) are present at similar relaxation times in Fig. S2.6 but appear poorly resolved by the optimised ILT. Figure S2.7 shows the T_1-T_2-map and resulting ILT spectra for T_1 (vertical) and T_2 (horizontal) using a sub-optimal regularisation factor (α = 1) to reduce the smoothing effect. The decrease in smoothing appears to help resolving the two different water populations found by discrete fit analysis, but even before reaching complete separation of the two peaks, an artefact called 'pearling' has become visible in the ILT spectra, meaning that data is being largely overfitted.

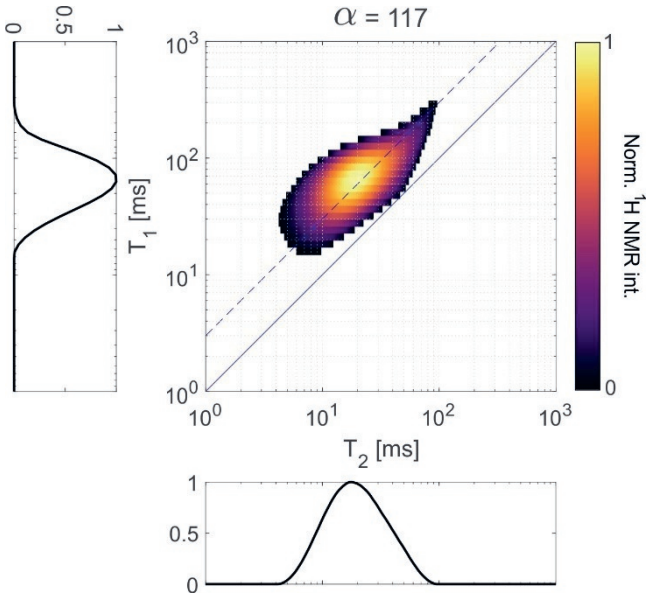

Fig. S2.6: *T1-T2-correlation results on SPC extruded at 160°C with MC of 56%. Sample was swollen in water overnight. Regularisation factor, α, was set to 117. The solid line represents $T_1 = T_2$ and the dashed line represents $T_1 = 3 \cdot T_2$. The signal intensity is normalised to the maximum intensity observed.*

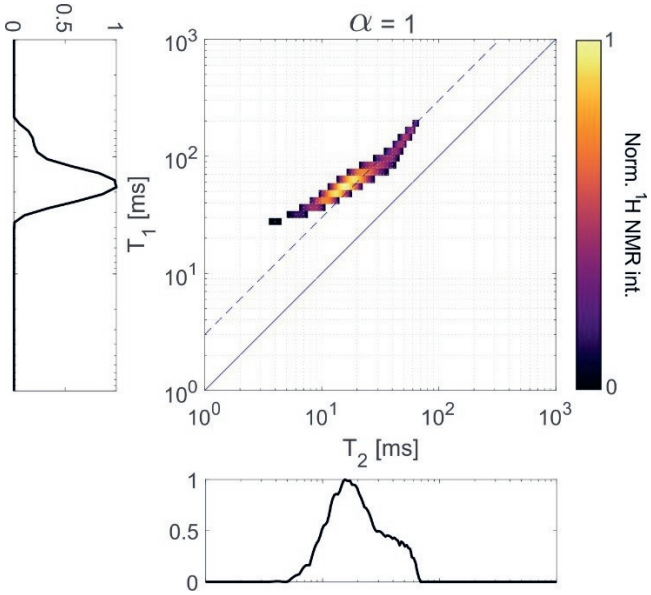

Fig. S2.7: *LF T_1-T_2-correlation results on SPC extruded at 160°C with MC of 56%. Sample was swollen in water overnight. Regularisation factor, α, was set to 1. The solid line represents $T_1 = T_2$ and the dashed line represents $T_1 = 3 \cdot T_2$. The signal intensity is normalised to the maximum intensity observed.*

2.6.6 T_1 sampling

The experiment presented in Fig. 2.3 has been repeated on a new non-swollen SPC sample using exactly the same parameters (48 acquisition with t_{delay} between 10-2000ms) for the IR and using an adjusted version that samples 60 times in the range of 0.1-2000 ms. Figure S2.8 shows (left) a copy of the data from Fig. 2.3; (middle) the repeat experiment; (right) the repeat experiment using a shorter delay time. These results reveal that T_1 relaxation recovery measurements are reproducible for the heterogenous protein extrudate samples but are very sensitive to the sampling distribution used. By changing the sampling, the relative fractions of the discrete fit shift. Due to the denser sampling inherent to the echo-based CPMG pulse sequence, this discrepancy is not present as can be seen in Fig. 2.4.

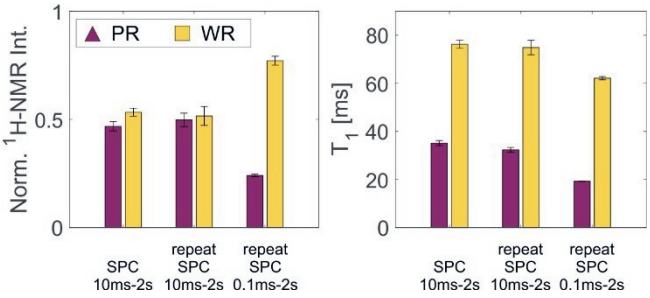

Fig. S2.8: *Repeat measurement of SPC sample extruded at 160°C. Amplitude (left) and T_1 relaxation time (right). The first group is copied data from Fig. 2.3, the second and last group are of duplicate SPC sample using the same (second) and short delay (last) IR protocols. Error = triplicate sample*

2.6.7 CLSM image of SPC extrudate sample

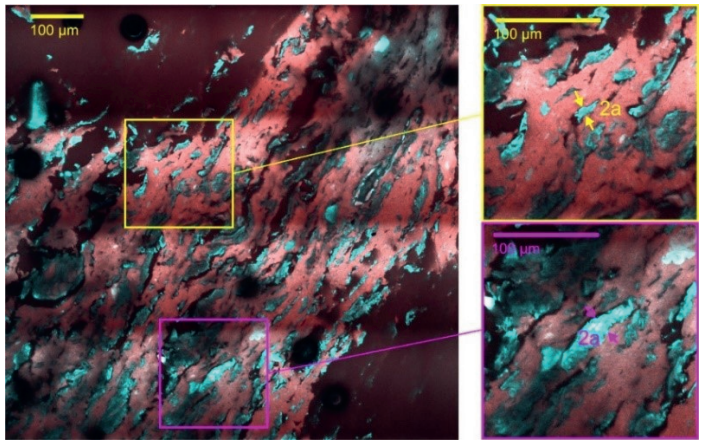

Fig. S2.9: *CLSM image of an SPC extrudate, manufactured using a peak barrel temperature of 160 °C and MC of 60%. Red: Rhodamine B to selectively stain proteins. Blue: Calc Fluor White to selectively stain carbohydrates. Examples of a large (magenta) and small (yellow) compartment size 2a, as used in the diffusional averaging estimates of Fig. 2.5 are overlayed. Horizontal and vertical waves through the images are the result of stitching 16 CLSM images together in a 4x4 grid. Note that the air voids (black) are due to sample handling of the stained and swollen extrudates samples. The > < space bars indicate thickness of the fibre regions.*

2.6.8 Water self-diffusion in SPC extrudate sample

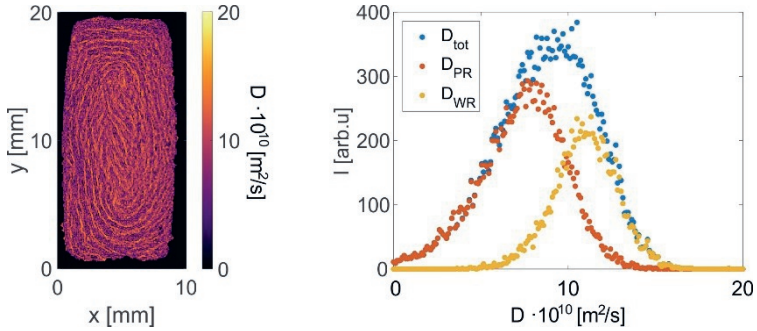

Fig. S2.10: *(left) Trace image of SPC extrudate measured using Diffusion Tensor MRI. Parameters were set to:* T_E *= 22 ms,* T_R *= 1 s, δ = 2 ms, Δ = 15 ms, acquiring 4 averages. The diffusion tensor was calculated using a 'multi-shell' experiment in Paravision 360 consisting of: 4 images at b = 130, 8 images at b = 300, 12 images at b= 600 and 16 images at b = 1000 s/mm*^{2}*. (right) Histogram of the diffusion coefficients shown in the trace image in blue. Overlayed are the diffusion coefficients found for the protein-rich (PR) and water-rich (WR) respectively. The diffusion coefficient D used in Fig. 2.6 is determined at the peak of the curves shown. The error is calculated using the full-width-half-maximum of the curves shown.*

Chapter

3

Underpinning hierarchical anisotropic structure formation in soy protein high-moisture extrudates by magnetic resonance imaging

A version of this chapter was published as:

Kuijpers, S.A.; Gobes, M.I.; Mayar, M.; Vergeldt, F.J.; Hohlbein, J.; Huppertz, T.; Van Duynhoven, J.P.M.; Terenzi, C. Underpinning hierarchical anisotropic structure formation in soy protein high-moisture extrudates by magnetic resonance imaging, *Curr. Res. Food Sci.*, 2026, 13, 101575

Abstract

Plant-based meat alternatives are fibrous anisotropic food protein products that mimic the texture and palatability of animal-based foods. The main industrially scalable production technique for manufacturing such structured protein materials is high-moisture extrusion, which involves the thermo-mechanical processing, and subsequent cooling, of a hot protein melt in the presence of shear and temperature gradients. Yet, the complex mechanisms governing fibrous structure formation in plant-protein extrudates are poorly characterised, in turn limiting the rational design and optimisation of the extrusion process. In the present work, we aimed at characterising the hierarchical nature of anisotropic structures in pH-shifted high-moisture extrudates of soy protein concentrate (SPC) by Magnetic Resonance Imaging (MRI). T_2-weighted MRI images, and corresponding Rotated Fourier Transform (RFT) analysis results, showed phase-separated protein-rich (PR) and water-rich (WR) lamellae at the 10^2 µm length scale. Chemical Exchange Saturation Transfer (CEST) MRI measurements showed the presence of dissolved proteins in the WR regions. Diffusion Tensor (DT)-MRI, probing the hindrance of water self-diffusion down to the 10^{-1} µm length scale, revealed that the PR lamellae had an underlying anisotropic structure, as shown by the Principal Diffusion Direction (PDD) maps. The latter finding was confirmed by Confocal Laser Scanning Microscopy (CLSM) measurements. The detailed features of RFT and PDD(DT) maps of these extrudates could be reproduced by simulating the effect of the cross-sectional cooling die geometry. Additionally, we found that the presence of structural order at the smallest length scale is a prerequisite for observing water diffusional anisotropy. We foresee that, in the future, the developed measurement methods will be deployed in the design and characterisation of protein-based products with a fibrous texture.

3.1 Introduction

Plant-based meat alternatives are textured protein products that provide consumers with a healthier and more sustainable alternative to animal meat, whilst offering a similar product palatability [1–3]. These products are commonly produced using High-Moisture Extrusion (HME) of commercially available plant-protein isolates, concentrates or flours obtained mostly from soy or pea [4, 5]. HME involves a mixing and hydration step, followed by thermo-mechanical processing of the resulting protein dough inside the barrel section of the extruder [5]. The high temperature and shear forces imparted on the protein dough during extrusion and subsequent cooling in a cooling die give rise to a meat-like fibrous texture. The key for understanding such protein texture is to understand the relationship with the underlying hierarchical anisotropic structure [6–8]. An important part in the anisotropic structure formation is the phase separation between protein and water during cooling under shear inside the cooling die. This anisotropic structure formation can be directed by tuning thermo-mechanical processing conditions [9], processing aids [7, 10], protein source [4] and fibre content [11, 12].

To characterise such multiscale phase-separated anisotropic structured materials, an array of measuring modalities is required to cover the multiple length scales involved. For studies of protein networks, polarised fluorescence spectroscopy [13] can probe anisotropy at the molecular length scale. Small angle scattering techniques, either using a neutron or X-ray beamline, provide nm-scale insights into the building blocks that make up the anisotropic protein network [7, 14]. Diffuse light reflectance provides a mm-scale average of sub-µm scale structural anisotropy [6, 15]. X-ray tomography under cryogenic conditions has been used to spatially resolve the phase-separated sub-mm-scale anisotropic structure of HM extrudates [10, 16]. Magnetic Resonance Imaging (MRI) has been used for the same purpose, but does not require cryogenic conditions [17]. CLSM has been used to visualise the µm-scale structural anisotropy in HM extrudates of soy proteins [10, 11]. Recently, Rotated Fourier Transform (RFT) analysis has been introduced to quantify structural anisotropy in two-dimensional images [18]. In the present work we set out to quantify anisotropic structure in pH-shifted extrudates at 10^{-1} µm and 10^{2} µm-scale, respectively by CLSM and T_2-weighted MRI. To probe structural order at the smaller length scales, we used the Diffusion Tensor (DT-)MRI technique [19]. In food science, DT-MRI has been used to assess the quality of muscle fibres in meat [20] and seafood [21]. DT-MRI makes use of Pulsed Field Gradients (PFGs) prior to the MRI signal acquisition to encode the water self-diffusion, and it uses linear combinations of these PFGs along the three Cartesian directions to probe the anisotropy of water self-diffusion. Measurements using six or more different diffusion encoding directions can be used to calculate a diffusion tensor for each voxel, which provides both a magnitude and direction to the self-diffusion of water [19, 22–24]. In order to understand the factors governing water self-diffusion, Chemical Exchange

Saturation Transfer (CEST) MRI [25, 26] was employed to assess the composition of the PR and WR domains.

3.2 Materials and methods

3.2.1 Materials

Commercial soy protein concentrate (SPC, Arcon SJ® IP, 93% DM with 69% protein in dry base, 4% fat, 19% dietary fibre and carbohydrates and 2% ash), from Solae (St. Louis, MO, USA) was used in this work. The acidity and alkalinity of the water feed were adjusted by HCl (Merck, Germany) and NaOH (Merck, Germany), respectively. Commercially manufactured mozzarella was purchased from a local retailer.

3.2.2 High-moisture extrusion

Extrusion trials were performed as described in our previous works [7, 17]. A co-rotating twin-screw extruder (XTS 19, Xtrutech, UK) with a screw diameter of 19 mm and length-to-diameter (L/D) ratio of 25 was used. The extruder was equipped with a rectangular cooling die (17 mm (width) x 7 mm (height) x 300 mm (length)) and coupled to the extruder through a die adapter. The extruder barrel included four consecutive temperature-controlled zones, respectively heated to 80 °C, 120 °C, 160 °C, and 135 °C in zones 1 to 4.

The barrel exit temperature was set to 135 °C. The water used to cool the cooling die was maintained at a temperature of 65 °C. Extrusion was performed using tap water, and pH-shifted extrudates were obtained by changing the liquid feed to 0.35 M HCl or 0.05 M NaOH as described in Kuijpers *et al.* (2025) and Ellwanger *et al.* (2024) [7, 27]. The extrusion trials were run at a screw speed of 350 rpm and at a moisture content of ca. 60%. Extrudate samples were collected from the cooling die outlet after reaching a steady-state, as indicated by constant process responses. The samples were put in a zip-lock bag, immediately cooled in ice-water, and subsequently, frozen and stored at -18 °C.

3.2.3 Sampling reference system

In the present work, combinations of Cartesian positions and anatomical planes are used to describe the position and orientation of the imaging planes within the sample with respect to the extrusion direction. In Fig. 3.1, two such planes, namely the sagittal and axial planes, are represented with respect to a schematic extrudate sample. The X and Y-axis refer to the width and height of the sample, and the Z-axis corresponds to the flow direction of the extruder. MRI imaging slices will refer to anatomical planes, namely, axial (XY) and sagittal (YZ). Principal Diffusion Direction (PDD) maps, calculated from Diffusion Tensor (DT-)MRI data, will encode diffusion directions with respect to the Cartesian axes using the colour scheme shown in Fig. 3.1. The location within an intact extrudate sample, where the

Chemical Exchange Saturation Transfer (CEST) measurement was performed, is shown by the green volume in the latter figure.

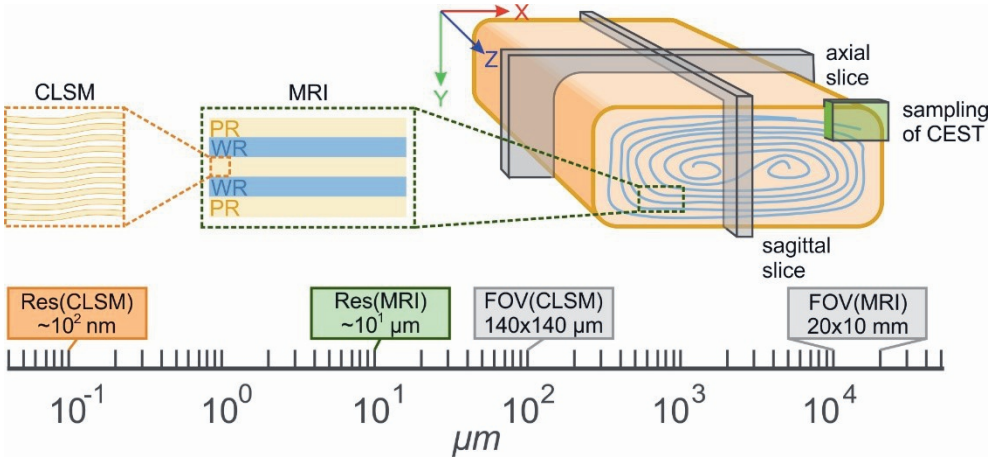

Fig. 3.1: *A schematic representation of an extrudate sample showing the MRI slice planes with respect to the Cartesian axes. The extruder flow direction is along the Z-axis. The slice thickness for MRI is 0.5 mm for T_2-weighted images and 1.0 mm for DT-MRI images. The green box denotes the size and location of the CEST MRI sample, imaged using a slice thickness of 100 µm. The field strength and employed MRI acquisition parameters allow for a theoretical MRI resolution of ~10^1 µm [28]. CLSM in combination with an Airyscan detector has a theoretical resolution of ~10^2 nm, below the limit imposed by the diffraction of light [29].*

3.2.4 Magnetic Resonance Imaging (MRI)

MRI sample preparation

For ^{1}H MRI CEST measurements, a 2 mm thin slice was cut from a frozen extrudate ribbon of approximately 1 cm long (Fig. 3.1) along the extruder flow direction (see Fig. S3.1 in SI). The thawed sample was swollen in demineralised water inside a 5 mm NMR tube for 15 min, and subsequently placed in a vacuum desiccator for 20 min for removing residual air bubbles. The sample was left in demineralised water to swell overnight for ca. 18 h. Prior to measuring, a Pasteur pipette was used to remove the excess water around the sample inside the 5 mm NMR tube, and the tube was sealed with parafilm to prevent water evaporation during MRI measurements.

For Rapid Acquisition with Refocused Echoes (RARE) and DT-MRI measurements, a sample of approximately 3 cm long was cut from a frozen extrudate ribbon and placed in a 50 mL tube. This sample was left in demineralised water to swell overnight for ca. 17 h at room temperature. The volume ratio of water to sample was 15:1. Air bubbles were removed from the sample by placing the tube in a vacuum desiccator for 20 minutes. After swelling, excess moisture was removed from the outer surface of the extrudate using a paper towel. The

sample was placed in a 25 mm NMR tube, which was sealed with parafilm to prevent water evaporation during MRI measurements.

MRI imaging procedure

^{1}H CEST MRI measurements [25] were performed using a 1.2 GHz (28 T) narrow-bore spectrometer (Ascend 1.2GHz, Avance Neo, Bruker, Germany) equipped with a 2.85 T/m gradient system (Micro 5, Bruker, Germany) and a 5 mm micro-imaging probe (Iprobe, Bruker, Germany). The measurements were conducted in Paravision 360 version 3.3. In the CEST MRI pulse sequence, a saturation pulse was first applied, consisting of 10 hard pulses, each of length t_p = 100 ms and with inter-pulse delay, t_{delay} = 10 µs, resulting in a total saturation time T_{sat} = 1 s [30]. The amplitude of the saturation pulse, B_1 = 1.5 µT, was optimised for detecting water-protein chemical exchange and relayed Nuclear Overhauser Enhancement (rNOE) effects in the CEST spectrum [26, 30]. The image readout was performed with a RARE sequence [31] and a single MRI slice was excited at the centre of the sample in the axial plane with a thickness of 100 µm (Fig. 3.1). The saturated MRI images, S_{sat}, were acquired at varying frequency offsets, $\Delta\omega$. For the saturation pulse, 65 values were chosen between -10 and 10 ppm. From -10 to -6 ppm and 6 to 10 ppm, frequency offset values were placed 0.3 ppm apart. Between -4 ppm and 4 ppm, the resolution was increased to 0.1 ppm between frequency offsets values. In addition, two reference unsaturated MRI images, S_0, were acquired at $\Delta\omega$ = ±450 ppm. The RARE imaging parameters were as follows: echo time T_E = 5 ms; repetition time T_R = 3.6 s; RARE-factor of 2; 4 signal averages; Field-Of-View (FOV) of 5 x 5 mm^2; MRI resolution of 50 x 50 x 100 µm^3. This resulted in a measurement duration of about 12 min per $\Delta\omega$ value, and of 13 h for the full CEST MRI measurement.

^{1}H DT-MRI and RARE measurements were performed using a 600 MHz (14 T) wide-bore spectrometer (Ascend 600WB, Avance NEO, Bruker, Germany) equipped with a 1.5 T/m imaging gradient system (Micro 2.5, Bruker, Germany) and a 25 mm quadrature ^{1}H probe (MicWB40/025 QTR, Bruker, Germany). The measurements were performed using Paravision 360 version 3.6. T_1- and T_2-weighted MRI images of SPC extrudates were measured using the RARE sequence in both the axial and sagittal orientation (Fig. 3.1). Acquisition parameters were set as follows: T_E = 10 ms; T_R = 1 s; RARE-factor of 2; 4 signal averages and 4 imaging slices were excited at the centre of the sample of 0.5 mm thick and spaced 1 mm apart; FOV of 22.5 x 12.5 mm^2 or 25 x 12.5 mm^2, respectively for axial or sagittal images; MRI resolution of 39 x 39 x 500 µm^3 with a total measurement duration per image acquisition of 11 min for each orientation.

Water self-diffusion anisotropy measurements were performed using a stimulated-echo based DT-MRI pulse sequence [19]. Pulsed field gradients (PFGs) are used to encode the water self-diffusion, with the amount of diffusion encoding being defined by $b =$

$(\gamma\delta G)^2\left(\Delta-\frac{\delta}{3}\right)$ in s/mm^2. This parameter is determined by the gyromagnetic ratio of hydrogen, γ, the strength of the diffusion encoding gradient, G, the duration of diffusion-encoding gradients, δ, and the self-diffusion encoding time Δ [32]. The stimulated-echo acquisition scheme was chosen in order to account for the short T_2 values for the SPC extrudates at 14 T, which are typically between 8 and 30 ms [17]. Thus, to enable the use of long enough Δ values between consecutive PFG pulses, magnetisation was stored along the -Z axis, where longitudinal relaxation takes place. The T_1 longitudinal relaxation constant is, for the investigated samples, typically between 500 and 1500 ms [17]. An optimal Δ value, of 50 ms was chosen to observe water self-diffusion with sufficient Signal-to-Noise ratio (SNR) (see Fig. S3.2 in SI) while avoiding excessive T_1 relaxation effects.

DT-MRI acquisition parameters were set as follows: T_E = 13 ms; T_R = 1 s; δ = 2 ms; Δ = 50 ms; 8 signal averages (see Fig. S3.3 in SI) per axial imaging slice at the centre of the sample (Fig. 3.1); FOV of 22.5 x 12.5 mm^2; MRI resolution of 52 x 52 x 1000 µm^3. In the Bruker Paravision 360 software, version 3.6, multiple so-called 'experimental shells' can be defined to vary both the number of diffusion encoding directions and the diffusion-weighing b-values, within one measurement. For each DT-MRI acquisition, a two-shell acquisition scheme was chosen, with directions and diffusion encoding values determined as described in Kingsley (2006abc) [22–24]. The first shell consisted of 8 reference MRI images without use of diffusion-encoding gradients, hereafter called A_0-images. Due to the gradients required, either for imaging or for signal crushing between subsequent acquisitions, even in the absence of diffusion encoding gradients, an effective b -value, namely b_{eff} = 120 s/mm^2, was produced for the acquisition of the A_0-images. A_0-images were manually set as the first experimental shell with a b_{eff} of 120 s/mm^2 (See Fig. S3.4 in SI). The second experimental shell contains the different diffusion encoding gradient combinations which enable probing diffusion in different directions. The optimal number of directions was determined to be 36 (See Fig. S3.5 in SI) and the probed diffusion directions are calculated in Paravision using a model that simulates opposed point charges [22, 33]. Here, 36 unit vectors are created along the same Cartesian axis, and due to the simulated repelling charges between these vectors, all vectors evenly distribute along a unit half-sphere. The projections of each vector on the Cartesian axes are used to calculate the required PFG strength of the read, phase and slice-selective gradients. These 36 diffusion encoding directions were acquired using a b_{eff} of 1000 s/mm^2. The resulting total measurement duration per sample was 23.5 hours.

DT-MRI tensor calculations are known to be sensitive to noise, resulting in partly inaccurate or negative-valued tensor elements [23, 34]. Thus, the imaging parameters above were determined by analysing a series of measurements to assess the impact of Δ (Fig. S3.2 in SI), the number of averages (Fig. S3.3 in SI) or number of diffusion encoding directions (Fig. S3.5 in SI) on the SNR.

MRI data analysis

^{1}H MRI data processing and image analysis was performed in MATLAB R2022b using the pvmatlab package by Bruker for extracting raw MRI data from Paravision 360 version 3.6. In house scripts for automated data processing, such as normalisation, background masking and exporting data, were written using either standard MATLAB functions or functions provided by the Image Processing Toolbox version 11.6 and Curve Fitting Toolbox version 3.8 from MATLAB.

CEST MRI data was corrected for B_0 inhomogeneity by performing a per-voxel fitting of the S_{sat} values as a function of $\Delta\omega$ using a smoothing-spline interpolation. The water frequency shift was defined as the $\Delta\omega$ value corresponding to the position of the minimum in the fitted signal intensity curve (resolution 0.01 ppm). A ΔB_0 map, representing the B_0 inhomogeneity, was constructed per-voxel by correcting the position of the minimum of the measured signal intensity dispersion curve to $\Delta\omega$ = 0 ppm [35]. CEST spectra were constructed per voxel by normalising the B_0-corrected S_{sat} images by the reference unsaturated image, S_0. Intensity thresholding of the S_0 image at $\Delta\omega$ = 450 ppm was conducted using Otsu's method with three threshold values [36]. Voxels with intensities above the third, and below the second, threshold value were respectively attributed to the water- and protein-rich regions. CEST spectra were averaged over either the water- or protein-rich voxels to determine the spatial distribution of proteins over the two phases.

Calculations of the diffusion tensor, average diffusivity (D_{av}) and fractional anisotropy (FA) from the diffusion-weighted images, were performed in MATLAB using the procedures described in Kingsley (2006abc) [22–24]. The D_{av} and FA are calculated using linear combinations of the three tensor eigenvalues: λ_1, λ_2 and λ_3, respectively corresponding to the major, intermediate and minor diffusion components as follows:

$$D_{av} = (\lambda_1 + \lambda_2 + \lambda_3)/3, \qquad \text{Eq. 3.1}$$

$$FA = \sqrt{\frac{3[(\lambda_1 - D_{av})^2 + (\lambda_2 - D_{av})^2 + (\lambda_3 - D_{av})^2]}{2[\lambda_1^2 + \lambda_2^2 + \lambda_3^2]}}. \qquad \text{Eq. 3.2}$$

The eigenvalues are conventionally sorted by their magnitude, $\lambda_1 > \lambda_2 > \lambda_3$. However, this method may introduce statistical artifacts in the eigenvalue distribution caused by background noise in the acquired data affecting the tensor calculation. The result is a bias in the mean eigenvalues within a homogeneous region of interest (ROI), especially in more isotropic regions [37]. To correct for this, after having sorted the eigenvalues by their magnitude, the inter-voxel overlap between two diffusion tensors is calculated as described by Basser *et al.* (2000) [37]:

$$C_t = \frac{\sum_{i=1}^{3} \lambda_i \lambda_i' (\epsilon_i \epsilon_i')^2}{\sum_{i=1}^{3} \lambda_i \lambda_i'}. \qquad \text{Eq. 3.3}$$

Here, $0 < C_t \leq 1$, with 0 indicating no overlap and 1 indicating complete overlap of the tensors. The sum of each eigenvalue-eigenvector (ε) pair is compared between the voxel of interest (λ_i, ε_i) and a reference tensor (λ'_i, ε'_i). This reference tensor is taken as the mean diffusion tensor of an ROI around the voxel of interest. The optimal size of the ROI was found to be a 9 x 9 voxel area, defined as the area where a further increase in the ROI size does not alter the mean eigenvalue distribution anymore (SI Fig. S3.6). For each voxel in the image, C_t is calculated for the six unique possible eigenvalues-sorting combinations and, thus, the sorting order with the highest overlap is chosen. From these ROI-sorted eigenvalues, PDD maps are created by encoding the angle of the eigenvectors of each eigenvalue for a Red, Green and Blue (RGB) value based on their direction [38]. This results in three images corresponding to the three different eigenvalues of the tensor. The resulting RGB-values between 0 and 1 are weighted by their respective FA values, to highlight regions with high anisotropy. Tensors with one or more negative eigenvalues were omitted from the calculations of the diffusion coefficient, FA or PDD maps.

3.2.5 Confocal Laser Scanning Microscopy (CLSM)

CLSM sample preparation

A frozen extrudate ribbon, of approximately 1 cm long, was thawed. A ~0.5 mm thin slice was taken from the middle of the thawed ribbon (similar to taking a sagittal MRI image slice, see Fig. 3.1) using a razor blade. The sample was placed on a 125 µm thick glass slide. A droplet of dye was placed on the sample and allowed to equilibrate with the sample for ca. 1 h. The dye consisted of Rhodamine B (RhB, Exciton, Lockbourne, USA) to stain proteins, and Calc-Fluor white (CFW, ID: 18909, 1 g/L with 0.5 g/L Evans blue, liquid form, Merck, Rahway, USA) to stain polysaccharides. A solution of RhB in ethanol was first prepared by dissolving 50 mg of RhB in 1.5 mL of 98% pure ethanol (Reagent Grade, Sigma-Aldrich, Germany). The mixture was placed on a vortex to dissolve all dye. Then, 15 µL of the RhB solution and 50 µL of the liquid CFW solution were dissolved in 1.5 mL of PEG-200.

CLSM imaging procedure

CLSM imaging was performed on a Zeiss confocal microscope (Zeiss LSM 880, Zeiss, Germany) equipped with an Airyscan detector and Zeiss Plan-Apochromat 63x/1.4 NA DIC M27 Oil immersion objective (Zeiss, Germany). Hereafter, the CSLM-Airyscan combination will be referred to as CLSM. The Zeiss confocal used a 405 nm and 514 nm laser line, respectively at 4% and 5% laser power. The detector ranges are 410 – 509 nm for CFW and

531 – 703 nm for RhB. Three images were obtained per pH-shifted sample using a spatial resolution of 44 x 44 nm^2 and a FOV of 140 x 140 μm^2.

Rotated Fourier Transform (RFT) analysis

RFT analysis was used to obtain quantitative vector field maps, displaying structural orientational order, from MRI and CLSM images, as described in full detail elsewhere [18]. ImageJ (FIJI, 64-bit) version 1.54j [39] was used with the RFT plugin version 0.1 installed to extract feature angles from square 51 pixel or 301 pixel image windows, respectively for MRI or CLSM images, and using an overlap setting of 75%. An in-house developed Python 3.12 routine was used to convert feature angles per window into 2D spatial maps of feature angle, relative angle intensity and Weighted Order Parameter (WOP) [18]. The WOP map presented in this work are acquired by analysing a 5 x 5 vector ROI per WOP value. To limit the effect of sample edges on the vector field and WOP calculation, the initially masked background of the MRI images was changed from zero to the mean pixel intensity of each sample prior to RFT analysis. The 51 pixel image windows in MRI correspond to a size of 2 x 2 mm^2 and the calculated WOP value averages information from a 4 x 4 mm^2 region. Concurrently, the 301 pixel image windows in CLSM correspond to a size of 13 x 13 μm^2 and the corresponding WOP values averages information from a 26 x 26 μm^2 region.

3.2.6 Generation of synthetic axial MRI data for cooling die geometries

Generally, the cross-sectional cooling die geometry is rectangular with rounded corners, as was used in this work. At pilot-scale HME conditions, sometimes these corners are completely rounded and create a so-called bullnose geometry [6]. For the purpose of simulating the effect of significantly varying the cross-sectional cooling die geometries, we have considered two additional extreme cases of square-corner and elliptical geometries. The synthetic axial MRI data for each cooling die geometry was generated as follows. (i) A uniform high-intensity image, normalised to a value of 1, containing 1000 x 500 pixels in the XY-plane (Fig. 3.1) was created using the same aspect ratio (2:1) as in the axial MRI images. (ii) At the image centre, a zero-intensity circular outline was placed with a diameter of 25 pixels. (iii) The latter step was repeated for increasing circle diameters up to the full image size in the Y-dimension, while avoiding any overlap between circles. (iv) The image intensities were inverted to create a zero-intensity background with high-intensity features, and the image was saved in tiff format. This process was repeated for ellipses with different ratio between the major and minor axes up to 2:1, as well as for rectangles with full rounded edges and sharp edges. Images were analysed by RFT [18] using a window size of 51 pixels and an overlap op 75%. Resulting vector field maps were converted to WOP and PDD maps as described in previous sections.

3.3 Results and discussion

3.3.1 Assessment of solubilised protein fractions in water-rich regions

To aid the characterisation of the self-diffusion of water in the phase-separated structure of the SPC extrudates, the presence or absence of solubilised proteins in the water-rich (WR) phase was assessed using CEST MRI measurements performed at ultra-high field (28 T). At such condition, the high ^{1}H MRI sensitivity enabled sufficient SNR for CEST MRI at near isotropic voxel sizes of 50 x 50 x 100 µm^3. The T_2-weighted MRI image (Fig. 3.2A) of the SPC extrudate shows a separation into high- and low-intensity voxels, respectively corresponding to the WR and protein-rich (PR) phases [17]. These two phases were quantified by intensity thresholding using Otsu's Method (Fig. 3.2B) [36], respectively using the lower and upper threshold values of 0.23 – 0.45 for the PR phase and 0.59 – 1 for the WR phase. The WR phase made up 15.1% of the sample volume, whereas the PR phase was more dominant, constituting 51.7%. The remaining 33.2% of voxels likely still contained both WR and PR phases due to partial volume effects and were therefore omitted from the analysis of the CEST spectra.

The CEST spectra (Fig. 3.2C) of both the WR and PR phases show the amide ($\Delta\omega$= 3.5 ppm) and hydroxyl ($\Delta\omega$ = 1.3 ppm) chemical exchange peaks at positive offsets with respect to the direct water saturation (DWS) peak. These peaks arise from ^{1}H chemical exchange between mobile proteins or peptides and water. Additionally, a peak resulting from the relayed Nuclear Overhauser Enhancement (rNOE) can be observed at $\Delta\omega$ = -3 ppm. The rNOE effect arises from a two-step process in which magnetisation of non-exchangeable protons is transferred via through-space dipolar coupling to neighbouring exchangeable protons, and subsequently to water via ^{1}H chemical exchange [40]. The rNOE peak was also observed at the same $\Delta\omega$ in the CEST spectrum of a 1 wt% soy protein isolate (SPI) solution (see Fig. S3.7 in SI), indicating that the rNOE peak for the WR phase of the SPC extrudate resulted from the presence of protein and not from the hydroxyl groups of cellulose, the latter being present in SPC. The through-space dipolar coupling effect is characteristic of large, but mobile, proteins (rotational correlation times of ~100 ns) [40, 41]. Therefore, the rNOE peak indicates the presence of solubilised proteins in the WR phase. These features observed in the CEST spectra indicate the presence of proteins in both phases. The intensity of the peaks, and thus the concentration of proteins, is lower in the WR phase than in the PR phase. Low-intensity amide and rNOE peaks were observed in the CEST spectra of the WR phase of a swollen fresh SPC extrudate (see Fig. S3.8 in SI). This indicates that the delaminated WR phase of SPC extrudates before freeze-thawing already contains solubilised proteins. Using this method, it cannot be excluded that proteins from the PR phase were solubilised into the WR phase during swelling. However, DT-MRI measurements performed in this work are

on frozen, thawed and swollen extrudates and, thus, have experienced the same post-processing steps as the sample used to acquire the CEST MRI data in Fig. 3.2C.

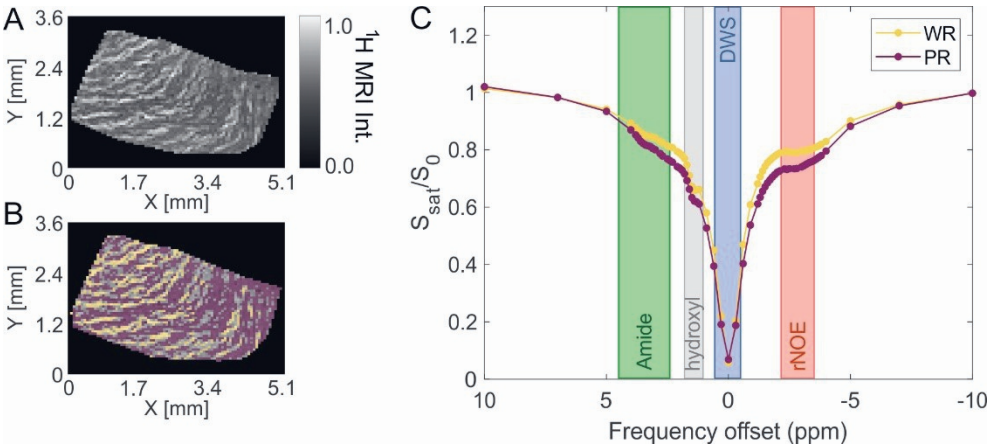

Fig. 3.2: *(A) Axial T_2-weighted ^{1}H MRI image of a frozen, thawed and swollen SPC extrudate in which WR and PR regions are respectively having higher and lower intensity. (B) Segmentation of the WR (yellow) and PR (purple) regions based on intensity thresholding with lower and upper threshold values of 0.23 – 0.45 for the PR phase and 0.59 – 1 for the WR phase. (C) ^{1}H CEST spectrum of the WR and PR regions in the SPC extrudate.*

3.3.2 Anisotropic structure quantification at 10^{-1} µm and 10^{2} µm-scale

Fig. 3.3 shows the sagittal MRI images of pH-shifted SPC extrudates. In line with our previous MRI results on pH-shifted SPC extrudates [7], anisotropic phase-separated lamellar structure is visible at pH 7.0. At pH 5.0, approaching the iso-electric point of SPC (pI ~ 4.2) [7], the phase-separated structure appears heterogeneously distributed. Concomitantly, at pH >> pI, here pH 7.8, the lamellar phase structure appears coarser than at pH 7.0 [7]. The WOP(MRI) maps follow a similar trend to our previous work [7], with WOP(MRI) values being the lowest at pH 5.0 where no evidence of a uniform aligned phase-separated structure is observed along the extruder flow direction. At pH 7.0 and 7.8, the phase-separated lamellae are oriented along the flow direction, and the WOP(MRI) values are high throughout the sample. Towards the middle of the sample, at Y = 6 mm (cyan arrow), lower WOP(MRI)-values are obtained, reflecting the local change in lamellae orientation [18]. Additionally, regions with air bubbles exhibit lower structural order. Similar features are observed for the axial image orientation presented in Fig. 3.3. In the centre of the axial images, a perturbation of the lamellar structure can be observed, which indicates that the hot protein melt entered the cooling die with a memory of the co-rotating screws in the extruder [6]. As shown in Fig. 3.3 and previous work [6, 7, 18], RFT is able to quantify anisotropic structure in MRI images. However, due to the requirement of several voxels per vector calculation and subsequently several vectors per calculated WOP(MRI) value, the smallest assessable length scale is more

than ten times the initial voxel size. To analyse the 10^{-1} µm-scale structure of pH-shifted SPC extrudates, CLSM images were acquired of the same pH-shifted samples as for the previous MRI experiments. The bottom half of Fig. 3.3 shows the CLSM images of pH 5.0, 7.0 and 7.8 samples, and their respective WOP(CLSM) maps. In the MRI images of Fig. 3.3A-C, yellow squares (sagittal) and lines (axial) are drawn that show the location and orientation, relative to the extrudate volume, where CLSM images were acquired. For visualisation, this indicator is enlarged ten times. The CLSM image of SPC extrudate at pH 5.0 shows a fibrillar protein structure. Correspondingly, the WOP(CLSM) map of this protein network shows regions with relatively high order. Similar observations are done for the pH 7.0 sample. At pH 7.8, no clearly oriented protein network is observed at the 10^{-1} µm-scale and WOP(CLSM) values are low due to the absence of an aligned structure, which is expected for the disordered fibrillar network due to electrostatic inter-fibril repulsion at pH >> pI [7].

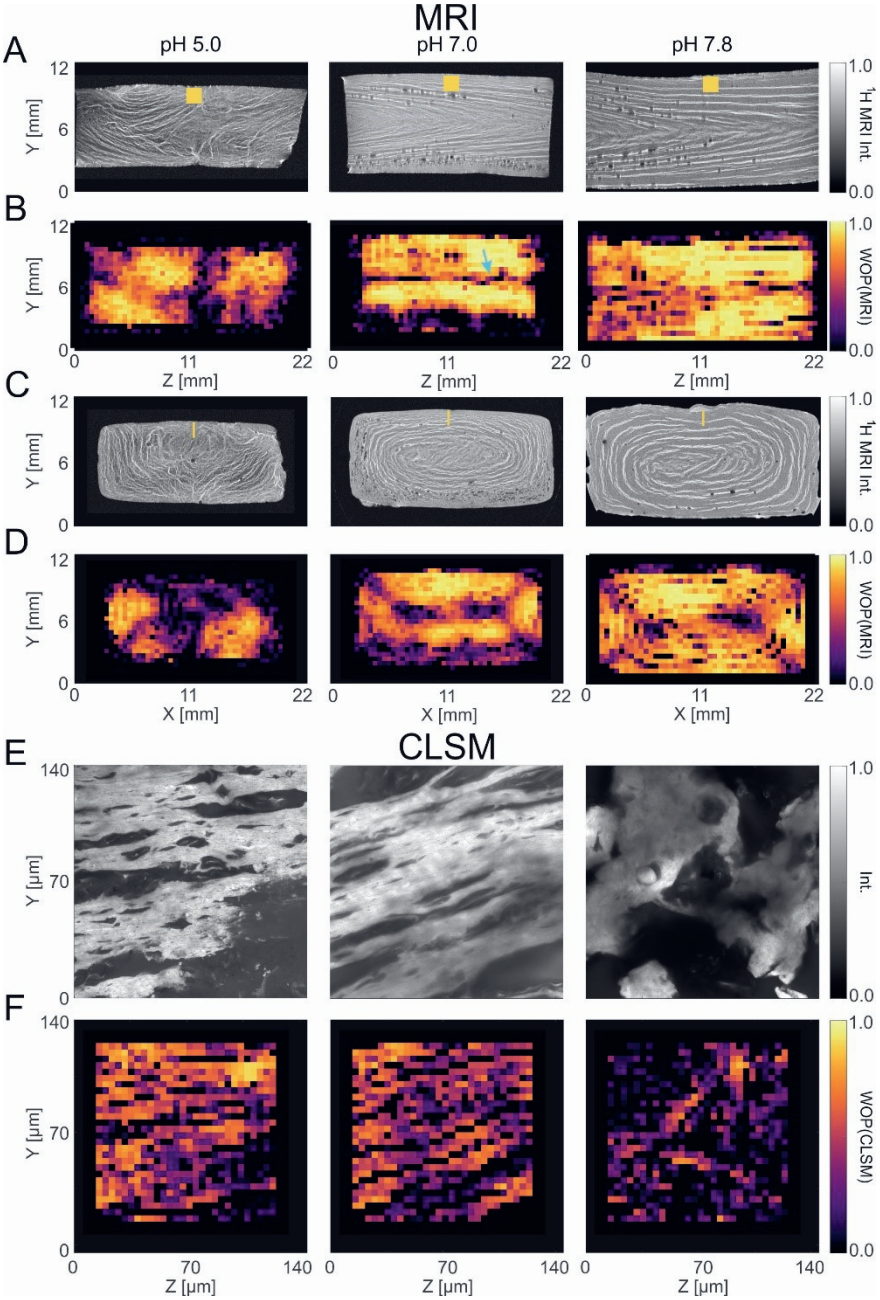

Fig. 3.3: *For SPC extrudates pH-shifted to pH 5.0 (left), pH 7.0 (middle) or pH 7.8 (right): sagittal (A) or axial (C) MRI T_1- and T_2-weighted images, and CLSM images (E). Below each image, the corresponding sagittal and axial WOP(MRI) or WOP(CLSM) map are shown (B, D, F). The relative sampling location of CLSM images is denoted by a yellow square (A) or by a yellow line (C) in the MRI images, 10x enlarged for visualisation. The cyan arrow highlights the region where two different orientations of phase-separated lamellae meet, and WOP(MRI) values are lower.*

3.3.3 Assessment of 10^{-1} µm-scale anisotropic structure by DT-MRI

In the previous section, CLSM and MRI provided quantitative measures for anisotropic structure, respectively, at the 10^{-1} and 10^{2} µm length scales. In order to approach the 10^{-1} µm length scale with MRI, we measured the self-diffusion behaviour of water to probe structural anisotropy within the WR and PR lamellae. DT-MRI measurements enable per-voxel determination of a water self-diffusion tensor. In turn, this enables mapping of the mean diffusivity (D_{av}), the Fractional Anisotropy (FA) and the Principal Diffusion Direction (PDD) (see Fig. 3.4). The self-diffusion MRI map in Fig. 3.4A, referring to the SPC extrudate at pH 7.0, shows two distinct water regions with faster or slower self-diffusion, corresponding to the PR and WR phases seen in the T_2-weighted MRI data (Fig. 3.3A-C). The respective self-diffusion coefficients are $(9.4 \pm 1.4)\cdot10^{-10}$ m^2/s and $(13 \pm 1)\cdot10^{-10}$ m^2/s. Correspondingly, Fig. 3.4B shows two distinct populations with FA values of either (0.3 ± 0.1) or (0.2 ± 0.1). As shown by the CLSM data in Fig. 3.3E-F, the PR phase is an aligned protein network and, thus, it exhibits higher diffusional anisotropy compared to the WR phase. The respective diffusion length scale was estimated to be ~20 µm, by using the Einstein equation for the mean square displacement of self-diffusion in three dimensions (see Fig. S3.2 in SI). This value is smaller than the width of the WR lamellae, which are roughly around 100–300 µm [17]. Nevertheless, the FA values found in the WR phase indicate that the water self-diffusion is not fully isotropic in these regions. The deviation from fully isotropic diffusion possibly arises from partial-volume effects, to be expected when using an image slice thickness of 1 mm. Additionally, previous work has shown that, at pH >> pI, protein fibrils form a less aligned network due to inter-fibril electrostatic repulsion [7]. The SPC sample shifted to pH 5.0 shows water self-diffusion coefficients, and FA values similar to those for the sample at pH 7.0, which is in line with the fibrillar protein network observed by CLSM in Fig. 3.3E.

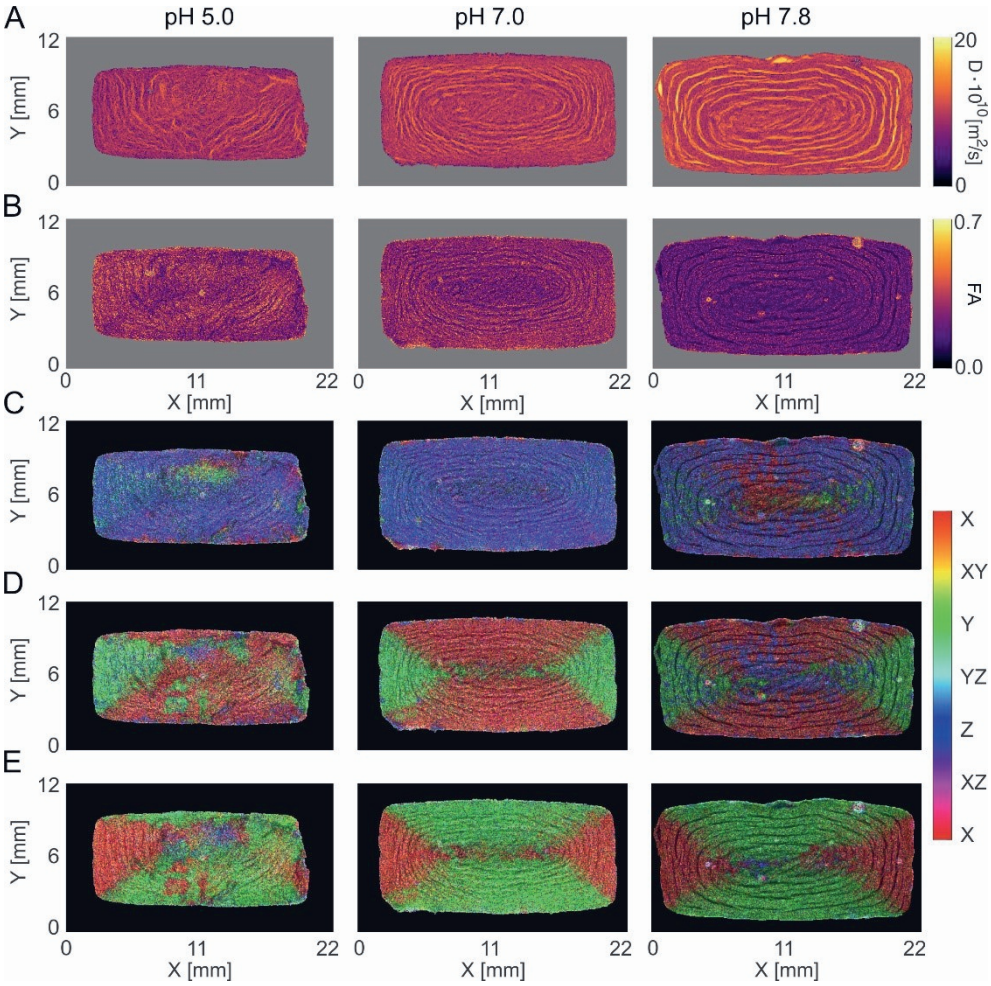

Fig. 3.4: *DT-MRI axial images of SPC extrudate samples pH-shifted to pH 5.0 (left), pH 7.0 (middle) or pH 7.8 (right). The maps in panels from top to bottom display: (A) the water self-diffusion coefficient, D (Eq. 3.1), (B) the Fractional Anisotropy, FA (Eq. 3.2), and the Principal Diffusion Direction (PDD) for either the primary (C), secondary (D) or the tertiary (E) tensor eigenvalues. The latter three images, respectively, correspond to the directions where self-diffusion is fastest, intermediate or slowest and are weighted by FA. These diffusion tensor eigenvalues are sorted by the ROI-based method established in Basser* et al. *(2000) [37] and the respective eigenvector directions are colour-coded for either X (red), Y (green) or Z (blue).*

To acquire information about the orientation of the diffusion anisotropy, PDD(DT) maps are utilised to colour-code the orientation of the eigenvectors associated with each tensor eigenvalue. The PDD(DT) maps of three pH-shifted SPC extrudates are shown in Fig. 3.4C-E, for the primary (C), secondary (D) and tertiary (E) eigenvalues, respectively indicating the fastest, intermediate and slowest self-diffusion. To mitigate the effect of noise in the PDD maps, DT-MRI data is often pre-processed using denoising algorithms [42]. In this work, such denoising step yielded smoothed PDD maps at the expense of the resolution between WR

and PR features in the FA maps. To retain such imaging details, smoothing of the PDD maps was performed solely by re-sorting the tensor eigenvalues using the ROI-method established in Basser *et al.* (2000) [37] outlined in section 3.2.4 and Eq. 3.3. At pH 7.0, the primary visible colour in the primary PDD(DT) map (Fig. 3.4C) is blue, which corresponds to the direction of shear in the extruder. Concomitantly, in panel D and E, this colour is nearly absent. The secondary PDD(DT) map (Fig. 3.4D) unveils two separated populations with distinct self-diffusion directions along the cross-section of the cooling die. These regions are shown in green (left and right, along Y) or in red (top and bottom, along X) in Fig. 3.4D. In Fig. 3.4E, the colours of these regions invert to red (left and right, along Y) and green (top and bottom, along X). This indicates that structuring occurs not only along the extruder flow direction, but also along the phase-separated lamellae formed within the cross-section of the cooling die (Fig. 3.3C). The slowest diffusion direction in Fig. 3.4E is observed perpendicular to these lamellar phase-separated structures. Such observations indicate that, inside the PR phase, an anisotropic phase-separated structure is present at a length scale below 20 µm. Likely these are the 10^{-1} µm-scale protein fibrils observed in Fig. 3.3E that arrange in lamellae. These 10^{-1} µm-scale lamellae are oriented along the extruder flow direction and shear direction of the HME screws. Similar anisotropic diffusion features are observed for the sample shifted to pH 7.8, but a larger contribution of green (Y) and red (X) is visible in the primary PDD(DT) map (Fig. 3.4C), and vice versa, a larger contribution of blue (Z) is visible in the secondary PDD(DT) map (Fig. 3.4D). The distribution of colours remains unchanged in the tertiary PDD(DT) map (Fig. 3.4E) compared to that of the pH 7.0 sample. Together with the roughly 25% lower FA values observed in (Fig. 3.4B), this indicates that the tensor in these voxels is closer to a disk-like shape where the eigenvalues of the primary and secondary diffusion directions are similar in magnitude. In the PDD(DT) map of the sample shifted to pH 5.0, clear regions with a primary diffusion direction other than the extruder flow direction can be observed. Additionally, in the secondary as well as in the tertiary PDD(DT) map, non-uniformly coloured regions are observed. These observations are in line with the more disordered lamellar structure observed in Fig. 3.3C. This shows that, similarly to pH 7.0 and pH 7.8, the secondary diffusion direction is generally parallel to the lamellar phase separation, regardless of the direction of these lamellae.

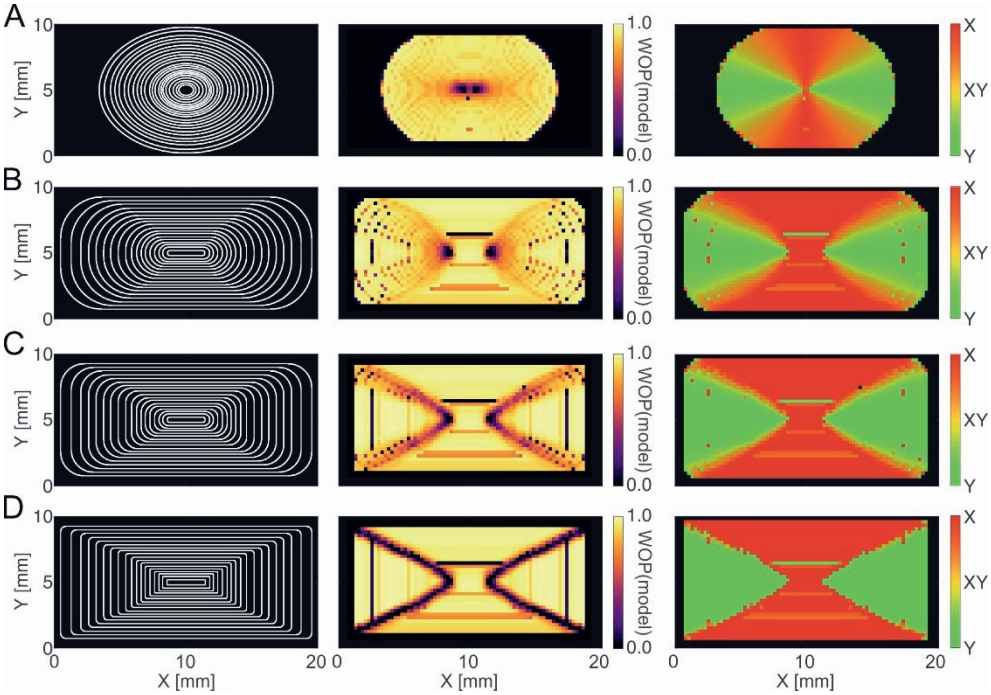

Fig. 3.5: *Synthetic axial images (left), mimicking the lamellar phase separation in SPC extrudates as seen by axial MRI data Fig. 3.3C, obtained for cross-sectional cooling die geometries with increasingly sharper corners ranging from elliptical (top) to rectangular (bottom) shaped. The synthetic MRI data, generated as described in section 3.2.6, was further analysed by the RFT algorithm to create a vector field (data not shown). This vector field was used to calculate the corresponding WOP(model) (middle) and PDD(model) (right) maps.*

3.3.4 The effect of cooling die geometry on lamellar phase-separation

In order to investigate the influence of the cross-sectional cooling die geometry on the morphology of the phase-separated lamellar structure of SPC extrudates, synthetic axial MRI images were generated, as described in section 3.2.6. In Fig. 3.5A, the simulated axial image (left) for a cooling die with an ellipse-like cross-sectional geometry, along with its WOP(model) (middle) and PDD(model) (right) maps, are shown. The latter maps (Fig. 3.5), respectively simulating the 10^2 (Fig. 3.3D) or 10^{-1} µm length scale (Fig. 3.4C), were calculated using the same RFT algorithm adopted for the WOP(MRI) maps (see section 3.2.5). In Fig. 3.5A, the orientation and curvature of the lamellar phase-separated structure evolve smoothly along the XY plane as expected, without sharp corner regions. Correspondingly, the WOP(model) values for this data are ($\sim$0.93 ± 0.02), determined as outlined in Fig. S3.10, and reflect a highly ordered, homogeneous ellipse-like lamellar structure (Fig. 3.5A). These findings are consistent with DT-MRI and WOP(MRI) maps acquired for a pilot-scale SPC extrudate shifted to pH 7.0, produced as described in Garina *et al.* (2026) [6] using a cooling

die with fully rounded edges. The latter data revealed a uniform WOP(MRI) distribution even across the rounded-edge region (See Fig. S3.9A-B), in analogy to the WOP(model) results in Fig. 3.5A. In the corresponding PDD(model) maps (Fig. 3.5A, right), simulating the 10^{-1} µm-scale, the vector angle orientation is seen to gradually evolve between X (red), at the top and bottom, and Y (green), at the left and right sides of the map, with combinations of X-Y directions being displayed in a gradient (orange).

In Fig. 3.5B-D, the synthetic axial images, WOP(model) and PDD(model) maps for cross-sectional cooling die geometries with increasingly sharper rectangular profiles are shown. These geometries display progressively more abrupt changes at the corner edges in the axial plane, in the spatial orientation of the lamellar phase-separated structure. The WOP(model) map in Fig. 3.5B shows a value of (0.96 ± 0.02) in the region where structure is oriented horizontally (see Fig. S3.10). In the corner regions, the WOP(model) value decreases to (0.86 ± 0.13) with the more disordered corner region having a width of 3.3 mm (see Fig. S3.10). In panel C, WOP(model) values decrease from (0.97 ± 0.01) in the horizontally ordered region to (0.62 ± 0.17) in the more disordered corner region. The width of this disordered region decreased to 1.9 mm. By creating a sharper rectangular profile, with a disordered corner region of 1.1 mm (Fig. 3.5D), WOP(model) values decrease from (0.97 ± 0.01) in the horizontally ordered region to (0.28 ± 0.17) in the disordered corner regions. The WOP(MRI) map in Fig. 3.3D, of the sample shifted to pH 7.0, shows a decrease in WOP values in between similar to those found in the simulations shown in Fig. 3.5C-D. When considering the PDD(model) maps for the rectangle-like shape with rounded corners (Fig. 3.5B, right), the spatial variation of the vector angle appears similarly gradual to the ellipse-like shape shown in Fig. 3.5A. When the rounded corners become sharper, the corresponding X-Y transition region in the PDD(model) map rapidly decreases in thickness. The secondary diffusion direction observed for the sample shifted to pH 7.0 (Fig. 3.4D, right), shows an angle distribution similar to the simulated PDD(model) map in Fig. 3.5C. We notice that, for the pilot-scale sample shifted to pH 7.0, an angle distribution more similar to Fig. 3.5B (right) is observed (see Fig. S3.9E).

3.2.7 Structural hierarchy at 10^{-1}-10^{2} µm length scale in SPC extrudates

The CLSM images in Fig. 3.3E-F and DT-MRI FA data in Fig. 3.4B show that an aligned fibrillar protein network is observed, at the 10^{-1} µm-scale, for the SPC extrudates shifted to pH 5.0 and 7.0. This indicates that pH-shifting down to values closer to the pI, near pH 5.0, leads to an isotropic particulate protein network [7]. Also, at the 10^{2} µm-scale, a lack of an aligned lamellar structure is observed by MRI images and WOP(MRI) maps in Fig. 3.3A-D at pH 5.0. The structuring at this length scale has been shown to primarily occur in the cooling die of the extruder [6]. The pH of the protein melt affects its rheological properties and thus flow behaviour occurring inside the cooling die. At pH 5.0, the yield stress of the protein melt is

higher compared to that at pH 7.0 and 7.8 [18]. The stress applied to the protein melt at pH 5.0 is likely not sufficiently high to create the sheared laminar flow through the cooling die that results in the parallel lamellae seen in Fig. 3.3A at pH 7.0 and 7.8. However, at the 10^{-1} µm-scale, the phase-separated structure observed by PDD(DT) maps closely follows the orientation of the phase-separated lamellae observed at the 10^{2} µm-scale. Thus, structure formation at the 10^{-1} µm-scale, likely precedes that of phase-separated structuring in the cooling die. This is in line with SANS measurements that have shown that during HME of SPC, protein structure formation at the 10^{-1} µm-scale already takes place in the last barrel sections of the extruder [6]. This indicates that an optimum pH exists at which (i) fibrillar network alignment occurs at the 10^{-1} µm-scale and (ii) the yield stress of the protein melt is sufficiently low to drive lamellar phase separation, at the 10^{2} µm-scale, during flow through the cooling die (see Fig. S3.12 in SI).

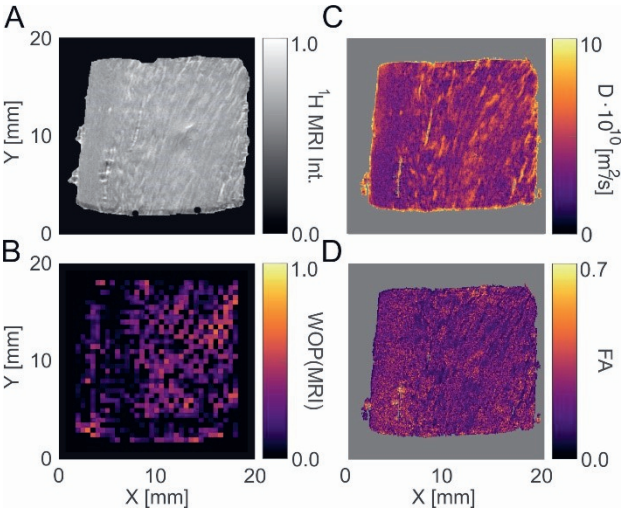

Fig. 3.6: MRI, DT-MRI and RFT results for commercial high-moisture bovine mozzarella cheese. A cube of sample was cut and placed in a 25-mm MRI tube containing a NaCl solution matching the salt content on the packaging, to prevent drying of the cheese during measurements. (A) T_1- and T_2-weighted RARE image acquired using: T_E = 15 ms, T_R = 1 s, 2 signal averages, MRI resolution = 78x78x1000 µm^3. The background signal was removed from the image by masking of the pixels outside the sample area. (B) WOP(MRI) results of the image in panel A. (C) Apparent diffusion coefficient map resulting from a DT-MRI STE experiment acquired using: T_E = 12.5ms, T_R = 1 s, 8 signal averages, MRI resolution = 78x78x1000 µm^3, 8 A_0-images at b = 120 s/mm^2 and 36 images at b = 1000 s/mm^2. (D) FA map resulting from the diffusion tensor calculations.

3.2.8 MRI and DT-MRI assessment of hierarchical structure in mozzarella

Here, we applied T_2-weighted MRI and DT-MRI to investigate the hierarchical structure of commercial high-moisture mozzarella, which is industrially produced through the heating, between 60 – 80 °C, and stretching of full fat or skim cheese curd [43, 44]. The stretching of the heated curd is what determines the parallel alignment of casein fibrils and imparts structure. In Fig. 3.6, MRI and DT-MRI results of a commercial high-moisture bovine mozzarella (~64 wt%), are shown. In Fig. 3.6A, a phase-separated structure is distinguishable with a homogeneous alignment parallel to the left sample edge, which is the exterior of the sample relative to the uncut mozzarella product. In the WOP(MRI) map Fig. 3.6B, this region is marked as having high anisotropic order at the 10^2 µm length scale. Similar results are observed in microscopy images of high-moisture (~56 wt%) bovine-mozzarella cheese shown in Nguyen *et al.* (2017) [45]. However, an aligned anisotropic structure is not observed at the lower length scale probed by DT-MRI and shown in the FA map in Fig. 3.6D. The absence of anisotropic alignment at such lower length scales is confirmed by SANS measurements, which showed isotropic scattering profiles at length scales below 90 nm (Fig. S3.11 in SI). Scattering profiles remained isotropic after contrast enhancement using D_2O [14]. This indicates that nm-scale structural alignment is required to observe 10^{-1} µm-scale aligned structures by DT-MRI. For mozzarella, such 10^{-1} µm-scale anisotropic aligned structure is less apparent, in contrast to SPC extrudates where nm-scale protein fibrillar alignment is clearly observed by SANS measurements [6, 7].

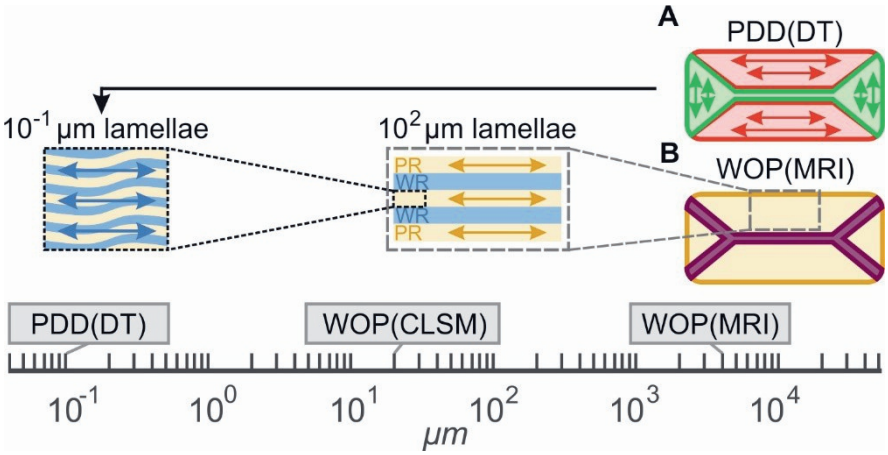

Fig. 3.7: *Schematic diagram of hierarchy in the anisotropic structure of SPC extrudates. (A) DT-MRI PDD(DT) maps where the water self-diffusion direction, hindered by the protein fibrils seen in CLSM (Fig. 3.3E) at the 10^{-1} µm-scale, is colour-coded for X (red) and Y (green) as shown in Fig. 3.4D; (B) WOP(MRI) maps of 10^2 µm-scale lamellar alignment (Fig. 3.3D), where high alignment (yellow) is observed along the sample edges and low alignment (purple) where two or more alignment directions meet. Alignment is averaged over a ~$4{\cdot}10^3$ µm-scale area; in the WOP(CLSM) maps (Fig. 3.3F) protein fibril alignment is averaged over a ~$2{\cdot}10^1$ µm-scale area.*

3.4 Conclusions

In this work, we set out to investigate the hierarchical structure of pH-shifted SPC extrudates on a wide range of length scales, from 10^{-1} µm (Fig. 3.7A) to 10^{2} µm (Fig. 3.7B). To cover such wide range of structural length scales, we exploited an array of techniques, including CEST MRI, T_2-weighted and DT-MRI mapping, as well as advanced image analysis and simulation methods.

In SPC extrudates, RFT analysis of T_2-weighted MRI images featured aligned PR and WR lamellae at the 10^{2} µm length scale (Fig. 3.7B) at pH 7.0 and 7.8, yet a more disordered lamellar structure at pH 5.0. CEST MRI showed the presence of dissolved proteins in the WR lamellae. According to DT-MRI, these WR lamellae do not display structural anisotropy. DT-MRI did show that the PR lamellae had an underlying anisotropic structure at the 10^{-1} µm length scale, which can be semi-quantified by Principal Diffusion Direction (PDD) maps (Fig. 3.7A). The presence of structural anisotropy at this small length scale was confirmed by CLSM, which showed alignment of protein fibrils at the 10^{-1} µm length scale at pH 5.0 and 7.0. The MRI-based RFT and PDD maps provided a quantitative measure of the impact of pH-shifting on hierarchical anisotropic structure formation in the cooling die and showed how fibrillar alignment at the 10^{-1} µm length scale may impact lamellar phase-separation at the 10^{2} µm length scale. The detailed MRI features observed in the RFT and PDD maps of SPC extrudates could be explained by simulating the effect of the cross-sectional cooling die geometry.

We note that the observed hierarchical character of structural anisotropy is specific to SPC extrudates. In a different anisotropic protein-based material, here mozzarella, we observed order only at the 10^{2} µm length scale. Due to the lack of order at lower length scales, DT-MRI showed no evidence of diffusional anisotropy.

We conclude that high-resolution MRI is a versatile measurement technique suitable to characterise hierarchical anisotropic structures in extruded protein-based food materials. We envisage future applications of such methods for tuning and optimising formulations, including the use of novel protein sources, and processing routes.

Authors statement

Sam A. Kuijpers: Conceptualisation, Data curation, Formal analysis, Investigation, Methodology, Visualisation, Software, Writing - original draft. Martijn I. Gobes: Data curation, Investigation, Software. Morwarid Mayar: Data curation, Investigation, Methodology, Frank Vergeldt: Methodology, Software, Data curation, Writing - review & editing. Johannes Hohlbein: Writing - review & editing. Thom Huppertz: Writing - review & editing. John P.M. van Duynhoven: Conceptualisation, Funding acquisition, Resources, Supervision, Writing - review & editing. Camilla Terenzi: Conceptualisation, Funding acquisition, Resources, Supervision, Writing - review & editing, Project administration.

Declaration of competing interest

John P.M. van Duynhoven and Thom Huppertz are employed by companies that manufacture and market plant-based meat alternatives (JvD) and structured dairy protein products (TH). The other authors declare that they have no known competing financial interests or personal relationships that could have appeared to influence the work reported in this paper.

Acknowledgements

This work is part of the project "Measurement and Modelling of Multiscale Processed Protein Products (MP3)" (with project number 18744) of the research programme OTP TTW, financed by the Dutch Research Council and by the consortium partners Unilever, Cargill, dsm-firmenich, FrieslandCampina and Wageningen Food and Biobased Research. This project was also supported by the uNMR-NL Grid: A distributed, state-of-the-art Magnetic Resonance facility for the Netherlands (NWO grant 184.035.002). Peter Basser (NIH, USA) is gratefully acknowledged for insightful discussions on processing of DT-MRI data. Finally, we thank Kalyan Panda and Claudia Zimmermann (Unilever Global Food Innovation Centre, Wageningen) for having performed extrusion trials. We gratefully acknowledge the Science and Technology Facilities Council (STFC) for access to neutron beamtime at ISIS through the ISIS Xpress service. We thank Steven Parnell (ISIS) and Ekaterina Garina (Technical University of Delft) for their assistance with Xpress measurements.

References

[1] H. Aiking and J. de Boer, “The next protein transition,” *Trends Food Sci. Technol.*, vol. 105, pp. 515–522, 2020, doi: 10.1016/j.tifs.2018.07.008.

[2] A. C. Hoek, S. Malekpour, R. Raven, E. Court, and E. Byrne, “‘Towards environmentally sustainable food systems: decision-making factors in sustainable food production and consumption,’” *Sustain. Prod. Consum.*, vol. 26, pp. 610–626, 2021, doi: 10.1016/j.spc.2020.12.009.

[3] E. S. Collier *et al.*, “Identifying barriers to decreasing meat consumption and increasing acceptance of meat substitutes among Swedish consumers,” *Appetite*, vol. 167, no. August, p. 105643, 2021, doi: 10.1016/j.appet.2021.105643.

[4] Y. Wang *et al.*, “The development process of plant-based meat alternatives: Raw material formulations and processing strategies,” *Food Res. Int.*, vol. 167, no. February, p. 112689, 2023, doi: 10.1016/j.foodres.2023.112689.

[5] H. Akdogan, “High moisture food extrusion,” *Int. J. Food Sci. Technol.*, vol. 34, no. 3, pp. 195–207, 1999, doi: 10.1046/j.1365-2621.1999.00256.x.

[6] E. D. Garina *et al.*, “Mapping anisotropic structure formation of soy protein during high-moisture extrusion,” *Food Hydrocoll.*, vol. 172, no. P2, p. 112037, 2026, doi: 10.1016/j.foodhyd.2025.112037.

[7] S. A. Kuijpers *et al.*, “Impact of pH-shifting on multiscale structural anisotropy of high-moisture extrudates of soy proteins,” *Food Hydrocoll.*, vol. 168, no. April, p. 111456, 2025, doi: 10.1016/j.foodhyd.2025.111456.

[8] R. G. M. Van der Sman and A. J. Van der Goot, “Hypotheses concerning structuring of extruded meat analogs,” *Curr. Res. Food Sci.*, vol. 6, no. May, p. 100510, 2023, doi: 10.1016/j.crfs.2023.100510.

[9] V. L. Pietsch, J. M. Bühler, H. P. Karbstein, and M. A. Emin, “High moisture extrusion of soy protein concentrate: Influence of thermomechanical treatment on protein-protein interactions and rheological properties,” *J. Food Eng.*, vol. 251, pp. 11–18, Jun. 2019, doi: 10.1016/j.jfoodeng.2019.01.001.

[10] J. Li *et al.*, “Understanding the effect of pH on structure formation in high moisture extrudates produced from soy protein-dietary fiber blends,” *Food Hydrocoll.*, vol. 170, no. June 2025, p. 111710, 2026, doi: 10.1016/j.foodhyd.2025.111710.

[11] Q. Deng *et al.*, “High-moisture extrusion of soy protein: Effects of insoluble dietary fiber on anisotropic extrudates,” *Food Hydrocoll.*, vol. 141, no. March, p. 108688, 2023, doi: 10.1016/j.foodhyd.2023.108688.

[12] J. Li *et al.*, “The interplay between soy proteins and dietary fiber in determining the structure and texture of high moisture extrudates,” *Food Hydrocoll.*, vol. 156, no. February, p. 110256, 2024, doi: 10.1016/j.foodhyd.2024.110256.

[13] H. Patel, C. Barnés-Calle, Å. Rinnan, S. B. Engelsen, and F. W. J. van den Berg, “Characterization of the anisotropy in proteinaceous semi-solid food matrices through polarized fluorescence spectroscopy,” *J. Food Compos. Anal.*, vol. 140, no. September 2024, 2025, doi: 10.1016/j.jfca.2025.107237.

[14] E. D. Garina *et al.*, “SANS and SAXS : A Love Story to unravel structural evolution of soy proteins and polysaccharide fibres during high moisture extrusion for meat alternatives,” *Food Hydrocoll.*, vol. 155, no. January, p. 110121, 2024, doi: 10.1016/j.foodhyd.2024.110121.

[15] R. Van Beers, B. Aernouts, M. M. Reis, and W. Saeys, “Anisotropic light propagation in bovine muscle tissue depends on the initial fiber orientation, muscle type and wavelength,” *Opt. Express*, vol. 25, no. 18, p. 22082, 2017, doi: 10.1364/oe.25.022082.

[16] M. Nieuwland, W. Heijnis, A. J. van der Goot, and R. Hamoen, “XRT for visualizing microstructure of extruded meat replacers,” *Curr. Res. Food Sci.*, vol. 6, p. 100457, 2023, doi: 10.1016/j.crfs.2023.100457.

[17] S. Kuijpers, G.-J. Goudappel, T. Huppertz, J. Van Duynhoven, and C. Terenzi, “Quantification of phase separation in high moisture soy protein extrudates by NMR and MRI,” *Food Res. Int.*, vol. 197, no. P1, p. 115225, 2024, doi: 10.1016/j.foodres.2024.115225.

[18] M. I. Gobes, S. A. Kuijpers, C. Terenzi, R. G. M. van der Smaan, J. P. M. van Duynhoven, and J. Hohlbein, “Rotated Fourier transform (RFT) enables the quantification of anisotropic structure in high-moisture plant-protein extrudates,” *Food Struct.*, vol. 44, no. June, p. 100437, 2025, doi: 10.1016/j.foostr.2025.100437.

[19] P. J. Basser, J. Mattiello, and D. LeBihan, “MR diffusion tensor spectroscopy and imaging,” *Biophys. J.*, vol. 66, no. 1, pp. 259–267, 1994, doi: 10.1016/S0006-3495(94)80775-1.

[20] J. M. Bonny and J. P. Renou, “Water diffusion features as indicators of muscle structure ex vivo,” *Magn. Reson. Imaging*, vol. 20, no. 5, pp. 395–400, 2002, doi: 10.1016/S0730-725X(02)00515-5.

[21] K. E. Anderssen, M. Kranz, S. Syed, and S. K. Stormo, “Diffusion tensor imaging for spatially-resolved

characterization of muscle fiber structure in seafood," *Food Chem.*, vol. 380, no. September 2021, p. 132099, 2022, doi: 10.1016/j.foodchem.2022.132099.

[22] P. B. Kingsley, "Introduction to diffusion tensor imaging mathematics: Part II. Anisotropy, diffusion-weighting factors, and gradient encoding schemes," *Concepts Magn. Reson. Part A Bridg. Educ. Res.*, vol. 28, no. 2, pp. 123–154, 2006, doi: 10.1002/cmr.a.20049.

[23] P. B. Kingsley, "Introduction to diffusion tensor imaging mathematics: Part III. Tensor calculation, noise, simulations, and optimization," *Concepts Magn. Reson. Part A Bridg. Educ. Res.*, vol. 28, no. 2, pp. 155–179, 2006, doi: 10.1002/cmr.a.20050.

[24] P. B. Kingsley, "Introduction to diffusion tensor imaging mathematics: Part I. Tensors, rotations, and eigenvectors," *Concepts Magn. Reson. Part A Bridg. Educ. Res.*, vol. 28, no. 2, pp. 101–122, 2006, doi: 10.1002/cmr.a.20048.

[25] K. M. Ward, A. H. Aletras, and R. S. Balaban, "A New Class of Contrast Agents for MRI Based on Proton Chemical Exchange Dependent Saturation Transfer (CEST)," *J. Magn. Reson.*, vol. 143, no. 1, pp. 79–87, 2000, doi: 10.1006/jmre.1999.1956.

[26] P. C. M. Van Zijl and N. N. Yadav, "Chemical exchange saturation transfer (CEST): What is in a name and what isn't?," *Magn. Reson. Med.*, vol. 65, no. 4, pp. 927–948, 2011, doi: 10.1002/mrm.22761.

[27] F. Ellwanger, M. Fuhrmann, and H. P. Karbstein, "Influence of Lowering the pH Value on the Generation of Fibrous Structures of Protein Gels with Different Network Types," *gels*, vol. 10, no. 173, pp. 1–14, 2024.

[28] P. T. Callaghan and C. D. Eccles, "Diffusion-Limited Resolution in Nuclear Magnetic Resonance Microscopy," *J. Magn. Reson.*, vol. 78, pp. 1–8, 1988, doi: https://doi.org/10.1016/0022-2364(88)90151-5.

[29] J. Hohlbein, "Single-molecule localization microscopy as an emerging tool to probe multiscale food structures ☆," *Food Struct.*, vol. 30, no. October, p. 100236, 2021, doi: 10.1016/j.foostr.2021.100236.

[30] M. Mayar, P. Smeets, J. van Duynhoven, and C. Terenzi, "In vitro 1H MT and CEST MRI mapping of gastro-intestinal milk protein breakdown," *Food Struct.*, vol. 36, no. September 2022, p. 100314, 2023, doi: 10.1016/j.foostr.2023.100314.

[31] J. Hennig, A. Nauerth, and H. Friedburg, "RARE imaging: A fast imaging method for clinical MR," *Magn. Reson. Med.*, vol. 3, no. 6, pp. 823–833, 1986, doi: 10.1002/mrm.1910030602.

[32] E. O. Stejskal and J. E. Tanner, "Spin diffusion measurements: Spin echoes in the presence of a time-dependent field gradient," *J. Chem. Phys.*, vol. 42, no. 1, pp. 288–292, 1965, doi: 10.1063/1.1695690.

[33] D. K. Jones, M. A. Horsfield, and A. Simmons, "Optimal strategies for measuring diffusion in anisotropic systems by magnetic resonance imaging," *Magn. Reson. Med.*, vol. 42, no. 3, pp. 515–525, 1999, doi: 10.1002/(SICI)1522-2594(199909)42:3<515::AID-MRM14>3.0.CO;2-Q.

[34] D. K. Jones and P. J. Basser, "'Squashing peanuts and smashing pumpkins': How noise distorts diffusion-weighted MR data," *Magn. Reson. Med.*, vol. 52, no. 5, pp. 979–993, 2004, doi: 10.1002/mrm.20283.

[35] J. Stancanello, E. Terreno, D. Delli Castelli, C. Cabella, F. Uggeri, and S. Aime, "Development and validation of a smoothing-splines-based correction method for improving the analysis of CEST-MR images," *Contrast Media Mol. Imaging*, vol. 3, no. 4, pp. 136–149, 2008, doi: 10.1002/cmmi.240.

[36] N. Otsu, "A Threshold Selection Method from Gray-Level Histograms," *IEEE Trans. Syst. Man. Cybern.*, vol. 9, no. 1, pp. 62–66, 1979, doi: https://doi.org/10.1109/TSMC.1979.4310076.

[37] P. J. Basser and S. Pajevic, "Statistical artifacts in diffusion tensor MRI (DT-MRI) caused by background noise," *Magn. Reson. Med.*, vol. 44, no. 1, pp. 41–50, 2000, doi: 10.1002/1522-2594(200007)44:1<41::AID-MRM8>3.0.CO;2-O.

[38] N. Makris *et al.*, "Morphometry of in vivo human white matter association pathways with diffusion-weighted magnetic resonance imaging," *Ann. Neurol.*, vol. 42, no. 6, pp. 951–962, Dec. 1997, doi: https://doi.org/10.1002/ana.410420617.

[39] J. Schindelin *et al.*, "Fiji: An open-source platform for biological-image analysis," *Nat. Methods*, vol. 9, no. 7, pp. 676–682, 2012, doi: 10.1038/nmeth.2019.

[40] Y. Zhou, C. Bie, P. C. M. van Zijl, and N. N. Yadav, "The relayed nuclear Overhauser effect in magnetization transfer and chemical exchange saturation transfer MRI," *NMR Biomed.*, vol. 36, no. 6, pp. 1–21, 2023, doi: 10.1002/nbm.4778.

[41] C. K. Jones *et al.*, "Nuclear Overhauser enhancement (NOE) imaging in the human brain at 7T," *Neuroimage*, vol. 77, pp. 114–124, 2013, doi: 10.1016/j.neuroimage.2013.03.047.

[42] J. L. Olesen, A. Ianus, L. Østergaard, N. Shemesh, and S. N. Jespersen, "Tensor denoising of multidimensional MRI data," *Magn. Reson. Med.*, vol. 89, no. 3, pp. 1160–1172, 2023, doi: 10.1002/mrm.29478.

[43] P. Tremonte, F. Nazzaro, and R. Coppola, “Mozzarella Cheese,” in *Dairy Foods Processing*, 1st ed., A. G. da Cruz, T. C. Pimentel, E. A. Esmerino, and S. Verruck, Eds. Humana Press, 2024, pp. 31–54. doi: https://doi.org/10.1007/978-1-0716-4144-6.

[44] C. Yu and S. Gunasekaran, “A systems analysis of pasta filata process during Mozzarella cheese making,” *J. Food Eng.*, vol. 69, no. 4, pp. 399–408, 2005, doi: 10.1016/j.jfoodeng.2004.08.031.

[45] H. T. H. Nguyen, L. Ong, C. Lopez, S. E. Kentish, and S. L. Gras, “Microstructure and physicochemical properties reveal differences between high moisture buffalo and bovine Mozzarella cheeses,” *Food Res. Int.*, vol. 102, no. June, pp. 458–467, 2017, doi: 10.1016/j.foodres.2017.09.032.

[46] O. Arnold *et al.*, “Mantid - Data analysis and visualization package for neutron scattering and μ SR experiments,” *Nucl. Instruments Methods Phys. Res. Sect. A Accel. Spectrometers, Detect. Assoc. Equip.*, vol. 764, pp. 156–166, 2014, doi: 10.1016/j.nima.2014.07.029.

3.5 Supplementary Information

3.5.1 Sample preparation

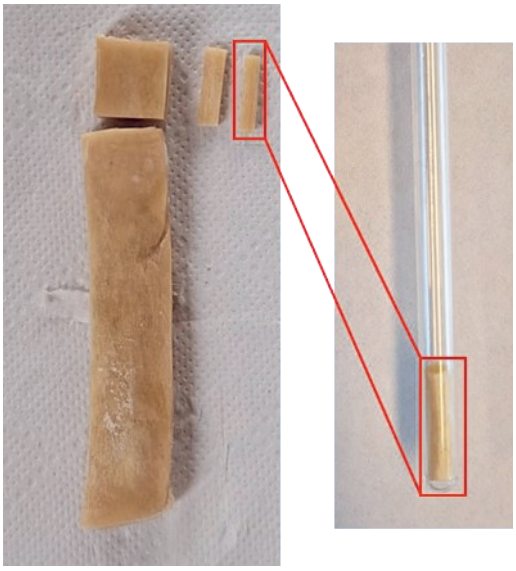

Fig. S3.1. *Photograph of the extrudate sample used for the CEST MRI measurements.*

3.5.2 Effect of diffusion mixing time on tensor calculations

To observe the diffusional anisotropy of water inside an SPC extrudate, restricted diffusion has to be ensured. In our previous work, the average compartment size of the PR phase was estimated from CLSM data to be 15±5 µm [17]. To ensure that water within such compartment experiences restricted diffusion, the diffusion mixing time should ensure that mean square displacement of water, calculated using Einstein's formula in 3D, is sufficiently large. A diffusion radius, $\langle r^2 \rangle$ of 9 µm – 33 µm is expected using Δ values between 10 and 150 ms (Fig. S3.2) and the average diffusion coefficient of water inside an SPC extrudate of $1.25 \cdot 10^{-9}$ m^2/s (Fig. S3.2B). FigS1.2A shows that the relative amount of non-physical tensor elements, i.e. with eigenvalues < 1, increases with increasing Δ. This occurs due to the decreased SNR resulting from the additional T_1-weighing at longer mixing times in an STE acquisition (See S1.3). Figure S3.2B shows that, with increasing Δ, the mean diffusion coefficient shifts down. However, due to the longer mixing times required, the minimum effective b-value used for the A_0-images increased from 120 s/mm^2 to 330 s/mm^2, which shifts the slope of the linear least-squares regression towards lower diffusion coefficient values. Additionally, a shift in the FA values towards 1 can be seen in Fig. S3.2C similar to data shown in Fig. S3.3C.

Based on the results of Fig. S3.2, a Δ of 50 ms was chosen, corresponding to a $\langle r^{-2} \rangle$ of roughly 20 µm, which is sufficiently large to allow for restricted diffusion yet short enough to ensure a sufficient SNR and limited effects on FA.

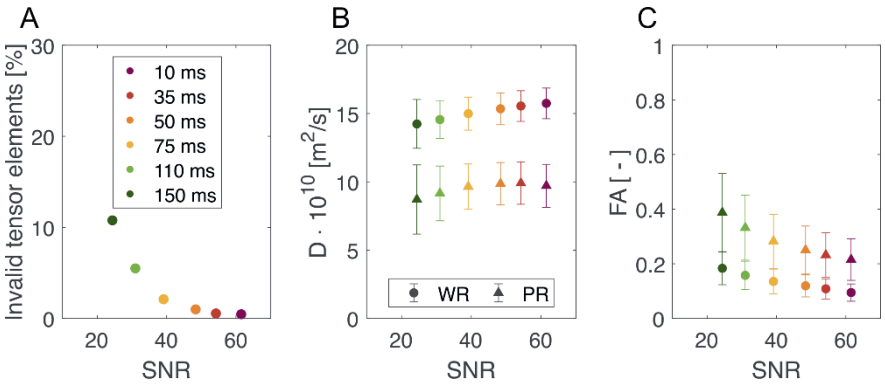

Fig. S3.2: *DT-MRI results acquired on a pH 7 SPC extrudate using an increasing mixing time for diffusion. Data was acquired using 6 manually set A0-images at b_{eff} = 120 s/mm² (b_{eff} = 250 s/mm² at Δ = 110 ms and b_{eff} = 330 s/mm² at Δ = 150 ms) and 32 images at b = 1000 s/mm². Acquisition parameters were as follows: STE with TE = 12 ms; TR = 1000 ms; voxel size = 78x78x1000 µm³; δ = 2 ms and 4 averages were used. Images were masked for the background. (A) relative amount of non-physical tensor elements assessed by reviewing the number of voxels with one or more negative tensor elements. (B) Distribution of diffusion coefficients calculated from the trace of the diffusion tensors. (C) Distribution of fractional anisotropy values calculated per voxel from the tensor eigenvalues.*

3.5.3 Effect of signal-to-noise ratio on tensor calculations

When either of the two datapoints, used by the linear regression model to calculate the diffusion value, has a significant enough contribution from noise, such that it cannot be distinguished from a measurement in a different gradient direction, the tensor calculation can become erroneous [22]. Figure S3.3 shows the results of an experiment where the noise was artificially increased by reducing the number of sampling averages per acquisition. One way to observe the effect of erroneous tensor calculations is to review how many tensors have one or more negative eigenvalues [22]. Figure S3.3A shows that as the SNR decreases, the relative amount of erroneous tensor calculations goes up. Figure S3.3B shows that only a minor effect on the diffusion coefficient is found for both the WR and PR phases. However, the effect is more noticeable on the FA calculation. A decrease in SNR is associated with an increase in FA and is not a physical property of the sample but the result of inaccurate tensor calculations. The data shows that the optimal SNR for this sample at the chosen resolution is between 4 and 6. Based on the data shown in Fig. S3.3, the data in the main text figures was acquired using 8 averages due to the smaller voxel size of 52x52x1000 µm³.

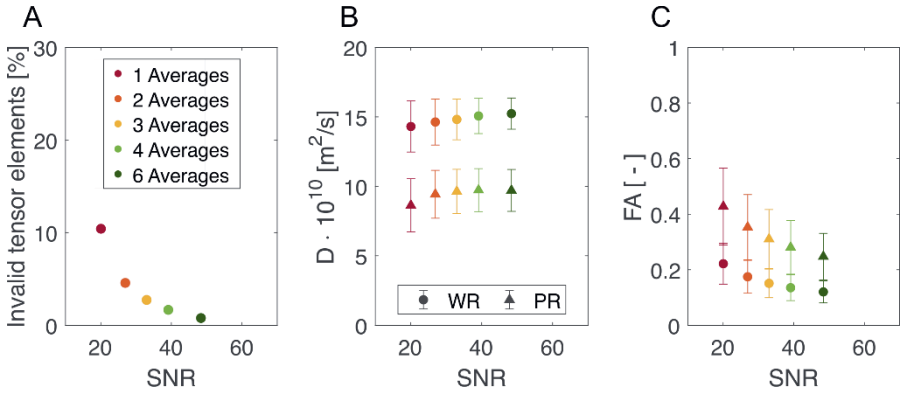

Fig. S3.3: *DT-MRI results acquired on a SPC extrudate at pH 7 using an increasing number of averages to shift the SNR of the acquisition. Data was acquired using 6 manually set A_0-images at b_{eff} = 120 s/mm² and 32 images set at a b-value of 1000 s/mm². Acquisition parameters were as follows: STE with T_E = 12 ms; T_R = 1000 ms; voxel size = 78x78x1000 µm³; δ = 2 ms and Δ = 50 ms. Images were masked for the background. (A) relative amount of non-physical tensor elements assessed by reviewing the number of voxels with one or more negative tensor elements. (B) Distribution of diffusion coefficients calculated from the trace of the diffusion tensors. (C) Distribution of fractional anisotropy values calculated per voxel from the tensor eigenvalues.*

3.5.4 Diffusion reference image acquisition

Due to a bug in the Paravision software version used in this work, the b-values are incorrectly calculated when using the stimulated-echo sequence, resulting in consistently underestimated diffusion coefficients of free water as shown by Fig. S3.4. As a workaround, the A_0-images were manually set as the first experimental shell with a minimum b_{eff} of 120 s/mm², resulting from the imaging and spoiler gradients.

Fig. S3.4AC shows that the use of the built-in A_0 images in Paravision leads to the underestimation of the diffusion coefficient which now becomes dependent on Δ. In a conventional DWI measurement using a multitude of b-values, this can be easily alleviated by omitting these values from the fitting as shown in Fig. S3.4BD. However, for DT-MRI generally only two b-values are used, those of the A_0-images close to 0 s/mm² and one between 800 and 2000 s/mm² depending on the system [22–24]. The data is typically fitted using a linear least squares algorithm and due to the limited b-values, this fit is largely dependent on the correct acquisition of the A_0-images.

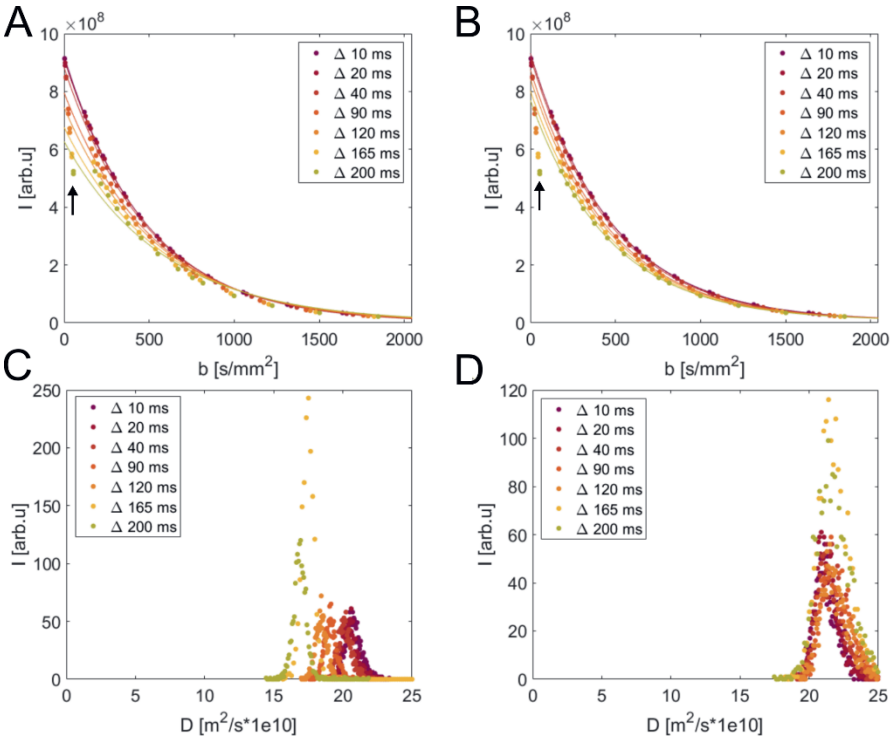

Fig. S3.4: *DWI results acquired on a 10 mm tube of demineralised water using different mixing times in a STE sequence. Two A_0-images were acquired, and 14 b-values were geometrically chosen between 110 s/mm² and 1600 s/mm². The resulting images were masked for the background, and the mean intensity of the water was plotted. (A) DWI intensity results fitted using an exponential decay including the A_0-image intensity. (B) DWI intensity results fitted using an exponential decay excluding the A_0-images from fitting. The black arrow points to the A_0-image intensities. (C) The distribution of diffusion values acquired from per voxel exponential fitting of the intensity decay data including the A_0-image intensities. (D) The distribution of diffusion values acquired from per voxel exponential fitting of the intensity decay data excluding the A_0-image intensities. The expected diffusion coefficient of water at the room temperature of 21°C is $2.07 \cdot 10^{-9}$ m²/s.*

3.5.5 Effect of number of diffusion directions on tensor calculations

A minimum of six diffusion directions along the six unique cartesian vectors (xx, yy, zz, xy, xz, yz) are required to calculate the diffusion tensor. However, if just one of these directions contains noisy data, the entire tensor calculation can become inaccurate [22]. Therefore, it is advised to include the acquisition of additional diffusion encoding directions, as well as, spacing these directions not along the six unique cartesian vectors but instead on a hemisphere [22]. The inclusion of more than six diffusion acquisitions will inherently decrease the sensitivity of the tensor calculation to noise. Additionally, by choosing uniformly distributed diffusion encoding directions, the anisotropy of diffusion restriction can be more accurately assessed, at the cost of longer measurement times. In the Fig. S3.5, different encoding schemes of increasing number of directions have been used to acquire a DT-MRI image of a pH 7 SPC extrudate. The imaging parameters were kept constant, thus, the SNR between acquisitions is constant. However, the amount of invalid tensor elements decreases as more imaging directions are added, highlighting the effect noise has on the tensor calculation. Between 32 and 48 directions, the number valid tensor elements and resulting FA calculations remained constant with increasing directions. In this work, 36 imaging directions are used.

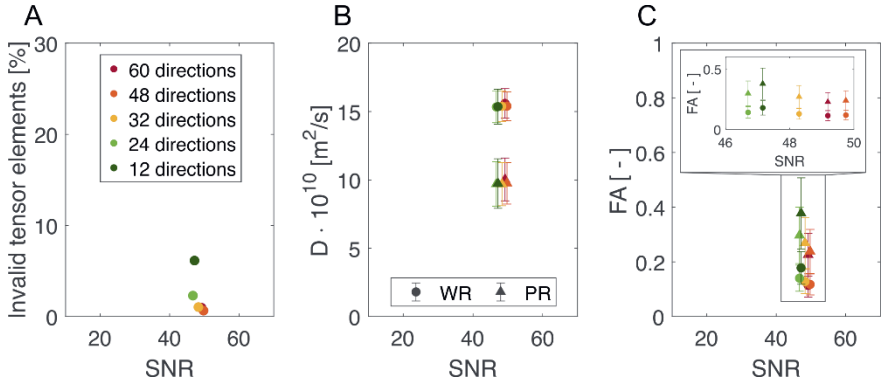

Fig. S3.5: *DT-MRI results acquired on a pH 7 SPC extrudate using an increasing number of diffusion directions. Data was acquired using 8 manually set A_0-images at b_{eff} = 120 s/mm² and between 12 and 60 images at b = 1000 s/mm². Acquisition parameters were as follows: STE with T_E = 12 ms; T_R = 1000 ms; voxel size = 78x78x1000 µm³; δ = 2 ms and 4 averages were used. Images were masked for the background. (A) relative amount of non-physical tensor elements assessed by reviewing the number of voxels with one or more negative tensor elements. (B) Distribution of diffusion coefficients calculated from the trace of the diffusion tensors. (C) Distribution of fractional anisotropy values calculated per voxel from the tensor eigenvalues.*

3.5.6 ROI-based Eigenvalue sorting

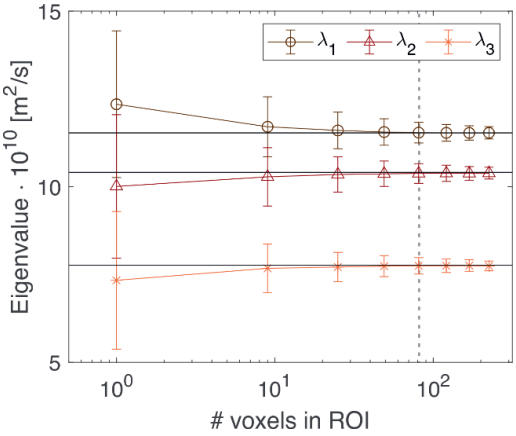

Fig. S3.6: *Mean eigenvalue distribution of ROI-based sorting for each eigenvalue* [37]*. The first datapoint at 10^0 voxels, i.e. a ROI of 1x1 voxel, is identical to the magnitude sorting of eigenvalues. At #voxels = 81, i.e. a 9x9 ROI region (dashed line), the eigenvalue distribution does not change with respect to ROI size. The solid lines represent the equilibrium value for the eigenvalue distribution. The error bars represent the standard error in the ROI-sorting based on ROI size, i.e. a larger ROI represents a more precise sorting. By magnitude sorting, the three eigenvalues inherently evenly distribute. However, after ROI-based sorting, the difference between the first and second eigenvalue decreases, which is expected based on the fractional anisotropy values found in these voxels of ca. 0.25.*

3.5.7 CEST of SPI dispersion

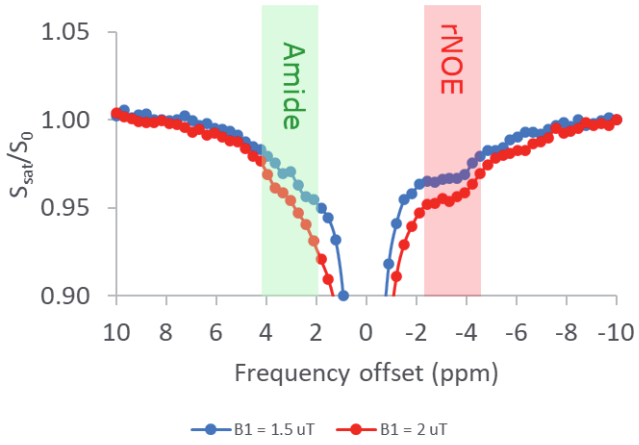

Fig. S3.7: *CEST MRI spectra of 1 wt% SPI solution measured on a wide-bore 600 MHz spectrometer with T_{sat} = 1 s, B_1 = 1.5 or 2 µT, T_R of 1 s, T_E = 10 ms, RARE-factor = 4, N_{avg} = 1.*

3.5.8 CEST of soaked fresh SPC extrudate

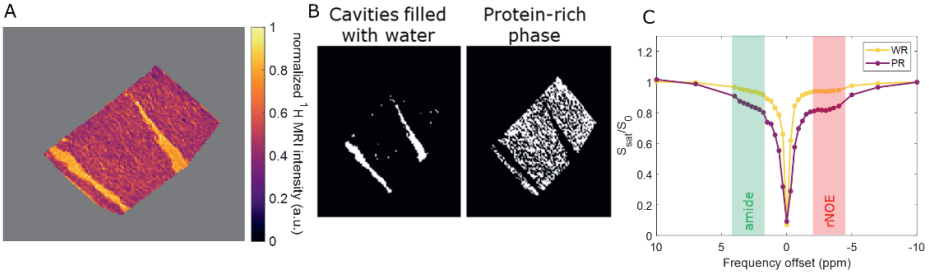

Fig. S3.8: *(A) T_2-weighted MRI image of fresh SPC extrudate from a pilot-plant extruder with high ^{1}H MRI intensities in the cavities filled with water during soaking, and in the WR phase and low intensities in the PR phase. (B) Masks for the cavities filled with water and the PR phase. (C) CEST spectra for the water-filled cavities and the PR phase.*

3.5.9 MRI and DT-MRI of pilot-scale SPC extrudate

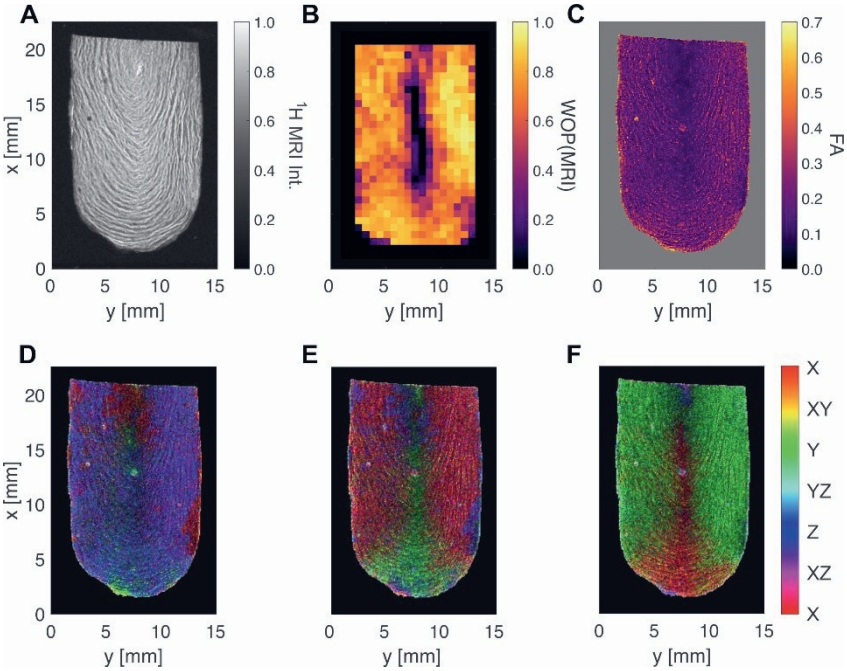

Fig. S3.9: *For SPC extrudate produced at pilot-scale and at pH 7 using a round edged cooling die: T_2-weighted image (A) and respective WOP(MRI) map (B), along with DT-MRI results (C-F). Processing temperature and moisture content are similar to the extrudate samples analysed in the main text. Data was acquired using 8 manually set A_0-images at b_{eff} = 120 s/mm^2 and 36 images at b = 1000 s/mm^2. Acquisition parameters were as follows: STE with T_E = 12 ms; T_R = 1000 ms; voxel size = 78x78x1000 µm^3; δ = 2 ms and 4 averages were used. (A) T_2-weighted MRI image acquired at b_{eff} = 120 s/mm^2 showing the phase-separated structure in PR and WR phases (B) RFT WOP map of MRI image in (A), analysed using a 31 pixel window and 75% overlap, showing a mostly uniform WOP value as the structure orientation changes in the rounded corner. (C) FA map showing similar values compared to lab-scale produced SPC extrudate samples. PDD map of (D) first eigenvalue (E) second eigenvalue and (F) third eigenvalue. Eigenvalues are sorted using the ROI-based sorting established in Basser* et al. *(2000) using an ROI size of 9x9 voxels* [37]. *Interestingly, as predicted by the modelling results of Fig. 3.5 in the main text, the dominant microstructural alignment more gradually evolves from the Y- to X-direction using a rounded die edge.*

3.5.10 Mean WOP areas of synthetic cross-sectional cooling die data

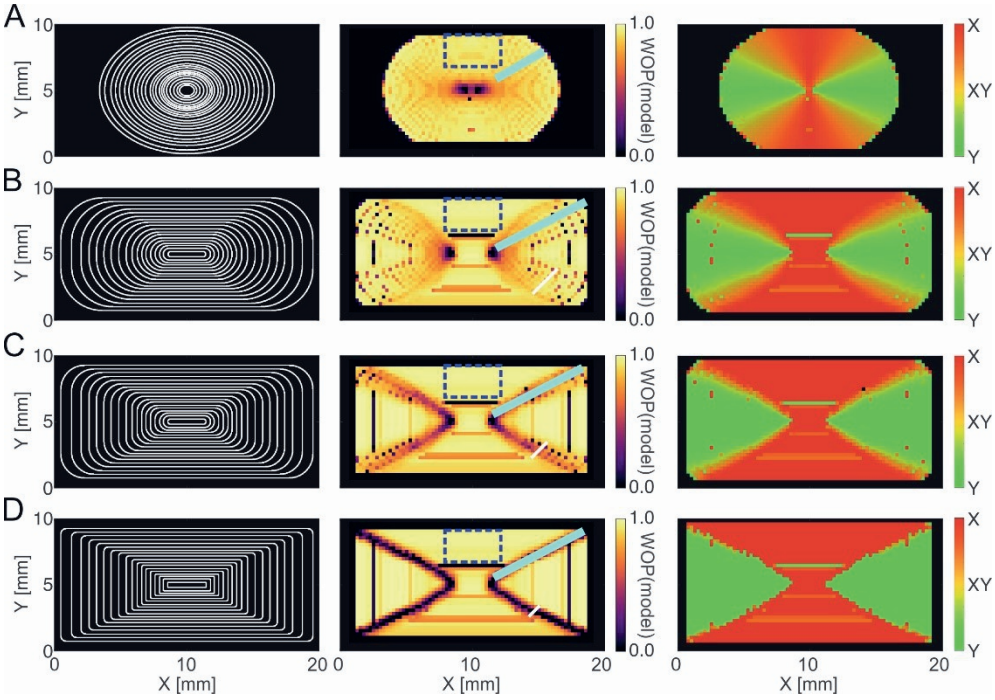

Fig. S3.10: *Synthetic axial images (left), mimicking the lamellar phase separation in SPC extrudates as seen by axial MRI data Fig. 3.3C, obtained for cross-sectional cooling die geometries with increasingly sharper corners ranging from elliptical (top) to rectangular (bottom) shaped. The synthetic MRI data, generated as described in section 3.2.7 of the main text, was further analysed by the RFT algorithm to create a vector field (data not shown). This vector field was used to calculate the corresponding WOP(model) (middle) and PDD(model) (right) maps. The square outlined area in dark blue shows the region of high order horizontally aligned WOP(model) values. The cyan line outlines the area used to calculate the mean WOP(model) values in the corner regions. The white line shows the location and length of the width of the corner regions as presented in section 3.3.3 of the main text.*

3.5.11 SANS data of mozzarella cheese

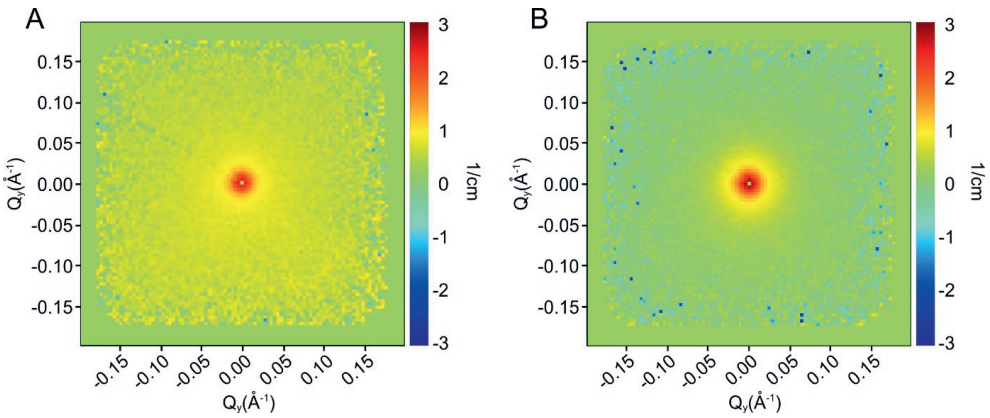

Fig. S3.11: *SANS results for a commercial high-moisture mozzarella sample. The time-of-flight LOQ instrument at ISIS Neutron and Muon source (STFC Rutherford Appleton Laboratory, UK) was used. Following standard procedures, raw data was treated to yield normalised scattering intensities I(Q) in* cm^{-1}*, where the momentum transfer is related to the scattering angle,* θ*, by* $Q = (4\pi/\lambda) \sin(\theta/2)$ *. The observed Q range was 0.007–0.23* $Å^{-1}$*. The samples were loaded into gel cell sample holders with demountable quartz windows and had a nominal thickness of 1 mm. The* D_2O *samples were soaked for ~1 hour prior to measurement. Data was reduced using the Mantid framework* [46]*. (A) The 2D scattering profile acquired without contrast enhancement and (B) with contrast enhancement by swelling the sample in* D_2O [14]*. In both 2D scattering plots an isotropic pattern is observed, indicating that no significant alignment is present at length scales below 125 nm.*

3.5.12 Effect of pH on the hierarchical structure of SPC extrudates

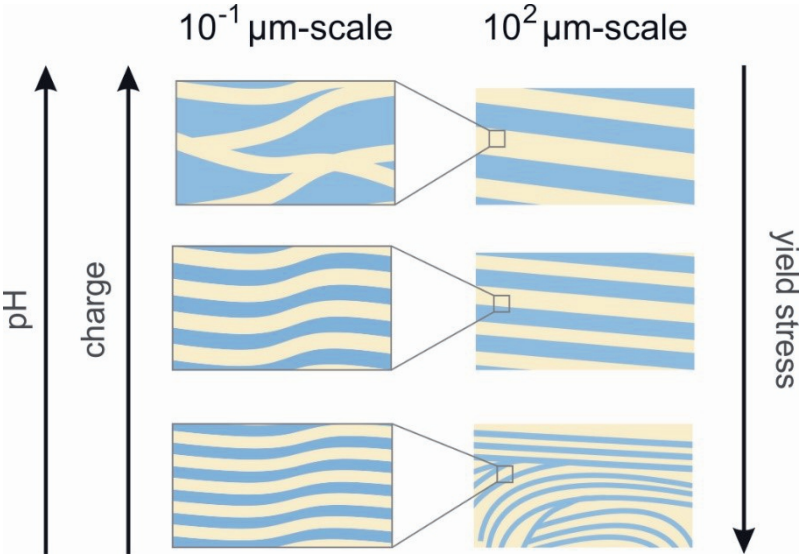

Fig. S3.12: *Diagram of discussion presented in section 3.5 in the main text. At alkaline pH, alignment of protein fibrils at the 10^{-1} µm-scale is lacking, due to high inter-fibril electrostatic charge repulsion, resulting in low yield stress of the protein melt and lamellar structure formation at the 10^{2} µm-scale. When a balance is struck between fibrillar alignment and their electrostatic repulsion at the 10^{-1} µm-scale, an aligned fibrillar protein network forms that still exhibits laminar flow behaviour in the cooling die. At acidic pH, closer to the pI, the aligned fibrillar protein network at the 10^{-1} µm has sufficiently increased the yield stress of the protein melt to hamper the laminar flow behaviour inside the cooling die, resulting in a disordered phase-separated structure at the 10^{2} µm-scale.*

Chapter

4

Mapping anisotropic structure formation of soy protein during high-moisture extrusion

This chapter was published as:

Garina, E.D., Kuijpers, S.A. Gobes, M.I., Sein, A., Den Adel, R., Smith, G.N., Sztucki, M., Hohlbein, J., Terenzi, C., Van Duynhoven, J.P.M., Bouwman, W.G., Mapping anisotropic structure formation of soy protein during high-moisture extrusion, *Food Hydrocoll.* 2026, *172*, 112037.

Abstract

The development of novel plant-based meat alternatives, that closely mimic the anisotropic structure of animal meat, offers a solution to mitigate the adverse effects of animal meat consumption. The currently most widely adopted production route is shear processing through high-moisture extrusion (HME). The complex structure formation mechanisms that determine the final fibrous texture of extrudates have yet to be fully understood. The main obstacle is the lack of multiscale studies investigating the principles governing structure formation from the nano- to the macro-structural level. This work aims to address this knowledge gap by studying materials, collected after a dead-stop operation of an industrial pilot-plant scale extruder, with multiple characterisation techniques, such as Magnetic Resonance Imaging (MRI) and Small Angle Scattering (SAS). We demonstrate that the nm-to-µm scale structure is formed already within the extruder barrels, and that sub-mm scale anisotropy develops within the cooling die. Furthermore, we show that diffuse light reflectance (DR) probes the size and coarseness of the lamellar phase-separated regions.

4.1 Introduction

It is widely acknowledged that shifting towards plant-based diets is of crucial importance to mitigate the adverse effects of meat consumption on health, environment, and animal welfare [1–3]. The development of novel plant-based meat alternatives, which closely mimic the anisotropic structure of animal meat, offers a promising solution without sacrificing the eating experiences that meat-eaters are used to [4]. High-moisture extrusion (HME) is the dominant industrial processing method for producing fibrous meat alternatives from plant proteins in an efficient and scalable manner [5]. The HME process involves the mixing and hydration of plant proteins, followed by thermo-mechanical treatment and subsequent cooling under shear in a cooling die [6]. The plant protein ingredients are typically concentrates obtained through industrial fractionation at a large scale. Such concentrates are less refined than isolates and contain significant amounts of carbohydrate fibres that can also contribute to structure formation [7].

The formation of fibrous structures during HME is believed to occur at different length scales [8–10], with the alignment of protein aggregates being considered to be the first structuring process occurring at the smallest length scale. For protein aggregates, it is hypothesised that the balance between their growth and breakdown governs the resulting size [10]. The growth of protein aggregates is believed to occur in the screw sections at temperatures in the range of 90 °C < T <120 °C. Meanwhile, shear-induced fragmentation is likely to occur in the subsequent sections where T > 120 °C. These aggregates are resistant to further breakdown by shear forces and likely constitute the building blocks for protein fibrils. Therefore, protein fibril alignment is expected to occur [11] at length scales larger than that of a single protein aggregate. A second structuring process involves phase separation into protein- and water-rich domains, resulting in syneresis. The underlying mechanisms are, however, still under debate. It has been hypothesised [12, 13] that phase separation results from spinodal decomposition, whereas others [10] proposed contraction of the cross-linked protein matrix as the underlying cause. A third structuring process occurs when, besides a continuous anisotropic protein phase, a dispersed phase is present. Such a dispersed phase can deform and elongate under shear [5, 14]. For example, carbohydrate fibres present in industrial plant-protein concentrates can co-align, along the extrusion direction, with the anisotropic protein network [15] in high-moisture extrudates.

In the context of the aforementioned hypotheses, it is evident that, while HME is an established technology in the food industry, the underlying mechanisms that lead to fibrous structure formation are not yet fully understood. Empirical approaches that attempt to correlate independent processing variables (e.g., screw speed, barrel temperatures, throughput, water content, and cooling temperature) with final product structure and characteristics are still the primary means of optimising the extrusion process [10, 16–18].

The main source of these knowledge gaps, about SPC structure formation mechanisms during HME, is the lack of complementary and multiscale experimental data that could verify the proposed hypotheses. Hence, this work focused on studying the formation of multiscale anisotropic structures during HME of a soy protein concentrate (SPC). In the interest of industrial relevance, HME was carried out on a pilot-plant scale extruder. Dead-stop experiments were performed with the aim to characterise *ex situ* the formation of multiscale structure *inside* the extruder barrel and cooling die. The obtained HME SPC samples were studied using multiple imaging and scattering measurement techniques to cover length scales from the macro- to nano-structural level. Magnetic Resonance Imaging (MRI) has recently been shown to provide insights into phase separation in SPC extrudates [19] at the µm-mm length scale range. From these high-resolution MRI images, quantitative maps of a weighted structural order parameter (WOP) could be extracted by means of the recently developed Rotated Fourier Transform (RFT) image processing method [20]. In the present work, RFT was also used to assess the coarseness of lamellar phase separation. Additionally, we mapped structural heterogeneity at the mm-scale by two-dimensional scanning [21] of sub-mm structural anisotropy as quantified by diffuse light reflectance (DR) [22–24]. Measurements by means of (Ultra-)Small-Angle Scattering, of either neutrons (SANS) or X-rays ((U)SAXS), were performed to characterise nm- up to sub-mm scale structural anisotropy in SPC extrudates [15, 25, 26]. We recently demonstrated that in SANS, the scattering contrast primarily arises from the difference in scattering length density (SLD) between soy proteins and water, while in (U)SAXS, polysaccharide fibres contribute more significantly to the signal. With the joint deployment of these two scattering measurement techniques, we can thus obtain a complementary view on structure formation of both proteins and polysaccharides, at the nm- and µm-scales, in SPC high-moisture extrudates [15].

4.2 Materials and methods

4.2.1 Materials

Commercial SPC (Alpha 8® IP, 96% DM with 70% protein in dry base, 2% fat, 7% ash, 18% dietary fibre, and total carbohydrates of 19.6%) from Solae (St. Louis, MO, USA) was used in this work.

4.2.2 Extrusion processing

The extrusion trials were conducted on a pilot-plant scale co-rotating BCTM PolyTwin extruder from Bühler (Switzerland). The extruder had a screw diameter of 30 mm and a length-to-diameter (L/D) ratio of 40. A rectangular PolyCool 50 cooling die (Bühler, Switzerland) (Fig. S4.1 (A)) had a die opening of 60 mm x 10 mm with full bullnose edges and a length of 1200 mm, and was attached at the end of the extruder. The extruder barrel was segmented into ten temperature-controlled zones. Barrel temperatures were regulated

using tempering units. The temperature in the cooling die was regulated by running water functioning as a cooling medium, and the temperature was regulated by a tempering unit. The dry protein concentrate was fed into the extruder with a solid MSDF 20A feeder (Bühler, Switzerland). The powder was free to fall into the extruder at the first barrel through an inlet funnel. Water from the feed was heated to 80 °C and injected into the third barrel.

The extrusion trials were run at the screw speed of 300 rpm and moisture content of ca. 60%. The exact HME conditions for the dead-stop operation were selected based on the results of a design of experiments (DoE) [27] as described in S4.2. The dead-stop operation was performed as described in [15] with settings #1 in Table S4.4. Samples were taken from the extruder barrel (barrels 4, 5, 7, 9, and 10), transition, die, and cooling die zones, transferred to a watertight zip-lock bag, cooled using ice water, and then frozen for storage at -18 °C. We note that for the dead-stop samples, the moisture loss upon sampling and freeze-thawing was negligible. However, the extrudate lost approximately ~10% of moisture due to steam expansion upon exiting the cooling die.

4.2.3 Sampling reference system

It is worth clarifying the terminology used in this work to refer to the different sample planes and positions. The sampling is generally described in Cartesian coordinates [28], where the X and Y axes represent the width and height of the cooling die, respectively, and the Z-axis represents the flow direction (Fig. 4.1). Consequently, there are three sample planes: sagittal (Y-Z plane), coronal (X-Z plane), and axial (X-Y plane). To account for the existing temperature gradient in the cooling die, perpendicular to the extrusion direction [29], skin and core regions are distinguished along the Y-axis, while edge and middle regions are distinguished along the X-axis.

4.2.4 Diffuse Light Reflectance (DR)

DR experimental procedure

A Lumentum 1108P polarised Helium-Neon Laser with an emission wavelength of 633 nm and a beam diameter of 0.48 mm was used to obtain diffuse reflectance images. The incident light was delivered upon the sample at an angle of 70° (Fig. 4.1). The diffusely reflected light spot had a diameter of around 1 cm and was captured by a Mako G-234C colour camera.

DR image processing

The diffuse reflectance images were processed using the Halcon 21.11 software package (MVTec, Germany) and a custom-made Halcon script (Imfaimon, Barcelona, Spain) that allows for finding the major axis length (R_1) and the minor axis length (R_2) of a fitted ellipse. The anisotropy index (AI(DR)) was calculated as $(R_1/R_2)-1$. In the absence of anisotropy, AI = 0 and the light reflectance pattern is a perfect circle. For an anisotropic sample, AI > 0.

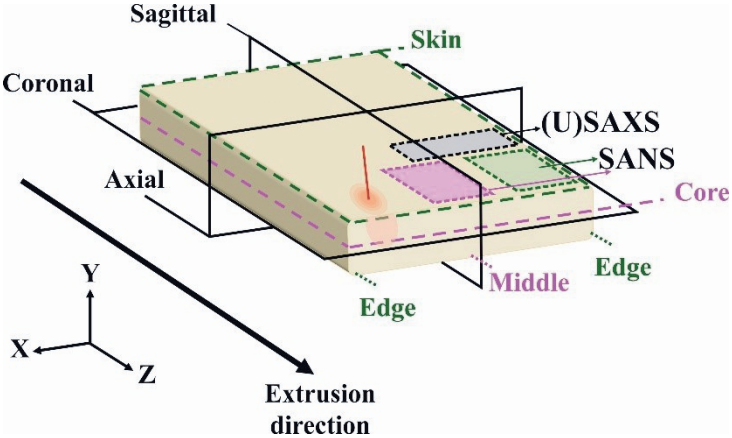

Fig. 4.1: *The schematic representation shows the MRI slices taken, along sagittal, coronal, and axial planes and slices taken for SANS and (U)SAXS measurements of an extrudate sample (yellow volume). Skin and core regions are defined along the Y-axis. Edge and middle regions are defined along the X-axis. Additionally, the schematic illustrates the orientation of the laser beam (red spot) for diffuse reflectance measurements (red line) and its approximate penetration depth in the sample*

2D AI(DR) mapping

2D AI(DR) maps were obtained by moving the sample in X- or Y- direction under the laser beam, rather than using a galvanometer scanner to move the laser beam in a previous implementation [21]. The samples were placed on a sample-bed driven by a flat gantry (DLE-FG-0001-AC-100-100 drylin®) with an X, Y travel length of 100 mm. The camera was rigidly mounted in the middle of the work area. Before each scan, the focus was adjusted once to the top surface of the sample and then kept fixed during acquisition. The exposure and lens settings were identical for all scans. The gantry itself was a toothed belt driven by an encoder with a specified repeatability of 0.5 mm (iGus, Germany). Signal conversion between programming software and gantry was done via iRC software (IGus, Germany). The sample was placed in a shallow chamber in order to position the samples in a reproducible manner. The robotic coordinates were programmed in the Igus Robot Gantry software (Igus, Germany) for the movement of the table. For every sample, an area of around 70 x 50 (Z x X; see Fig. 4.1) mm^2 was scanned with a step size of 2 mm in between measurements. The complete system was placed in a black box to block ambient light throughout the measurements. For every spatial coordinate, an AI(DR) value was obtained, thus yielding 2D AI(DR) maps. These maps were subdivided into three equal-size regions that are used to calculate a mean AI(DR) value for the right edge (RE), left edge (LE), and middle (M) regions of each sample (see Fig. 4.1).

4.2.5 Magnetic Resonance Imaging (MRI)

MRI sample preparation

Frozen dead-stop samples from the extruder barrel, transition zone, cooling die, and a frozen extrudate sample were swollen in demineralised water overnight at room temperature, using a water:sample weight ratio of 15:1. Swelling substantially increases ^{1}H MRI signal-to-noise ratio and the contrast between the protein-rich and water-rich phases, emphasising the lamellar structure visible by MRI [19]. After swelling, excess moisture was removed from the outer surface of the extrudate using a paper towel. Samples were marked on one side to identify the flow direction and orientation with respect to the extruder. Subsequently, the sample was cut into three pieces of approximately 25 mm to fit the NMR tube, and each tube was sealed with parafilm.

MRI experimental procedure

^{1}H MRI measurements were performed using a 600 MHz (14 T) wide-bore MRI spectrometer (Ascend 600WB Avance NEO, Bruker, Germany) equipped with a 1.5 T/m imaging gradient system (Micro 2.5, Bruker, Germany) and a 25 mm diameter quadrature dual channel $^{1}H/^{1}H$ detection coil (MicWB40/025 QTR, Bruker, Germany). Optimal excitation and refocusing pulse parameters were calculated by the software. Samples were measured using the Rapid Acquisition with Relaxation Enhancement (RARE) sequence [30], which allows for shorter measurement times compared to conventional spin echo sequences. Acquisition parameters were set as follows: echo time, T_E= 10 ms; repetition time, T_R= 1 s; a RARE-factor of 2; a total of 4 averages and 5 slices recorded per image acquisition; a voxel volume of 39 x 39 x 500 μm^3; a field-of-view (FOV) of 30x15 mm^2 and 30x22.5 mm^2, respectively, for images in the sagittal and coronal plane, with a total measurement duration per image acquisition of 11 and 16 minutes.

MRI data processing

^{1}H MRI data processing and image analysis were performed in MATLAB R2022b, using the pvmatlab package from Bruker to extract the data from Paravision 360 version 3.3. In-house scripts for automated data processing were written using either standard MATLAB functions or functions provided by the Image Processing Toolbox version 11.6 and Curve Fitting Toolbox version 3.8 from MATLAB.

Assessment of anisotropic structure in MRI data

RFT was used to calculate the Weighted Order Parameter (WOP) as described elsewhere [20]. RFT plugin version 0.1 was used in ImageJ (FIJI, 64-bit) version 1.54j [31]. The images were analysed using an RFT window size of 31 px and 75% overlap between windows. Angle amplitude data were further processed using a routine [20] written in Python 3.12, to convert the position-dependent probability of angular features into 2D spatial maps showing dominant angles, the relative angle intensity, and weighted order parameter

(WOP). The WOP(MRI) maps of the coronal images were used to assess the anisotropic structure evolution as a function of travel distance. Similarly to the AI(DR) maps, the WOP(MRI) maps were subdivided into three equal-size regions that are used to calculate a mean WOP value for the RE, LE, and M regions of each sample (see Fig. 4.1).

To assess the relative height of the exterior lamellar structured region ($H_{exterior}$), the sagittal WOP(MRI) maps were further processed using the following steps: (i) each WOP map was divided along the Y-direction (i.e. the sample height, see Fig. 4.1) into strips of four WOP values wide (Z-direction). (ii) The mean of each strip was calculated along the Z-direction, and the values were inverted according to: $WOP_{inv} = 1 - WOP$, resulting in a Gaussian-shaped profile for each strip. (iii) Of these profiles, WOP_{inv} baseline and peak value were determined, and the full-width-half-maximum (FWHM) of the entire profile was calculated based on these two values. (iv) A horizontal line was projected at this FWHM value and the distance between the two points (W_{FWHM}) intersecting the WOP_{inv} profile was used to assess the height of the exterior aligned structured region according to: $H_{exterior} = W_{FWHM} - H_{sample}$. Here, H_{sample} is the height of the sample and was determined from the MRI images used to calculate the WOP(MRI) maps. To correct for variations in sample height, the acquired $H_{exterior}$ is normalised to the sample height of the middle slice in the extrudate sample.

Assessment of lamellar structural coarseness in MRI data

The structural coarseness of the lamellar separation was quantified by determining the Weighted Characteristic Length (WCL) of the angular features. A smaller WCL value indicates a finely resolved structure, while a larger value signifies a broader separation of lamellar features. Using RFT [20] to obtain WCL values, we analysed the data as further described in SI section 4.5.3. Briefly, the procedure involves: (i) deriving a metric for the width of each angular feature, referred to as σ, using a Gaussian fit; (ii) converting σ into a wavelength using $\lambda_{px} = \frac{W}{ppw(\sigma)}$ via a calibration curve created from simulated data (*ppw*) and *W* being the window size; and (iii) calculating an average WCL value via λ_{px} weighted by the amplitude: $WCL = \overline{\lambda_{px}}$. The assessment of statistical variation in the WCL was conducted via Multiple Linear Regression modelling (MLR) (JMP 17.2 JMP Statistical Discovery LLC.).

Additionally, to characterise the evolution of structural coarseness along the cooling die, spatial autocorrelations between neighbouring coordinates in MRI images were expressed in terms of the Global Moran's Index (I) defined as [32]:

$$I = \frac{N}{W} \frac{\sum_i \sum_j w_{ij}(x_i - \bar{x})(x_j - \bar{x})}{\sum_i (x_i - \bar{x})^2}. \qquad \text{Eq. 4.1}$$

Here, *N*, is the number of cells, x_i is the cell of interest, $\bar{x}$ is the spatial mean of *x*, w_{ij} is the spatial weights matrix and *W* is the sum of all w_{ij}. Calculations were performed in MATLAB. An index value of -1 indicates anti-correlation between a specific cell of interest and its neighbouring cells. When the Moran's Index (I) is zero, the cell of interest and its immediate neighbours are uncorrelated. When the Moran's I is one, cells are clustered and thus correlated to their neighbours. Moran's I values were calculated for a neighbouring distance of 5 pixels, using line-shaped weight matrices parallel and perpendicular to the extrusion direction.

4.2.6 Small-Angle Scattering (SAS)

SAS sample preparation

The SAS sample preparation procedure for SAS measurements has been described in more detail elsewhere [15]. Briefly, the samples were sliced along the coronal orientation (Fig. 4.1) at a thickness of 500 µm using a cryo-microtome (Cryostar NX70, ThermoFisher Scientific, Germany). As shown in Fig. 4.1, different slices were taken from the cooling die ribbon and extrudate samples to account for the existing temperature gradient in the cooling die: separate skin edge and middle slices were prepared and measured by SANS, and one slice covering both edge and middle regions was prepared and measured by (U)SAXS. Only one slice was taken from the samples collected from the extruder barrel and non-cooled die zones. The acquired slices were sandwiched between microscope slides covered with Ultralene thin film (Spex® SamplePrep, USA) and subsequently sealed. This procedure ensured the stability of the product during its further storage (at -18 °C). Note that the slides and Ultralene film were removed for the following SAS measurements.

SANS experimental procedure and data analysis

SANS measurements were conducted on the Larmor Instrument at the ISIS Neutron and Muon Source (STFC Rutherford Appleton Laboratory, UK) [33]. The time-of-flight configuration of the instrument facilitated a simultaneous Q range of 0.005-0.7 $Å^{-1}$ by employing an incident wavelength range of 0.9-13 Å. The magnitude of the momentum transfer or scattering vector, denoted as Q, is defined by the equation:

$$Q = \frac{4\pi}{\lambda}\sin(\theta). \qquad \text{Eq. 4.2}$$

where 2θ represents the scattering angle and λ – the wavelength of the incoming neutron beam. Given the samples' anisotropic nature, the instrument was set up using a symmetric square sample aperture (6 x 6 mm^2). The samples were placed into gel cell sample holders with demountable quartz windows to maintain an airtight environment throughout the measurements. During measurements, the samples were mounted with the specific rotation angle, ϕ_0, of 45°, as explained elsewhere [15].

The analysis of SANS data has been described in more detail elsewhere [15]. Briefly, all 2D scattering data were processed using the instrument-specific software Mantid [34]. The raw data were placed on an absolute scale (cm^{-1}) by measuring the scattering of a mixture of hydrogenous and deuterated polystyrene with a known radius of gyration and scattering cross-section [35]. The data were corrected for detector sensitivity. The scattering background from the quartz windows was subtracted. Isotropic 2D SANS patterns were radially averaged to produce one-dimensional (1D) scattering profiles, $I(Q)$. In cases where 2D SANS data exhibited anisotropy, sector averages with a width of ±15° around the incident beam were calculated parallel (∥) and perpendicular (⊥) to the extrusion direction.

The SasView software [36] was employed to fit both radial and sector averages of the data. The fitting process utilised a shape-independent empirical broad peak model represented by:

$$I(Q) = \frac{A}{Q^n} + \frac{C}{1 + (|Q - Q_0|\xi)^m} + B. \quad \text{Eq. 4.3}$$

In Eq. 4.3, A signifies the power-law scale factor, n is the power-law exponent, C represents the Lorentzian scale factor, ξ denotes the Lorentzian correlation length, m is the exponent of Lorentz function, and B corresponds to the flat background. Q_0 is the peak position related to the characteristic centre-to-centre distance (D) between the scattering inhomogeneities, where $D = 2\pi/Q_0$.

Insights into the nano-structure anisotropy were obtained from analysing the annular intensity averages. The averaging of 2D SANS data was performed over a Q range of $Q_{min} < Q < Q_{trans}$, where Q_{min} indicates the lowest accessible scattering vector for probing the largest dimensions of the scatterers, and Q_{trans} corresponds to the transition from isotropic to anisotropic structure (Fig. 4.4 (left)). The resulting annular intensity averages were fitted with a Legendre series expansion [37]:

$$I(Q, \phi) = \sum_{n=0}^{\infty} a_n P_{2n}(cos\phi^*), \quad \text{Eq. 4.4}$$

where $\phi^* = \phi - (\phi_0) + \pi/2$, with ϕ_0 the orientation angle, a_n are fitting coefficients, and P_{2n} are even Legendre polynomials. From Eq. 4.4, the nematic order parameter, $\overline{P_2}$, was calculated as:

$$\overline{P_2} = \frac{a_1}{5a_0}. \quad \text{Eq. 4.5}$$

Here, a_0 is the isotropic (baseline) term ($P_0 = 1$), representing the mean annular intensity, and a_1 is the coefficient of the second-order Legendre polynomial $P_2(\cos\ \phi^*)$, which

accounts for anisotropy. Thus, the value of P_2 describes the degree of nano-alignment around a specific orientation angle, ϕ_0. A value closer to zero suggests a more isotropic sample, while the maximum value of the order parameter is determined by the scattering characteristics of a perfectly oriented structure.

(U)SAXS experimental procedure and data analysis

SAXS and USAXS measurements were performed on the upgraded beamline ID02 of the European Synchrotron Radiation Facility (ESRF, Grenoble, France) [38]. A long evacuated detector tube allowed for automated adjustments of the sample-to-detector distance (SDD) ranging from 1 to 30.9 m, enabling the collection of SAXS and USAXS data using the same setup. For this study, three SDDs (1, 8, and 30.9 m) were used to cover a Q range of 0.0002-0.8 $Å^{-1}$ with an X-ray wavelength of 1.014 Å.

The sample slices were positioned on the sample holder. The holder was then covered with an Ultralene film, which ensured an air-tight environment. The beam of 100 x 150 $µm^2$ (v x h) allowed for local examinations of different sample locations over a range of up to 28.5 mm with a step size of 0.5 mm in between measurements (the exact range was determined by the dimensions of the sample presented for the measurements), thereby covering both edge and middle regions as presented in Fig. 4.1.

The (U)SAXS data analysis procedure has been described in more detail in [15]. Accordingly, all 2D scattering data were reduced and normalised to an absolute scale (cm^{-1}) through standard procedures [38]. The dedicated software SAXSutilities [39] was employed for scattering background subtraction of the Ultralene film, merging measurements recorded at different SDDs and executing other specific operations. In order to account for material heterogeneity, averaging of the obtained data was performed [15]. It was evaluated whether the merged intensity curves displayed characteristic shoulder-like features, or obeyed a power-law behaviour over part of the explored Q range. As for the SANS data, information regarding the structural anisotropy was derived from analysing the annular intensity averages. The annular intensity averages, $I(\phi)$, were calculated for each measurement frame. The averaging was performed over a Q range of $0.0002 < Q < 0.025$ $Å^{-1}$ (i.e. at SDD of 30.9 m), where anisotropy was most clearly observable. The obtained annular intensity averages were fitted $I(\phi)$ with a Legendre series expansion as previously described.

4.3 Results and discussion

4.3.1 Development of µm-to-mm scale structure

Structure formation at the µm-to-mm scale during HME was investigated on samples taken from the extruder barrel, the transition zone, cooling die or the final extrudate. The samples taken from the barrel section and transition zone upon dead-stop of the extruder already

show lamellar structure by MRI (Fig. S4.2 in SI). This indicates that anisotropic structure formation at µm-to-mm scale is already taking place within the extruder. Example MRI and AI(DR) images for the dead-stop sample collected from the cooling die at a travel distance of 90 cm (CD 90 cm) are displayed in Fig. 4.2 (A). The 2D AI(DR) map, shown in Fig. 4.2 (A1), unveils heterogeneity in the structural anisotropy at the mm-scale. The coronal (see Fig. 4.1) MRI images (Fig. 4.2 (A2)), acquired from exactly the same sample, show this feature in the µm-to-mm scale range. The areas in the RE, LE, and M regions, highlighted by rectangles in Fig. 4.2 (A2), were then processed using RFT to obtain the WOP(MRI) maps presented in Fig. 4.2 (A4). In addition, the axial (see Fig. 4.1) MRI image is provided in Fig. 4.2 (A3). We note that due to the rounded edges of the cooling die, the 2D AI(DR) map (Fig. 4.2 (A1)) obtained on the sample surface, does not cover the far edges of the right/left slabs captured with MRI (Fig. 4.2 (A2,A3) as indicated by dashed red lines. Differences in the sample areas/volumes used for AI(DR) and WOP mapping are highlighted in Fig. 4.2 (A3).

From inspection of Fig. 4.2 (A), a difference in structural anisotropy is revealed between the anisotropic edges (RE and LE) and more isotropic middle (M) regions along the X-axis, previously defined in Fig. 4.1. This difference in anisotropy likely arises from the larger cooling surface per volume at the rounded edges of the die, as opposed to the middle region of the die where only two cooling surfaces (Fig. 4.2 (A3)) are effective. Thus, due to locally faster cooling during shear, structural alignment is more pronounced towards the rounded edges, rather than in the middle region, of the cooling die. In the coronal MRI images (Fig. 4.2 (A2)) of this sample, two horizontal features with high signal intensities can be identified. These correspond to domains where the content, and/or the molecular mobility, of water is highest. As shown elsewhere [19], these regions correspond to the positions of the twin screws in the extruder barrel.

Surprisingly, the structural anisotropy appears more pronounced at the right edge (RE, AI = 0.13) than at the left edge (LE, AI = 0.09) in the 2D AI(DR) (Fig. 4.2 (A1)) maps. This asymmetry can also be visually observed in the coronal and axial MRI images (Fig. 4.2 (A2,3)), but is not reflected in the coronal WOP(MRI) maps (Fig. 4.2 (A4)). We also assessed the coarseness of the lamellar structure in the coronal MRI images by quantifying the width of an angular feature (σ) in the RFT analysis via the WCL (see SI section 4.5.3). Here a small, but significant, difference in the coarseness of the RE and LE coronal images was found (Fig. S4.13). We confirmed this finding by also determining the Global Moran's I as a measure for spatial heterogeneity,

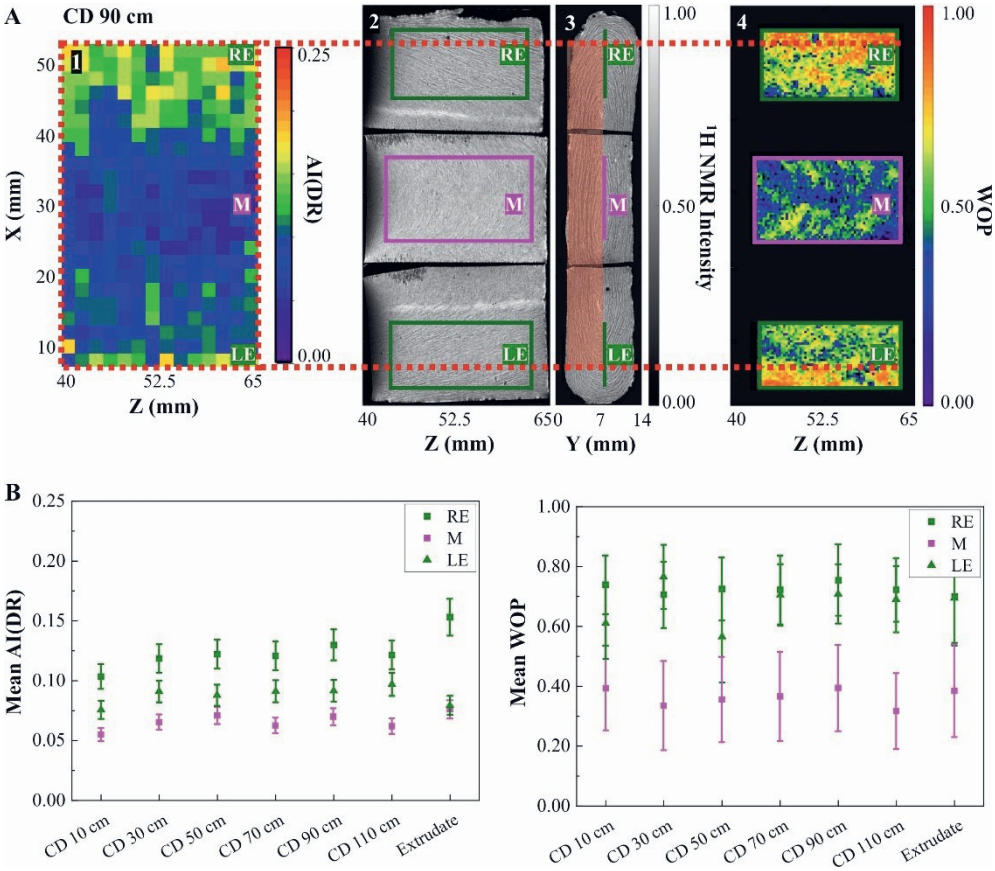

Fig. 4.2: *(A) 2D AI(DR) maps (1), coronal and axial MRI images (2 and 3, respectively), obtained for the cooling die (CD) dead-stop sample at a travel distance of 90 cm. Areas highlighted by rectangles in (2) were further processed by RFT to obtain the WOP map in (4). The red rectangle in (3) schematically demonstrates the volume sampled by 2D AI(DR). The green and magenta lines in (3) refer to the location of the RFT analysed sample volumes taken to obtain the coronal WOP maps. (B) Structural evolution along the cooling die is characterised by plotting the mean AI(DR) (left) and mean WOP (right) calculated from the respective 2D AI(DR) and coronal WOP maps of CD dead-stop and extrudate samples (Fig. S4.4).*

which showed differences in RE and LE coronal images (Fig. S4.14). We attribute the RE vs LE asymmetry in AI(DR) and in the lamellar coarseness to differences in the sub-mm phase separation of the protein phase [19]. One possible reason for the observed asymmetry in the formation of an anisotropic phase separation could be unequal cooling of the right and left edges of the cooling die. However, the spiral design of the cooling channels in the die (see Fig. S4.1 (A)) makes it unlikely that an asymmetric temperature profile would develop across the width of the die. A more plausible explanation is that, in the absence of a breaker plate, structural heterogeneity in the protein melt, as it may have built up in the barrels and transition zone, is partially consolidated in the cooling die [6]. To verify this explanation, we repeated extrusion in the presence of a breaker plate with horizontal slots (Fig. S4.1 (B))

using processing settings comparable to settings #1 in Table S4.4. This experiment resulted in a symmetric anisotropic lamellar structure in the extrudate, as evident from axial MRI images (Fig. S4.3 (A)) and 2D AI(DR) maps (Fig. S4.3 (B)). Furthermore, the inclusion of a breaker plate also effectively erased the imprint that the two extruder screws left in the cooled samples. We conclude that the use of a breaker plate promotes a more homogeneous distribution of structure and/or temperature inside the protein melt as the latter enters the cooling die, resulting in a more homogeneous anisotropic lamellar structure formation. Without a breaker plate, a hot mass with structure and/or temperature memory enters the cooling die, where such heterogeneities are consolidated.

2D AI(DR) maps, coronal MRI images, and WOP(MRI) maps, demonstrating the evolution of anisotropic structure along the cooling die up to the obtained extrudate, are displayed in Fig. S4.4. Mean AI(DR) and mean WOP(MRI) values were calculated from the respective maps, as described in subsection 2.5, the resulting plots are shown in Fig. 4.2 (B). As evident from Fig. 4.2 (B) (left), an increase is observed in AI(DR) values as a function of cooling die travel distance, with the trend being statistically significant at RE (linear regression: slope = 0.00268 per 10 cm, $p = 0.022$). However, no effect of passage over the cooling die is seen in the WOP results (Fig. 4.2 (B) (right)) nor in the coarseness of the phase separation quantified from the coronal MRI images (Fig S4.4 in SI).

The sagittal MRI images (Fig. 4.3 (A), Fig. S4.5) reveal a lamellar structure, with an approximately parabolic shape, observed already at the beginning of the cooling die. As the material progresses through the cooling die, a region with aligned lamellae develops near the walls of the cooling die and the parabolic shape in the interior becomes more pronounced and sharper. The morphology development is seen in the WOP(MRI) maps, which in turn unveil generally increasing anisotropy in the exterior phase-separated regions (near the cooling die walls along the Y-axis and thus close to the skin, as shown in Fig. 4.1). The WOP(MRI) maps also show the widening of these regions during the passage of the material through the cooling die and after exiting it. This structure development was further assessed by calculating the height of the exterior lamellar structured region, as described in section 4.2.5. The resulting plot is presented in Fig. 4.3 (B1) for the RE, M, and LE regions of the dead-stop samples, collected at increasing travel distance along the CD and after exiting it. Figure 4.3 (B2) schematically shows the orientation and slice locations used to obtain these values. As seen in Fig. 4.3 (B1), the height of the aligned lamellar region increases in the early section of the cooling die and remains roughly unchanged as the material progressed further along the cooling die: segmented linear regression analysis indicates an early increase at M (70 cm: 0.139 mm per 10 cm, $p = 0.017$) and at LE (30 cm: 0.531 mm per 10 cm, $p = 0.023$), while downstream slopes are not statistically significant (all $p > 0.3$).

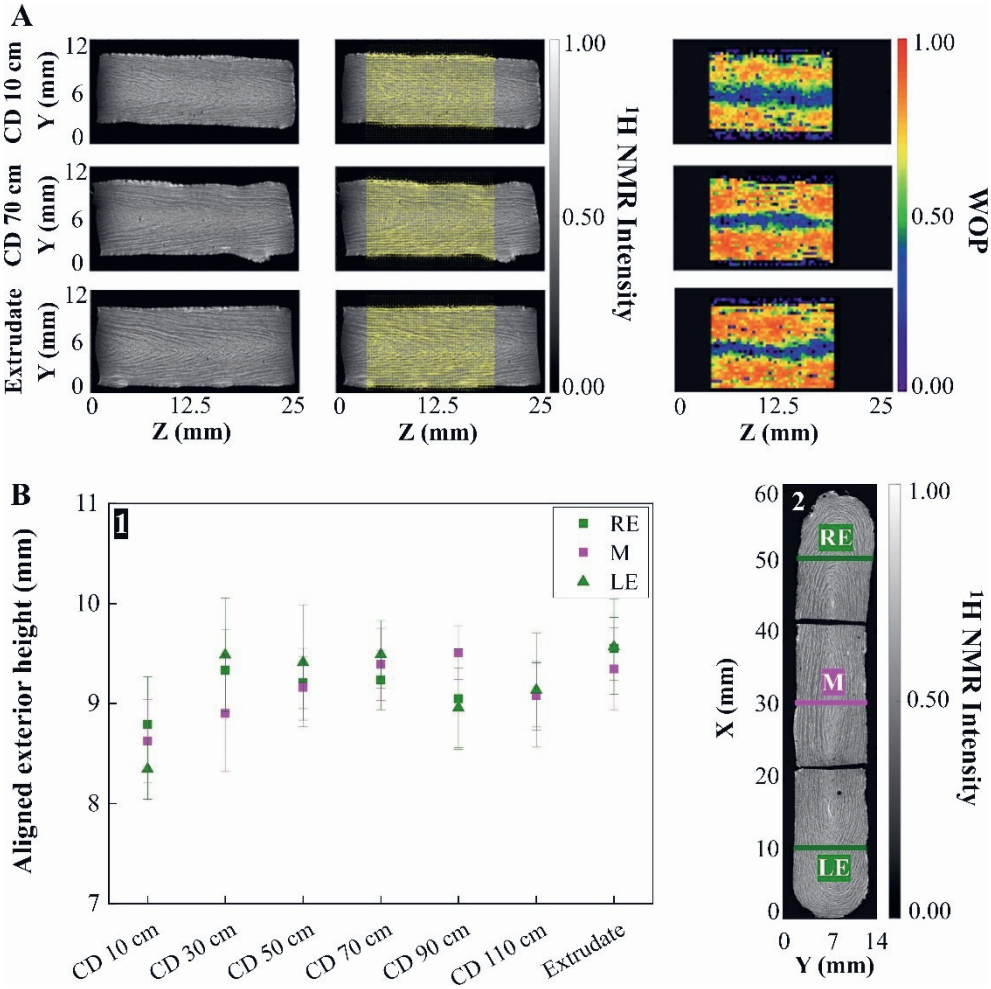

Fig. 4.3: *(A) Selected sagittal MRI images without (left) or with (centre) overlaid angle distribution map (yellow lines), and WOP(MRI) maps (right) for the dead-stop SPC samples collected at increasing distance, from top to bottom, within the cooling die (CD). The bottommost row refers to an SPC extrudate sample. (B) (1) Structural evolution demonstrated by the height of the exterior aligned lamellar structure calculated from the WOP maps of the sagittal MRI images of CD dead-stop and extrudate samples. (2) Axial MRI image demonstrating schematically the orientation and slice locations used to obtain these values.*

The AI(DR) and quantitative analysis of the MRI images indicate that the main effect of passage through the cooling die is the development of a layer of lamellar phase-separated material near the cooled wall. The coarseness of the lamellae appears to be set by the conditions in the barrel sections and does not develop during the passage of the cooling die, which is in line with our previous study [19]. AI(DR) appears to be sensitive to both the size of the exterior lamellar aligned material and to its coarseness.

4.3.2 Development of nm-to-µm structure

Small-Angle Neutron Scattering (SANS)

To obtain insights into the structure formation at the nm-to-µm scale, SAS measurements were performed on the extrudate and dead-stop samples collected from the barrel, transition, non-cooled die, and cooling die zones. Since HME induces a preferred orientation along the flow direction, 2D SANS data were averaged in 30°-wide sectors around the incident beam in the directions parallel and perpendicular to the orientation direction. From Fig. 4.4 (left), it is evident that protein structures in the extrudates are aligned already at length scales above ca. 20 nm. This finding is in agreement with previous observations of alignment of calcium caseinate fibrils in sheared gels at similar length scales [25]. Furthermore, formation of fibril structures consisting of highly compacted ultra-thin filaments with a thickness of 20-30 nm has been observed in soy protein extrudates [28, 40].

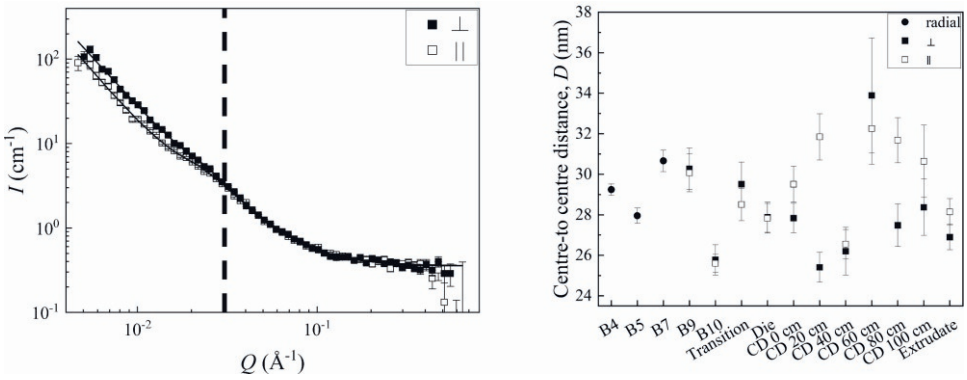

***Fig. 4.4**: (Left): Sector averages of 2D SANS data taken in the directions parallel (∥) and perpendicular (⊥) to the orientation direction for the extrudate skin edge slices. Square symbols represent the experimental data and lines represent the fit with the broad peak model. The vertical dashed line indicates the transition between isotropic and anisotropic structures. (Right): Centre-to-centre distances between scattering inhomogeneities (protein aggregates) estimated from the broad peak model for the extrudate and dead-stop samples collected from barrel (B), transition, non-cooled die, and cooling die (CD) zones. Since the 2D data from barrels 4, 5, and 7 displayed no anisotropy, radially averaged intensities were fitted with the model (circle symbols). For the other dead-stop and extrudate samples, sector intensities were used for the fit (square symbols). Note that for clarity, the data from the cooling die and extrudate samples are shown for (right) edge slices only. All fitting parameters are presented in Table S4.1.*

A distinctive shoulder-like feature is observed in the Q range between ca. 0.015 and 0.065 Å^{-1}. The empirical broad peak model provides a good fit along the entire Q range and reproduces this shoulder feature. The fit allows for determining the characteristic sizes of the nanostructures present in the material. In Zink *et al.* (2024) [28], the peak position (Q_0) was attributed to the main average centre-to-centre distance (D) between agglomerated

proteins, connected by electrostatic or covalent forces, to form the fibrous structure of meat alternatives. Figure 4.4 (right) shows that D remains roughly unchanged along the extruder barrel and the entire cooling die section. The same observation was made in our previous work [15], where sampling of the screw section was performed at the final extruder barrel section of a lab scale extruder. In the current work, the use of a larger scale pilot-plant extruder allowed samples to be collected from earlier screw sections. The obtained results imply that the equilibrium size protein aggregate building blocks are already formed in the beginning sections of the extruder barrel. Considering that the barrel 4 (B4) sample was taken from the barrel section at T > 120 °C (Table S4.4 #1), the data are consistent with the hypothesised protein aggregation mechanism proposed earlier by [10]: protein aggregates grow in the screw sections at 90 °C < T < 120 °C and are subsequently size-limited by shear induced fragmentation at T > 120 °C, resulting in shear-resistant aggregates that act as fibrillar building blocks.

The broad peak model fit also provides the Lorentzian correlation length (ξ) (Table S4.1), defined as the size of the smallest discernible scattering object [25]. Similar to the centre-to-centre distance, it does not change along the extruder or the entire cooling die. A ξ of ca. 10 nm seems to be close to the diameter of native glycinin and β-conglycinin molecules, the two major globulins in soy storage proteins [41]. This finding would imply that the building blocks of protein fibrils are constituted from moderately unfolded but still globular proteins; under HME conditions protein most likely behave as globular polymers rather than random-coil chains [26]. Preservation of the globular shapes of proteins and their aggregation during heat treatment was also shown in Nakamura *et al.* (1984) [42] and in Guan *et al.* (2024) [26], where similar ξ values were obtained from SANS data.

The extent of alignment of the protein fibrils was quantified by fitting the annular intensity averages with the Legendre series expansion, as described in section 4.2.6. Figure 4.5 displays the calculated nematic order parameter that describes nano-anisotropy evolution at ca. 20 – 125 nm. Note that the edge slices for the SAS measurements were taken only from the right edge that demonstrated more anisotropy, as determined by DR (Fig. 4.2). The results indicate that the anisotropic structure is already formed before the melt arrives at the cooling die section in line with the hypothesis proposed by [10]. When the protein melt enters the cooling die, this anisotropic fibrillar aggregation is emphasised by the cooling and subsequent solidification of the protein network, and driven further by the shear forces generated therein [6, 10, 29].

Interestingly, our previous work [15] showed only marginal change in the SANS nematic order parameter when the material entered the short cooling die of a lab scale extruder. In the present work, however, we observe a drastic increase in the protein nanoscale nematic order in the early section of the cooling die, which is also in line with the results on the height of the exterior aligned region in Fig. 4.3 (B1). We note that the temperatures of the

protein melt, when entering the cooling dies of the lab- and pilot-plant extruders (T = 141 °C and T = 127 °C, respectively), as well as the respective dosed moisture contents (54% and 60%), are different. Our current explanation is that the higher moisture content used in our pilot-plant extruder trial led to a less viscous protein melt entering the cooling die. This allowed for a further increase in the protein nanoscale nematic order in the first section of the cooling die.

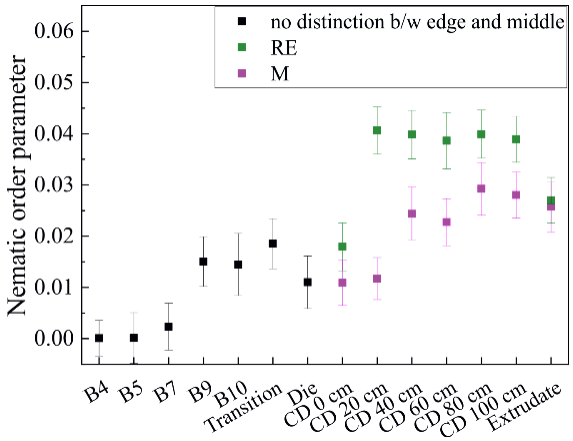

Fig. 4.5: *Nematic order parameter (Eq. 4.5) calculated from SANS measurements of SPC ribbon samples from a dead-stop experiment, collected within the barrel (B) section, the transition region or the cooling die (CD), as well as of an SPC extrudate. Green and magenta symbols, respectively, refer to exterior (RE) and interior (M) regions of the CD samples, affected by the temperature gradient inside the cooling die (for reference, see Fig. 4.1). In the other zones (black symbols), there is no such temperature gradient, so no distinction was made between the regions during sampling.*

Similarly to the 2D AI(DR) and WOP(MRI) results, the nematic order parameter, which describes anisotropy at the nanoscale, demonstrates the difference between the anisotropic edge and the isotropic middle region (Fig. 4.5) and is also visible from the confocal laser scanning microscopy (CLSM) images (Fig. S4.6 (G,H)). Consistency in the results obtained from SANS, MRI and DR suggests that there is a connection between fibrillation aggregation at the nm-to-µm scale and phase separation at the µm-to-mm scale. Therefore, we adhere to the hypothesis proposed by [10], which suggests that phase separation occurs due to the contraction of the cross-linked protein matrix. Our previous research [43] indicated that this contraction is likely the consequence of the formation of a fibrillar protein network, whereby the presence or absence of anisotropic fibrillar protein aggregation appears to determine whether phase separation is lamellar or isotropic.

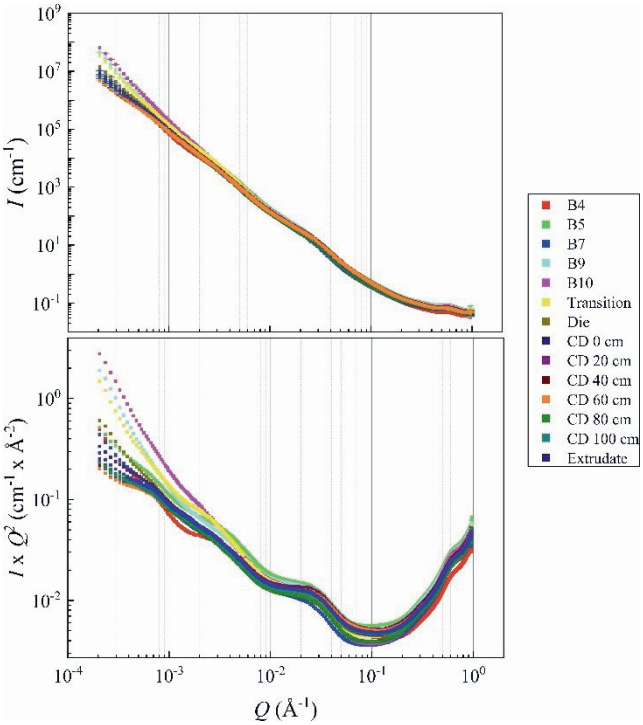

***Fig. 4.6**: Radially averaged (U)SAXS data additionally averaged over all measurement frames (top); corresponding Kratky plots (bottom). Data were obtained by combining three SDDs.*

(Ultra-)Small-Angle X-ray Scattering ((U)SAXS)

As explained in section 4.2.6., SAXS and USAXS measurements were performed on different sample spots over a distance of up to 28.5 mm along X-axis (see Fig. 4.1). In order to observe structural evolution along the extruder barrel and cooling die sections, averaging over all measurement frames was performed. An example of the integrated scattering curves of all sample positions along the cooling die width is shown in Fig. S4.7. The resulting scattering profiles are displayed in Fig. 4.6.

Similarly to the SANS data, a shoulder-like feature is evident in the Q range between ca. 0.01 and 0.07 Å^{-1} and, therefore, attributed to protein aggregate building blocks. In SANS data, the higher-Q range (Q > 0.07 Å^{-1}) was dominated by incoherent background scattering (Fig. 4.4 (left)), but in SAXS data, an additional shoulder-like feature becomes distinguishable (Fig. 4.6 (top)). This feature is related to a real-space position of ca. 1 nm (Q of ca. 0.6 Å^{-1}) and, therefore, might correspond to the inter-β-sheet distance [28]. The presence of additional shoulder features is detected in the lower-Q region, which was not achievable with SANS (Q < 0.005 Å^{-1}). In [15, 28], the shoulder in the Q range between ca. 0.002 and 0.007 Å^{-1}, corresponding to real-space distances of ca. 90 – 315 nm, was attributed to fibrillar structures of proteins. Furthermore, scattering intensities of all samples display an

additional shoulder in the Q range between ca. 0.0004 and 0.0008 $Å^{-1}$. However, this feature is less pronounced in the extruder barrel and transition zone samples, where the lowest Q region (Q < 0.001 $Å^{-1}$) seems to be more dominated by the power-law compared to the cooling die. In Garina *et al.* (2024) [15], this was attributed to the presence of more clustered or densely packed polysaccharide fibres in the extruder barrel, which undergo deformation and distribute more homogeneously in the cooling die.

Consistent with our SAXS results reported previously [15], all shoulder positions in SAXS profiles remain roughly unchanged with the sample's position along the extruder barrel or cooling die. This implies that, starting from barrel 4 (T > 120 °C), proteins do not undergo clear conformational changes, as indicated by the steady shoulder at ca. 1 nm. These proteins assemble into aggregates of the equilibrium size, as described in section 4.3.2, and constitute the nanometre scale building blocks of protein fibrils, which in turn seem to be formed already in the first barrel zones at T > 120 °C. CLSM results support these observations and demonstrate the presence of protein fibrils along the entire extruder barrel section (Fig. S4.6).

Interestingly, in contrast to the SANS results (Fig. 4.5), the nematic order parameter determined from USAXS data shows the highest alignment in the transition zone (Fig. 4.7) (for statistical analysis, see Tables S4.2 and S4.3). We note that since the calculated values varied significantly at different sample locations along X-axis (Fig. S4.8), Fig. 4.7 displays the mean nematic order parameter across several measurement frames. In Garina *et al.* (2024) [15], these differences between the SANS and (U)SAXS results were explained by a contrast difference in SLD encountered for proteins and polysaccharide fibres. In SANS, the scattering contrast arises primarily from the SLD difference of soy proteins relative to water, accordingly, the SANS nematic order parameter reflects protein alignment. Even though it is impossible to completely separate the contributions of these two biopolymers, it is still clear that dispersed polysaccharide fibres, originating from cell wall fragments, contribute more to (U)SAXS than to SANS. It is this contribution of cell wall fragments that appears to be responsible for the strongest local alignment observed in the transition zone, where tensile stresses are the highest. Despite the apparent structural relaxation in the cooling die, an increase in the extent of alignment closer to the cooling die walls along the X-axis is still evident, as shown in Fig. S4.8. These observations are in agreement with the SANS results showing stronger alignment in the sample edge compared to the middle (Fig. 4.5).

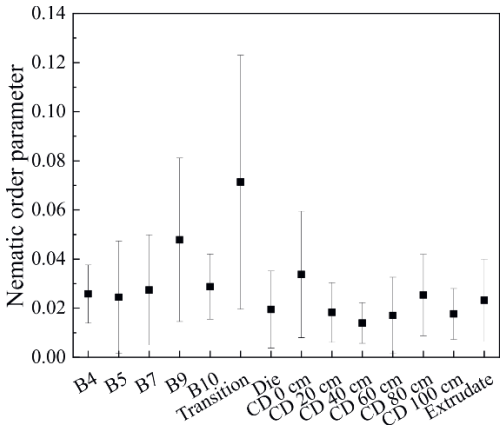

Fig. 4.7: *Nano- and microstructure evolution during HME demonstrated by nematic order parameters (Eq. 4.5) calculated from USAXS data at SDD of 31 m, i.e., at length scales of ca. 30 nm – 3 µm. Plotted values are the means across several measurement frames taken along a single transverse scan from the RE toward the interior (Fig. 4.1).*

4.4 Conclusions

This work has demonstrated how multiscale structure, probed from the nano- to the macro scale, evolves during pilot-plant HME. Figure 4.8 schematically reflects this multiscale structure development.

The mm-scale heterogeneity in structural anisotropy is described by 2D AI(DR) maps (Fig. 4.8 (top right)). The monotonic development of structural anisotropy is evident as the material progresses through the cooling die. Perpendicular to the flow direction we observed more structural anisotropy at the edges where more cooling surface per volume is present. MRI showed that local µm-to-mm scale alignment is already present at the end of the barrel and in the transition zone, with substantial lamellar alignment found at the beginning of the cooling die (Fig. 4.8 (top)).

The height of the structured lamellar region increases in the early sections of the cooling die, whereas no effect of the passage over the cooling die is found for WOP(MRI) and coarseness of the lamellar phase-separation. AI(DR) and MRI showed that in the absence of a breaker plate coarseness of the sub-mm lamellar structure is asymmetric perpendicular to the extrusion direction. In the presence of a breaker plate, these and other structural heterogeneities are absent, indicating a homogeneous structure and/or temperature distribution of the protein melt as it enters the cooling die. The local USAXS order parameter (Fig. 4.8 (middle)) describes the alignment of polysaccharide fibres and reaches its maximum in the transition zone where the tensile stresses are highest. The SANS nematic order parameter (Fig. 4.8 (middle)), in turn, describes the alignment of protein fibrils, and shows that the nm-scale anisotropic protein structure is formed already in the extruder barrel, and further develops in the early sections of the cooling die. The protein fibrils are shown to be

formed from the protein aggregate building blocks with a characteristic centre-to-centre distance (CC in Fig. 4.8 (bottom)), which are constituted from moderately unfolded, yet globular, proteins with a characteristic correlation length (CL in Fig. 4.8 (bottom)). Both CC distance and CL remain roughly unchanged as the protein melt progresses through the extruder barrel to the cooling die.

The deployment of imaging and scattering measuring modalities, as discussed in this work, provides a comprehensive view on the structural events occurring during HME at pilot-plant scale. We foresee further deployment of these techniques in establishing mechanistic links between the events that occur during HME at different length scales. For this purpose, we envisage future *in situ* characterisation of structure formation by both MRI velocimetry and SAS measurements during HME.

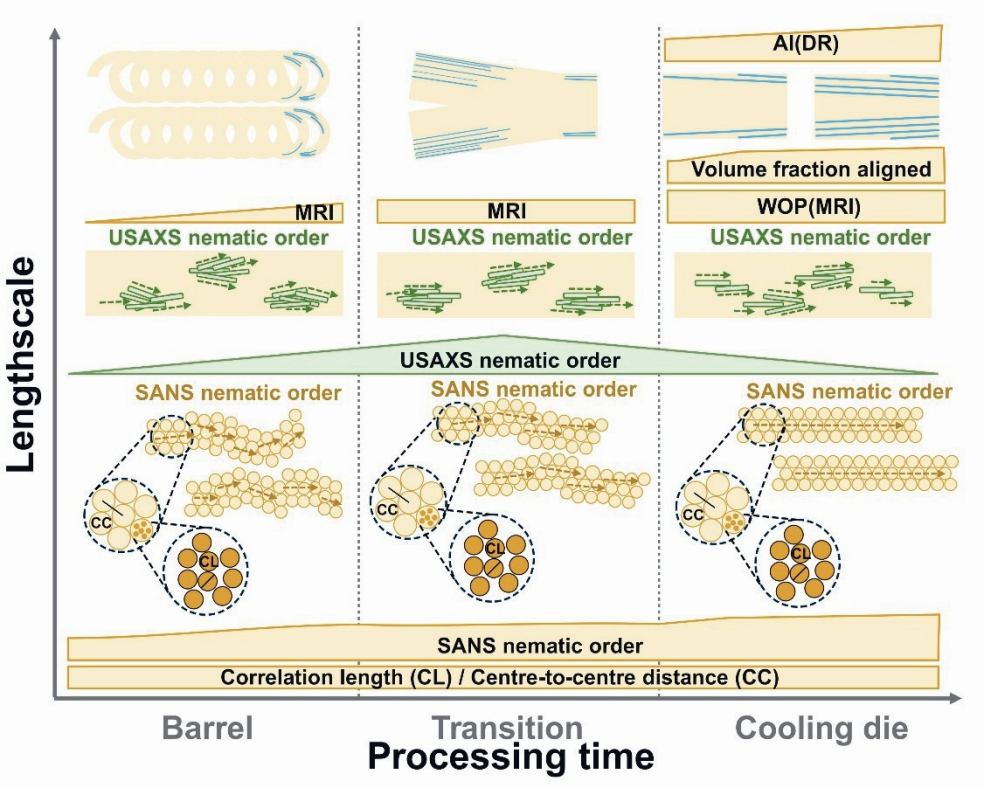

Fig. 4.8: *Schematic diagram reflecting multiscale structure formation in HME at: the mm-scale, as probed by 2D AI(DR); the sub-mm scale, as probed by MRI-WOP; the nm- and sub-µm scale, as probed by SAS.*

Authors statement

Ekaterina D. Garina: Conceptualisation, Data curation (SAS), Formal analysis, Investigation, Methodology, Visualisation, Writing – original draft. Sam A. Kuijpers: Conceptualisation, Data curation (MRI, DR), Formal analysis, Investigation, Methodology, Visualisation, Writing – review & editing. Martijn I. Gobes: Conceptualisation, Data curation (CLSM, MRI), Methodology, Formal analysis, Software, Writing – review & editing. Arjen Sein: Methodology, Resources, Writing – review & editing. Ruud den Adel: Methodology ((U)SAXS). Gregory N. Smith: Data curation (SANS), Software, Formal analysis, Writing – review & editing. Michael Sztucki: Data curation ((U)SAXS), Software, Formal analysis, Writing – review & editing. Johannes Hohlbein: Conceptualisation, Writing – review & editing, Supervision. Camilla Terenzi: Conceptualisation, Funding acquisition, Project administration, Supervision, Writing review & editing. John P.M. van Duynhoven – Conceptualisation, Funding acquisition, Resources, Supervision, Writing – review & editing. Wim G. Bouwman – Conceptualisation, Funding acquisition, Supervision, Writing – review & editing.

Declaration of competing interest

John P.M. van Duynhoven and Ruud den Adel are employed by a company that manufactures and markets plant-based meat alternatives. Arjen Sein is employed by a company that sells plant-based ingredients. The other authors declare that they have no known competing financial interests or personal relationships that could have appeared to influence the work reported in this paper.

Acknowledgements

This work is part of the project "Measurement and Modelling of Multiscale Processed Protein Products (MP3)" (with project number 18744) of the research programme OPT TTW, which is financed by the Dutch Research Council as well as by contributions from consortium partners Unilever, Cargill, dsm-firmenich, FrieslandCampina and Wageningen Food and Biobased Research. We gratefully acknowledge the Science and Technology Facilities Council (STFC) for access to neutron beamtime at ISIS through RB 2369100. We also acknowledge the European Synchrotron Radiation Facility (ESRF) for the provision of synchrotron radiation facilities. This project was further supported by the uNMR-NL Grid: A distributed, state-of-the-art Magnetic Resonance facility for the Netherlands (NWO grant 184.035.002). This work benefited from the use of the SasView application, originally developed under NSF Award DMR-0520547. SasView also contains code developed with funding from the EU Horizon 2020 programme under the SINE2020 project Grant No. 654000.

Unilever is thanked for the use of the 2D AI(DR) instrument. Eduard Mooy and Remon Lippens are thanked for skillfully constructing this instrument. Finally, we thank the dsm-firmenich Extrusion Test Centre in Tau (Norway) for access to the pilot-plant extruder and Tore Stendahl and Bolor Borjgen for their support during extrusion trials.

Data availability

SANS data are available at https://doi.org/10.5286/ISIS.E.RB2369100. (U)SAXS data are available at https://doi.org/10.5281/zenodo.14651762.

References

[1] N. González, M. Marquès, M. Nadal, and J. L. Domingo, "Meat consumption: Which are the current global risks? A review of recent (2010–2020) evidences," *Food Res. Int.*, vol. 137, no. April, p. 109341, 2020, doi: 10.1016/j.foodres.2020.109341.

[2] C. Bonnet, Z. Bouamra-Mechemache, V. Réquillart, and N. Treich, "Viewpoint: Regulating meat consumption to improve health, the environment and animal welfare," *Food Policy*, vol. 97, no. February, p. 101847, 2020, doi: 10.1016/j.foodpol.2020.101847.

[3] J. He, N. M. Evans, H. Liu, and S. Shao, "A review of research on plant-based meat alternatives: Driving forces, history, manufacturing, and consumer attitudes," *Compr. Rev. Food Sci. Food Saf.*, vol. 19, no. 5, pp. 2639–2656, 2020, doi: 10.1111/1541-4337.12610.

[4] G. Andreani, G. Sogari, A. Marti, F. Froldi, H. Dagevos, and D. Martini, "Plant-Based Meat Alternatives: Technological, Nutritional, Environmental, Market, and Social Challenges and Opportunities," *Nutrients*, vol. 15, p. 452, 2023.

[5] B. L. Dekkers, R. M. Boom, and A. J. van der Goot, "Structuring processes for meat analogues," *Trends Food Sci. Technol.*, vol. 81, no. May, pp. 25–36, 2018, doi: 10.1016/j.tifs.2018.08.011.

[6] S. H. V. Cornet, S. J. E. Snel, F. K. G. Schreuders, R. G. M. van der Sman, M. Beyrer, and A. J. van der Goot, "Thermo-mechanical processing of plant proteins using shear cell and high-moisture extrusion cooking," *Crit. Rev. Food Sci. Nutr.*, vol. 62, no. 12, pp. 3264–3280, 2022, doi: 10.1080/10408398.2020.1864618.

[7] Y. Wang *et al.*, "The development process of plant-based meat alternatives: Raw material formulations and processing strategies," *Food Res. Int.*, vol. 167, no. February, p. 112689, 2023, doi: 10.1016/j.foodres.2023.112689.

[8] P. Wittek, N. Zeiler, H. P. Karbstein, and M. A. Emin, "High moisture extrusion of soy protein: Investigations on the formation of anisotropic product structure," *Foods*, vol. 10, no. 1, Jan. 2021, doi: 10.3390/foods10010102.

[9] A. S. Beniwal, J. Singh, L. Kaur, A. Hardacre, and H. Singh, "Meat analogs: Protein restructuring during thermomechanical processing," *Compr. Rev. Food Sci. Food Saf.*, vol. 20, no. 2, pp. 1221–1249, 2021, doi: 10.1111/1541-4337.12721.

[10] R. G. M. Van der Sman and A. J. Van der Goot, "Hypotheses concerning structuring of extruded meat analogs," *Curr. Res. Food Sci.*, vol. 6, no. May, p. 100510, 2023, doi: 10.1016/j.crfs.2023.100510.

[11] H. Akdogan, "High moisture food extrusion," *Int. J. Food Sci. Technol.*, vol. 34, no. 3, pp. 195–207, 1999, doi: 10.1046/j.1365-2621.1999.00256.x.

[12] E. Kaunisto, S. Wassén, and M. Stading, "A thermodynamical finite element model of the fibre formation process during extrusion of high-moisture meat analogues," *J. Food Eng.*, vol. 362, no. 111760, 2024, doi: 10.1016/j.jfoodeng.2023.111760.

[13] J. L. Sandoval Murillo, R. Osen, S. Hiermaier, and G. Ganzenmüller, "Towards understanding the mechanism of fibrous texture formation during high-moisture extrusion of meat substitutes," *J. Food Eng.*, vol. 242, pp. 8–20, Feb. 2019, doi: 10.1016/j.jfoodeng.2018.08.009.

[14] V. B. Tolstoguzov, "Thermoplastic extrusion-the mechanism of the formation of extrudate structure and properties," *J. Am. Oil Chem. Soc.*, vol. 70, no. 4, pp. 417–424, 1993, doi: 10.1007/BF02552717.

[15] E. D. Garina *et al.*, "SANS and SAXS : A Love Story to unravel structural evolution of soy proteins and polysaccharide fibres during high moisture extrusion for meat alternatives," *Food Hydrocoll.*, vol. 155, no. January, p. 110121, 2024, doi: 10.1016/j.foodhyd.2024.110121.

[16] M. A. Emin and H. P. Schuchmann, "A mechanistic approach to analyze extrusion processing of biopolymers by numerical, rheological, and optical methods," *Trends Food Sci. Technol.*, vol. 60, pp. 88–95, 2017, doi: 10.1016/j.tifs.2016.10.003.

[17] I. Zahari, K. Östbring, J. K. Purhagen, and M. Rayner, "Plant-Based Meat Analogues from Alternative Protein: A Systematic Literature Review," *Foods*, vol. 11, no. 18, 2022, doi: 10.3390/foods11182870.

[18] V. Guyony, F. Fayolle, and V. Jury, "High moisture extrusion of vegetable proteins for making fibrous meat analogs: A review," *Food Rev. Int.*, vol. 39, no. 7, pp. 4262–4287, 2023, doi: 10.1080/87559129.2021.2023816.

[19] S. Kuijpers, G.-J. Goudappel, T. Huppertz, J. Van Duynhoven, and C. Terenzi, "Quantification of phase separation in high moisture soy protein extrudates by NMR and MRI," *Food Res. Int.*, vol. 197, no. P1, p. 115225, 2024, doi: 10.1016/j.foodres.2024.115225.

[20] M. I. Gobes, S. A. Kuijpers, C. Terenzi, R. G. M. van der Smaan, J. P. M. van Duynhoven, and J. Hohlbein, "Rotated Fourier transform (RFT) enables the quantification of anisotropic structure in high-moisture plant-protein extrudates," *Food Struct.*, vol. 44, no. June, p. 100437, 2025, doi: 10.1016/j.foostr.2025.100437.

[21] J. Ranasinghesagara, F. H. Hsieh, H. Huff, and G. Yao, "Laser scanning system for real-time mapping of fiber formations in meat analogues," *J. Food Sci.*, vol. 74, no. 2, 2009, doi: 10.1111/j.1750-3841.2008.01032.x.

[22] J. Ranasinghesagara, F. Hsieh, and G. Yao, "A photon migration method for characterizing fiber formation in meat analogs," *J. Food Sci.*, vol. 71, no. 5, 2006, doi: 10.1111/j.1750-3841.2006.00038.x.

[23] J. Li, X. Xia, C. Shi, X. Chen, H. Tang, and L. Deng, "A Reliable Method for Determining the Degree of Orientation of Fibrous Foods Using Laser Transmission and Computer Vision," *Foods*, vol. 12, no. 19, p. 3541, 2023, doi: 10.3390/foods12193541.

[24] R. Van Beers, B. Aernouts, M. M. Reis, and W. Saeys, "Anisotropic light propagation in bovine muscle tissue depends on the initial fiber orientation, muscle type and wavelength," *Opt. Express*, vol. 25, no. 18, p. 22082, 2017, doi: 10.1364/oe.25.022082.

[25] B. Tian *et al.*, "Small angle neutron scattering quantifies the hierarchical structure in fibrous calcium caseinate," *Food Hydrocoll.*, vol. 106, no. March, p. 105912, 2020, doi: 10.1016/j.foodhyd.2020.105912.

[26] T. Guan *et al.*, "In situ studies of plant-based meat analog texturization," *Food Hydrocoll.*, vol. 155, no. March, 2024, doi: 10.1016/j.foodhyd.2024.110215.

[27] G. E. P. Box, W. H. Hunter, and S. Hunter, *Statistics for experimenters*, 1st ed. John Wiley & Sons, Ltd, 1978.

[28] J. I. Zink *et al.*, "Structural and mechanical anisotropy in plant-based meat analogues," *Food Res. Int.*, vol. 179, no. December 2023, p. 113968, 2024, doi: 10.1016/j.foodres.2024.113968.

[29] P. Wittek, F. Ellwanger, H. P. Karbstein, and M. A. Emin, "Morphology development and flow characteristics during high moisture extrusion of a plant-based meat analogue," *Foods*, vol. 10, no. 8, Aug. 2021, doi: 10.3390/foods10081753.

[30] J. Hennig, A. Nauerth, and H. Friedburg, "RARE imaging: A fast imaging method for clinical MR," *Magn. Reson. Med.*, vol. 3, no. 6, pp. 823–833, 1986, doi: 10.1002/mrm.1910030602.

[31] J. Schindelin *et al.*, "Fiji: An open-source platform for biological-image analysis," *Nat. Methods*, vol. 9, no. 7, pp. 676–682, 2012, doi: 10.1038/nmeth.2019.

[32] P. A. P. Moran, "Notes on Continuous Stochastic Phenomena," *Biometrika*, vol. 37, no. 1, pp. 17–23, 1950, doi: https://doi.org/10.2307/2332142.

[33] Anon, "ISIS Larmor," 2023. https://www.isis.stfc.ac.uk/Pages/Larmor.aspx (accessed Jul. 21, 2023).

[34] O. Arnold *et al.*, "Mantid – Data analysis and visualization package for neutron scattering and μ SR experiments," *Nucl. Instruments Methods Phys. Res. Sect. A Accel. Spectrometers, Detect. Assoc. Equip.*, vol. 764, pp. 156–166, 2014, doi: 10.1016/j.nima.2014.07.029.

[35] G. D. Wignall and F. S. Bates, "Absolute calibration of small-angle neutron scattering data," *J. Appl. Crystallogr.*, vol. 20, no. 1, pp. 28–40, Feb. 1987, doi: https://doi.org/10.1107/S0021889887087181.

[36] M. Doucet *et al.*, "SasView version 5.0.5," 2022, doi: 10.5281/zenodo.6331344.

[37] C. Burger, B. S. Hsiao, and B. Chu, "Preferred orientation in polymer fiber scattering," *Polym. Rev.*, vol. 50, no. 1, pp. 91–111, 2010, doi: 10.1080/15583720903503494.

[38] T. Narayanan *et al.*, "Performance of the time-resolved ultra-small-angle X-ray scattering beamline with the Extremely Brilliant Source," *J. Appl. Crystallogr.*, vol. 55, pp. 98–111, 2022, doi: 10.1107/S1600576721012693.

[39] M. Sztucki, "SAXSutilities: a graphical user interface for processing and analysis of Small-Angle X-ray Scattering data (1.024)," 2021, doi: 10.5281/zenodo.5825707.

[40] J. H. Chiang, W. Tay, D. S. M. Ong, D. Liebl, C. P. Ng, and C. J. Henry, "Physicochemical, textural and structural characteristics of wheat gluten-soy protein composited meat analogues prepared with the mechanical elongation method," *Food Struct.*, vol. 28, no. January, p. 100183, 2021, doi: 10.1016/j.foostr.2021.100183.

[41] R. A. Badley, D. Atkinson, H. Hauser, D. Oldani, J. P. Green, and J. M. Stubbs, "The structure, physical and chemical properties of the soy bean protein glycinin," *BBA – Protein Struct.*, vol. 412, no. 2, pp. 214–228, 1975, doi: 10.1016/0005-2795(75)90036-7.

[42] T. Nakamura, S. Utsumi, and T. Mori, "Network structure formation in thermally-induced gelation of glycinin," *J. Agric. Food Chem.*, vol. 32, no. 2, pp. 349–352, Mar. 1984, doi: 10.1021/jf00122a042.

[43] S. A. Kuijpers *et al.*, "Impact of pH-shifting on multiscale structural anisotropy of high-moisture extrudates of soy proteins," *Food Hydrocoll.*, vol. 168, no. April, p. 111456, 2025, doi: 10.1016/j.foodhyd.2025.111456.

[44] K. Moder, "Alternatives to F-test in one way ANOVA in case of heterogeneity of va riances (a simulation study)," *Psychol. Test Assess. Model.*, vol. 52, no. 4, p. 343, 2010.

[45] P. A. Games, H. J. Keselman, and J. J. Clinch, "Tests for homogeneity of variance in factorial designs.," *Psychol. Bull.*, vol. 86, no. 5, p. 978, 1979.

[46] J. N. M. Boots, N. P. K. Humblet-Hua, L. Tonneijck, R. Fokkink, J. van der Gucht, and T. E. Kodger, "Characterization of the local mechanical texture of animal meat and meat replacements using multi-point indentation," *J. Food Eng.*, vol. 300, no. September 2020, p. 110505, 2021, doi: 10.1016/j.jfoodeng.2021.110505.

4.5 Supplementary Information

4.5.1 Pilot-plant extruder dead-stop trial

Table S4.1: *Fitting parameters obtained from applying the broad peak model to the SANS data for dead-stop and extrudate samples taken from the pilot-scale extruder.*

		A (cm^{-1})	n	C (cm^{-1})	D (nm)	ξ (nm)	m	X^2
Screw zone								
Barrel 4	r	$(1.9 \pm 0.2) \times 10^{-3}$	2.21 ± 0.03	8.5 ± 0.4	32.3 ± 0.6	8.6 ± 0.2	2.29 ± 0.04	1.53
Barrel 5	r	$(2.7 \pm 0.5) \times 10^{-4}$	2.41 ± 0.03	2.4 ± 0.1	28.0 ± 0.4	9.2 ± 0.4	1.46 ± 0.03	1.95
Barrel 7	r	$(1.1 \pm 0.2) \times 10^{-4}$	2.60 ± 0.04	3.2 ± 0.1	30.7 ± 0.5	7.8 ± 0.2	1.53 ± 0.03	1.90
Barrel 9	⊥	$(2.4 \pm 0.8) \times 10^{-4}$	2.51 ± 0.06	4.2 ± 0.3	30.3 ± 1.0	8.4 ± 0.5	1.52 ± 0.06	1.80
	∥	$(8.7 \pm 2.2) \times 10^{-5}$	2.77 ± 0.05	4.4 ± 0.3	30.1 ± 0.9	7.5 ± 0.4	1.58 ± 0.05	1.35
Barrel 10	⊥	$(1.9 \pm 0.6) \times 10^{-4}$	2.52 ± 0.07	2.1 ± 0.2	25.8 ± 0.7	8.6 ± 0.8	1.35 ± 0.07	1.59
	∥	$(3.0 \pm 1.0) \times 10^{-4}$	2.41 ± 0.07	2.1 ± 0.2	25.6 ± 0.4	10.3 ± 1.0	1.24 ± 0.06	1.28
Transition zone								
Transition	⊥	$(9.8 \pm 3.8) \times 10^{-5}$	2.68 ± 0.08	3.5 ± 0.3	29.5 ± 1.1	7.9 ± 0.4	1.69 ± 0.06	1.45
	∥	$(2.0 \pm 0.6) \times 10^{-4}$	2.51 ± 0.06	3.2 ± 0.2	28.5 ± 0.8	9.0 ± 0.6	1.60 ± 0.06	1.41
Die zone								
Die	⊥	$(1.7 \pm 0.4) \times 10^{-4}$	2.61 ± 0.05	3.5 ± 0.2	27.9 ± 0.7	8.8 ± 0.5	1.54 ± 0.06	1.72
	∥	$(2.5 \pm 0.8) \times 10^{-4}$	2.48 ± 0.07	3.5 ± 0.3	27.8 ± 0.7	9.0 ± 0.6	1.52 ± 0.06	1.58
Cooling die zone								
Skin Edge								
0 cm	⊥	$(3.5 \pm 0.7) \times 10^{-4}$	2.49 ± 0.04	3.5 ± 0.2	27.8 ± 0.7	9.4 ± 0.7	1.61 ± 0.06	1.30
	∥	$(3.2 \pm 1.1) \times 10^{-4}$	2.45 ± 0.07	4.3 ± 0.3	29.5 ± 0.9	8.7 ± 0.5	1.69 ± 0.05	1.97
20 cm	⊥	$(1.2 \pm 0.2) \times 10^{-3}$	2.24 ± 0.04	2.2 ± 0.2	25.4 ± 0.7	11.0 ± 1.3	1.60 ± 0.11	1.25
	∥	$(8.2 \pm 3.6) \times 10^{-5}$	2.71 ± 0.09	5.5 ± 0.4	31.8 ± 1.1	7.9 ± 0.4	1.67 ± 0.06	1.40
40 cm	⊥	$(1.9 \pm 0.2) \times 10^{-3}$	2.16 ± 0.03	1.7 ± 0.2	26.2 ± 1.2	9.2 ± 1.0	2.23 ± 0.28	1.12
	∥	$(1.0 \pm 0.4) \times 10^{-3}$	2.22 ± 0.08	3.3 ± 0.3	26.5 ± 0.7	8.2 ± 0.5	2.68 ± 0.06	1.13
60 cm	⊥	$(2.6 \pm 1.1) \times 10^{-4}$	2.52 ± 0.08	3.5 ± 0.6	33.8 ± 2.8	7.4 ± 0.6	1.87 ± 0.09	0.92
	∥	$(1.7 \pm 0.9) \times 10^{-4}$	2.52 ± 0.10	4.0 ± 0.4	32.3± 1.8	7.3 ± 0.4	1.80 ± 0.07	0.62
80 cm	⊥	$(7.8 \pm 1.9) \times 10^{-4}$	2.32 ± 0.05	2.5 ± 0.3	27.5 ± 1.1	9.6 ± 1.0	1.63 ± 0.08	1.45
	∥	$(1.4 \pm 0.7) \times 10^{-4}$	2.60 ± 0.10	4.7 ± 0.4	31.7 ± 1.1	7.8 ± 0.3	1.66 ± 0.05	1.02
100 cm	⊥	$(5.9 \pm 1.8) \times 10^{-4}$	2.33 ± 0.06	1.6 ± 0.3	28.4 ± 1.4	8.8 ± 1.1	1.61 ± 0.10	1.70
	∥	$(3.0 \pm 1.5) \times 10^{-4}$	2.37 ± 0.10	2.6 ± 0.4	30.6 ± 1.8	7.3 ± 0.5	1.67 ± 0.07	1.43
Extrudate	⊥	$(1.0 \pm 0.2) \times 10^{-3}$	2.34 ± 0.05	5.3 ± 0.4	26.9 ± 0.6	9.1 ± 0.6	1.45 ± 0.05	1.76
	∥	$(7.2 \pm 1.8) \times 10^{-4}$	2.41 ± 0.05	6.2 ± 0.4	28.1 ± 0.7	8.7 ± 0.5	1.49 ± 0.04	1.96
Skin Middle								
0 cm	⊥	$(3.8 \pm 1.0) \times 10^{-4}$	2.51 ± 0.05	5.4 ± 0.4	31.0 ± 1.2	8.1 ± 0.4	1.70 ± 0.05	1.12
	∥	$(1.1 \pm 0.3) \times 10^{-3}$	2.27 ± 0.05	4.4 ± 0.4	27.5 ± 0.7	9.5 ± 0.6	1.70 ± 0.06	1.63
20 cm	⊥	$(8.7 \pm 2.1) \times 10^{-4}$	2.30 ± 0.05	3.0 ± 0.3	26.8 ± 1.0	8.3 ± 0.6	1.77 ± 0.07	1.29
	∥	$(5.1 \pm 1.8) \times 10^{-4}$	2.40 ± 0.07	3.4 ± 0.4	28.5 ± 1.2	7.3 ± 0.4	1.69 ± 0.06	1.70
40 cm	⊥	$(8.0 \pm 2.2) \times 10^{-4}$	2.29 ± 0.06	2.0 ± 0.3	26.5 ± 0.9	8.8 ± 0.9	1.62 ± 0.08	1.30
	∥	$(1.6 \pm 0.8) \times 10^{-4}$	2.56 ± 0.09	3.7 ± 0.4	32.4 ± 2.0	7.0 ± 0.4	1.75 ± 0.07	1.25
60 cm	⊥	$(2.3 \pm 0.8) \times 10^{-4}$	2.52 ± 0.07	3.1 ± 0.4	31.7 ± 1.6	8.4 ± 0.6	1.58 ± 0.07	0.80
	∥	$(2.6 \pm 1.1) \times 10^{-4}$	2.44 ± 0.09	3.0 ± 0.3	30.0 ± 1.4	7.6 ± 0.5	1.62 ± 0.07	1.25
80 cm	⊥	$(7.8 \pm 0.3) \times 10^{-4}$	2.27 ± 0.09	1.8 ± 0.4	29.7 ± 1.9	8.4 ± 1.0	1.72 ± 0.11	1.45
	∥	$(2.0 \pm 0.1) \times 10^{-4}$	2.48 ± 0.11	3.1 ± 0.4	30.7 ± 1.7	7.2 ± 0.4	1.70 ± 0.06	1.07
100 cm	⊥	$(2.4 \pm 0.8) \times 10^{-4}$	2.51 ± 0.07	2.7 ± 0.3	30.1 ± 1.3	8.7 ± 0.7	1.43 ± 0.08	0.86
	∥	$(2.2 \pm 0.8) \times 10^{-4}$	2.47 ± 0.08	2.7 ± 0.3	29.2 ± 1.3	7.4 ± 0.5	1.55 ± 0.07	1.07
Extrudate	⊥	$(2.5 \pm 0.2) \times 10^{-3}$	2.05 ± 0.02	1.3 ± 0.1	24.5 ± 0.6	11.5 ± 1.1	2.51 ± 0.32	1.26
	∥	$(1.2 \pm 0.4) \times 10^{-3}$	2.16 ± 0.07	2.6 ± 0.1	26.5 ± 0.9	8.2 ± 0.6	1.70 ± 0.07	1.42

The symbols in the second column represent averages used for the fit: r, ⊥, and ∥ stand for radial, perpendicular sector, and parallel sector averages, respectively.

Table S4.2: *Results of Welch's ANOVA* [44]*, performed to determine if there is a statistically significant difference between nematic order parameters determined from USAXS data from different extruder and cooling die zones (Fig. 4.7 in main text). Note, Welch's ANOVA was chosen over the classic ANOVA because the data have unequal variances. The results showed that at least two of the 14 groups have significantly different means.*

DF Num	DF Den	F-Value	P-Value
13	200.686	9.927	5.551×10^{-16}

Table S4.3: *Games-Howell Pairwise Comparisons* [45] *show the probability (p-value) that the difference between the sample means are at least as large as what has been observed under the assumption that the population means are equal. The smaller the p-value, the stronger the evidence is that the two populations have different means. In the table below: the redder the cells, the smaller the p-value; the bluer the cells, the larger the p-value. Table below demonstrates p-values; cells with p< 0.05 are highlighted. The results showed that Barrel 9 and transition sections are significantly different from most other sections and appear to have stronger alignment compared to other sections (Fig. 4.7 in main text).*

	Barrel 4	Barrel 5	Barrel 7	Barrel 9	Barrel 10	Transition	Die	CD 0 cm	CD 20 cm	CD 40 cm	CD 60 cm	CD 80 cm	CD 100 cm	Extrudate
Barrel 4		1.0000	1.0000	**0.0363**	0.9987	**0.0006**	0.6083	0.8049	0.1580	**0.0000**	0.1408	1.0000	**0.0455**	0.9999
Barrel 5	1.0000		1.0000	0.1085	0.9998	**0.0011**	0.9991	0.9476	0.9899	0.6241	0.9683	1.0000	0.9748	1.0000
Barrel 7	1.0000	1.0000		0.1819	1.0000	**0.0019**	0.8742	0.9958	0.6684	0.0898	0.5522	1.0000	0.5389	0.9996
Barrel 9	**0.0363**	0.1085	0.1819		0.1444	0.5817	**0.0024**	0.7211	**0.0011**	**0.0001**	**0.0007**	**0.0445**	**0.0007**	**0.0169**
Barrel 10	0.9987	0.9998	1.0000	0.1444		**0.0018**	0.2161	0.9971	**0.0420**	**0.0001**	**0.0358**	0.9993	**0.0140**	0.9360
Transition	**0.0006**	**0.0011**	**0.0019**	0.5817	**0.0018**		**0.0001**	**0.0138**	**0.0000**	**0.0000**	**0.0000**	**0.0006**	**0.0000**	**0.0003**
Die	0.6083	0.9991	0.8742	**0.0024**	0.2161	**0.0001**		0.0891	1.0000	0.7051	1.0000	0.9050	1.0000	0.9976
CD 0 cm	0.8049	0.9476	0.9958	0.7211	0.9971	**0.0138**	0.0891		**0.0276**	**0.0005**	**0.0198**	0.8555	**0.0142**	0.5461
CD 20 cm	0.1580	0.9899	0.6684	**0.0011**	**0.0420**	**0.0000**	1.0000	**0.0276**		0.8120	1.0000	0.6101	1.0000	0.9464
CD 40 cm	**0.0000**	0.6241	0.0898	**0.0001**	**0.0001**	**0.0000**	0.7051	**0.0005**	0.8120		0.9961	**0.0139**	0.8594	0.0885
CD 60 cm	0.1408	0.9683	0.5522	**0.0007**	**0.0358**	**0.0000**	1.0000	**0.0198**	1.0000	0.9961		0.4903	1.0000	0.8684
CD 80 cm	1.0000	1.0000	1.0000	**0.0445**	0.9993	**0.0006**	0.9050	0.8555	0.6101	**0.0139**	0.4903		0.4097	1.0000
CD 100 cm	**0.0455**	0.9748	0.5389	**0.0007**	**0.0140**	**0.0000**	1.0000	**0.0142**	1.0000	0.8594	1.0000	0.4097		0.8467
Extrudate	0.9999	1.0000	0.9996	**0.0169**	0.9360	**0.0003**	0.9976	0.5461	0.9464	0.0885	0.8684	1.0000	0.8467	

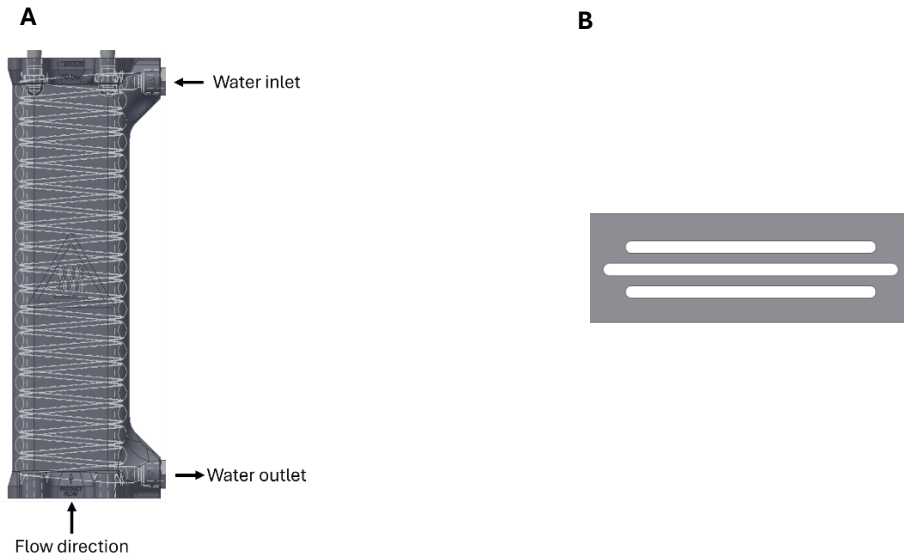

Fig. S4.1: *Schematic representations of: (A)the spiral cooling channel in the PolyCool 50 cooling die (Bühler, Switzerland), (B) the breaker plate with slots (1 x (2.5 mm x 60 mm), 2 x (2.5 mm x 51 mm)).*

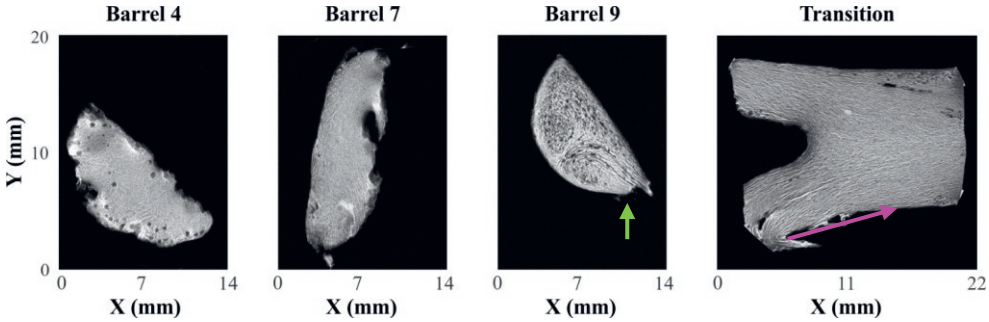

Fig. S4.2: *Sagittal MRI images of dead-stop samples taken from barrel sections 4, 7, 9, and the transition zone between the barrel and cooling die. In barrel 4, prior to the heating but after the initial mixing zone, little to no phase-separated structures are visible. In barrel 7, at the mixing zone of the first heated barrel, some phase-separated structure can be discerned at the sample edges. In barrel 9, after the heating and mixing of the protein into a hot melt, many air bubbles are visible in the material but in sections with little air, a clearly phase-separated lamellar structure can be distinguished (green arrow). In the transition zone, it is visible how, from left to right, the barrel screw ends and two streams of protein melt are pushed through the narrower die exit into the cooling die. The phase-separated lamellar structure is visible and follows this movement into the cooling die (magenta arrow).*

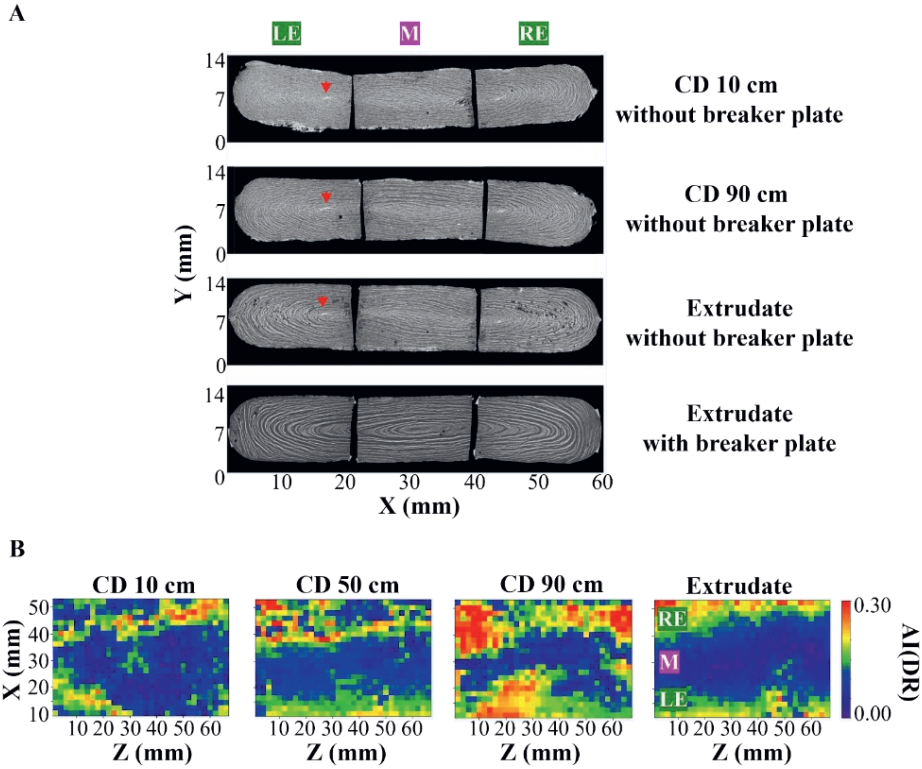

Fig. S4.3: *(A) Axial MRI images (see Fig. 4.1 in main text) for the samples collected upon extrusion with and without a breaker plate. Red arrows indicate the position of the twin screws inside the extruder. (B) Structural evolution as demonstrated by 2D AI(DR) maps for, from left to right, SPC dead-stop samples along the cooling die (CD) and an SPC extrudate sample (rightmost panel) collected upon extrusion with a breaker plate in use. RE, M, LE stand for right edge (X-range 40-60 mm), middle (X-range 20-40 mm), and left edge (X-range 0-20 mm), respectively.*

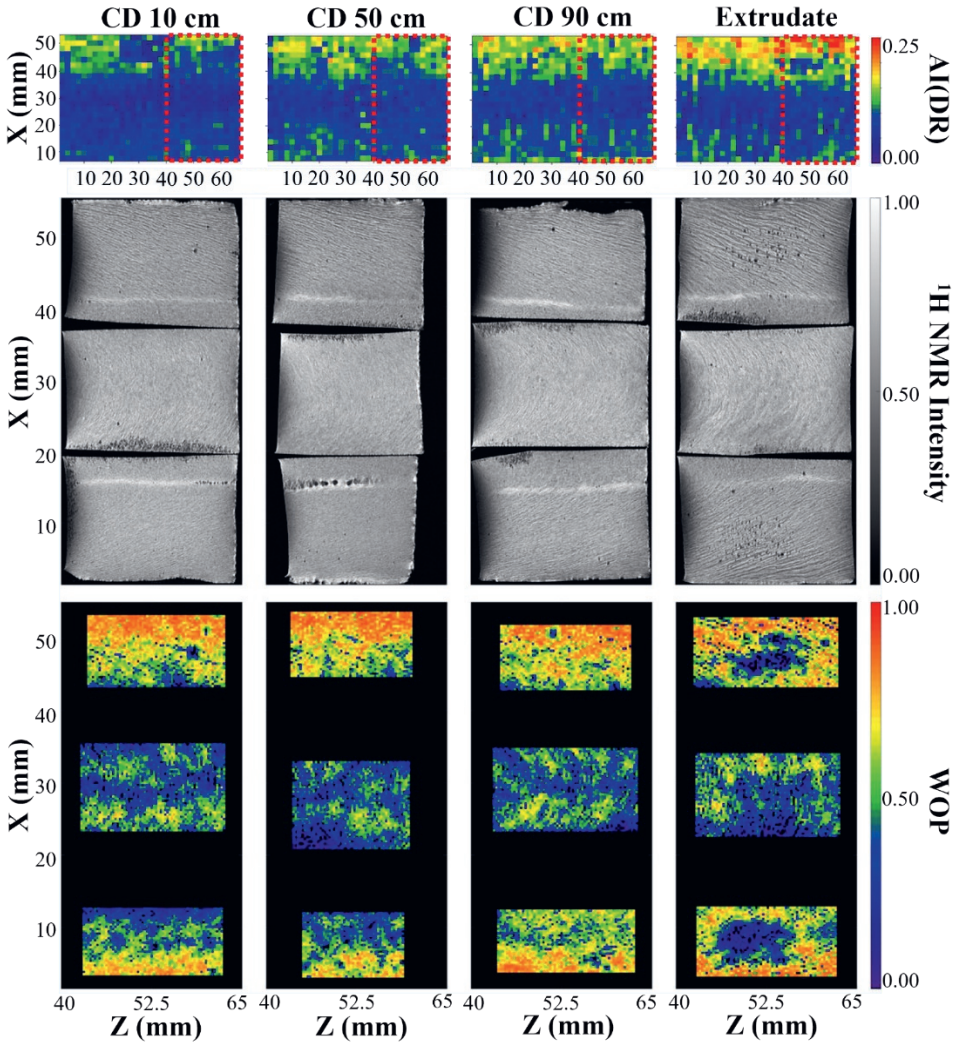

Fig. S4.4: *Structural evolution in the absence of a breaker plate. From left to right, SPC dead-stop samples along the cooling die (CD) and the obtained SPC extrudate sample (rightmost column). Data represent 2D AI(DR) maps (top) or coronal MRI images (middle): the latter were further processed by RFT to obtain the WOP maps (bottom). Red dashed rectangles in (top) indicate sample areas imaged by MRI (middle, bottom). RE, M, LE stand for right edge (X-range 40-60 mm), middle region (X-range 20-40 mm), and left edge (X-range 0-20 mm), respectively.*

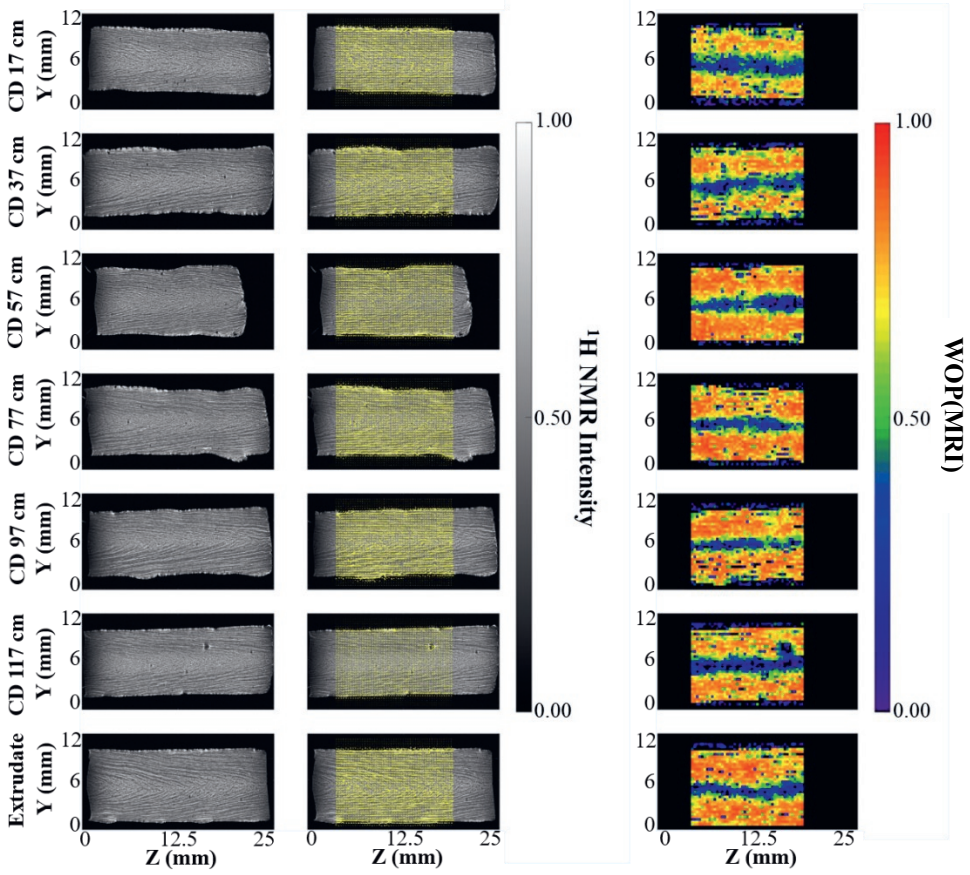

Fig. S4.5: *Sagittal MRI images without (left) or with (centre) overlaid angle distribution map (yellow lines), and WOP(MRI) maps (right) for the dead-stop SPC samples collected at increasing distance, from top to bottom, within the cooling die (CD). The bottommost row refers to an SPC extrudate sample.*

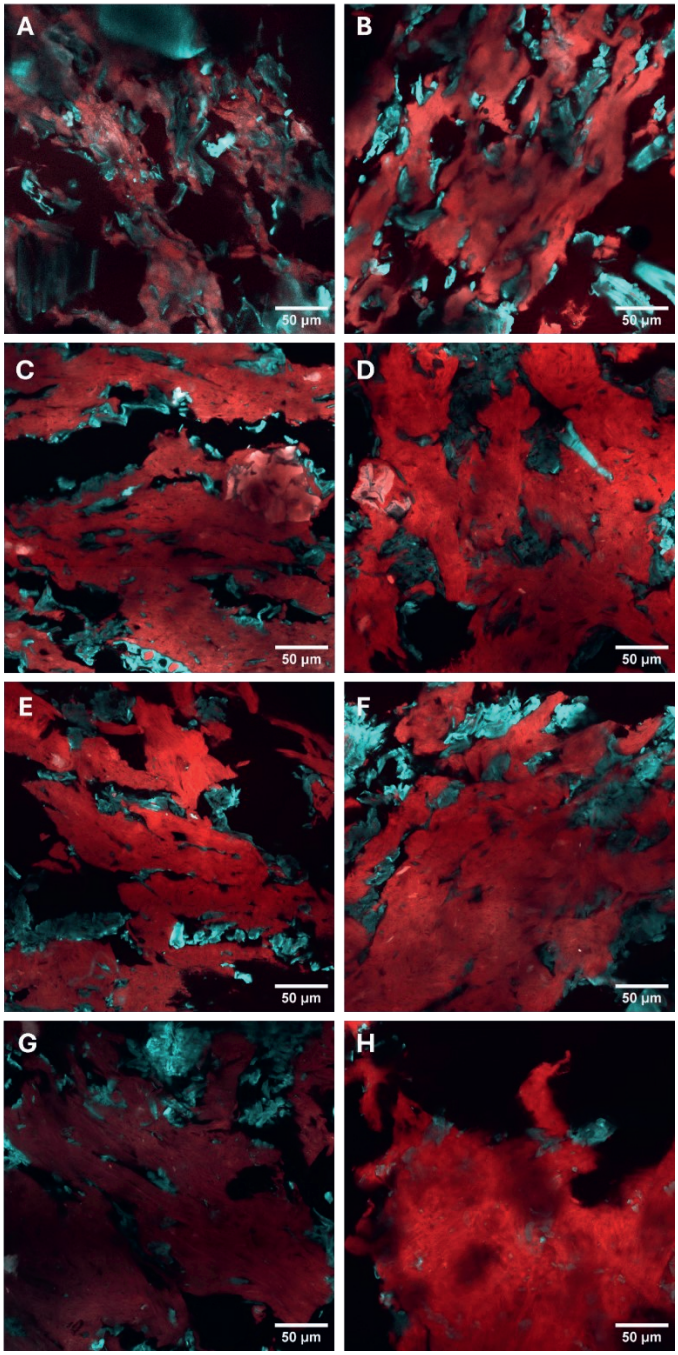

***Fig. S4.6**: CLSM images taken from Barrel 4 (A), Barrel 7 (B), Barrel 9 (C), die (D), the coronal slices of: beginning of cooling die edge (E), beginning of cooling die middle (F), extrudate edge (G), extrudate middle (H). Polysaccharides are coloured in blue, protein in red.*

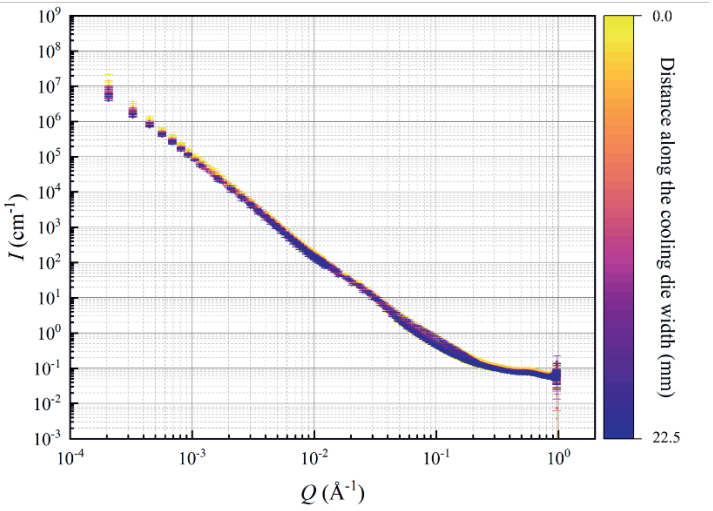

Fig. S4.7: *Radially averaged (U)SAXS data from the end of the cooling die section (100 cm). Data were obtained by combining three sample-to-detector distances. The distance is indicated from the edge to middle (for reference see Fig. 4.1 in main text).*

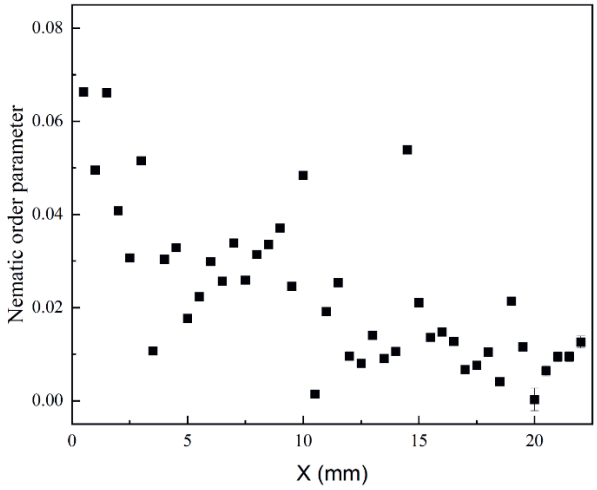

Fig. S4.8: *Nematic order parameters determined over a range of 22 mm for the extrudate at sample-to-detector distance of 31 m. 0 mm along the X-axis corresponds to the edge (Fig. 4.1).*

4.5.2 DoE pilot-plant extruder trial

The choice of HME conditions, used for the dead-stop trial, was made based on the Design of experiments (DoE) summarised in Table S4.4:

Table S4.4: DoE used for pilot-plant extrusion trials and respective dependent process responses. T = manually set temperature, TP = throughput, SME = specific mechanical energy, P = endplate pressure, Tact = temperature measured by an external probe.

	Screw speed (rpm)	$T_{Barrel,2-3}$ (°C)	$T_{Barrel,4-6}$ (°C)	$T_{Barrel,7-8}$ (°C)	$T_{Barrel,9-10}$ (°C)	TP (kg/h)	SME (Wh/kg)	P (bar)	$Tact_{Barrel,5}$ (°C)	$Tact_{Barrel,8}$ (°C)	$Tact_{Barrel,10}$ (°C)
#1	300	85	150	185	100	35	33.8	20.0	126.0	170.2	127.8
#2	300	85	150	150	100	20	54.5	26.6	129.0	142.7	118.5
#3	300	85	150	158	100	28.7	42.2	28.1	129.2	153.9	121.2
#4	300	85	150	150	100	35	38.5	30.6	128.0	146.5	120.1
#5	300	85	150	165	100	20	49.4	21.3	129.0	153.3	126.5
#6	300	85	150	185	100	25.3	39.2	17.4	128.4	167.2	128.2
#7	300	85	150	147	100	27.5	43.5	28.3	132.6	142.7	118.2
#8	300	85	150	171	100	22.8	47.0	24.4	129.9	158.9	123.8
#9	300	85	150	190	100	20	47.1	15.6	129.3	166.5	136.7

During the extrusion trials, extrudate samples were collected from the cooling die outlet after reaching a steady state, as indicated by constant process responses. A portable DR setup allowed for at-line measurements on freshly obtained extrudates. Diffuse reflectance images were obtained at the middle of the extrudate and ~1 cm from the edge (Fig. 4.1 in main text). The system was covered with a black box in order to block the ambient light throughout the procedure and AI(DR) values were measured at the edge and middle part of the samples. AI(DR) data from the DoE samples were analysed in JMP® using analysis of variance method (ANOVA) by least-square fit. A poor correlation (R = 0.72, P = 0.0701) existed between the edge and middle regions. Since AI(DR) values from the edge regions were larger, these were taken for further statistical analysis.

As evident from Fig. S4.9(A), only the temperature factor was found to be significant. Figure S4.9 (B) is the Actual by Predicted plot that visually demonstrates the performance of the standard least squares model. A high model accuracy is indicated by all the data points aligning along the red diagonal line, which shows that the actual values match the predicted values (R^2= 0.9858, P = 0.0001). To forecast the temperature effect on the fibre formation, a predictive profiler was generated (Fig. S4.9 (C)). As expected, higher temperatures result in increased anisotropy. Thus, settings #1 in Table S4.4 were chosen for the dead-stop pilot-plant extruder trial as they provided the most anisotropic structure.

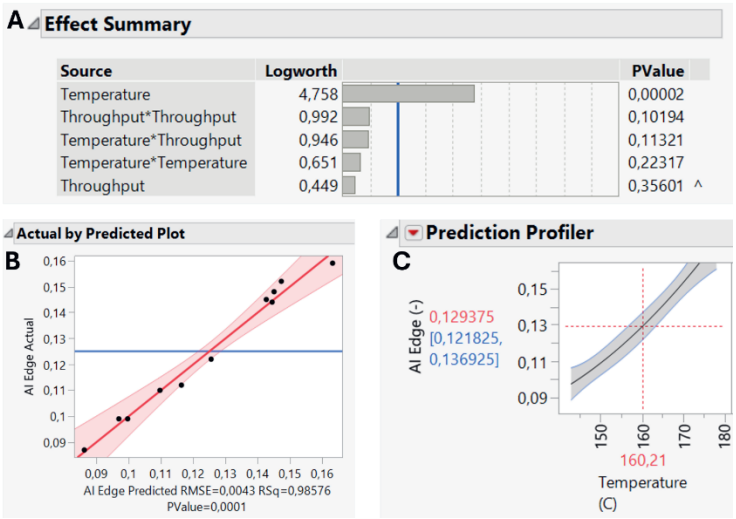

Fig. S4.9: *Overview of Multiple Linear Regression models constructed for AI(Edge) based on the DOE in Table S4.4. (A) Effect summary report. Assessment of factor importance by the Standard Least Squares model. Blue vertical line denotes LogWorth = 2 = P-value 0.01. (B) Actual by Predicted plot, showing how far discrete measurements deviate from the predicted model. (C) Predictive profiler generated by the JMP software using the fitted least squares model (black curve). The blue lines and the grey area are the confidence limits.*

4.5.3 Assessment of lamellar coarseness

Assessment of lamellar coarseness via Rotation Fourier Transform (RFT)

RFT enables analysing images for the presence of structural alignment by obtaining angular distributions [20]. Each image to be analysed is first divided into partially overlapping (sub)windows of a certain size. For each window, RFT then obtains one or more dominant angular orientations (θ_i) and their respective standard deviation (σ_i) and amplitude (A_i). As σ is a measure for the 'width' of a structural feature in angular space, it represents a measure of length in real space. As the analysis in RFT involves Fourier Transforms and their integrations, however, direct back-calculation of a length from distributions of angular orientations and their width σ is not straightforward. Therefore, we decided to investigate the relationship between σ and a characteristic length via a comprehensive synthetic dataset (Fig. S4.10). The synthetic dataset consists of 720 images showing a sinusoidal distribution of intensities (Fig. S4.10). Each image is 512x512 pixels in size and features one of 20 different wavelengths (meaning structural features that show a periodicity given by the wavelength) and one of 36 angular orientations distributed between 0° and 180° [20]. These images are analysed at (sub)window sizes *W* 51, 75, 101, 151, and 201 pixels thereby covering 10%, 15%, 20%, 30%, or 40% of the total image width/height respectively with an overlap of 75% chosen between windows. The input wavelengths are normalised to the window size when fitting σ. This approach provides a metric for how much of a single period of a given wavelength a window covers: periods per window (*ppw*).

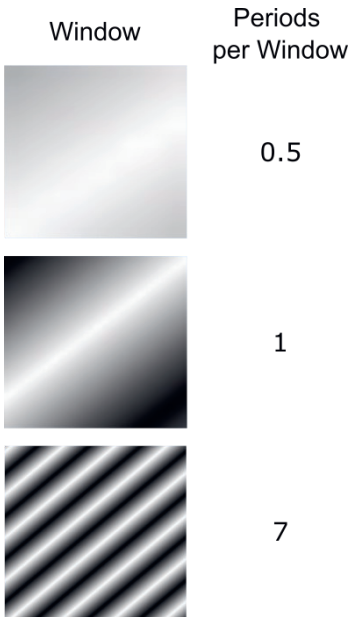

Fig. S4.10: *An example for three different periods per window: 0.5, 1 and 7.*

In Fig. S4.11, we can see a relationship between the *ppw* and the σ as calculated by RFT. At *ppw* < 1, we are below the Nyquist frequency and thus σ has a large variance. At *ppw* ≥ 1 we see a low variance in σ. A linear relationship is observed between σ and *ppw* at range of 0.3 < *ppw* < 3. An empirically found sigmoidal function is fitted to the data (Eq. S4.1). Then, via wavelength (λ_{px}) = Window size (W) / ppw (Eq. S4.2), we can recover the (wave)length of a feature given the σ and window size *W*. The recovered length is representative for separation of the underlying the angular orientation. By taking an average of this recovered length, weighted by A_i , for the entire image, we obtain a weighted characteristic length (*WCL*) (Eq. S4.3).

$$ppw = 0.4 + \frac{24.16}{1+\left(\frac{\sigma}{0.91}\right)^{1.54}} \quad \text{Eq. S4.1}$$

$$\lambda_{px} = W/ppw \quad \text{Eq. S4.2}$$

$$WCL = \overline{\lambda_{px}} \quad \text{Eq. S4.3}$$

The WCL was determined for each position along the extrusion direction and the location perpendicular to the extrusion direction (LE, M, and RE). For our analysis, we used window sizes ranging from 25 to 225 px with steps of 25 px, with the overlap set to 75%. When *ppw* < 1, the WCL cannot be accurately calculated. This is much more likely to occur when the window size is smaller, effectively putting an upper limit on the λ_{px} that can be calculated using Eq. S4.3. Our small image size (~400 x 500 px) limits us to smaller window sizes and thus we encounter this issue. We compensate for this by scanning a wide range of window sizes to obtain meaningful statistical relationships between the calculated WCL and the parameters (position in the cooling die and the location (LE, M, RE)). The mean WCL/W can be seen in Fig. S4.12, where we can already see a separation between the M and the RE/LE data. By dividing the WCL by the window size, we (partially) correct for the window size dependency.

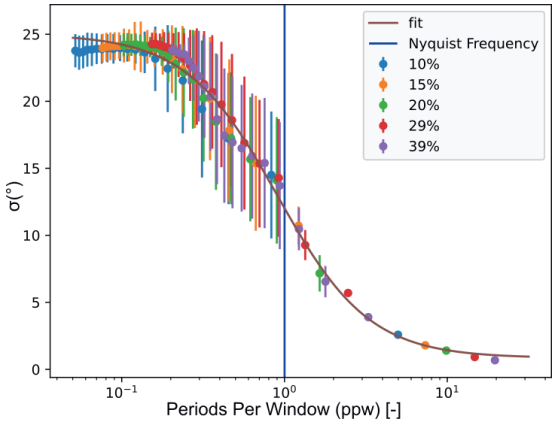

Fig. S4.11: *Obtaining a fit for the periods per window (ppw) via the σ of the fitted Gaussian. The σ obtained via RFT plotted against the ppw is shown of the analysed image. The datasets are coloured according to the fraction of the entire image that each subwindow covers (10-40%). The Nyquist Frequency (ppw = 1) is marked with a blue vertical line. A sigmoidal fit (Eq. S4.1) is shown in beige.*

These relationships were analysed using a least-squares multiple regression model (JMP 17.2, 2025, JMP Statistical Discovery LLC.). We constructed the model including base effects such as window size, location (LE, M, RE), and position in the cooling die as well as their interaction and higher-order effects. We then successively removed all effects with a p-value p>0.02 that were not considered base effects. Figure S4.13 shows the model output for effect summary (a) and the significance of parameter estimates (b).

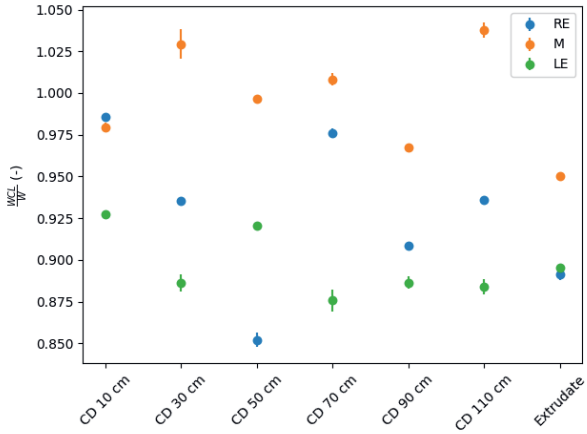

Fig. S4.12: *The mean weighted characteristic length (WCL), corrected by window size (W). The population of M, regardless of position in the cooling die, has a higher length than the edges (LE, RE).*

The results demonstrate that window size is the dominant factor for determining the WCL. This is due to WCL scaling with the window size at small image sizes ($p < 0.0001$, t-ratio:29.63). The position along the extrusion direction in the cooling die does not have a significant effect on WCL ($p = 0.0264$, t-ratio: -2.25) whereas there is a significant yet small effect of position perpendicular to the extrusion direction, i.e. between LE, M, RE ($p < 0.0001$, t-ratio: 7.86).

a

Source	Logworth	PValue
Window Size	49,986	0,00000
Location	11,187	0,00000
Window Size*Location	3,466	0,00034
Position	1,578	0,02644

b

Term	Estimate	Std Error	t Ratio	Prob>|t|
Intercept	0,1811504	0,137471	1,32	0,1907
Window Size	0,0211725	0,000715	29,63	<,0001*
Position	-0,014235	0,006316	-2,25	0,0264*
Location[1]	-0,064152	0,035729	-1,80	0,0757
Location[2]	0,2806851	0,035729	7,86	<,0001*
(Window Size-175,4)*Location[1]	0,0002876	0,00101	0,28	0,7766
(Window Size-175,4)*Location[2]	0,0034914	0,00101	3,46	0,0008*

Fig. S4.13: *Results of multiple regression modelling of WCL as function of window size, location perpendicular to extrusion direction (RE, M and LE) and position along the extrusion direction in the cooling die(a) effect summary, (b) significance of parameter estimates.*

Assessment of lamellar coarseness via Global Moran's I

The global Moran's Index, determined using a spatial autocorrelation function, was assessed according to reference [46] for coronal MRI images. Figure S4.14 shows Moran's I for dead-stop samples taken from the cooling die and the final extrudates. Both a vertical and horizontal weight matrix were used to determine Moran's I, respectively oriented perpendicular and parallel with respect to the extrusion direction. The middle part (M) of the samples show low Moran's I values, indicating a homogeneous structure. At the right and left edges of the samples, higher Moran's I values are observed indicating heterogeneity, which can be attributed to lamellar coarseness. At the right edge (RE) of the samples lamellae are coarser compared to the left edge (LE). No change of lamellar coarseness during passage of the cooling die can be observed. There is however an increase in coarseness in the final extrudate. This can be attributed to expansion of the extrudate upon leaving the cooling die due to steam expansion.

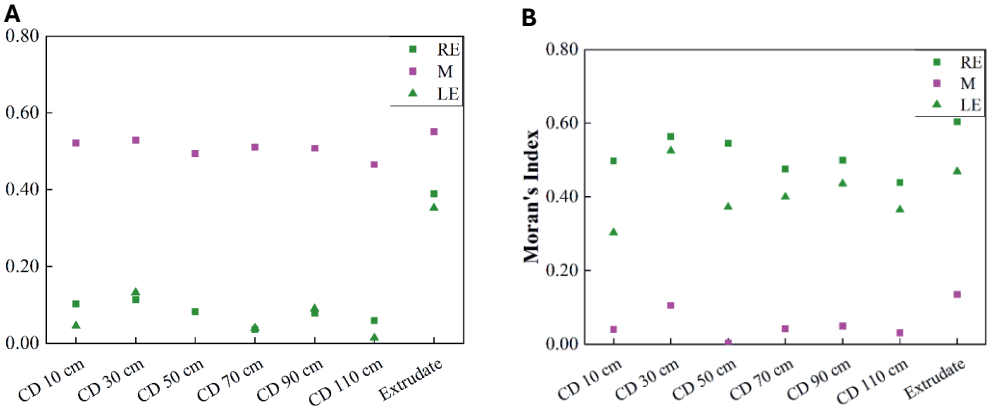

Fig. S4.14: *Global Moran's Index results of dead-stop and extrudate coronal images. Re, M, Le respectively indicate Right Edge, Middle and Left Edge of dead-stop and extrudate samples. (a): Using a vertical weighing matrix to obtain the Moran's Index with a height of 5 pixels. (b): Using a horizontal weighing matrix to obtain the Moran's Index with a width of 5 pixels.*

Chapter

5

Impact of pH-shifting on multiscale structural anisotropy of high-moisture extrudates of soy proteins

This chapter was published as:

Kuijpers, S.A.; Garina, E.D.; Gobes, M.I.; Den Adel, R.; Smith, G.N.; Sztucki, M.; Hohlbein, J. Bouwman, W. G; Van Duynhoven, J.P.M. and Terenzi, C., Impact of pH-shifting on multiscale structural anisotropy of high-moisture extrudates of soy proteins, *Food Hydrocoll.*, 2025, 168, 111456.

Abstract

High-moisture extrusion (HME) is a proven industrial food processing technique used to create textured plant-protein materials that can serve as alternatives for animal meat. The required multiscale anisotropic structure of the extrudate can be achieved by selecting suitable HME process conditions, as well as by pH-shifting. In this work, we explored pH-shifting via the water feed, which is an attractive industrially-scalable approach. Soy protein concentrate (SPC) was extruded on lab-scale and extrudates were characterised ex situ, from molecular to mm-scale, using Diffuse Reflectance (DR), Magnetic Resonance Imaging (MRI), Small-Angle-Scattering of Neutrons (SANS) or X-rays (SAXS). pH-shifting had a non-monotonic effect on extrudate hardness and anisotropic structure at both sub-mm (MRI) and µm (DR) scale. At the sub-µm scale, SANS and SAXS data indicated that, at pH > pI, the radius of protein nano-aggregates monotonically increases, accompanied by a transition from particulate to fibrillar protein aggregation. When pH was further shifted to alkaline conditions, the decrease in clustering strength and nematic order parameter pointed to an increase in intra- and inter-fibrillar repulsion, respectively. Protein extractability experiments indicated that the effects of pH-shifting on anisotropic structure formation could not be attributed to covalent intermolecular crosslinking. Thus, repulsive non-covalent electrostatic protein-protein interactions play a dominant role in the formation of multiscale anisotropic structure during SPC extrusion. The formation of an optimal anisotropic SPC extrudate structure is determined by the pH-dependent balance between fibrillar nano-aggregate clustering and electrostatic repulsion. Alkalisation or acidification via the water feed implies that protein charge and structure may not be in equilibrium yet with the imposed pH conditions. The transient nature of pH-shifting via the water feed results in an intricate interplay with extrusion conditions. Therefore, control of anisotropic structure formation, via the water feed, in SPC extrudates, is extruder specific.

5.1 Introduction

In many western countries, a transition from a mostly animal- to a plant-based diet is occurring [1]. However, replicating the unique textural properties resulting from the highly hierarchical structural organisation of fibres in animal meat is not trivial [2]. Currently, high-moisture extrusion (HME) is the dominant, industrially-scalable, process for creating fibrous texture from plant proteins [3] that are commercially available in bulk as isolates, concentrates or flours [4]. The HME process involves a mixing and hydration step, followed by a thermo-mechanical treatment of the resulting protein dough inside the barrel section of the extruder. The final step involves the cooling of the protein melt, and induces solidification of the protein network. The concomitant contraction of this protein network leads to the expulsion of water [5]. When the rates of protein network solidification and contraction are balanced, phase separation into protein- and water-rich domains at a µm-scale occurs [5, 6]. By shearing the protein melt during cooling, these phase-separated protein-rich domains become elongated along the extrusion direction, and give rise to anisotropic lamellar structures at a larger, sub-mm scale [5, 7]. Models describing both phase-separation [8] as well as fibre formation [5, 6], mostly lack quantitative experimental verification.

It is generally accepted that transient molecular-level interactions during the thermo-mechanical treatment in the barrel section become fixed *before* the hot protein mass enters the cooling die [5, 9]. Within the barrel section, noncovalent bonds become dissociated above the denaturation temperature and exchange between sulfhydryl (SH) and disulphide (SS) groups takes place, which in turn promotes the formation of inter-molecular crosslinks [5, 10, 11]. Under the strongly sheared flow inside the extruder barrel, proteins aggregate and align at the nm-scale along the flow direction [5, 12, 13]. The principles of controlling the fibrous structure of extrudates by adjusting HME process conditions have been outlined earlier [4, 5, 14]. Whether such a fibrous structure can eventually be obtained depends largely on the choice of commercially available protein ingredients [4]. In this respect, protein solubility has been proposed as a parameter that can be used to predict the formation of anisotropic protein structures during HME [15, 16]. Protein solubility is considered to be a proxy for protein hydrophobicity and surface charge and is, thus, also closely related to zeta potential [15, 17]. Both protein solubility and zeta potential depend on pH [17, 18], which offers an opportunity to control protein structure formation during HME. As to the underlying mechanism, a role has been attributed to pH-mediated protein surface charge [17] and to its effect on the electrostatic repulsion between protein molecules. Close to the iso-electric point (pI), the net charge is near zero, and minimal electrostatic repulsion is present, which has been shown to promote random aggregation of proteins into particle-like structures. At pH > pI, the electrostatic repulsion between proteins results in fibrillar aggregates [19, 20]. Besides these charge-mediated mechanisms,

SH/SS exchange has been proposed as a pH-dependent mechanism for formation of covalent inter-molecular protein crosslinks [21, 22]. Monahan *et al.* (1995) have shown that, at mild elevated temperatures around 70–90 °C, SH/SS interchange occurs for whey protein gels even at pH < 7 [23]. In a first systematic study of pH-shifting of plant proteins for use in HME [24], pea protein isolate dispersions were prepared with alkalised or acidified water. Upon resting, these pH-shifted dispersions were pumped into an extruder and a significant effect on hardness and swelling in water was observed. In an alternative approach, pH-shifted dispersions were spray-dried in order to obtain powders that could conventionally be dosed into the feeder of an extruder [25]. Also here, a significant effect of pH-shifting on anisotropic structure of extrudates could be observed. Thus, pH-shifting presents an attractive route to control structure and texture of plant-protein extrudates. However, both aforementioned pH-shifting methods are too cumbersome to be implemented on an industrial scale. Ellwanger *et al.* (2024) showed a more scalable pH-shifting approach by acidifying the extruder water feed [26]. In contrast to previous approaches, the latter does not necessarily allow for equilibration of protein charge and structure at the applied pH conditions. Results showed that extrudates of soy [26] or pea protein isolate [24], become increasingly hard and solid with pH decreasing from neutral conditions down to ∼pI. Yet, little variation in protein extractability of pH-shifted extrudates in a reducing buffer was observed, pointing to a limited effect of pH on covalent SS crosslinking [26].

In the present work, alkalisation and acidification of the extruder water feed was explored as a means to control multiscale anisotropic structure of soy protein concentrate (SPC) extrudates. SPC was chosen due to its industrial potential as an ingredient with high structuring capacity at relatively low cost. Textural functionality of pH-shifted extrudates was determined by hardness measurements with a texture analyser. Protein extractability in denaturing and reducing solvents was assessed to semi-quantify the effect of pH-shifting on covalent and non-covalent protein crosslinking [9, 27]. To enable the characterisation of the multiscale structure of SPC extrudates at complementary and overlapping length scales, multiple measuring modalities were deployed. Small-Angle Neutron or X-ray Scattering (SANS, SAXS) measurements were performed to assess the effect of pH on protein aggregation at the nm-to-μm scale [13], while Magnetic Resonance Imaging (MRI) data, processed using an in house developed method called Rotational Fourier Transform (RFT) [28], enabled quantitative mapping of anisotropic SPC structures at the μm-to-mm scale [7]. Diffusive Reflectance (DR) measurements were performed to semi-quantify the effect of pH-shifting on anisotropic structure formation at μm-scale [29, 30].

5.2 Materials and methods

5.2.1 Materials

Commercial SPC (Arcon SJ® IP, 93% DM with 69% protein in dry base, 4% fat,19% dietary fibre and carbohydrates and 2% ash) from Solae (St. Louis, MO, USA) was used. The acidity and alkalinity of the water feed were adjusted by food-grade citric acid (CA, Merck, Germany) or food-grade trisodium-phosphate (TSP, Merck, Germany), respectively. The molarity of the acidic and alkaline solutions, respectively, ranged from 0 to 0.35 M for CA and from 0 to 0.25 M for TSP. CA and TSP were chosen due to their widespread use as food grade acid and base.

5.2.2 Differential Scanning Calorimetry (DSC) and Wide Angle X-ray Diffraction measurements (WAXD)

DSC measurements on non-hydrated SPCs were performed using a Perkin Elmer DSC8000 instrument. An amount of 30 mg of non-hydrated SPC was weighed on a steel pan, and heated from 5 to 90 °C at 10 °C/min, held at 90 °C for 1 min, and cooled to 5 °C at 10 °C/min, held at 5 °C for 2 min and then heated to 90 °C at 10 °C/min. DSC measurements were also performed on hydrated samples, using a TA DSC Q200 instrument with a protocol adapted from Verfaillie *et al.* (2023), with 30 mg SPC in the presence of 80% (w/w) moisture [31]. The hydrated sample was heated to 180 °C at 5 °C/min, cooled down and then reheated to 180 °C at the same heating rate. The endothermic peak observed during the first heating, and absent in the second heating, was used to calculate the denaturation enthalpy per gram of protein.

WAXD measurements were performed on a Bruker D8 Discover X-ray diffractometer in a theta/theta configuration. One dimensional X-ray diffraction patterns were determined from the 2D images using the GADDS (version 1.28) software. The obtained X-ray diffraction patterns were imported in the Bruker EVA software (version 12.0) and relative intensities were determined.

5.2.3 Protein solubility and zeta potential

Dispersions of 1% w/w and 2.5% w/w SPC were made using demineralised water. The pH of the dispersions was adjusted from 2 up 12 using 1M CA and 0.5M TSP stock solutions. The dispersions were mixed in 50 ml Greiner tubes on a roller bank at room temperature for 16 h. The pH of dispersions was measured, followed by sample centrifugation at 4000 g for 30 min at 20 °C with a swing-out rotor using an acceleration setting of 9. The supernatant was decanted into a new set of 50 ml Greiner tubes and weighed. For the 1% w/w protein dispersions, the total protein content of the supernatant and the dry protein concentrate was determined with the Dumas nitrogen combustion method (Elementar Rapid Max N

Exceed, Germany) using a protein conversion factor of 5.71. Protein solubility was calculated as the percentage of solubilised proteins in the supernatant with regard to total dispersed protein. Measurements were performed in triplicate.

For measuring the zeta potential, a 2.5% w/w SPC dispersion was injected into a disposable folded capillary cell. The capillary cell was placed into a temperature-controlled holder (25 °C), and the electrophoretic mobility was measured by a Zeta Sizer Nano Sizer (ZEN3600, Malvern instruments, UK). Three replicates were measured per sample.

5.2.4 pH measurements

The pH of extrudates was measured using a pH-meter (Metrohm, 913 pH Meter, Switzerland) equipped with a combined electrode (Metrohm, Spearhead electrode) and temperature sensor (Metrohm, Pt1000 temperature sensor). The pH-shifted SPC extrudates were measured by directly piercing the pH electrode into the extrudate sample. Measurements were performed in duplicate.

5.2.5 High-moisture extrusion

Extrusion trials were performed using a co-rotating twin-screw extruder (XTS 19, Xtrutech, UK) with a screw diameter of 19 mm and length-to-diameter (L/D) ratio of 25. A rectangular cooling die (17 mm (width) × 7 mm (height) × 300 mm (length)) was coupled to the extruder through a die adapter, and a breaker plate was placed before the cooling die.

The extruder barrel was segmented into four temperature-controlled zones, heated to 80 °C, 120 °C, 160 °C, and 135 °C in zones 1 to 4. The die temperature was set at 135 °C. The dry protein concentrate was fed into the extruder with a volumetric feeder (Brabender Technologie, Utrecht, Netherlands). Water was injected via an inlet channel with the use of a constant-flow pump (Master Flex Easy Load II, USA). pH-shifted extrudates were obtained by changing the liquid feed between tap water and different molarities of CA (0.025 M, 0.05 M, 0.075 M, 0.1 M, 0.25 M and 0.35 M) and TSP (0.05 M, 0.075 M, 0.1 and 0.25 M) as described by Ellwanger and co-workers [26].

The extrusion trials were run at the screw speed of 350 rpm and moisture content of ca. 60%, keeping a constant throughput of product at 5 kg/h. The cooling water for the cooling die was maintained at a temperature of 65 °C. Once steady-state HME process conditions were reached, the extrudate samples were collected from the cooling die outlet. The samples were placed in a zip-lock bag, immediately cooled in ice-water, frozen and stored at -18 °C. Samples were measured in the thawed state. We note that freeze-thawing may impart structural changes. However, in commercial supply chains, HM extrudates are also stored frozen and this is, thus, taken as a starting condition in this study.

Additionally, pH-shifting using water feed CA molarities of 0.0 M, 0.025 M, 0.05 M and 0.075 M, was performed using a pilot-scale PolyTwin extruder (Bühler, Switzerland) to study the effect of extruder scale. This extruder has a screw diameter of 44 mm and an L/D ratio of 34. The cooling die is rectangular with rounded edges (40 mm (width) x 11 mm (height) x 1200 mm (length)) and was maintained at a temperature of 65 °C. The extruder barrel was segmented into four temperature-controlled zones, heated to 30 °C, 140 °C, 180 °C, and 105 °C in zones 1 to 4. The screw speed was maintained at 190 rpm with a moisture content of ca. 60% and a constant product throughput of 57.5 kg/h.

5.2.6 Hardness measurements

Measurements were performed using a texture analyser (TA.XT plis, Stable Micro Systems, United Kingdom) equipped with a mini Kramer-cell, consisting of five parallel dull blades. Extrudate ribbons were cut into 2.4 cm pieces using a flat knife, with sample dimensions of 2.4 x 1.8 x 0.7 cm3 (L x W x H). The blades of the mini Kramer-cell were placed perpendicular to the extrusion direction. The surface was compressed a single time by 4 mm with a speed of 1 mm/s. Data collection started after a trigger force of 0.1 N was reached. Hardness values are presented as the average over measurements on ten extrudate samples of the same ribbon.

5.2.7 Diffuse Reflectance (DR)

Structural anisotropy was assessed via diffuse light reflectance [29, 30]. The incident light of a linear polarised He-Ne laser (Lumentum model 1108/P, class CDRH II) with a wavelength of 633 nm and a beam diameter of 0.48 mm was applied on extrudate samples at an angle of α = 70°. The extrudate samples were placed with the flow direction parallel to the incident laser beam. To prevent ambient light from influencing the measurement, the system was covered by an optical enclosure built from Thorlabs components (Thorlabs, Germany). The spot of diffusely scattered light, with a diameter of around 1 cm, was captured by a Mako G-234C colour camera and processed by the Halcon 21.11 software package (MVTec, Germany) using a custom made Halcon script (Imfaimon, Barcelona, Spain) that calculates the major axis length (R_1) and the minor axis length (R_2) of a fitted ellipse. The structural Anisotropy Index as determined by diffuse reflectance (AI(DR)) was calculated as (R_1/R_2-1), providing values between 0 (isotropic) and 1 (anisotropic).

5.2.8 Protein extractability

Samples of approximately 2 cm in length were cut from extrudate ribbon and flash-frozen by keeping a round-bottom flask containing the samples in liquid nitrogen for 30 seconds. The frozen samples were subsequently freeze-dried over a period of 5 days at -80°C. Freeze-dried samples were ground to a fine powder. Protein extractability in plain, denaturing and reducing buffers was determined according to an established procedure [27].

5.2.9 Magnetic Resonance Imaging (MRI)

Sample preparation

A frozen extrudate ribbon, of approximately 3 cm in length, was swollen in tap water overnight at 4 °C in a 50 mL tube, using a water:sample weight ratio of 15:1. Swelling substantially increases ^{1}H MRI signal-to-noise ratio and the contrast between protein-rich and water- rich phases, emphasising the lamellar structure visible by MRI [7]. After swelling, excess moisture was removed from the outer surface of the extrudate using a paper towel. The sample was placed in a 25 mm NMR tube and sealed with parafilm to prevent water evaporation.

MRI measurements

^{1}H MRI measurements were performed using a 600 MHz (14 T) wide-bore MRI spectrometer (Ascend 600WB Avance NEO, Bruker, Germany) equipped with a 1.5 T/m imaging gradient system (Micro 2.5, Bruker, Germany) and a 25 mm diameter quadrature ^{1}H probe (MicWB40/025 QTR, Bruker, Germany). The duration of the radio frequency (r.f.) 90° excitation and 180° refocusing pulses was optimised to 2.1 ms at 0.4 W and 1.7 ms at 5.3 W, respectively, for all MRI measurements, using Paravision 360 version 3.3 software. Extrudates were measured using the Rapid Acquisition with Relaxation Enhancement (RARE) sequence [32]. Acquisition parameters were set as follows: echo time, T_E = 10.5 ms; repetition time, T_R = 500 ms; RARE-factor of 3; a total of 8 averages and 8 slices recorded per image acquisition; field-of-view (FOV) of 30 × 12 mm^2, respectively for images in the sagittal plane; in-plane spatial resolution of 39 × 39 × 500 µm^3. The total measurement duration per image acquisition was 7 min.

Analysis of MRI data

^{1}H MRI data processing and image analysis was performed in MATLAB R2022b, using the pvmatlab package from Bruker to extract the data from Paravision 360 version 3.3. In house scripts for automated data processing were written using either standard MATLAB functions or functions provided by the Image Processing Toolbox version 11.6 and Curve Fitting Toolbox version 3.8 from MATLAB.

The methodology used to calculate the Weighted Order Parameter (WOP) is described elsewhere [28]. ImageJ (FIJI, 64-bit) version 1.54j [33] was used with the RFT plugin version 0.1 installed [28]. Images were analysed using a window size of 25 pixels and 75% overlap between adjacent windows. Angle probability data was further processed using an in house developed routine [28] written in Python 3.12, to convert angle probability into 2D spatial maps of feature angle, relative angle intensity and WOP.

5.2.10 Slice preparation for Small-Angle Scattering (SAS)

The preparation of sample slices for SAS measurements was performed according to the protocol described elsewhere [13]. Using a cryo-microtome (Cryostar NX70, ThermoFisher Scientific, Germany), the samples were sliced at a thickness of 500 µm. The specimen head and blade temperatures used for sectioning were, respectively, -12 °C and -10 °C. To secure the samples to the specimen holder, the materials were embedded into the Tissue-Tek® O.C.T. Compound (Sakura Finetek, USA) embedding medium. To ensure the slice stability during storage at -18 °C, the obtained slices were kept between microscope slides covered with Ultralene thin film (Spex® SamplePrep, USA), and then sealed. Prior to SAS measurements, the slides and Ultralene film were removed.

5.2.11 Small-Angle Neutron Scattering (SANS)

SANS experimental procedure

SANS measurements were performed on the Larmor Instrument at the ISIS Neutron and Muon Source (STFC Rutherford Appleton Laboratory, UK) [34]. Using an incidence wavelength range of 0.9–13 Å, the time-of-flight configuration at ISIS allowed for simultaneous Q-range of 0.005–0.7 Å^{-1}. The parameter Q describes the magnitude of the scattering angle, defined as:

$$Q = \frac{4\pi}{\lambda}\sin(\theta), \qquad \text{Eq. 5.1}$$

where 2θ represents the scattering angle, and λ stands for the incident neutron wavelength. Given the anisotropic nature of the samples, the instrument was set up with a symmetric squared sample aperture (6 x 6 mm^2). Extrudate samples were placed into gel cell sample holders with demountable quartz windows to maintain an air-tight environment during the measurements.

SANS data analysis

The SANS data analysis procedure was performed according to the protocol described elsewhere [13]. Briefly, all two-dimensional (2D) scattering data was processed with the instrument-specific software Mantid [35]. By choosing various wavelength bands during data reduction, it was confirmed that no multiple scattering effects were present in the observations. The raw data was placed on an absolute scale (cm^{-1}) corrected for detector sensitivity. The scattering background of the quartz windows was subtracted. For all 2D SANS data, the measured scattering intensities were averaged over a sector, with width of ±15°, for both directions parallel (∥) and perpendicular (⊥) to the alignment direction, as shown in Fig. S5.3 in SI. The SasView software [36] was used to fit these sector averages.

The shape-independent empirical broad peak model was applied to fit the data. The model is given by:

$$I(Q) = \frac{A}{Q^n} + \frac{C}{1 + (|Q - Q_0|\xi)^m} + B, \quad \text{Eq. 5.2}$$

where A represents the power-law scale factor, n denotes the power-law exponent, C is the Lorentzian scale factor, ξ is the Lorentzian correlation length, m refers to the exponent of the Lorentz function, B is the flat background that accounts for incoherent scattering from the hydrogenous material. Q_0 is the peak position corresponding to the characteristic centre-to-centre distance (D) between the scattering inhomogeneities, where $D = 2\pi/Q_0$. The first term A/Q^n becomes a key parameter to evaluate the clustering strength.

Insights into nano-structural anisotropy were obtained through the analysis of the annular intensity averages. The 2D SANS data was averaged over a limited Q-range, $Q_{min} < Q < Q_{trans}$, where Q_{min} represents the lowest measurable scattering vector, and Q_{trans} corresponds to the transition from isotropic to anisotropic structure takes place. The obtained annular intensity averages were fitted with a Legendre series expansion as outlined in [37]:

$$I(Q, \phi) = \sum_{n=0}^{\infty} A_n P_{2n}(\cos(\phi^*)) \quad \text{Eq. 5.3}$$

where $\phi^* = \phi - (\phi_0) + \pi/2$, with ϕ_0 denoting the orientation angle, a_n are fitting coefficients, and P_{2n} are even Legendre polynomials. From Eq. 5.3, the nematic order parameter, $\overline{P_2}$, was calculated as:

$$\overline{P_2} = \frac{a_1}{5a_0}. \quad \text{Eq. 5.4}$$

The value of P_2 indicates the degree of nano-alignment around a certain orientation angle, ϕ_0: the closer P_2 is to zero, the more isotropic the sample. The maximum value of the order parameter is defined by the scattering characteristics of a perfectly aligned structure.

5.2.12 (Ultra-)Small-Angle X-ray Scattering ((U)SAXS)

(U)SAXS experimental procedure

SAXS and USAXS measurements were performed on the upgraded beamline ID02 of the European Synchrotron Radiation Facility (ESRF, Grenoble, France) [38]. A long evacuated detector tube facilitated an automated change of the sample-to-detector distance (SDD) from 1 to 30.9 m, allowing for the SAXS and USAXS data collection using the same setup.

Three SDDs (1, 8, and 30.9 m) were employed to cover a Q range of 0.0002–0.8 $Å^{-1}$ with an X-ray wavelength of 1.014 Å.

Sample slices were positioned on the sample holder. The holder was covered with an Ultralene film, which was sealed with double-sided tape. This was intended to ensure an air-tight environment. The small beam size of 100 x 150 $µm^2$ (vertical x horizontal) allowed for probing 20 measurement frames over a length of 8 mm in the plane perpendicular to the extrusion direction.

(U)SAXS data analysis

All 2D scattering data was reduced and normalised to an absolute scale (cm^{-1}) following standard procedures [38]. The instrument-specific software SAXSutilities [39] was utilised for scattering background subtraction of the Ultralene film, merging measurements recorded at different SDDs and other specific operations. Averaging was performed according to the protocol described elsewhere [13] to account for material heterogeneity. It was investigated whether the merged intensity curves exhibited characteristic shoulder-like features or obeyed a power-law at some Q regions.

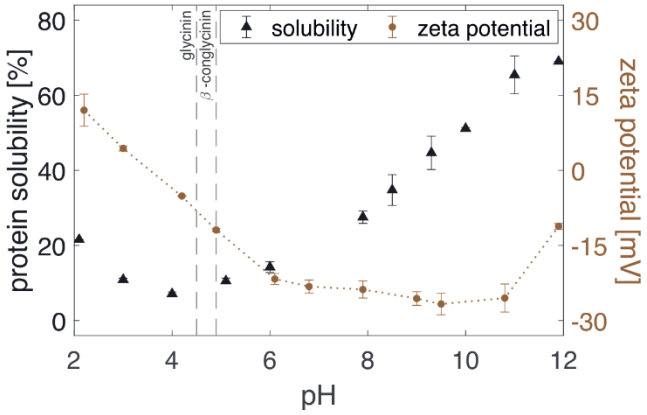

Fig. 5.1: *Protein solubility (black solid triangles) and zeta potential (brown solid circles) data for SPC dispersions as a function of pH. Error bars refer to duplicate measurements. Vertical lines indicate pI values for soy proteins from literature* [40–42].

5.3 Results and discussion

5.3.1 Characterisation of SPC

Protein characteristics, such as level of denaturation and solubility, can vary significantly among different commercially available protein sources. Hence, we characterised composition and structural features of the Arcon® SJ SPC that was used as ingredient for manufacturing extrudates. No denaturation enthalpy was detected by DSC measurements

at 80% moisture. When this material was measured as is, a denaturation enthalpy of 2.9 J/gram protein was observed, which points to the presence of residual secondary structure. This finding was confirmed by WAXD measurements, which showed diffraction lines at 4.6 Å corresponding to the presence of β-sheet structures [43, 44]. The assignment of the denaturation enthalpy measured in non-hydrated state to residual β-sheet structure is corroborated by the observed correlation between DSC and WAXD for a range of protein concentrates and isolates shown in SI Fig. S5.5. Results of solubility and zeta potential measurements for Arcon® SJ SPC are shown in Fig. 5.1. At pH 4, the solubility is low and the zeta potential is about zero, which is lower than the reported pI values for soy proteins, respectively 4.6 and 4.9 for glycinin and β-conglycinin [40, 41]. We attribute this to the presence of cell-wall polysaccharides, such as cellulose and pectin, that generally have pI < 3 [42]. At pH > pI the zeta potential decreases, thus the net negative surface charge and solubility increase. At pH 7, the zeta potential reaches a plateau, while the solubility continues to increase. This is likely due to partial protein unfolding at increasingly more alkaline pH conditions [45].

5.3.2 Effect of pH on multiscale anisotropic structure formation

Hardness and structural anisotropy

Figure 5.2A-B shows the results of structural anisotropy measured by AI(DR) (red solid triangles) and of extrudate hardness measurements (blue solid circles). Near the pI $\sim$ 4.2, hardness and AI(DR) are both roughly a factor 3 lower than their respective highest value near neutral pH. At pH $\sim$ pI, a weak network is formed that lacks an anisotropic fibrous structure at the µm-scale. This lack of structure can be attributed to the absence of charges electrostatically shielding the proteins (Fig. 5.1), which in turn promotes particulate protein aggregation and yields the formation of a weak isotropic network [19, 24, 46]. At pH > pI, both hardness and AI(DR) values increase towards their optimum value, respectively at pH $\sim$ 6.5 and pH $\sim$ 5.4, which likely corresponds to protein aggregation transitioning from particulate to fibrillar [19, 20]. At pH >> pI, both the hardness and AI(DR) values decrease, indicating a weakening of the protein network.

The optimum in anisotropic structure formation found for hardness and AI(DR) is in line with the sub-mm scale lamellar phase separation seen in sagittal MRI images of pH-shifted SPC samples, shown in Fig. 5.2C. At pH $\sim$ pI, the desired lamellar phase-separated structure is nearly absent. At pH $\sim$ 5.4, corresponding to the optimum value observed by AI(DR) measurements, a lamellar phase-separated structure becomes visible and further develops at pH $\sim$ 6.5, where the highest hardness value is observed. Further increasing the pH, away from pI, leads to a loss in the lamellar phase-separated structure. Quantitative analysis of the sagittal MRI images in Fig. 5.2C using RFT analysis [28] (Fig. S5.1 in SI) shows that the WOP values, calculated at each pH condition as the spatial average within the corresponding

MRI image, follow a non-monotonic pH-dependence (Fig. 5.2D), and is in good agreement with the behaviour found for both the hardness and AI(DR) parameters (Fig. 5.2A-B).

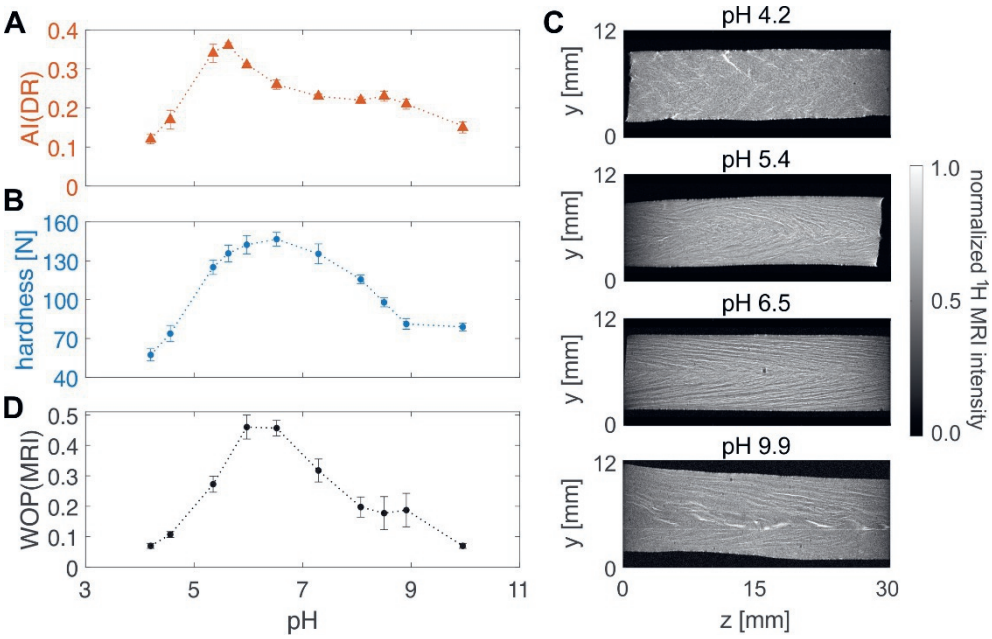

Fig. 5.2: *For pH-shifted SPC extrudates: (A) AI(DR) values (solid orange triangles); (B) Kramer-cell hardness results (blue solid circles); (D) WOP(MRI) values obtained from vector fields maps (Fig. S5.1 in SI) for sagittal ^{1}H MRI images, in turn displayed for four pH-shifted samples in (C). SI Fig. S5.4 shows a folded extrudate sample at neutral and acidic pH, respectively illustrating the presence or absence of macroscopic fibrous structure.*

The non-monotonic pH-dependence found for hardness, AI(DR) and WOP(MRI) parameters show that, at pH ~ pI or pH >> pI, the network structure is weaker compared to that around pH 5.4 – 6.5, at both sub-mm and sub-µm scales. To investigate the role of covalent and non-covalent crosslinking, protein extractability of pH-shifted extrudates has been assessed using non-reducing and reducing denaturing buffers [27, 47]. Protein extractability in a non-reducing denaturing buffer (Fig. S5.2 in SI) was (39 ± 5)% over the examined pH range and, within the experimental error, it remained unaffected by pH-shifting. This finding suggested a negligible effect of pH on non-covalent crosslinking of proteins. In a reducing denaturing buffer roughly 2.5 times more protein could be extracted, but also this amount remained unaffected by pH-shifting. Therefore, we conclude that the amount of *both* covalently and non-covalently crosslinked proteins is unaffected by pH-shifting. This result is in agreement with previous findings from pH-shifting via the extruder water feed of soy protein isolates [26].

Sub-µm scale structural order

SANS measurements of pH-shifted SPC extrudates were performed to investigate the anisotropic structure formation at nm to sub-µm length scale. The analysis of such series of SANS data, described in section 5.2.11, resulted in four independent fitting parameters as a function of pH, namely (i) the correlation length, (ii) the centre-to-centre distance, (iii) the clustering strength, and (iv) the nematic order parameter. The parameters (i)-(iii) could be separately fitted for the sector averages taken in the directions parallel (∥) or perpendicular (⊥) to the extrusion flow direction (examples of the fit are shown in Fig. S5.3 (right) in SI).

The correlation length, defined as the size of the smallest discernible scattering object [48], has values around 8–10 nm for SPC extrudates [49]. As shown in Fig. 5.3 (top), at pH 7.3 the correlation length was ca. 8 nm, which is close to the diameter values for native glycinin and β-conglycinin molecules [50]. Upon pH-shifting, the correlation length followed the trend observed for zeta potential and solubility (Fig. 5.1), first decreasing at acidic conditions and then reaching a plateau at alkaline pH values (Fig. 5.1 (top)). The correlation length, thus, likely describes (partially) folded globular proteins that, due to a net surface charge, have an 'effective' volume.

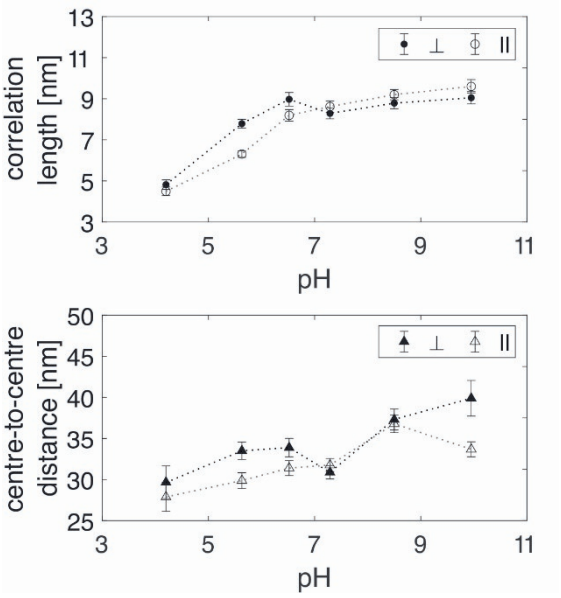

Fig. 5.3: *Correlation length (top) and centre-to-centre distance values (bottom) estimated from fitting the broad peak model (Eq. 5.2) to the SANS sector averages taken in the parallel (∥) or perpendicular (⊥) direction with respect to the extrusion flow direction.*

The centre-to-centre distance represents the main distance between scattering objects. Centre-to-centre distance values of ~ 35–41 nm are generally found for SPC extrudates [13,

49], which is close to the value of ca. 31 nm observed for the SPC extrudate at pH 7.3 (Fig. 5.3 (bottom)). Similar to the correlation length, the centre-to-centre distance increases with increasing pH (Fig. 5.3 (bottom)). We interpret the centre-to-centre distance to be the size of nano-aggregates consisting of multiple partially folded globular proteins with a characteristic correlation length. The observed increase in correlation length and electrostatic repulsion, due to a higher pH-induced negative net charge on the protein (Fig. 5.1), yields larger nano-aggregates. Subsequently, these nano-aggregates are clustered together and form a fibrillar network at the sub-µm scale [13, 49]. The SANS results provide an explanation for the structural changes shown in Fig. 5.2 between pH 4 and 7, but cannot account for the decrease in structural order seen at alkaline conditions. One possible explanation is that pH-shifting is accompanied by a change in ionic strength of the liquid phase, which does not affect the structure formation at nm-scale and, thus, is not detected by SANS measurements. However, pH-shifting with HCl and NaOH, which have smaller ionic strength contributions, gave similar results as with citric acid and TSP (data not shown).

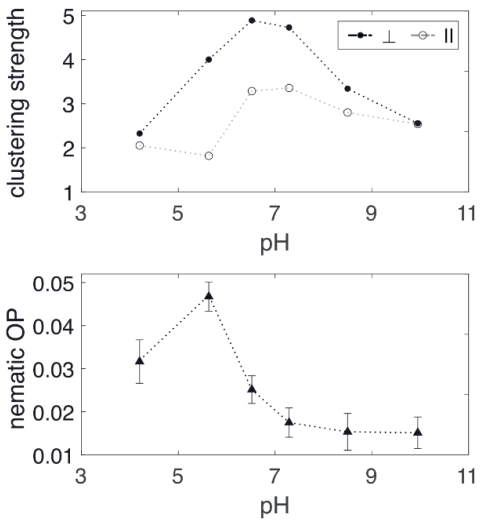

Fig. 5.4: *For pH-shifted SPC extrudates: (top) SANS clustering strength, measured along both directions parallel (∥) and perpendicular (⊥) to extrusion, and (bottom) nematic order parameter, in turn indicative of nano-anisotropy at length scales of ca. 13–125 nm. The clustering strength is obtained by fitting the broad-peak model (section 5.2.11) to the SANS data.*

The clustering strength, A/Q^n, is calculated from the broad-peak model, using Q = 0.02 Å^{-1}, since at Q < ca. 0.02 Å^{-1} (corresponding to real-space distances > 60 nm) the power-law behaviour becomes dominating. The clustering strength is generally interpreted as a measure of the interaction strength between scattering objects [51]. High and low values of the clustering strength, respectively, are attributed to the presence or absence of network formation [52, 53].

Clustering strength data for pH-shifted SPC extrudates, determined along both directions, are shown in Fig. 5.4 and follow a similar non-monotonic trend to the AI(DR) and hardness values reported in Fig. 5.2. This is especially evident for the direction perpendicular to extrusion. Since the clustering strength is determined at the length scales above the size of single nano-aggregates, we interpret it to be a measure of the fibrillar aggregation of these nanoaggregates. At acidic conditions, the clustering strength values measured in both the ∥ and ⊥ direction, as well as the electrostatic repulsion between proteins, (Fig. 5.1) are low. The latter result was expected for nano-aggregates of these proteins, yielding efficient formation of a network of particulate clusters, rather than of fibril bundles [19], at these pH conditions. The opposite effect is likely seen at alkaline conditions where, due to excessive electrostatic repulsion among nano-aggregates, thin linear chains are formed that do not create a cohesive network [19]. At alkaline pH values, the clustering strength is similar for both the ∥ and ⊥ direction and is lower than that at optimum pH, here around pH 7. These results indicate that, when the electrostatic shielding and electrostatic repulsion are balanced, the interaction strength between nano-aggregates is high. This suggests the formation of a cohesive network at optimum pH, and is in agreement with evidence provided by hardness and AI(DR) measurements (Fig. 5.2).

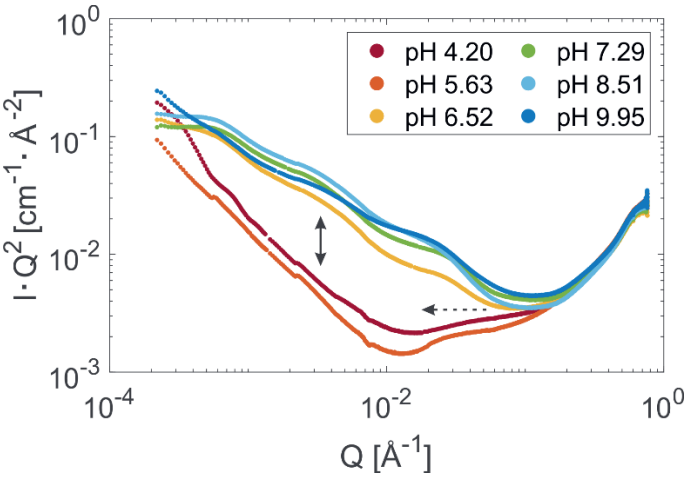

Fig. 5.5: *(U)SAXS results of pH-shifted SPC extrudates. Arrows indicate either a peak shift in the high-Q region for low-pH samples (dashed line) or the disappearance of a low-Q intensity shoulder at low pH (solid line).*

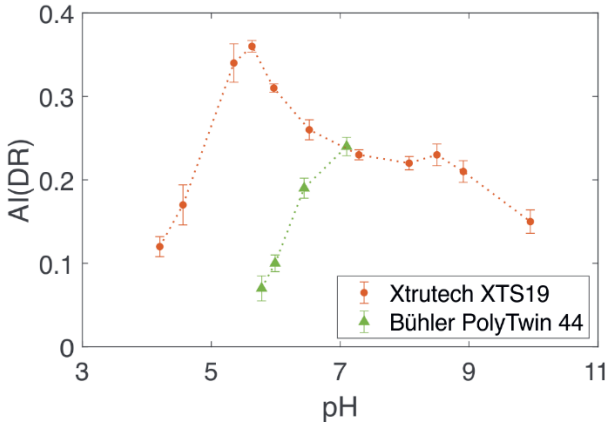

Fig. 5.6: *AI(DR) results for pH-shifted Arcon SJ SPC extrudates using two different scale extruders: a lab-scale Xtrutech XTS19 (orange solid circles), operating at 5 kg/h, and a pilot-scale Bühler PolyTwin 44 (green solid triangles), operating at 57.5 kg/h.*

The nematic order parameter, obtained from SANS data, is a measure of nano-alignment at the length scales of ca. 13–125 nm [48], and has been shown previously to vary with process conditions during extrusion of SPC [13]. Results shown in Fig. 5.4 are in good agreement with the clustering strength data, and provide additional insight in the type of aggregate that these nano-aggregates form. At the optimal pH, the nematic order parameter is higher than at acidic or alkaline conditions, suggesting the presence of fibril alignment along the extrusion direction, and is in line with AI(DR) results Fig. 5.2. While no fibrillar structure is expected to be present at low pH, aggregates are predominantly fibrillar at high pH. In the latter condition, the observed lower fibril alignment is likely a result of strong electrostatic repulsion among protein molecules in the presence of excessive surface charges [19, 24]. To further underpin this, Fig. 5.5 shows (U)SAXS data of these extrudates and qualitatively reveals that, at acidic conditions, indeed a change in aggregation behaviour is present. The solid arrow in Fig. 5.5 points to a low-Q USAXS intensity shoulder region that is associated with fibril formation at the 100–200 nm length scale for SPC extrudates [54]. In Fig. 5.5, this shoulder is roughly at the same location for neutral and alkaline pH conditions, but it disappears at pH < 6. Thus, at pH ~ pI, fibril formation is hampered and particulate clusters of nano-aggregates, devoid of a well-defined orientation, are formed as also suggested by nematic order parameter and AI(DR) results (Fig. 5.4). At alkaline conditions, this shoulder is present, confirming that fibrillar aggregates are formed [19, 20]. These fibrillar aggregates show little interaction, due to excessive electrostatic charges between proteins (Fig. 5.3), and do not form a cohesive network, in agreement with clustering strength (Fig. 5.4), AI(DR) and hardness results (Fig. 5.2). Additionally, a shifting high-Q shoulder is seen in the SAXS data (indicated with the dashed arrow in Fig. 5.5), which is also visible in the SANS data (Fig. S5.3 (right) in SI) and used to fit the centre-to-centre distance. The presence or absence of

fibrillar network formation at the nm-to-µm scale influences protein network contraction during cooling. This respectively results in the formation of lamellar or isotropic phase separation at the mm-scale as visible in MRI images in Fig. 5.2C.

5.3.3 Interplay of extrusion conditions and pH-shifting

In this work, we shifted the pH of the SPC dough in a lab-scale high-moisture extruder by adjusting the acidic and alkaline molarity of the water feed. In contrast to pH-shifting approaches that involved resting of the protein dough [24, 25], in our conditions we cannot assume an equilibration of the protein structure and aggregation state. The effect of pH-shifting on AI(DR) for both the lab-scale extruder used in this work, and a pilot-plant scale extruder, is shown in Fig. 5.6. In both cases, SPC has been extruded using identical dosed water contents, comparable barrel temperature profiles, as well as screw speeds and throughputs typical for these extruders. For the pilot-plant scale extruder (green solid triangles) the pH dependence of AI(DR) values is shifted towards higher pH values. This difference between the two extruders is likely due to corresponding differences in equilibration kinetics of protein structure and of noncovalent aggregation at acidic conditions. The pilot-plant extruder has a more extensive mixing section, and specific mechanical energies (SME) are much higher than for those in the lab-scale extruder (Table S5.1 in SI). Upon acidification of the water feed, this will promote particulate aggregation and, thus, impede anisotropic structure formation. In the lab-scale extruder there is less mixing and SMEs are lower. Hence, upon acidification fibrillar structure formation can still occur. The results in Fig. 5.6 indicate that anisotropic structure formation is determined by a complex interplay between pH-shifting and extrusion conditions. This finding implies that control of anisotropic structure formation by pH-shifting via the water feed is extruder specific.

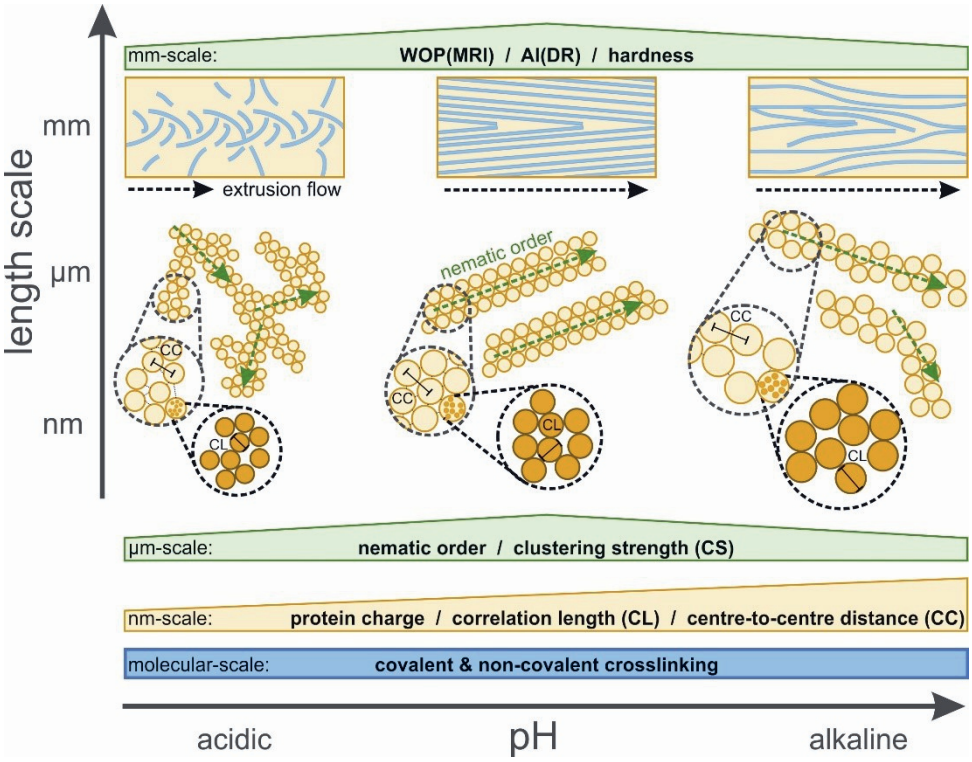

Fig. 5.7: *Schematic summary of the effect of pH-shifting on SPC extrudate structure. These effects are probed at the mm-scale, by WOP(MRI), AI(DR) and hardness (Fig. 5.2) measurements; at the µm-scale, by nematic order parameter and clustering strength (Fig. 5.4); at the nm-scale, by correlation length and centre-to-centre distance (Fig. 5.3); at the molecular scale by protein extractability.*

5.4 Conclusions

In this work, we resolved the multiscale structural changes that underlie the observed non-monotonic effect of pH-shifting via the water feed on the hardness of high-moisture extrudates of SPC. A schematic overview of the effects of pH-shifting on multiscale anisotropic extrudate structure is given in Fig. 5.7. pH-shifting had a non-monotonic effect on the sub-mm anisotropic structure as seen by MRI. Upon pH-shifting towards pH ~ pI, as well as at pH >> pI, MRI images showed an increase in structural disorder and the absence of an anisotropic structure (Fig. 5.7 top diagrams). This non-monotonic behaviour is also observed at the µm-scale by AI(DR). SANS data was used to underpin this nonmonotonic behaviour at the nm-scale and showed that, at pH > pI, the correlation length of partially folded globular proteins (Fig. 5.7 CL) and the size of their nano-aggregates (Fig. 5.7 CC) monotonically increase with pH. Additionally, SAXS data indicated the concomitant transition from particulate to fibrillar aggregation. The sub-µm scale effect of pH-shifting on the clustering strength and the nematic order parameter of the fibrillar aggregates is, again,

nonmonotonic (Fig. 5.7, green dashed arrows). The increase in clustering strength and nematic order at pH > pI is in line with a transition towards fibrillar aggregation. The decrease of clustering strength and nematic order parameter, when pH is further shifted to alkaline conditions, can be explained by electrostatic intra- and inter-fibrillar repulsion (Fig. 5.7 CS). Protein extractability measurements indicated that the effects of pH-shifting on anisotropic structure formation could not be attributed to covalent intermolecular crosslinking. An optimal anisotropic structure can, thus, be achieved, when a pH-dependent balance between electrostatic repulsion and fibrillar nano-aggregate clustering is struck. This optimum condition, however, is extruder dependent. pH-shifting via the water feed is therefore an industrially-scalable, yet extruder condition specific, technology capable of controlling multiscale anisotropic structure formation of plant proteins.

Authors statement

Sam A. Kuijpers: Conceptualisation, Data curation, Formal analysis, Investigation, Methodology, Visualisation, Software, Writing - original draft. Ekaterina D. Garina: Conceptualisation, Data curation, Formal analysis, Investigation, Methodology, Visualisation, Writing - review & editing. Martijn I. Gobes: Software, Data Curation. Ruud den Adel: Investigation, Methodology. Gregory N. Smith: Data curation (SANS), Software, Formal analysis, Writing - review & editing. Michael Sztucki: Data curation ((U)SAXS), Software, Formal analysis, Writing - review & editing. Johannes Hohlbein: Writing - review & editing. Wim G. Bouwman: Funding acquisition, Supervision, Writing - review & editing. John P.M. van Duynhoven: Conceptualisation, Funding acquisition, Resources, Supervision, Writing - review & editing. Camilla Terenzi: Funding acquisition, Supervision, Writing - review & editing, Project administration.

Declaration of competing interest

John P.M. van Duynhoven and Ruud den Adel are employed by a company that manufactures and markets plant-based meat alternatives. The other authors declare that they have no known competing financial interests or personal relationships that could have appeared to influence the work reported in this paper.

Acknowledgements

This work is part of the project "Measurement and Modelling of Multiscale Processed Protein Products (MP3)" (with project number 18744) of the research programme OPT TTW, which is financed by the Dutch Research Council as well as contributions from consortium partners Unilever, Cargill, dsm-firmenich, FrieslandCampina and Wageningen Food and Biobased Research. This project was also supported by the uNMR-NL Grid: A distributed, state-of-the-art Magnetic Resonance facility for the Netherlands (NWO grant 184.035.002). We gratefully acknowledge the Science and Technology Facilities Council (STFC) for access to neutron beamtime at ISIS through RB 2269101. We also acknowledge the European Synchrotron Radiation Facility (ESRF) for the provision of synchrotron radiation facilities. This work benefited from the use of the SasView application, originally developed under NSF Award DMR-0520547. SasView also contains code developed with funding from the EU Horizon 2020 programme under the SINE2020 project Grant No 654000. We thank Arno Wouters and Kristof Brijs (KU Leuven) for skillfully performing the protein extraction analyses. Finally, we thank Kalyan Panda and Claudia Zimmermann for performing extrusion trials and Gert-Jan Goudappel (Unilever Global Food Innovation Centre, Wageningen) for performing MRI measurements on extrudates.

Data availability

SANS data are available at https://doi.org/10.5286/ISIS.E.RB2269101. (U)SAXS data are available at https://doi.org/10.5281/zenodo.14002334.

References

[1] H. Aiking and J. de Boer, "The next protein transition," *Trends Food Sci. Technol.*, vol. 105, pp. 515–522, 2020, doi: 10.1016/j.tifs.2018.07.008.

[2] D. Pette and R. S. Staron, "Cellular and molecular diversities of mammalian skeletal muscle fibers.," *Rev. Physiol. Biochem. Pharmacol.*, vol. 116, pp. 1–76, 1990, doi: 10.1007/3540528806_3.

[3] H. Akdogan, "High moisture food extrusion," *Int. J. Food Sci. Technol.*, vol. 34, no. 3, pp. 195–207, 1999, doi: 10.1046/j.1365-2621.1999.00256.x.

[4] Y. Wang *et al.*, "The development process of plant-based meat alternatives: Raw material formulations and processing strategies," *Food Res. Int.*, vol. 167, no. February, p. 112689, 2023, doi: 10.1016/j.foodres.2023.112689.

[5] R. G. M. Van der Sman and A. J. Van der Goot, "Hypotheses concerning structuring of extruded meat analogs," *Curr. Res. Food Sci.*, vol. 6, no. May, p. 100510, 2023, doi: 10.1016/j.crfs.2023.100510.

[6] J. Zhang, Q. Chen, D. L. Kaplan, and Q. Wang, "High-moisture extruded protein fiber formation toward plant-based meat substitutes applications: Science, technology, and prospect," *Trends Food Sci. Technol.*, vol. 128, no. May, pp. 202–216, 2022, doi: 10.1016/j.tifs.2022.08.008.

[7] S. Kuijpers, G.-J. Goudappel, T. Huppertz, J. Van Duynhoven, and C. Terenzi, "Quantification of phase separation in high moisture soy protein extrudates by NMR and MRI," *Food Res. Int.*, vol. 197, no. P1, p. 115225, 2024, doi: 10.1016/j.foodres.2024.115225.

[8] E. Kaunisto, S. Wassén, and M. Stading, "A thermodynamical finite element model of the fibre formation process during extrusion of high-moisture meat analogues," *J. Food Eng.*, vol. 362, no. 111760, 2024, doi: 10.1016/j.jfoodeng.2023.111760.

[9] K. S. Liu and F. H. Hsieh, "Protein-protein interactions during high-moisture extrusion for fibrous meat analogues and comparison of protein solubility methods using different solvent systems," *J. Agric. Food Chem.*, vol. 56, no. 8, pp. 2681–2687, 2008, doi: 10.1021/jf073343q.

[10] J. Ubbink and B. J. Muhialdin, "Protein physical state in meat analogue processing," *Curr. Opin. Food Sci.*, vol. 45, p. 100822, Jun. 2022, doi: 10.1016/j.cofs.2022.100822.

[11] R. Osen, S. Toelstede, P. Eisner, and U. Schweiggert-Weisz, "Effect of high moisture extrusion cooking on protein-protein interactions of pea (Pisum sativum L.) protein isolates," *Int. J. Food Sci. Technol.*, vol. 50, no. 6, pp. 1390–1396, 2015, doi: 10.1111/ijfs.12783.

[12] C. J. R. Verbeek and L. E. Van Den Berg, "Extrusion processing and properties of protein-based thermoplastics," *Macromol. Mater. Eng.*, vol. 295, no. 1, pp. 10–21, 2010, doi: 10.1002/mame.200900167.

[13] E. D. Garina *et al.*, "SANS and SAXS : A Love Story to unravel structural evolution of soy proteins and polysaccharide fibres during high moisture extrusion for meat alternatives," *Food Hydrocoll.*, vol. 155, no. January, p. 110121, 2024, doi: 10.1016/j.foodhyd.2024.110121.

[14] S. H. V Cornet, S. J. E. Snel, J. Lesschen, A. Jan, V. Der Goot, and R. G. M. Van Der Sman, "Enhancing the water holding capacity of model meat analogues through marinade composition," *J. Food Eng.*, vol. 290, p. 110283, 2021, doi: 10.1016/j.jfoodeng.2020.110283.

[15] K. Gao, J. Rao, and B. Chen, "Plant protein solubility: A challenge or insurmountable obstacle," *Adv. Colloid Interface Sci.*, vol. 324, no. October 2023, p. 103074, 2024, doi: 10.1016/j.cis.2023.103074.

[16] D. Webb, Y. Li, and S. Alavi, "Chemical and physicochemical features of common plant proteins and their extrudates for use in plant-based meat," *Trends Food Sci. Technol.*, vol. 131, no. November 2022, pp. 129–138, 2023, doi: 10.1016/j.tifs.2022.11.006.

[17] L. Grossmann and D. J. McClements, "Current insights into protein solubility: A review of its importance for alternative proteins," *Food Hydrocoll.*, vol. 137, no. December 2022, p. 108416, 2023, doi: 10.1016/j.foodhyd.2022.108416.

[18] K. K. Ma, M. Greis, J. Lu, A. A. Nolden, D. J. McClements, and A. J. Kinchla, "Functional Performance of Plant Proteins," *Foods*, vol. 11, no. 4, pp. 1–23, 2022, doi: 10.3390/foods11040594.

[19] E. van der Linden and P. Venema, "Chapter 4. Similarities in Self-Assembly of Proteins and Surfactants: An Attempt to Bridge the Gap," *Food Colloids*, pp. 57–67, 2007, doi: 10.1039/9781847557698-00057.

[20] M. R. H. Krebs, K. R. Domike, and A. M. Donald, "Protein aggregation: More than just fibrils," *Biochem. Soc. Trans.*, vol. 37, no. 4, pp. 682–686, 2009, doi: 10.1042/BST0370682.

[21] T. E. Creighton, "Disulfide bond formation in proteins," *Methods Enzymol.*, vol. 107, no. C, pp. 305–329, 1984, doi: 10.1016/0076-6879(84)07021-X.

[22] I. Rombouts, B. Lagrain, K. Brijs, and J. A. Delcour, "β-Elimination reactions and formation of covalent cross-links in gliadin during heating at alkaline pH," *J. Cereal Sci.*, vol. 52, no. 3, pp. 362–367, 2010, doi: 10.1016/j.jcs.2010.06.006.

[23] F. J. Monahan, J. B. German, and J. E. Kinsella, “Effect of pH and Temperature on Protein Unfolding and Thiol/ Disulfide Interchange Reactions during Heat-Induced Gelation of Whey Proteins,” *J. Agric. Food Chem.*, vol. 43, no. 1, pp. 46–52, 1995, doi: 10.1021/jf00049a010.

[24] B. J. Muhialdin and J. Ubbink, “Effects of pH and aging on the texture and physicochemical properties of extruded pea protein isolate,” *Food Hydrocoll.*, vol. 140, no. November 2022, p. 108639, 2023, doi: 10.1016/j.foodhyd.2023.108639.

[25] A. Nisov, M. Nikinmaa, E. Nordlund, and N. Sozer, “Effect of pH and temperature on fibrous structure formation of plant proteins during high-moisture extrusion processing,” *Food Res. Int.*, vol. 156, p. 111089, Jun. 2022, doi: 10.1016/j.foodres.2022.111089.

[26] F. Ellwanger, M. Fuhrmann, and H. P. Karbstein, “Influence of Lowering the pH Value on the Generation of Fibrous Structures of Protein Gels with Different Network Types,” *gels*, vol. 10, no. 173, pp. 1–14, 2024.

[27] D. Verfaillie *et al.*, “Genetic and environmental variation in protein composition of Belgian soy determined with a novel size-exclusion chromatography method,” *J. Food Compos. Anal.*, vol. 130, no. October 2023, p. 106187, 2024, doi: 10.1016/j.jfca.2024.106187.

[28] M. I. Gobes, S. A. Kuijpers, C. Terenzi, R. G. M. van der Smaan, J. P. M. van Duynhoven, and J. Hohlbein, “Rotated Fourier transform (RFT) enables the quantification of anisotropic structure in high-moisture plant-protein extrudates,” *Food Struct.*, vol. 44, no. June, p. 100437, 2025, doi: 10.1016/j.foostr.2025.100437.

[29] J. Ranasinghesagara, F. Hsieh, and G. Yao, “A photon migration method for characterizing fiber formation in meat analogs,” *J. Food Sci.*, vol. 71, no. 5, 2006, doi: 10.1111/j.1750-3841.2006.00038.x.

[30] R. Van Beers, B. Aernouts, M. M. Reis, and W. Saeys, “Anisotropic light propagation in bovine muscle tissue depends on the initial fiber orientation, muscle type and wavelength,” *Opt. Express*, vol. 25, no. 18, p. 22082, 2017, doi: 10.1364/oe.25.022082.

[31] D. Verfaillie, F. Janssen, G. Van Royen, and A. G. B. Wouters, “A systematic study of the impact of the isoelectric precipitation process on the physical properties and protein composition of soy protein isolates,” *Food Res. Int.*, vol. 163, no. November 2022, p. 112177, 2023, doi: 10.1016/j.foodres.2022.112177.

[32] J. Hennig, A. Nauerth, and H. Friedburg, “RARE imaging: A fast imaging method for clinical MR,” *Magn. Reson. Med.*, vol. 3, no. 6, pp. 823–833, 1986, doi: 10.1002/mrm.1910030602.

[33] J. Schindelin *et al.*, “Fiji: An open-source platform for biological-image analysis,” *Nat. Methods*, vol. 9, no. 7, pp. 676–682, 2012, doi: 10.1038/nmeth.2019.

[34] Anon, “ISIS Larmor,” 2023. https://www.isis.stfc.ac.uk/Pages/Larmor.aspx (accessed Jul. 21, 2023).

[35] O. Arnold *et al.*, “Mantid - Data analysis and visualization package for neutron scattering and μ SR experiments,” *Nucl. Instruments Methods Phys. Res. Sect. A Accel. Spectrometers, Detect. Assoc. Equip.*, vol. 764, pp. 156–166, 2014, doi: 10.1016/j.nima.2014.07.029.

[36] M. Doucet *et al.*, “SasView version 5.0.5,” 2022, doi: 10.5281/zenodo.6331344.

[37] C. Burger, B. S. Hsiao, and B. Chu, “Preferred orientation in polymer fiber scattering,” *Polym. Rev.*, vol. 50, no. 1, pp. 91–111, 2010, doi: 10.1080/15583720903503494.

[38] T. Narayanan *et al.*, “Performance of the time-resolved ultra-small-angle X-ray scattering beamline with the Extremely Brilliant Source,” *J. Appl. Crystallogr.*, vol. 55, pp. 98–111, 2022, doi: 10.1107/S1600576721012693.

[39] M. Sztucki, “SAXSutilities: a graphical user interface for processing and analysis of Small-Angle X-ray Scattering data (1.024),” 2021, doi: 10.5281/zenodo.5825707.

[40] I. Koshiyama, “Purification and Physico-chemical Properties of 11S Globulin in Soybean Seeds,” *Int. J. Pept. Protein Res.*, no. 4, pp. 167–176, 1972.

[41] I. Koshiyama, “Chromatographic and Sedimentation Behavior of a Purified 7S Protein in Soybean Globulins,” *Cereal Chem.*, vol. 45, pp. 405–412, 1968.

[42] D. Myśliwiec, M. Chylińska, M. Szymańska-Chargot, S. Chibowski, and A. Zdunek, “Revision of adsorption models of xyloglucan on microcrystalline cellulose,” *Cellulose*, vol. 23, no. 5, pp. 2819–2829, 2016, doi: 10.1007/s10570-016-0995-x.

[43] A. H. Clark and C. D. Lee-Tuffnell, “Gelation of Globular Proteins,” in *Functional Properties of Food Macromolecules*, J. R. Mitchell and D. A. Ledward, Eds. London: Elsevier, 1986, pp. p203-272.

[44] V. P. Yuryev, D. V. Zasypkin, V. V. Alexeyev, Y. V. Genin, M. G. Ezernitskaya, and V. B. Tolstoguzov, “Structure of protein texturates obtained by thermoplastic extrusion,” *Food / Nahrung*, vol. 34, no. 7, pp. 607–613, 1990, doi: 10.1002/food.19900340707.

[45] B. Lagrain, K. De Vleeschouwer, I. Rombouts, K. Brijs, M. E. Hendrickx, and J. A. Delcour, “The kinetics of β-elimination of cystine and the formation of lanthionine in gliadin,” *J. Agric. Food Chem.*, vol. 58, no. 19,

pp. 10761–10767, 2010, doi: 10.1021/jf102575r.

[46] N. Chen, M. Zhao, F. Niepceron, T. Nicolai, and C. Chassenieux, “The effect of the pH on thermal aggregation and gelation of soy proteins,” *Food Hydrocoll.*, vol. 66, pp. 27–36, 2017, doi: 10.1016/j.foodhyd.2016.12.006.

[47] K. S. Liu and F. H. Hsieh, “Protein-protein interactions in high moisture-extruded meat analogs and heat-induced soy protein gels,” *JAOCS, J. Am. Oil Chem. Soc.*, vol. 84, no. 8, pp. 741–748, Aug. 2007, doi: 10.1007/s11746-007-1095-8.

[48] B. Tian *et al.*, “Small angle neutron scattering quantifies the hierarchical structure in fibrous calcium caseinate,” *Food Hydrocoll.*, vol. 106, no. March, p. 105912, 2020, doi: 10.1016/j.foodhyd.2020.105912.

[49] T. Guan *et al.*, “In situ studies of plant-based meat analog texturization,” *Food Hydrocoll.*, vol. 155, no. March, 2024, doi: 10.1016/j.foodhyd.2024.110215.

[50] R. A. Badley, D. Atkinson, H. Hauser, D. Oldani, J. P. Green, and J. M. Stubbs, “The structure, physical and chemical properties of the soy bean protein glycinin,” *BBA - Protein Struct.*, vol. 412, no. 2, pp. 214–228, 1975, doi: 10.1016/0005-2795(75)90036-7.

[51] B. Hammouda, D. L. Ho, and S. Kline, “Insight into clustering in poly(ethylene oxide) solutions,” *Macromolecules*, vol. 37, no. 18, pp. 6932–6937, 2004, doi: 10.1021/ma049623d.

[52] B. Wu, M. Siglreitmeier, C. Debus, D. Schwahn, H. Cölfen, and V. Pipich, “Ionic Dependence of Gelatin Hydrogel Architecture Explored Using Small and Very Small Angle Neutron Scattering Technique,” *Macromol. Biosci.*, vol. 18, no. 6, pp. 1–11, 2018, doi: 10.1002/mabi.201800018.

[53] M. Bayrak, A. E. Whitten, J. P. Mata, C. E. Conn, J. Floury, and A. Logan, “Real-time monitoring of casein gel microstructure during simulated gastric digestion monitored by small-angle neutron scattering,” *Food Hydrocoll.*, vol. 144, no. June, p. 108919, 2023, doi: 10.1016/j.foodhyd.2023.108919.

[54] J. I. Zink *et al.*, “Structural and mechanical anisotropy in plant-based meat analogues,” *Food Res. Int.*, vol. 179, no. December 2023, p. 113968, 2024, doi: 10.1016/j.foodres.2024.113968.

[55] Y. Ma, M. Schlangen, J. Potappel, L. Zhang, and A. J. van der Goot, “Quantitative characterizations of visual fibrousness in meat analogues using automated image analysis,” *J. Texture Stud.*, vol. 55, no. 1, pp. 1–12, 2024, doi: 10.1111/jtxs.12806.

5.5 Supplementary Information

5.5.1 RFT processing of sagittal MRI images of pH-shifted SPC extrudate.

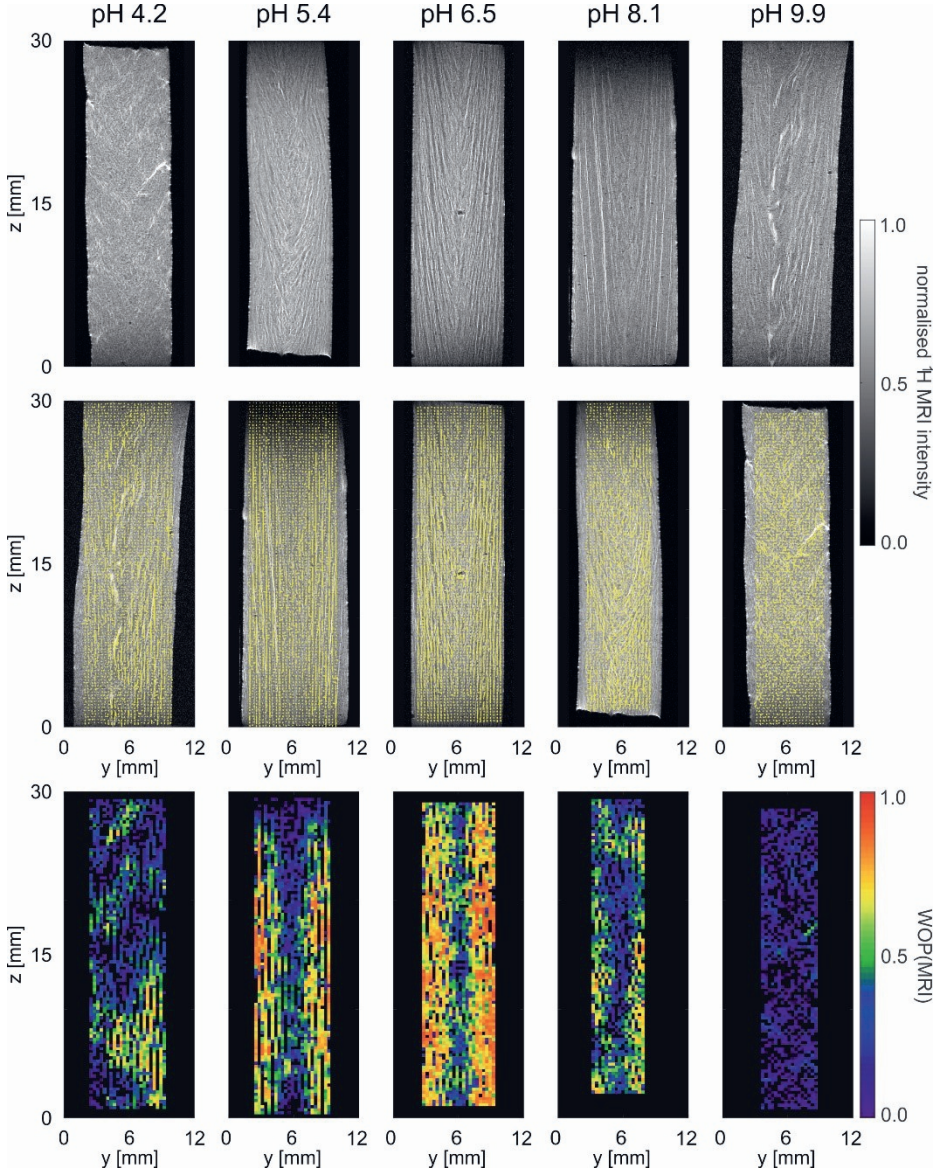

Fig. S5.1: *Rotational Fourier Transform (RFT) processing of MRI data. (top) Sagittal MRI images of pH-shifted SPC extrudates. (middle) Vector map quantification of MRI images, the length of vectors corresponds to the intensity weighing obtained from RFT analysis. (bottom) Weighted Order Parameter (WOP) maps calculated using a neighbourhood size of 5 vectors. Averages shown in Fig. 5.2B are the mean WOP obtained from the WOP map and the error is the standard deviation between the datapoints.* [28]

5.5.2 Protein extractability data

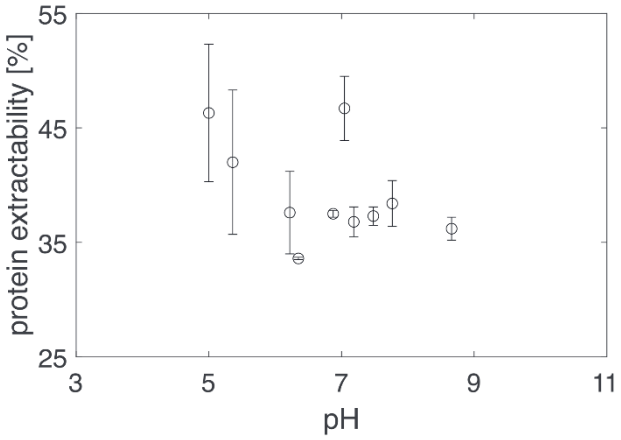

Fig. S5.2: *Size exclusion chromatography derived protein extractability results using non-reducing denaturing buffer consisting of Phosphate, SDS and Urea (PSU) for extracting non-covalently bound proteins. An extraction using reducing denaturing buffer containing PSU and DTT was used for extracting both covalent and non-covalently bonded proteins and is used for normalisation to 100% extraction. Error bars are from repeated extractions on the same freeze-dried SPC sample. The complete protocol is described elsewhere* [27].

5.5.3 SANS sector averaging and intensity profile

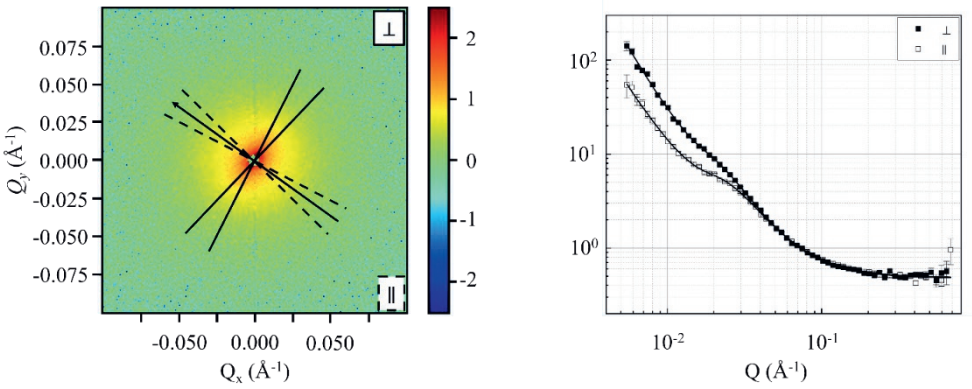

Fig. S5.3: *2D SANS data (scattering intensities are on logarithmic scales) (left) and sector averages taken in the directions parallel (∥) and perpendicular (⊥) to the shear (right) for extrudate at pH = 5.63. Black arrow (left) indicates extrusion direction. Lines (right) represent the fit with the broad peak model to the SANS data* [13].

5.5.3 Lab-scale and pilot-scale process conditions during pH-shifting

Table S5.1: Table containing extruder process conditions used to produce pH-shifted SPC extrudates. SME values were calculated by the extruder's software during extrusion. Values displaying a range indicate the variation seen during pH-shifting as a result of changing melt properties. To calculate residence times, an average protein melt viscosity of 1300 kg/m^3 has been used.

Process parameter	Xtrutech XTS19	Bühler Polytwin 44
L/D ratio [-]	25	34
Throughput [kg/h]	5	57.5
Screw speed [RPM]	300	250
End plate pressure [bar]	4 - 15	20 - 25
Specific mechanical energy [kJ/kg]	40 - 60	115 - 130
Free barrel volume [L]	0.15	1.76
Cooling die length [mm]	300	1200
Cooling die volume [L]	0.036	0.50
Barrel residence time [s]	120	165
Cooling die residence time [s]	30	40

5.5.4 Photographs of torn extrudate samples

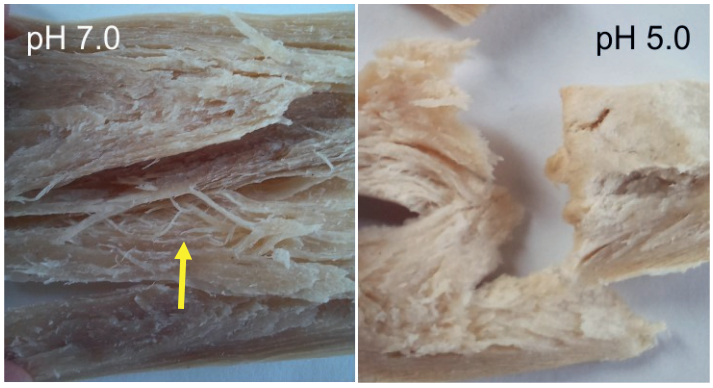

Fig. S5.4*: Images of frozen and thawed SPC extrudate extruded at pH 7 (left) and pH 5 (right) after performing a fold test similar to Ma et al. (2024)* [55]*. The pH 7 sample shows that, upon tearing, a fibrous structure (yellow arrow) is visible which corresponds to the distinct lamellar phase separated structure seen in Fig. S5.1. In the pH 5 sample the fibrous structure is less apparent which corresponds the isotropic phase-separated structure shown in Fig. S5.1.*

5.5.5 WAXD and DSC results of non-hydrated protein concentrates and isolates

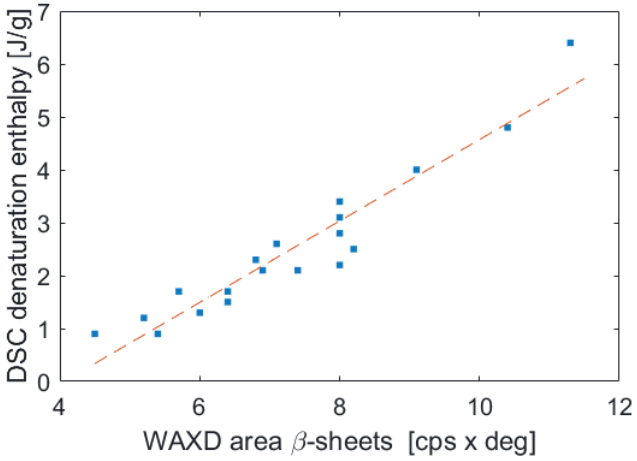

Fig. S5.5: *DSC denaturation enthalpy versus the area of WAXD peaks characteristic for β-sheet secondary structure. Results are presented for non-hydrated commercial soy and pea protein isolates and concentrates.*

Chapter

6

MRI velocimetry during high-moisture extrusion: probing wall-slip and yield stress of soy protein concentrate

Chapter in preparation as:

Kuijpers, S.A.; Vergeldt, F.J.; Gobes, M.I.; Philippi, J.; Hohlbein, J.; Van Duynhoven, J.P.M.; Terenzi, C. MRI velocimetry during high-moisture extrusion: probing wall-slip and yield stress of soy protein concentrate

Abstract

To enable the rational design of meat alternatives based on high-moisture extrusion (HME), involving temperatures up to 160 °C and pressures around 10 bars, a robust *in situ* experimental characterisation of this process is required. The role of the extruder cooling die is particularly critical for structure formation in plant-protein extrudates. Considerable research efforts have been devoted to *in silico* modelling the flow behaviour of the protein melts inside the extruder cooling die. Yet, the required parametrisation of wall-slip and rheological properties of such melts remains limited by the lack of robust *in situ* experimental data. Thus, the multiscale structure formation mechanisms during HME are, still to date, under debate. To overcome this bottleneck, we performed spatially-resolved low-field MRI velocimetry measurements during benchtop extrusion of a hot protein melt, from soy protein concentrate (SPC), inside a custom-made MRI-compatible cooling die. To influence the flow behaviour during extrusion, pH-shifting was applied. The spatially-resolved velocity profiles could be well described by an adapted Herschel-Bulkley model, which accounted for wall-slip and dependence of the dynamic yield stress upon temperature, pH and the distance from the cooling die walls. These results provide unique insights into the cooling die flow during HME of plant-proteins and will enable parametrisation of models for wall-slip and dynamic yield stress.

6.1 Introduction

In many western countries, there is an increasing awareness of the environmental burden posed by the large-scale meat production and, as a result, there is a growing shift towards diets centred around plant-based products [1, 2]. For consumers to embrace a transition towards a plant-based diet, these meat-alternative products should mimic the sensorial perception of animal meat [1, 3]. High-moisture extrusion (HME) is the current dominant technique to produce fibrous materials from commercially available plant-protein flours, concentrates or isolates, mostly originating from soy. [4–6]. In HME, protein and water are mixed and subsequently subjected to high thermal-mechanical energy supplied by a heated barrel section with two co-rotating screws [6, 7]. As depicted in Fig. 6.1, upon cooling of the protein melt inside the extruder cooling die, concomitant solidification and phase separation into protein-rich and water-rich domains occurs [6, 8]. The high shear forces in the cooling die promote the appearance of an anisotropic lamellar phase-separated structure [6, 9, 10]. The flow behaviour of the protein melt inside the cooling die, and the underlying rheology, have been identified as a key step for understanding the fibrous structuring of plant protein-based extrudates [6].

To elucidate this structuring mechanism, *in silico* models have been developed that describe the flow behaviour of a hot protein melt through the extruder cooling die. In the works from Sandoval Murillo *et al.* (2019) and Kaunisto *et al.* (2024) respectively a material-point- or finite-element-model, based on spinodal decomposition, was used to study phase separation [9, 11]. In the work of Wittek *et al.* (2021) numerical flow simulations were used to derive flow characteristics, such as shear stress, temperature, velocity and viscosity [12]. These models assumed a no-slip boundary condition between the protein melt and the cooling die wall during flow. However, in the work of Van der Sman & Van der Goot (2023) it was suggested that significant slip occurs at the cooling die wall, resulting in plug flow behaviour [6]. This would occur once the protein melt is solidified and the yield stress of the melt surpasses the shear stress applied at the cooling die wall. More recently, Högg *et al.* (2025) and Kaunisto *et al.* (2026) introduced wall-slip into their cooling die flow models and obtained estimated values through inverse modelling [13, 14]. The latter work also incorporated the effect of different cooling die temperatures on the cross-sectional flow velocity profile of the hot protein melt. As schematically depicted in Fig. 6.1, these works generally find that a bell-shaped velocity profile is present at the start of the cooling die. The material cools close to the cooling die wall and starts to act like a plug that slips along the inner cooling die wall with a uniform velocity over the die's cross section [13, 14]. Simulations by Kaunisto *et al.* (2026) showed that the hot protein core flows faster than the cooler solidified material close to the cooling die wall, which has been identified as the possible mechanism behind the characteristic V-shaped lamellar structure seen in extrudates (see Fig. 6.1) [14]. Furthermore, in the work of Högg *et al.* (2025) it was shown

that, with the onset of wall-slip, the cross-sectional velocity profile remains uniform, thus indicating plug flow behaviour [13]. In the latter work, however, wall-slip values and rheological properties of the protein melt were estimated from inverse modelling, but not experimentally determined. To enable parametrisation of models predicting flow in the cooling die, robust experimental assessment of wall-slip and of rheological behaviour of the protein melt at different temperatures is necessary. For this purpose, closed-cavity rheometry (CCR) experiments have been performed to estimate the bulk rheological behaviour of these protein melts [9, 12, 15, 16]. Such measurements, performed under steady-state conditions, indicate that plant-protein melts exhibit yield stress behaviour [17] governed by the ratio T_g/T [18, 19]. Here T_g is the moisture-dependent glass transition temperature of biopolymers which can provide a measure for the hydrogen bond density therein [20]. While these results provide insight in the bulk rheological behaviour of protein melts, they cannot be used for directly predicting flow in the cooling die, due to the closed-cavity shear geometry and the oscillatory nature of CCR measurements. To date, quantitative experimental characterisation of flow in the cooling die is still missing.

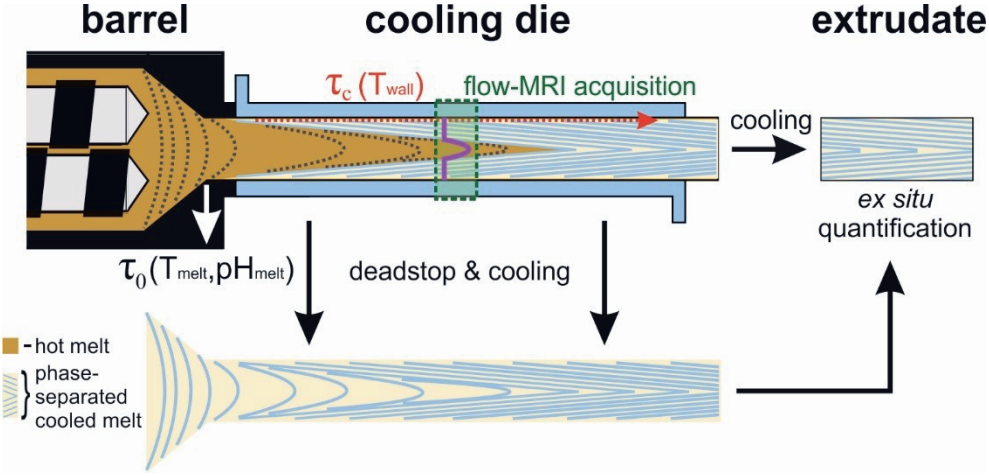

Fig. 6.1: *Diagram depicting the current hypothesis on phase-separated lamellar structure formation inside the cooling die. In the barrel section, µm-scale alignment of protein fibrils is already present in the hot protein melt (dashed grey). The yield stress, τ_0, depends on the melt temperature, T_{melt}, and pH. Upon entering the cooling die, the hot protein melt (brown) cools, solidifies and lamellar phase separation occurs (yellow/blue). When the critical shear stress, τ_c (red), dependent on the cooling die wall temperature, T_{wall}, is reached, wall-slip starts. As the protein melt solidifies the lamellar flow will transition to a plug flow profile (magenta). Upon performing a dead-stop and rapidly cooling the extruder, the ribbon inside the cooling die and final section of the barrel show a spatially-dependent lamellar structure. The green dashed area represents the active measurement volume of the flow-MRI platform.*

In the work of Kaunisto *et al.* (2024) a tracer colourant was used in combination with an extruder dead-stop for visualising the flow profiles, but this method is not well suited to quantify wall-slip and only provides an inaccurate view on the velocities inside the protein melt [9]. A Pulsed Ultrasound Velocity (PUV) method was used to acquire velocity profiles *in situ*, which could be used to improve model accuracy [14]. Yet, whilst PUV is able to semi-quantify the velocity profiles of the protein melt, its experimental constraints in terms of signal scattering make this technique unsuitable to characterise flow properties at the core of the protein melt, or for spatially resolving velocities close to the cooling die walls [21]. The latter properties are critical for characterising the rheological behaviour of the protein melt.

In this work, we used Magnetic Resonance Imaging (MRI) velocimetry, which is an established technique to quantify flow properties of complex fluids in chemical and food processing [22, 23]. MRI poses the advantage of providing quantitative velocity maps even for optically-opaque systems, provided that non-magnetic flow platforms are used. If the pressure drop over the measured sample region is known, local rheological properties and wall-slip can be quantitatively determined *in situ*. We used a benchtop extruder, equipped with a custom-built MRI-compatible cooling die, suited for use with compact low-field MRI equipment, for *in situ* measurements of protein melt velocities. The extruder cooling die was constructed according to the following design constraints: (i) be radiolucent, i.e. not made out of metal; (ii) able to withstand operating temperatures of up to 160°C for prolonged periods of time; (iii) able to withstand pressures of up to 20 bars at 160°C, (iv) an outer diameter that allows mounting within a magnet; (v) an inner diameter that allows a realistic temperature gradient to establish during cooling; (vi) an outer wall temperature that does not perturb the stability of the magnet used for MRI measurements (vii) enable the measurement of the pressure drop across the cooling die channel. Our flow-MRI platform is then used to study the cooling die flow of a soy protein concentrate (SPC) melt shifted to different pH values, to vary its yield stress response [18]. An adapted Herschel-Bulkley model will be introduced to fit the measured velocity profiles and pressure drop values, and obtain descriptors for the local rheological behaviour and wall-slip of the protein melt.

6.2 Materials and methods

6.2.1 Materials

Commercial soy protein concentrate (SPC, Arcon SJ® IP, 93% DM with 69% protein in dry base, 4% fat, 19% dietary fibre and carbohydrates and 2% ash), from Solae (St. Louis, MO, USA) was used in this work. The acidity and alkalinity of the water feed were adjusted by HCl (Merck, Germany) and NaOH (Merck, Germany), respectively, as described elsewhere [24].

6.2.2 Modelling of material performance and temperature gradient

COMSOL (version 6.4) was used to predict the three-dimensional temperature gradient within the cooling die. The material properties of PEEK were set to a specific heat of 1850 J/(kg·K) and a thermal conductivity of 0.24 W/(m·K). The material properties for the SPC extrudate were set to a density of 1300 kg/m^2, a specific heat capacity of 4400 J/(kg·K) and a thermal conductivity of 0.46 W/(m·K). The inlet temperature was set to 125 °C and the inlet mass flow, or throughput, was set to 1.2 kg/hr. The outer temperature of the PEEK was set to 30 °C to simulate the cooling water.

SolidWorks 2021 was used to verify the heat and pressure resistance of the cooling die. The material properties of PEEK, at 160°C, were set to an elastic modulus of $1.5 \cdot 10^9$ N/m^2 [25] and a yield strength of 20 MPa [26]. For the pressure resistance at 160°C, the finite-element-analysis module for structural simulation was used, applying ambient pressure on all external faces of the design and a pressure of 20 bars. To ensure safe use, the assessed pressure on the internal faces was twice the pressure expected during operation. The Von Mises stress was simulated by the software and a safety factor, defined as the ratio between the material's maximum strength and the applied stress, was calculated.

6.2.3 High-moisture extrusion

A benchtop co-rotating twin-screw extruder (Process 11, ThermoFisher Scientific, Germany) with a screw diameter of 11 mm and length-to-diameter (L/D) ratio of 40 was used. The Process 11 High-Moisture Meat Analogue (HMMA) screw configuration was used. The extruder was equipped with the stock polymer melt exit block which ends in a screw-hole to allow attachment of nozzles. A custom designed steel adapter, ending in a 50 mm flange, was screwed into the exit block to allow attachment of a custom cooling die. As schematically depicted in Fig. 6.2, a custom designed cylindrical cooling die, with a 10 mm outer diameter, 4 mm inner diameter and 210 mm length, made of PEEK, was securely attached to the adapter using a flange clamp. SolidWorks drawings of the custom developed parts can be found in Fig. S6.1 in the SI.

The extruder barrel section is divided into eight temperature-controlled zones, respectively heated to 40 °C, 60 °C, 80 °C, 100 °C, 130 °C, 160 °C and 160 °C in zones 1 to 7. The barrel exit temperature was set to 150 °C. The PEEK cooling die was maintained at a temperature of 30 °C, which is equal to the operating temperature of the low-field magnet. Extrusion was performed using tap water, and pH-shifted extrudates were obtained at pH 5.9 and 8.6, respectively, by changing the liquid feed to 0.1 M HCl or 0.1 M NaOH [24]. The extrusion trials were run at a screw speed of 400 RPM and at a moisture content of ca. 65%. The throughput was maintained at 1.0 kg/h.

Extrudates were collected from the cooling die outlet after reaching a steady-state, as indicated by constant process responses in the barrel exit pressure and melt temperature. The extrudates were put in a zip-lock bag and, thereafter, frozen and stored at -18 °C. The pH of the extrudate was measured after thawing and cutting 1.5 g of sample in roughly 2 mm sized pieces. The sample pieces were placed in 5 mL of 0.75% KCl solution for two hours while stirring, and thereafter measured by a pH-meter. Each sample was measured in duplicate. The pH of the extrudate was assumed to be similar to the pH of the protein melt within the cooling die.

6.2.4 Low-field MRI velocimetry

Flow-MRI setup and measurements

Flow-MRI measurements were performed on a 0.55 T (23.4 MHz for ^{1}H) Magspec compact MRI system (Pure Devices, Germany) with a 10 mm magnet bore size and controlled through a drive control system with an integrated magnetic field gradient amplifier of 0.25 T/m (Pure Devices, Germany). The magnetic field was generated by permanent NdFeB magnets arranged in an H-yoke with a total weight of ∼18 kg. The size of the magnet housing was 27 x 25 x 14 cm. The radio-frequency (RF) pulses were generated using a RF-100 Amplifier system (Pure Devices, Germany). The Magspec spectrometer is operated through an openMATLAB interface designed by Pure Devices, version R1396.

One-dimensional (1D) ^{1}H MRI velocimetry profiles were acquired using an in house developed spin-echo pulse sequence with a two-step phase cycle. In order to measure the 1D velocity profiles in the PEEK cooling die, we used all three available magnetic field gradients of the spectrometer as outlined in the pulse diagram in Fig. S6.2 in the SI. The acquisition parameters were as follows: echo time, T_E = 17 ms; repetition time, T_R = 1 s; RARE-factor of 2; number of averages, N_{avg} = 2; FOV in the x-direction of 10 mm^2 with spatial resolution of 78 µm and a 1 mm slice thickness in the z-direction taken through the middle of the cooling die (see Fig. 6.2G).The motion encoding pulsed field gradients (PFG), in the y-direction, were set with the following parameters: δ = 2 ms, and Δ = 10 ms and a +16 mT/m or -16 mT/m PFG strength which was alternated between acquisitions. A total of 17 acquisitions were performed per measurement, consisting of 16 measurements with

positive or negative PFG strength and one reference acquisition with null gradient. An example of two such acquisitions, one positive and one negative PFG, is presented in Fig. S6.2 in the SI. A single flow-MRI measurement consisted of one pair of acquisitions using a negative and positive PFG strength. Measurement sets were repeated four times per extrusion setting, resulting in a total of 32 individual flow measurements. The flow-MRI measurements were performed when the extruder was running in steady-state.

Flow-MRI data analysis

^{1}H flow-MRI data processing and fitting of velocity profiles was performed in MATLAB R2022b. In house scripts for automated data processing, such as signal normalisation, masking of imaging background and data exporting, were written using either standard MATLAB functions or functions provided by the Image Processing Toolbox version 11.6 and Curve Fitting Toolbox version 3.8 from MATLAB. To account for the measurement noise due to the low magnetic field strength, 10% of acquisitions, where the largest effect of noise is observed, were removed before further processing of the data. The remaining flow data was averaged, and a standard error was determined for all datapoints within each spatially-resolved velocity profile. This standard error was used as a reference for masking of the background noise outside the 4 mm cooling die flow channel.

Fitting of the flow profiles was performed in MATLAB using an in house script from [27], which has been adapted to incorporate wall-slip and a semi-empirical expression of the dynamic yield stress accounting for the T_g/T ratio [18].

6.2.5 High-field MRI

MRI sample preparation

A frozen extrudate ribbon, approximately 3 cm long, was swollen in demineralised water overnight (ca. 17 h) at room temperature in a 15 mL centrifuge tube, using a water:sample weight ratio of 15:1. Air bubbles were removed from the sample by placing the tube in a vacuum desiccator for 20 minutes. After swelling, excess moisture was removed from the outer surface of the extrudate using a paper towel. The sample was placed in a 10 mm NMR tube and sealed with parafilm to prevent water evaporation during high-field MRI measurements.

MRI imaging procedure

^{1}H MRI RARE measurements were performed using a 600 MHz (14 T) wide-bore spectrometer (Ascend 600WB, Avance NEO, Bruker, Germany) equipped with a 1.5 T/m imaging gradient system (Micro 2.5, Bruker, Germany) and a 10 mm diameter ^{1}H-^{13}C cryogenic probe (CP2.1 MIC, Bruker, Germany). The measurements were performed using Paravision 360 version 3.6.

Sagittal T_1- and T_2-weighted MRI images of SPC extrudates were measured using the RARE sequence [28]. Acquisition parameters were set as follows: T_E = 16 ms; T_R = 1 s; RARE-factor of 2; N_{avg} = 4; slice thickness of 0.5 mm at the centre of the sample; FOV of 25 x 10 mm^2; in-plane MRI resolution of 20 x 20 μm^2 with a total measurement duration per RARE image acquisition of 17 min.

MRI data analysis

^{1}H MRI data processing and image analysis was performed in MATLAB R2022b. To read raw MRI data from Paravision version 3.6, the pvmatlab package by Bruker was used. In house scripts for automated data processing, such as signal normalisation, background masking and exporting data, were written using either standard MATLAB functions or functions provided by the Image Processing Toolbox version 11.6 and Curve Fitting Toolbox version 3.8 from MATLAB.

6.3 Results and discussion

6.3.1 Design of the flow-MRI platform

A diagram of the *in situ* flow-MRI platform is shown in Fig. 6.2A-G, and a SolidWorks model of the in house developed parts can be found in Fig. S6.1 of the SI. We selected a spectrometer with a magnet that was compact enough to be able to work alongside a benchtop extruder with a magnet bore that could be positioned horizontally. The limited weight of the magnet (18 kg) and workable magnet bore size of 10 mm allowed placement over a cooling die with the same outer diameter. As the permanent magnet does not require cryogenic fluids its inner bore magnet could be placed horizontally without negatively affecting the functionality of the magnet. The outer diameter of the cooling die was designed to match the bore size of the compact MRI magnet (see section 6.2.4) used in this work. These considerations, and the design constraints (i-vii) listed in the introduction, were taken as starting points for designing a cooling die that could be inserted in the bore of the low-field magnet.

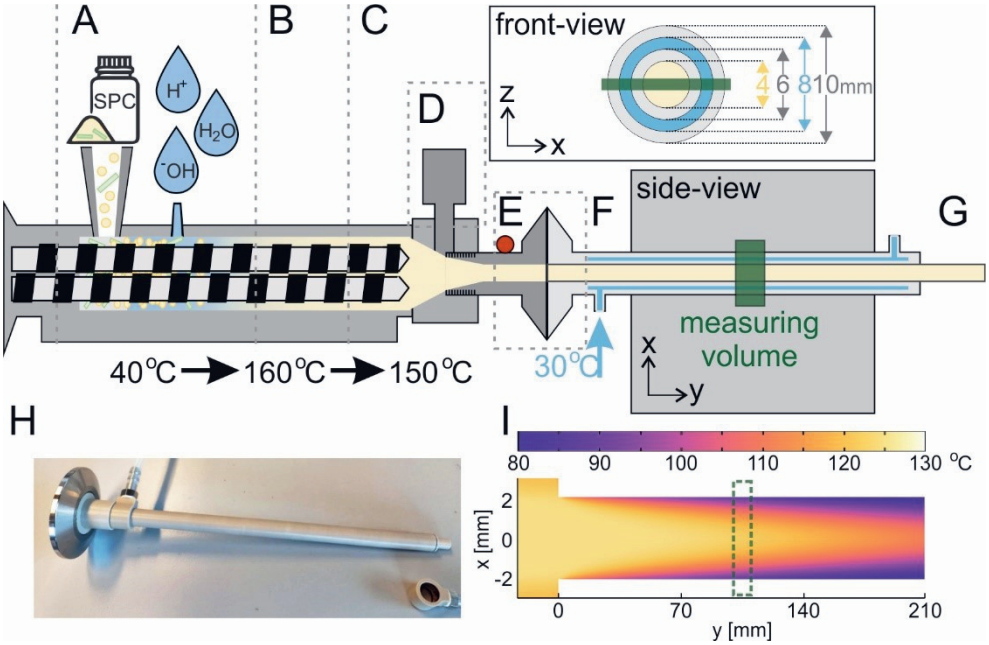

Fig. 6.2: *Diagram of the Process 11 extruder and in house developed cooling die. (A) Powder and liquid inlets. (B) Segmented heated barrel section. (C) Heated barrel exit. (D) Sensor measuring melt pressure and temperature. (E) In house developed steel flange. The red circle indicates the location of a multimeter temperature sensor measuring the die temperature. The flange and cooling die are held together by a flange clamp. (F) In house developed PEEK cooling die featuring a 4 mm circular channel for material flow and a 1 mm thick cooling mantle with cooling water maintained at 30 °C. The grey and green squares respectively indicate the location of the magnet and MRI measurement volume. The rectangular panel above shows a front view of the cooling die with the imaging slice highlighted in green and the dimensions of the cooling die channel, namely, protein melt channel (yellow), PEEK walls (grey), water channel (blue). (G) Cooling die exit and sampling location of extrudate. (H) Photo of the finalised PEEK cooling die. (I) Model prediction of temperature distribution across the cooling die.*

PEEK was selected as the material for the construction of an MRI-compatible cooling die because (i) it is a radiolucent thermoplastic and (ii) it withstands operating temperatures of up to 250 °C [29, 30]. The requirements of (iii) safe operation at pressures of 20 bars and (iv) a 10 mm maximum outer diameter as imposed by the magnet bore size, were satisfied by a cooling die geometry with 1 mm thick inner and outer PEEK walls comprising a 1 mm wide cooling water channel (Fig. 6.2F). The finite-element-analysis simulation performed in SolidWorks, using the material properties of 1 mm thick injection-moulded PEEK walls, predicted safe usage, with a safety factor of 9, for the PEEK cooling die operating at 160 °C and at pressures of 20 bars. A consequence of these design constraints was that the effective inner diameter of the cooling die had to be reduced to 4 mm (Fig. 6.2F). In order to estimate whether (v) a realistic temperature gradient, similar to gradients encountered in a conventional steel cooling die, would establish during passage of the cooling die, a mass and heat transport model was built in COMSOL. By using the thermal and rheological properties

of the protein melt [18], and the PEEK properties [31], the heat exchange between the cooling water and hot protein could be modelled using an entry temperature of 125 °C, similar to the inlet temperature of our HME setup (Fig. 6.2E).

As shown in Fig. 6.2I, at the cooling die exit, a temperature of ~80 °C was estimated at the wall and roughly ~110 °C in the protein melt core. Upon entering the sensitive region of the low-field instrument, along the length of the cooling die, the melt temperature at the wall will have decreased from 125 °C to 95 °C, whilst in the core it will have decreased to roughly 115 °C. Thus, during flow-MRI measurements, a cross-sectional temperature gradient was established within the 4 mm channel of the cooling die.

The heat and mass transport model also showed that (vi) the outer wall temperature of the cooling die could be maintained at the operating temperature of the permanent magnet, thus causing no drift in the magnetic field intensity (data not shown). In order to (vii) separately measure the pressure drop over the cooling die channel, required for obtaining local rheological properties from the velocity profiles, the pressure sensor at the barrel exit was used. The pressure drop was measured between the barrel exit (Fig. 6.2D) and the run-off of the extruder at ambient pressure. Initial designs included a modular system to incorporate a separate pressure sensor in the cooling channel as shown in Fig. S6.1 in the SI, but inclusion proved to compromise measurement of the velocity profiles and the acquired pressure values were nearly identical to the pressure values measured at the extruder barrel exit (See Fig. S6.3 in the SI). A picture of the constructed cooling die is shown in Fig. 6.2H.

6.3.2 *In situ* flow-MRI of a soy protein concentrate during HME

Validation of the in house developed pulse sequence was performed by placing a silicon tube of flowing water next to a sealed NMR tube of static water in the measurement volume, as shown in Fig. S6.4 in the SI. The tube containing static water showed null velocity. The flowing water showed a laminar profile with velocity values of close to zero at the wall and 17.5 mm/s in the centre, consistent with the calculated volume of water flowing through the silicon tube during the MRI acquisition time.

In Fig. 6.3, *in situ* flow velocimetry results of pH-shifted SPC during HME are shown. We note that, due to the high velocity of the cooling water, the cooling channel is not visible in the flow profile. The barrel exit temperature (Fig. 6.2C) was set to 150 °C and the actual melt temperature was measured at 145 °C for each pH setting (Fig. 6.2D). With the multimeter temperature sensor, shown in Fig. 6.2E, a temperature of (125 ± 1) °C was measured for each pH setting. The pH was shifted to pH 5.9, pH 7.1 and pH 8.6 and resulting barrel exit pressures were respectively measured at 6, 6 and 4 bar.

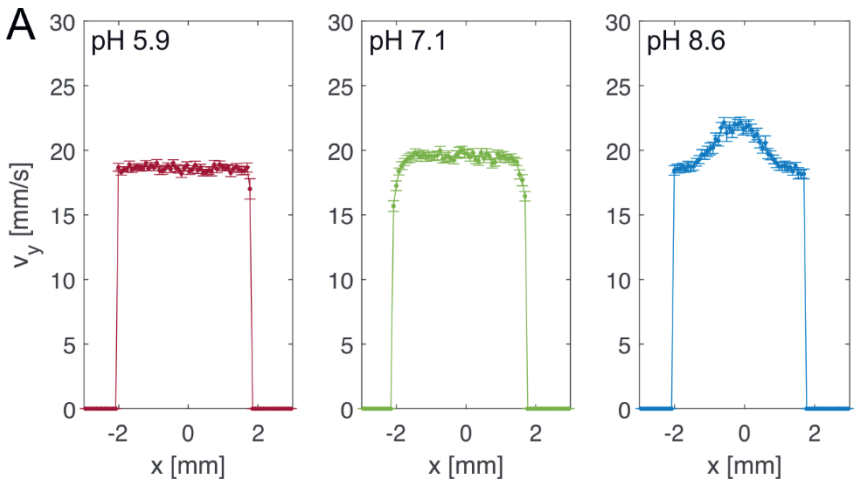

Fig. 6.3: *In situ MRI velocimetry results with T_{exit}= 150 °C. Velocity profiles as function of extrudate pH during extrusion. The predicted velocity based on extruder throughput and dimensions is 19 mm/s. The error bars represent the standard error (N = 28).*

At pH 5.9, a flat plug-like flow profile is observed in Fig. 6.3 with a velocity of (18.6 ± 0.3) mm/s (N = 28). This velocity value is close to the predicted velocity of 19.0 mm/s, as calculated from the extruder throughput and cooling die dimensions. This indicates that the applied stress at the barrel exit was insufficient to result in a sheared flow of the protein melt. The material passing through the MRI measurement volume was, thus, already solidified and the measured velocity is the wall-slip velocity of a plug. At pH 7.1, a mostly flat flow profile is observed with a mean velocity of (20.8 ± 0.5) mm/s (N = 28) between x = -1.7 and x = 1.3 mm. Here, close to the cooling die wall, a slower velocity is observed, starting at (16.1 ± 0.4) mm/s (N = 28) and sharply increasing to the mean velocity over a distance of 0.4 mm from the cooling die wall towards the centre of the cooling die channel. The appearance of the flow profile is similar to the Herschel-Bulkley flow of a non-Newtonian fluid. At pH 8.6, a bell-shaped centre of the flow profile is observed, whereas the edges near the cooling die wall appear mostly flat. The mean velocity of the flow profile is (19.5 ± 0.6) mm/s (N = 28) with a flow velocity of (18.5 ± 0.3) mm/s (N = 28) near the wall and (22.1 ± 0.4) mm/s (N = 28) at centre of the cooling die channel. The shape of this profile is similar to the simulated velocity profiles shown in Högg *et al.* (2025) and Kaunisto *et al.* (2026), that also show a superposition of a plug and bell-shaped velocity profile [13, 14].

6.3.3 Temperature-dependent Herschel-Bulkley model

The flow velocity profiles shown in Fig. 6.3 were fitted with an adapted Herschel-Bulkley model which includes a temperature-dependent dynamic yield stress $\tau_0(T)$ and a contribution of wall-slip, v_{slip}. A semi-empirical relation was used for the yield stress [18]:

$$log_{10}\left(\tau_0\big(T(x)\big)\right) = 27 \cdot T_g/T(x) - 0.038 \cdot pH - 10.2. \qquad \text{Eq. 6.1}$$

Here, T_g is the glass transition temperature of the protein melt, which was estimated to be ~165 K at a moisture content of 65% [18]. The pH pertains to the protein melt and T(x) is the spatially-dependent temperature of the protein melt. Since this yield stress was determined from steady-state measurements under flow, the relation pertains to the *dynamic* yield stress of the material. This is defined as the stress required to keep the material flowing, as opposed to the stress required to initiate flow from a static condition.

As shown in Fig. 6.2I, a three-dimensional temperature gradient, *i.e.* along the extrusion direction (y) as well as cross-sectional to the cooling die (x), establishes within the protein melt inside the cooling die. Such a temperature gradient, alongside gradients in the moisture distribution inside the protein melt, affect the local T_g/T ratio, and thus, local viscosity and dynamic yield stress [6, 18]. The parameter T_g/T has been shown to correlate linearly with the NMR T_2 values for carbohydrate solutions with $T_g/T < 1$, *i.e.* when the protein melt is in the rubbery state [32]. A confirmation for the presence of a cross-sectional gradient of T_g/T was provided by spatially-resolved T_2 NMR relaxation measurements, performed *in situ* directly after a dead-stop operation (See Fig. S6.5 in SI). This showed a roughly bell-shaped T_2 distribution along the cross-section of the cooling die. Thus, the temperature relation in Eq. 6.1 was made spatially-dependent using a parabolic temperature gradient, based on Fig. 6.2I, Fig. S6.5 in the SI and results by Högg *et al.* (2025), and included as a fitting parameter [13]. The following expression for the spatial temperature dependence was used:

$$T(x) = T_{core} - \left(\frac{T_{edge}}{w^2}\right)x^2, \qquad \text{Eq. 6.2}$$

with T_{core} and T_{edge}, respectively, the temperature at the core and edge in Kelvin of the protein melt, *w* the width of the cooling channel, namely 2 mm, and x the position along the cross-section of the cooling die.

The adapted HB model, used for fitting flow velocity profiles shown in Fig. 6.3, is thus:

$$v(x) = \begin{cases} v_{slip} + \int \left[\dfrac{\Delta P x/2L - \tau_0\big(T(x)\big)}{A}\right]^{1/n} dx, & \tau > \tau_0; \\ v_{slip} = C, & \tau > \tau_0. \end{cases} \qquad \text{Eq. 6.3}$$

Here, v(x) is the velocity acquired from flow-MRI measurements, and ΔP the pressure drop between the sensor and the cooling die exit with total distance, L = 0.235 m. These parameters are used to derive rheological properties of the protein melt, namely, the temperature-dependent dynamic yield stress, $\tau_0(T(x))$, the proportionality constant, A, with units $Pa \cdot s^{1/n}$ and the dimensionless power law index, n. When the stress applied to the protein melt is below the yield stress, a plug flow profile is observed with constant velocity. The velocity profiles of the SPC extrudates shifted to pH 7.1 and pH 8.6 were fitted in two steps. Firstly, a fit was performed using all five fit parameters (T_{core}, T_{edge}, A, n, v_{slip}). Secondly, the parameters for which the smallest relative fit error were found, namely n and v_{slip}, were fixed, to limit the degrees of freedom of the fit and acquire a better estimate of the remaining fit parameters. The temperature profile was constrained to the 30-160 °C range, between cooling and extrusion temperature. The initial temperature value of the fit was set to 125 °C and 90 °C, respectively for the melt core and at the wall, based on temperature measurement (Fig. 6.2F) and Fig. 6.2I. Values for A were set to $10 \cdot 10^3$, for both pH 7.1 and pH 8.6. The initial value for n was set to 0.54, based on Gobes *et al.* (2026) [18] and v_{slip} was set the lowest velocity value in the profile data, respectively 17 mm/s and 18.5 mm/s for pH 7.1 and pH 8.6. Fit results were used to estimate the dynamic yield stress at the cooling die wall, $\tau_{0,wall}$, and are shown in the bottom right corner of Fig. 6.4A for the extrudates at pH 7.1 and pH 8.6. The plug-flow profile at pH 5.9 was fitted by calculating a root-mean-square-error (RMSE) of the data with respect to v_{slip} values between 18 and 19 mm/s. The v_{slip} with the smallest RMSE was selected.

In Fig. 6.4A, the fitted velocity curves are shown along with their respective 95% confidence interval (shaded area). Fig. 6.4B shows the *ex situ* high-field MRI images of the respective extrudates produced during the HME run performed for the flow measurements. The obtained values for the fitted parameters are shown in Fig. 6.4C. We note that the dynamic yield stresses of the protein melt calculated at the wall, roughly 13 kPa for pH 7.1 and 4.8 kPa for pH 8.6, are in the same order of magnitude as found by Högg *et al.* (2025) and Gobes *et al.* (2026) [13, 18].

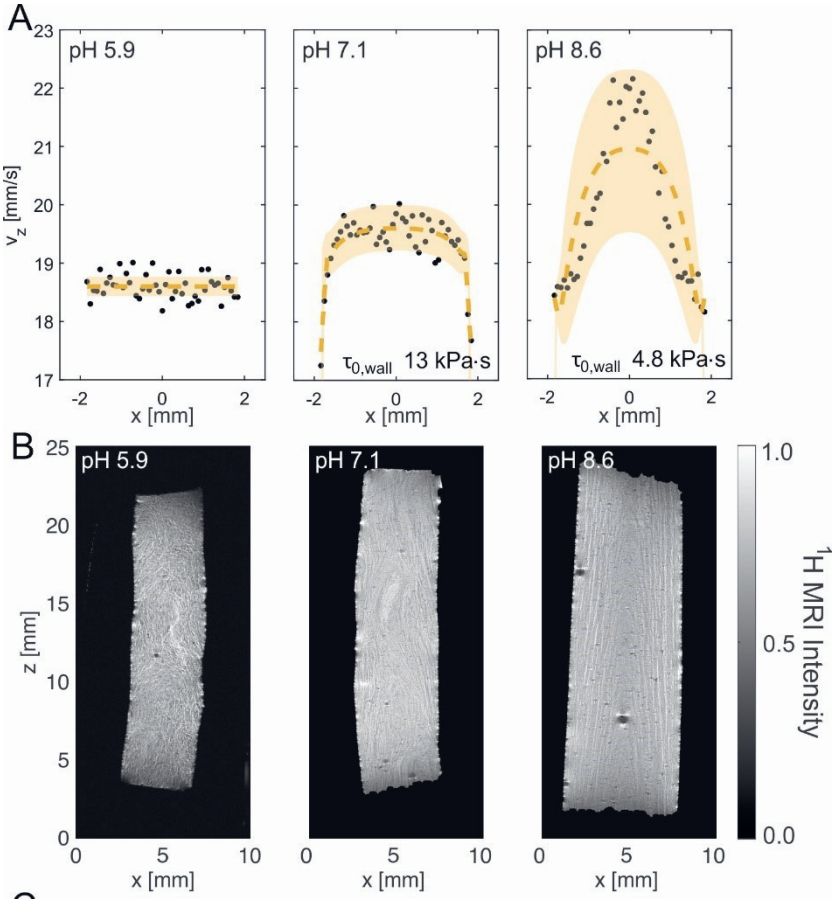

C

Fit parameter	pH 5.9	pH 7.1	pH 8.6
T_{core} [°C]	-	108 ± 12	111 ± 32
T_{edge} [°C]	-	89 ± 14	82 ± 38
A [$(kPa \cdot s)^{(1/n)}$]	-	3.5 ± 0.5	0.7 ± 0.1
n [-]	-	0.6 ± 0.1	0.64 ± 0.06
v_{slip} [mm/s]	18.6 ± 0.2	19.2 ± 0.4	18.2 ± 0.6

Fig 6.4: *Temperature-dependent HB model fit results. (A) MRI velocimetry profiles for SPC extrudates shifted to pH 5.9, 7.1 or pH 8.6 from Fig. 6.3A. The yellow dashed lines represent the fitted flow profiles with the 95% confidence interval as a shaded yellow area. For the pH 7.1 and 8.6 extrudates, the estimated dynamic yield stress of the protein melt at the cooling die wall is displayed. (B) HF cryo-probe MRI images of extrudates collected during measurements shown in panel A. The MRI resolution is 20 x 20 x 500 µm³. (C) Fit parameter results of secondary HB model fit with a fixed value for n and v_{slip}, acquired in the initial HB model fit performed on all five parameters. The HB model could not be applied to the pH 5.9 extrudate as it shows only plug flow. The wall-slip is calculated for this extrudate by linear least squares fitting.*

At pH 5.9, where the yield stress of the protein melt is high [18], plug flow was observed, indicating that the shear stress was insufficient to achieve laminar flow. A v_{slip} of (18.6 ± 0.2) mm/s was calculated, as shown in Fig. 6.4A and C. The MRI image of the corresponding extrudate (Fig. 6.4B) shows a phase-separated structure without a clear anisotropic orientation along the extruder flow direction. These imaging results are consistent with those previously obtained, for SPC extruded at lab-scale, using a similar acidic pH [24].

At pH 7.1, fit results in Fig. 6.4C yield T_{core} =(108 ± 12) °C and T_{wall} = (89 ± 14) °C, close to the respective predicted values of ∼120 and ∼95, shown in Fig. 6.2I. The HB power-law index, n, expected to be below 1 for a shear-thinning yield stress fluid, is calculated to be roughly (0.6 ± 0.1), and is in line with values found by [18]. The estimated values for the proportionality constant, A were in the order of what was found by CCR measurements, namely between 0.3-15 kPa·$s^{1/n}$ at pH values between pH 4-10 [18]. The MRI image in Fig. 6.4B shows aligned lamellar phase separation oriented along the flow direction of the extruder at the edges of the extrudate and a more heterogeneous structure in the centre of the extrudate. This observation is in line with the flow profile shown in Fig. 6.3 and Fig. 6.4A, where a velocity gradient is observed near the cooling die walls yet the velocity profile is flat in the core of the protein melt. Near the cooling die walls, the critical shear stress is reached and the material experiences sheared flow, resulting in the alignment of the phase-separated regions along the flow direction. Concomitantly, at the centre of the protein melt, the applied shear stress is insufficient for flow of the protein melt. As a result, the material solidifies and phase-separates in a spatial isotropic manner.

At pH 8.6, a similar T_{core} and T_{wall} are found compared to the pH 7.1 extrudate, which is expected when the thermal parameters during extrusion remain constant between extrudates. Additionally, a similar value for n, of (0.64 ± 0.06), is found. The value for A, namely (0.7 ± 0.1) kPa·$s^{1/n}$, is noticeably lower than for the extrudate at pH 7.1 which is in line with results in [18] that show a decreasing dynamic yield stress when pH increases. Li *et al.* 2026 showed that, with increasing pH, the complex viscosity of the protein melt decreases [33]. This coincides with the barrel exit pressure of 4 bar, which is 33% lower compared to pH 7.1, indicating a corresponding decrease in viscosity. The reduced viscosity of the protein melt corresponds with a lower yield stress, resulting in the flow profile observed in Fig. 6.3. A flat profile is observed at the edges of the flow profile with a v_{slip} of (18.2 ± 0.6) mm/s. Close to the cooling die walls, the protein melt has a lower temperature which increases the dynamic yield stress beyond the critical shear stress applied by the protein melt against the cooling die wall, thus resulting in wall-slip [13]. The core of the protein melt, however, is still sufficiently hot with a corresponding decreased viscosity, allowing it to continue flowing [14], thus, resulting in the more aligned lamellar phase-separated structure observed in Fig. 6.4B. Therefore, the flow velocity profile in Fig. 6.4A, shows a superposition of plug and bell-shaped flow velocity profiles. We note that, while individual datapoints fall within the confidence interval of the fit, the deviations appear to

be non-random. . As outlined in Fig. S6.6 of the SI, the fitting approach in this work utilises a model for the temperature-dependent yield stress (Eq. 6.1), which is derived from an *ex situ* study under rotational conditions. Additionally, this model (Eq. 6.1) is based on an interpolation of experimental values acquired at a limited number of pH conditions [18]. Thus, these model parameters may not match the *in situ* conditions used in this work, resulting in non-random deviations between our *in situ* data and the corresponding fit. To improve the accuracy of the fit, the relation between melt temperature and yield stress need to be derived directly from velocimetric data, as outlined in Fig. S6.6 of the SI. Such approach, however, will require an accurate prediction of the temperature gradient in the protein melt in the cooling die during extrusion.

6.3.4 Perspectives: model parametrisation with MRI velocimetry data

The results shown in this work reveal that the developed flow-MRI platform can effectively measure and quantify cooling die flow *in situ*. Velocity profiles could be fitted with an adapted HB model, and rheological parameters were close to those measured or modelled in literature [13, 18].

The velocity profiles shown in Fig. 6.3 reveal a dominant contribution of wall-slip, which has been identified as a key parameter in modelling the flow behaviour of a protein melt through a cooling die [13, 14] but could hitherto not be determined in a direct and accurate manner. Consequently, our *in situ* velocimetric assessment of flow and pressure drops in a cooling die will open up the possibility of further parametrising *in silico* models for both local wall-slip and dynamic yield stress (See Fig. S6.6 in SI). Such parametrised models should then become scalable for cooling die geometry and dimensions and would only need environmental conditions, such as temperature and pressure, to predict flow behaviour.

The current setup is limited to measure the flow profile at a travel distance of 150 mm after the protein melt entered the cooling die. As shown by Fig. 6.4, significant cooling of the protein melt has occurred as indicated by the estimated core and edge temperatures. By increasing the length of the cooling die, different positions could consecutively be measured providing a three-dimensional experimental view on how the flow profile changes as the protein melt progresses through the cooling die. Additionally, by utilising a wider cooling die design, the volume of the protein melt increases and the corresponding temperature gradient will take longer to establish. This will enable more detailed three-dimensional sampling, at the same MRI resolution, of the spatially-dependent effect of temperature on the flow velocity profile. By acquiring three-dimensional velocimetric data of the protein melt in the cooling die, models can be further refined for changes in flow behaviour therein. Such models can then be scaled to accommodate extrusion scales and cooling die geometries that are more industrially relevant.

To enable flow-MRI measurements of such configurations, larger magnet bore sizes are required. The permanent compact magnet used in this work could easily be installed and operated at a benchtop-scale extruder. Larger bore permanent magnets suitable for MRI measurements can weigh tens to hundreds of kilograms [34]. Such magnets will be difficult to install, move and operate at lab- or benchtop-scale extruders. This calls for the use of Halbach array magnets [35] which come at a low-cost and can be scaled to different magnet bore sizes [36], thus offering the opportunity to accommodating cooling dies with different geometries and dimensions.

6.4 Conclusions

The aim of this work was to develop and test a compact low-field flow-MRI platform capable of measuring cooling die flow *in situ*, during HME of SPC. This was achieved by constructing an MRI-compatible custom cooling die for use with a benchtop extruder. With this platform, quantitative velocity profiles could be acquired *in situ* during the operation of the extruder at high temperature and pressures. This allowed for characterising the flow profiles of hot protein melts in a spatially-resolved manner along the cross-section of the cooling die with spatial resolution of 78 µm. Measurements revealed the presence of superimposed plug and bell-shaped velocity profiles, and these profiles could be described by an adapted Herschel-Bulkley model. This model accounted for the effect of the spatial temperature gradient in the protein melt on the dynamic yield stress and wall-slip. The difference in velocity profiles and the underlying rheological parameters of the protein melt at different pH values could be used to explain the differences in phase-separated lamellar structure observed in *ex situ* high-field MRI images of the corresponding extrudates. Our flow-MRI platform will open up the possibility of parametrising models for wall-slip and dynamic yield stress, which is a key step in scaling current *in silico* models to industrial relevant extrusion conditions.

Authors statement

Sam A. Kuijpers: Conceptualisation, Data curation, Formal analysis, Investigation, Methodology, Visualisation, Software, Writing - original draft. Frank Vergeldt: Methodology, Software, Data curation, Writing - review & editing. Martijn I. Gobes: Data curation, Investigation, Software. John Philippi: Methodology. Johannes Hohlbein: Writing - review & editing. John P.M. van Duynhoven: Conceptualisation, Funding acquisition, Resources, Supervision, Writing - review & editing. Camilla Terenzi: Conceptualisation, Funding acquisition, Supervision, Writing - review & editing, Project administration.

Declaration of competing interest

John P.M. van Duynhoven is employed by a company that manufactures and markets plant-based meat alternatives. The other authors declare that they have no known competing financial interests or personal relationships that could have appeared to influence the work reported in this paper.

Acknowledgements

This work is part of the project "Measurement and Modelling of Multiscale Processed Protein Products (MP3)" (with project number 18744) of the research programme OPT TTW, which is financed by the Dutch Research Council as well as contributions from consortium partners Unilever, Cargill, dsm-firmenich, FrieslandCampina and Wageningen Food and Biobased Research. This project was also supported by the uNMR-NL Grid: A distributed, state-of-the-art Magnetic Resonance facility for the Netherlands (NWO grant 184.035.002). We thank Hans de Rooij of the Wageningen Technical Solutions for the finalised designs and their realisation. Additionally, we would like to thank Marjanne Verhoeven of the Food Quality and Design group at WUR for her support during the extrusion experiments.

References

[1] E. S. Collier *et al.*, "Identifying barriers to decreasing meat consumption and increasing acceptance of meat substitutes among Swedish consumers," *Appetite*, vol. 167, no. August, p. 105643, 2021, doi: 10.1016/j.appet.2021.105643.

[2] H. Aiking and J. de Boer, "The next protein transition," *Trends Food Sci. Technol.*, vol. 105, pp. 515–522, 2020, doi: 10.1016/j.tifs.2018.07.008.

[3] A. C. Hoek, S. Malekpour, R. Raven, E. Court, and E. Byrne, "'Towards environmentally sustainable food systems: decision-making factors in sustainable food production and consumption,'" *Sustain. Prod. Consum.*, vol. 26, pp. 610–626, 2021, doi: 10.1016/j.spc.2020.12.009.

[4] H. Akdogan, "High moisture food extrusion," *Int. J. Food Sci. Technol.*, vol. 34, no. 3, pp. 195–207, 1999, doi: 10.1046/j.1365-2621.1999.00256.x.

[5] Y. Wang *et al.*, "The development process of plant-based meat alternatives: Raw material formulations and processing strategies," *Food Res. Int.*, vol. 167, no. February, p. 112689, 2023, doi: 10.1016/j.foodres.2023.112689.

[6] R. G. M. Van der Sman and A. J. Van der Goot, "Hypotheses concerning structuring of extruded meat analogs," *Curr. Res. Food Sci.*, vol. 6, no. May, p. 100510, 2023, doi: 10.1016/j.crfs.2023.100510.

[7] C. J. R. Verbeek and L. E. Van Den Berg, "Extrusion processing and properties of protein-based thermoplastics," *Macromol. Mater. Eng.*, vol. 295, no. 1, pp. 10–21, 2010, doi: 10.1002/mame.200900167.

[8] S. Kuijpers, G.-J. Goudappel, T. Huppertz, J. Van Duynhoven, and C. Terenzi, "Quantification of phase separation in high moisture soy protein extrudates by NMR and MRI," *Food Res. Int.*, vol. 197, no. P1, p. 115225, 2024, doi: 10.1016/j.foodres.2024.115225.

[9] E. Kaunisto, S. Wassén, and M. Stading, "A thermodynamical finite element model of the fibre formation process during extrusion of high-moisture meat analogues," *J. Food Eng.*, vol. 362, no. 111760, 2024, doi: 10.1016/j.jfoodeng.2023.111760.

[10] E. D. Garina *et al.*, "Mapping anisotropic structure formation of soy protein during high-moisture extrusion," *Food Hydrocoll.*, vol. 172, no. P2, p. 112037, 2026, doi: 10.1016/j.foodhyd.2025.112037.

[11] J. L. Sandoval Murillo, R. Osen, S. Hiermaier, and G. Ganzenmüller, "Towards understanding the mechanism of fibrous texture formation during high-moisture extrusion of meat substitutes," *J. Food Eng.*, vol. 242, pp. 8–20, Feb. 2019, doi: 10.1016/j.jfoodeng.2018.08.009.

[12] P. Wittek, F. Ellwanger, H. P. Karbstein, and M. A. Emin, "Morphology development and flow characteristics during high moisture extrusion of a plant-based meat analogue," *Foods*, vol. 10, no. 8, Aug. 2021, doi: 10.3390/foods10081753.

[13] E. Högg, T. Horneber, and C. Rauh, "Modeling and experimental analysis of protein matrix solidification in cooling dies during high-moisture extrusion," *Front. Food Sci. Technol.*, vol. 5, no. February, pp. 1–19, 2025, doi: 10.3389/frfst.2025.1443376.

[14] E. Kaunisto, C. Ohgren, N. Lor, and M. Stading, "A mean-field phase separation model enabling the coupling of non-isothermal flow phenomena with fibre formation in high-moisture extrusion of meat analogues," *J. Food Eng.*, vol. 412, p. 112972, 2026, doi: 10.1016/j.jfoodeng.2026.112972.

[15] M. I. Gobes, Y. Buğday, J. P. M. van Duynhoven, J. Hohlbein, and R. G. M. van der Sman, "Impact of pH, temperature, and moisture on the rheological behaviour of soy protein concentrate doughs," *preprint*, vol. 11, no. 1, pp. 1–14, 2025.

[16] J. F. Dahl, O. Bouch, M. Schlangen, A. Jan, V. Der Goot, and M. Corredig, "Relationship between rheological parameters and structure formation in high moisture extrusion of plant protein biopolymers," *Food Hydrocoll.*, vol. 160, no. November 2024, p. 110843, 2025, doi: 10.1016/j.foodhyd.2024.110843.

[17] R. G. M. van der Sman, S. Renzetti, and B. Tian, "Rheology of edible soft glassy materials," *Food Hydrocoll.*, vol. 149, no. November 2023, p. 109586, 2024, doi: 10.1016/j.foodhyd.2023.109586.

[18] M. I. Gobes, Y. Bugday, J. P. M. van Duynhoven, J. Hohlbein, and R. G. M. van der Sman, "Impact of pH, temperature, and moisture on the rheological behaviour of soy protein concentrate doughs," *Food Hydrocoll.*, vol. 174, no. December 2025, p. 112316, 2025, doi: 10.1016/j.foodhyd.2025.112316.

[19] T. Purcell, G. Delaplace, A. Riaublanc, M. Demême, A. Derensy, and G. Della Valle, "A general viscosity model for high moisture extrudates of pea protein isolates / gluten blend," *Phys. Fluids*, vol. 37, no. 3, 2025, doi: https://doi.org/10.1063/5.0256835.

[20] R. G. M. van der Sman and L. J. Mauer, "Starch gelatinization temperature in sugar and polyol solutions explained by hydrogen bond density," *Food Hydrocoll.*, vol. 94, no. March, pp. 371–380, 2019, doi:

10.1016/j.foodhyd.2019.03.034.
[21] E. Kaunisto, B. Tsegaye, R. Kotzé, J. Wiklund, R. Kádár, and M. Stading, "Towards in-line rheology measurement of protein melts during high moisture extrusion by pulsed ultrasound velocimetry," *J. Food Eng.*, vol. 1, p. 112461, 2025, doi: https://doi.org/10.1016/j.jfoodeng.2024.112461.
[22] P. Coussot, "Progress in rheology and hydrodynamics allowed by NMR or MRI techniques," *Exp. Fluids*, vol. 61, no. 9, pp. 1–20, 2020, doi: 10.1007/s00348-020-03037-y.
[23] M. R. Serial, C. Terenzi, J. Van Duynhoven, and H. Van As, "MRI of Transport and Flow in Plants and Foods," *Magn. Reson. Microsc. Instrum. Appl. Eng. Life Sci. Energy Res.*, pp. 237–261, 2022, doi: 10.1002/9783527827244.ch11.
[24] S. A. Kuijpers *et al.*, "Impact of pH-shifting on multiscale structural anisotropy of high-moisture extrudates of soy proteins," *Food Hydrocoll.*, vol. 168, no. April, p. 111456, 2025, doi: 10.1016/j.foodhyd.2025.111456.
[25] A. D. Drozdov and J. deClaville Christiansen, "Thermo-Mechanical Behavior of Poly(ether ether ketone): Experiments and Modeling," *Polymers (Basel).*, vol. 13, no. 1779, pp. 44–46, 2021, doi: 10.3390/polym13111779.
[26] Z. El-Qoubaa and R. Othman, "Temperature, Strain Rate and Pressure Sensitivity of the Polyetheretherketone's Yield Stress," *Int. J. Appl. Mech.*, vol. 9, no. 7, pp. 1–19, 2017, doi: 10.1142/S1758825117500995.
[27] K. W. Milc, T. Oerther, J. A. Dijksman, J. P. M. van Duynhoven, and C. Terenzi, "Capillary Flow-MRI: Quantifying Micron-Scale Cooperativity in Complex Dispersions," *Anal. Chem.*, vol. 95, no. 41, pp. 15162–15170, 2023, doi: 10.1021/acs.analchem.3c01108.
[28] J. Hennig, A. Nauerth, and H. Friedburg, "RARE imaging: A fast imaging method for clinical MR," *Magn. Reson. Med.*, vol. 3, no. 6, pp. 823–833, 1986, doi: 10.1002/mrm.1910030602.
[29] D. J. Blundell and B. N. Osborn, "The morphology of poly(aryl-ether-ether-ketone)," *Polymer (Guildf).*, vol. 24, no. 8, pp. 953–958, 1983, doi: 10.1016/0032-3861(83)90144-1.
[30] D. Parker *et al.*, "Polymers, High-Temperature," in *Ullmann's Encyclopedia of Industrial Chemistry*, Wiley, 2012.
[31] L. Rivière, N. Caussé, A. Lonjon, É. Dantras, and C. Lacabanne, "Specific heat capacity and thermal conductivity of PEEK/Ag nanoparticles composites determined by Modulated-Temperature Differential Scanning Calorimetry," *Polym. Degrad. Stab.*, vol. 127, pp. 98–104, 2016, doi: 10.1016/j.polymdegradstab.2015.11.015.
[32] R. G. M. van der Sman, S. Renzetti, P. Voudouris, A. Asghari, and S. Khalloufi, "Correlation of T2 NMR with Tg/T and viscosity," *Curr. Res. Food Sci.*, p. 101309, 2026, doi: 10.1016/j.crfs.2026.101309.
[33] J. Li *et al.*, "Understanding the effect of pH on structure formation in high moisture extrudates produced from soy protein-dietary fiber blends," *Food Hydrocoll.*, vol. 170, no. June 2025, p. 111710, 2026, doi: 10.1016/j.foodhyd.2025.111710.
[34] J. P. Marques, F. F. J. Simonis, and A. G. Webb, "Low-Field MRI : An MR Physics Perspective," *J. Magn. Reson. Imaging*, vol. 49, no. 6, pp. 1528–1542, 2019, doi: 10.1002/jmri.26637.
[35] H. Raich and P. Blu, "Design and Construction of a Dipolar Halbach Array with a Homogeneous Field from Identical Bar Magnets : NMR Mandhalas," *Concepts Magn. Reson. Part B*, vol. 23B, no. 1, pp. 16–25, 2004, doi: 10.1002/cmr.b.20018.
[36] T. O'Reilly, W. M. Teeuwisse, D. de Gans, K. Koolstra, and A. G. Webb, "In vivo 3D brain and extremity MRI at 50 mT using a permanent magnet Halbach array," *Magn. Reson. Med.*, vol. 85, no. 1, pp. 495–505, 2021, doi: 10.1002/mrm.28396.
[37] T. J. Swift and R. E. Connick, "NMR-Relaxation Mechanisms of O17 in Aqueous Solutions of Paramagnetic Cations and the Lifetime of Water Molecules in the First Coordination Sphere," *J. Chem. Phys.*, vol. 37, no. 2, pp. 307–320, Jul. 1962, doi: 10.1063/1.1701321.
[38] B. P. Hills, S. F. Takacs, and P. S. Belton, "The effects of proteins on the proton N.M.R. transverse relaxation time of water II. Protein aggregation," *Mol. Phys.*, vol. 67, no. 4, pp. 919–937, 1989, doi: 10.1080/00268978900101541.

6.5 Supplementary Information

6.5.1 SolidWorks drawing of the in house developed cooling die

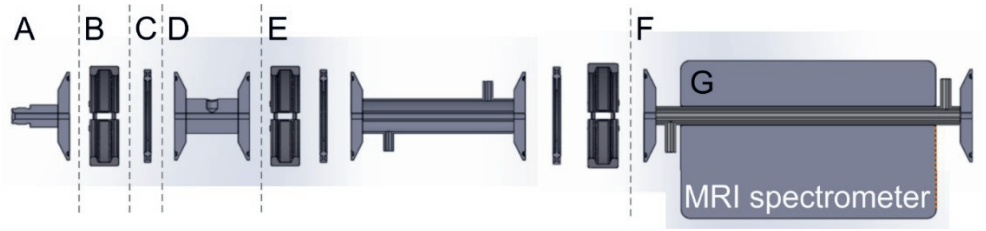

Fig. S6.1: *Solidworks model of the flow-MRI platform parts. (A) barrel exit adaptor to convert the barrel exit to a 50 mm flange system; (B) 50 mm flange clamp; (C) rubber gasket; (D) steel adaptor for holding an external pressure sensor; (E) Steel cooling die of the same inner diameter as the PEEK part for testing extrusion flow and/or elongating cooling die length; (F) PEEK cooling die with cooling channel, with an inner diameter of 4 mm.; (G) Magspec 0.55 T Pure Devices MRI spectrometer. The magnet has a 10 mm bore size.*

6.5.2 PFG spin-echo pulse sequence

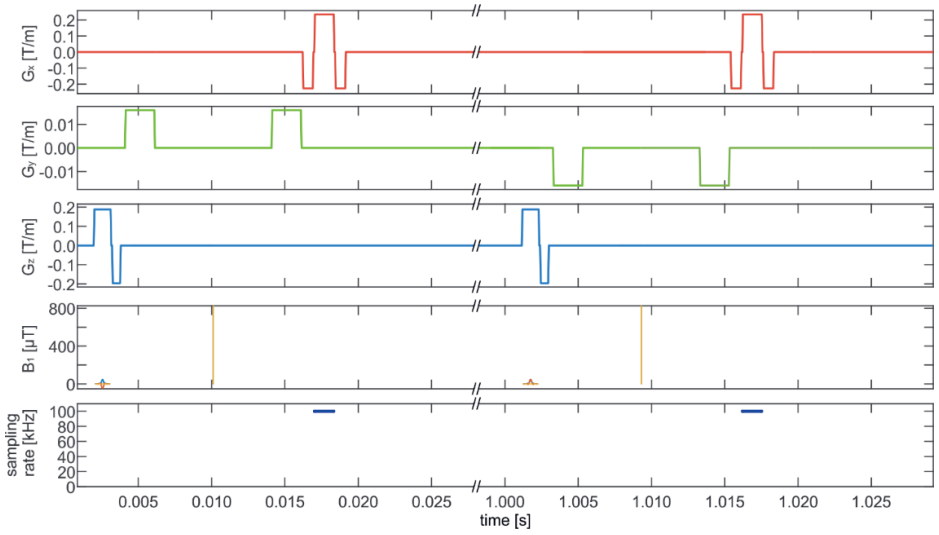

Fig. S6.2: *Diagram for the in house developed pulse sequence for velocimetry measurements with the low-field equipment, including one acquisition with a positive PFG strength and one acquisition with a negative PFG strength, yielding one flow profile. All three imaging gradients are used by the sequence to acquire a 1D velocimetry measurement. The G_x (red), G_y (green) and G_z (blue) magnetic field gradients, respectively, perform frequency-encoding, motion-encoding and slice-selection. Slice selection is required to prevent averaging of the signal originating from the material near the cooling die wall that is out-of-plane with the signal originating from the material at the in-plane centre of the cooling die. A low-power slice-selective pulse is given for excitation, and a hard refocussing pulse is used. The sampling rate is set to 100 kHz. As shown in the diagram the following parameters are used: T_E = 17 ms, T_R = 1 s, PFG strength respectively is 16 mT/m and -16 mT/m for the first and second acquisition.*

6.5.3 Inclusion of pressure sensor in the cooling die

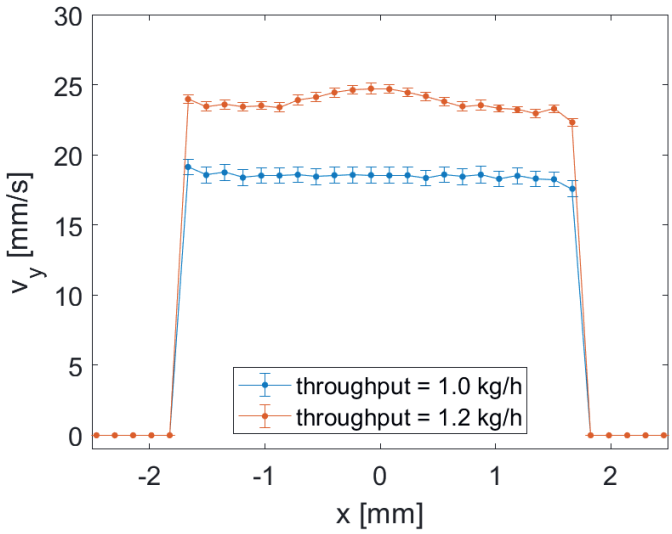

Fig. S6.3: *Velocity profiles acquired for SPC extrudates shifted to pH 8.6 using identical extrusion parameters to Fig. 6.3 in the main text. Here, the modular insert housing a pressure sensor (Fig. S6.1D) was used to enable measurement inside the cooling die channel. The elongation of the cooling die channel by a steel die increased the cooling experienced by the protein melt before entering the FOV of the spectrometer. At a throughput of 1.0 kg/h, only plug flow was observed. When the throughput was increased to 1.2 kg/h, the bell shape in the protein melt core could be recovered. However, extrusion at such throughput with the added steel die regularly kept pressures close to 20 bars, the simulated limit for the PEEK cooling die. Since the measured pressure values in the cooling die insert were nearly identical to the measured values at the die exit, the choice was made to omit the cooling die insert.*

6.5.4 Pulse sequence validation

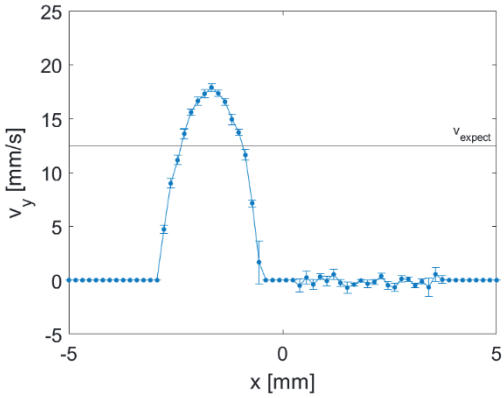

Fig. S6.4: *Flow velocimetry data of a tube of flowing (left) and static water (right). To validate the correct functioning and accuracy of the in house developed flow-MRI sequence, a silicon tube connected to two 50 mL tubes of demineralised water attached to a syringe pump as well as a closed glass tube of demineralised water were placed in the FOV of the spectrometer. Seven measurements were performed with ΔG values geometrically spaced between 8 mT/m and 56 mT/m. The mean flow profile of these seven measurements is shown, and error bars represent the standard error (N = 7). The data is masked against noise using the intensity profile of a measurement without PFG on. During the measurements, the syringe pump was set to output a volume corresponding to 12.5 mm/s of flow which is indicated by the horizontal line, v_{expect}, which should be roughly at the full-width-half-maximum of the flow profile for Poiseuille flow. Likewise, the static water sample should not show any directed flow of water. The in plane resolution is 156 µm.*

6.5.5 T_2 profile inside the cooling die channel

The transversal T_2 FID-CPMG decays of frozen-thawed but non-swollen HM SPC extrudates at ambient temperature contain four populations of water as shown by Kuijpers *et al.* (2024) [8]: immobile non-exchangeable protons from the crystalline carbohydrate phase and rigid protein cores (~10^{-2} ms), (non-)exchangeable protons from the gelled protein phase (~10^{-1} ms), water inside the protein- (~10 ms) and water-rich phases (~30 ms). Due to the CPMG echo time T_E = 5.3 ms, the first two phases cannot be observed. Due to the high temperatures in the cooling die (80-120 °C), separation into the two phase system may not have taken effect yet. Should phase separation have occurred then the contributions of the water- and protein-rich phases will have undergone diffusional averaging at the µm-scale [8]. At the larger length scale, we assume diffusion is dominant due to the elevated temperatures. Furthermore, the relatively long T_E with respect to the signal decay should also lead to the observation of an averaged T_2 relaxation time. The effect of temperature and viscosity on the relaxation time of bulk water can be found through Stokes-Einstein-Debye relation:

$$\frac{1}{T_2} \propto \tau_c = \frac{4\pi\eta a^3}{3kT} \qquad \text{Eq. S6.1}$$

where the T_2 is proportional to the rotational correlation time, τ_c, which depends on the viscosity of the liquid, η, the radius of the molecule, a, the Boltzmann constant, k, and the temperature, T. This relation applies to bulk water, but for an aggregated protein gel chemical exchange between the protein and water needs to be accounted for.

Assuming that in a diffusional-averaged system we only need to account for chemical exchange between protons from water and protein, we can use the Swift-Connick expression [37]:

$$\mathrm{T}_2^{-1} = \mathrm{T}_{2,w}^{-1} + \mathrm{P}_{pe}k_{pe}\left(\frac{T_{2,pe}^{-2} + T_{2,pe}^{-1}k_{pe} + (\delta\omega)^2}{\left(T_{2,pe}^{-1} + k_{pe}\right)^2 + (\delta\omega)^2}\right) \qquad \text{Eq. S6.2}$$

Here the transverse relaxation rate of a proton on water, T_2^{-1} at any CPMG inter-pulse spacing T_E is dependent on the intrinsic relaxation time of the water protons, $T_{2,w}$, the fraction of exchangeable protein protons, P_{pe}, the exchange rate between protons from water and protein, k_{pe}, the intrinsic relaxation rate of the protons on the protein, $T_{2,pe}$, and the frequency difference between the water and exchangeable protein protons, δω. Here it is assumed that the fraction of exchangeable protons on the protein is much smaller than the available protons on the water molecules, $P_{pe} << P_m$ [38]. When $T_{2,pe}^{-1} >> \delta\omega$, the terms $(\delta\omega)^2$, become insignificant in Eq. S6.2. At the field strength of 0.55 T, δω is estimated to be around 290 rad^{-1} [38]. From Kuijpers *et al*. (2024), $T_{2,pe}^{-1}$ is estimated to be in the order of 8000 s^{-1} for the gelled protein phase in SPC extrudate [8]. Under these circumstances, Eq. S6.2 reduces to [38]:

$$\mathrm{T}_2^{-1} = \mathrm{T}_{2,w}^{-1} + \frac{\mathrm{P}_{pe}}{T_{2,pe} + k_{pe}^{-1}} \qquad \text{Eq. S6.3}$$

The fast chemical exchange rate is estimated to be, $k_{pe} \sim 5000\ s^{-1}$ [38]. During the echo time of the experiment, chemical exchange occurs that contributes to the diffusional averaged T_2 relaxation of the water in the protein- and water-rich phases Both rotational (τ_c) as well as the chemical exchange rate (k_{pe}) are dependent on the temperature. Thus, the T_2 relaxation rate of a hot protein melt will increase with temperature.

Figure S6.5 shows the T_2 profiles of an *in situ* dead-stop operation with repeated measurements over the course of 10 minutes, which reveal that, in a time span of 200 s, the T_2 of the core decreases to an equilibrium value of (36 ± 2) ms. During this time, the T_2 relaxation time at the wall remains constant. After correcting for a non-uniform T_2 distribution at equilibrium, likely resulting from lamellar phase separation occurring during

cooling of the material, the T_2 is roughly 25% longer in the core of the protein melt with respect to the T_2 observed near the cooling die wall at t = 0 s. The short time span of 200 s is in line with the expected time scale of heat dissipation and indicates that the T_2 gradient corresponds to a temperature gradient. Thus, the internal temperature gradients modelled in figure 6.2I in the main text and those shown in Högg *et al* (2025) and Kaunisto *et al* (2026) are plausible [13, 14].

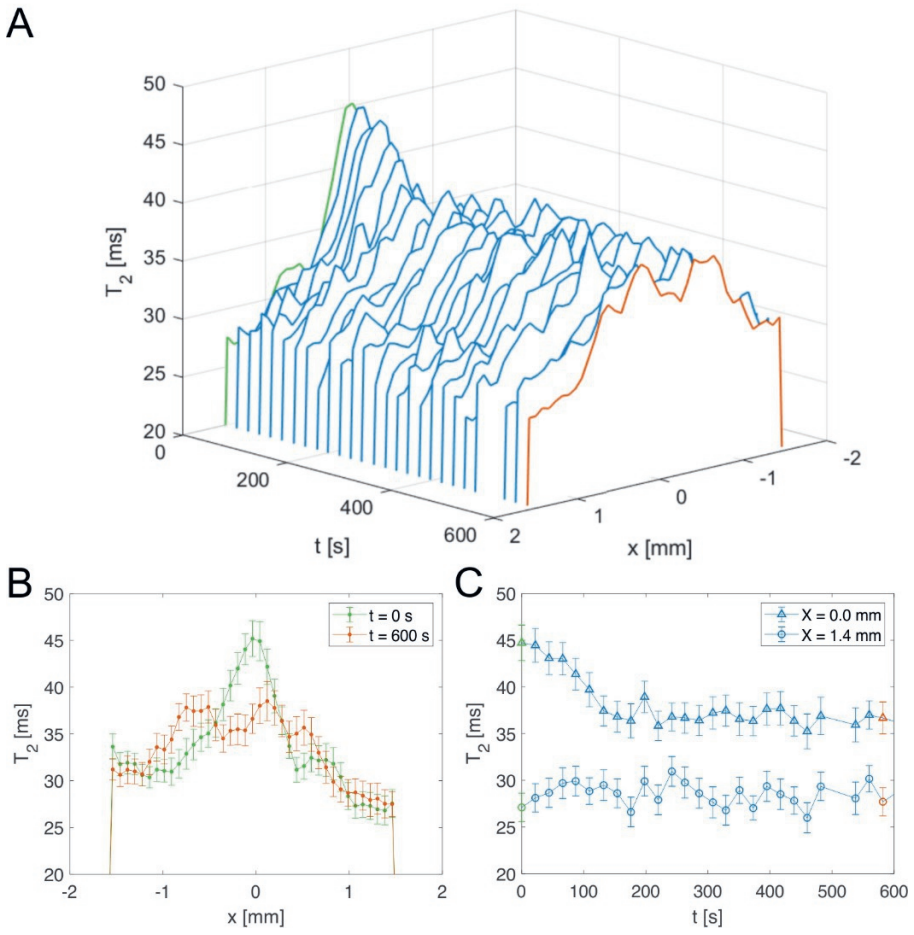

Fig. S6.5: *T_2 measurement results of dead-stop* in situ *MRI. The acquisition parameters were set to: T_E = 5.3 ms, TR = 1000 ms, NA = 8, N_{echoes} = 112, 96 voxels in the read direction at a resolution of 78x1000µm^2. (A) Waterfall plot of T_2 profiles. Every line represents the average profile over two consecutive T_2 measurements. (B) Individual T_2 profiles at t = 0 s, just after dead-stop operation when continued motion of the melt due to the backpressure ceased. t = 600 s where complete thermal equilibrium is assumed. (C) T_2 over time at the centre of the melt (x = 0.0 mm) and close to the cooling die wall (x = 1.4 mm). At the cooling die wall, data was too noisy for accurate fitting and thus omitted from the plots. The colours green and orange are used to highlight the profiles at t = 0 s and t = 600 s.*

6.5.6 Schematic of modelling approaches

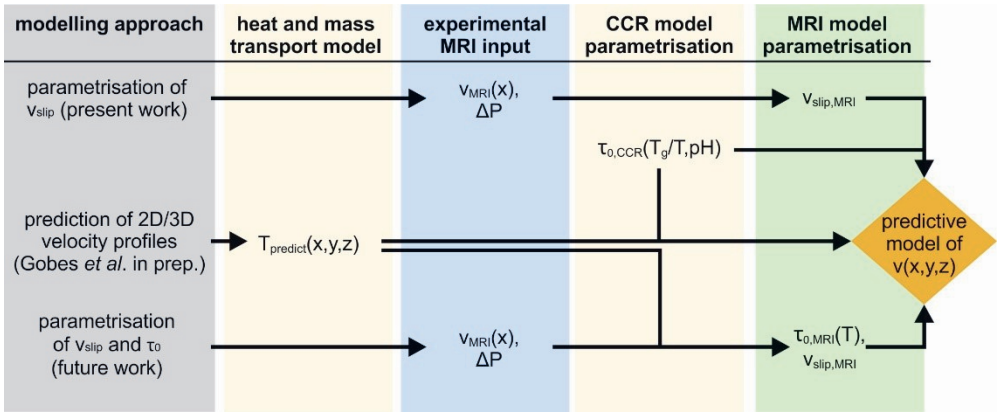

Fig. S6.6: *schematic overview of model parametrisation approaches for predicting cooling die flow in HME.*

Chapter

7

General discussion

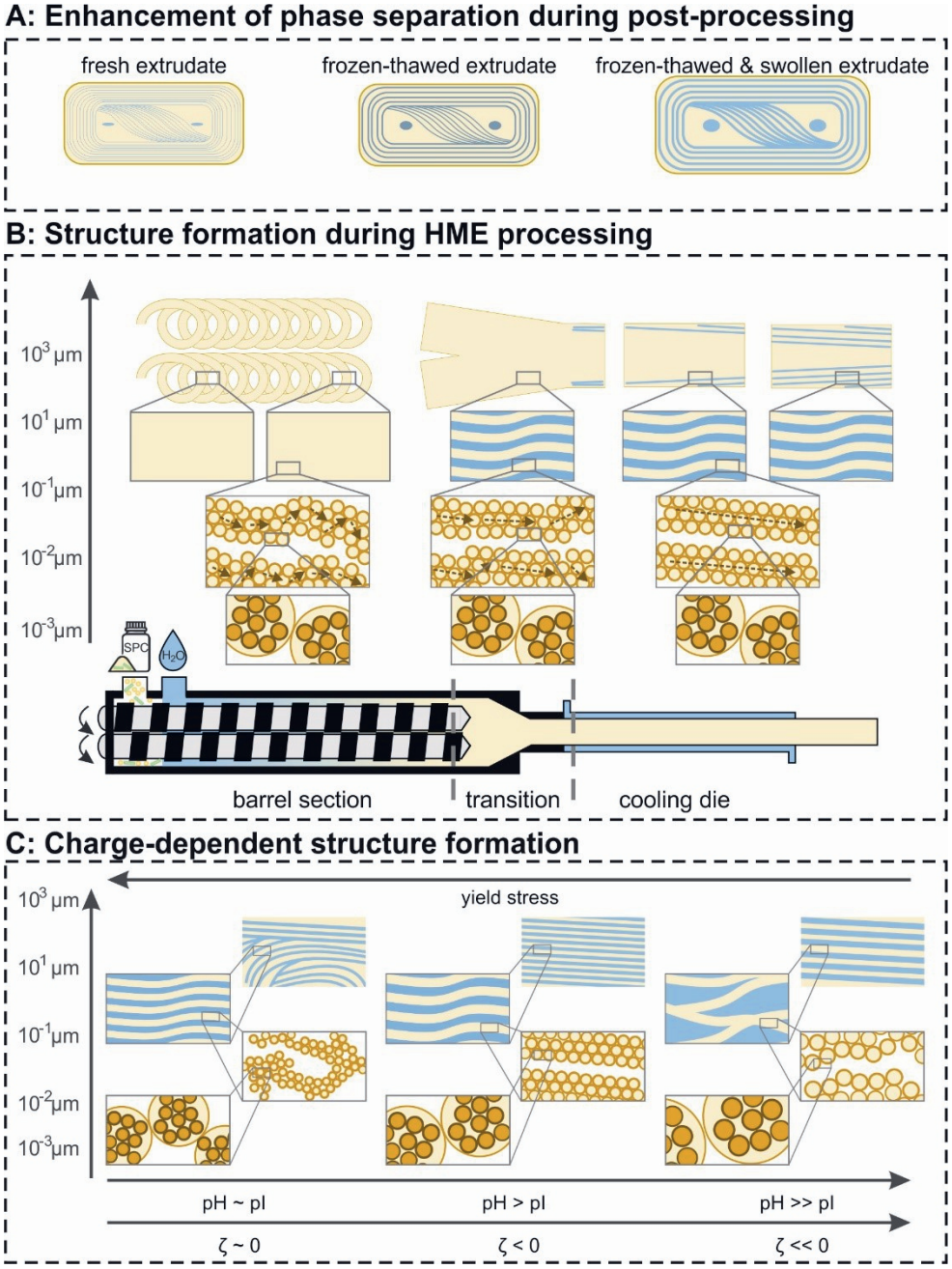

Fig. 7.1: *Overview of main ex situ findings and conclusions, showing (A) the effect of post-processing on the lamellar structure formation, (B) multiscale structure formation per location in the extruder and (C) the charge dependent structure formation. Nano-aggregates (yellow circles), made up of globulin subunits (brown circles) form fibrils that crosslink into a protein network structure. This protein network phase separates into water-rich (blue) and protein-rich (yellow) regions at multiple length scales.*

7.1 Main findings and conclusions

In this thesis, the aim was to develop and validate MRI-based methodologies to study the structure formation during high-moisture extrusion of soy protein. MRI-based techniques were chosen as the main measurement technique due to the ability to acquire spatially-resolved information at multiple length scales in a non-invasive manner. Additionally, the versatility of available instruments, such as low field strength benchtop magnets, facilitated the development of *in situ* capabilities for the direct measurement of the hot protein melt passing through the cooling die. With these and complementary measurement techniques, such as SANS and microscopy, the following research questions were addressed in this thesis:

RQ1: *Where inside the extruder, and at what length scales, does anisotropic structure formation occur during extrusion?*

RQ2: *What is the role of electrostatic protein interactions on the multiscale structure formation during extrusion?*

RQ3: *Does lamellar phase separation occur at µm- and/or mm-scale in extrudates?*

RQ4: *What is the contribution of wall-slip to the flow behaviour of the hot protein melt inside the cooling die?*

RQ5: *What is the effect of post-processing, such as freezing and swelling, on the phase-separated extrudate structure?*

In **Chapter 2**, the ability of MRI to quantitatively assess the phase-separated structure of SPC- and SPI-based extrudates, from lab-scale extrusion, was explored. HF ^{1}H MRI measurements have shown that both extrudates are composed of phase-separated lamellae at the 10^{2} µm-scale, namely the WR and PR phases. The difference in signal intensity between these phases has been exploited to answer **(RQ5)** and assess the effect of post-processing steps, through swelling and freeze-thawing, on the phase-separated structure of extrudates. This revealed that both post-processing steps enhance the SNR and emphasize the existing lamellar structure, as is schematically depicted in Fig 7.1A. LF (0.47 T) ^{1}H TD-NMR measurements of these samples revealed that two additional ^{1}H populations could be discerned originating from immobile semi-crystalline ($T_2 \sim 15$ µs) and gelled polymer ($T_2 \sim 150$ µs) phases. The spatially-determined fraction of PR and WR by HF MRI was corroborated by bulk LF TD-NMR assessment, providing a comprehensive assessment of the material by these complementary techniques. Additionally, this showed how the latter, industrially more accessible, technique can be used for quantification of phase separation. Finally, as a proof of principle, the distribution of lamellae across a dead-stop ribbon was assessed by MRI. This revealed how the width of the aligned phase-separated structure, used as a marker for development of fibrous structure, increases as the protein melt travels through the cooling die. This shows how MRI can be used to study structure formation during the final stage of the extrusion process.

To build on this, in **Chapter 3**, DT-MRI was used to spatially resolve the hierarchical structure of SPC extrudates down to the 10^{-1} µm-scale, which enabled answering **(RQ3)**. Results showed that, inside the PR phase, the fibrillar protein network forms a 10^{-1} µm-scale phase-separated lamellar structure that primarily aligns along the cooling die flow direction. The secondary direction of alignment is parallel to the cooling die walls Results from *in silico* generated images of different cross-sectional cooling die geometries, showed that the 10^{-1} µm-scale structure alignment can be directed. Additionally, the effect of pH, between 5.0 and 7.8, on the 10^{-1} µm-scale lamellar phase separation was investigated. The pH-mediated mechanism of structure formation is later unravelled in **Chapter 5**. A difference between level of order was found at the 10^{-1} µm-scale and 10^{2} µm-scale. This is corroborated by CLSM images and the SANS data presented in **Chapter 4**, that show that at the 10^{-1} µm-scale, structure formation has taken place before entering the cooling die. At the 10^{2} µm-scale, however, structure formation primarily occurs in the cooling die and is determined by the rheological properties of the protein melt.

In **Chapter 4**, material from the cooling die and barrel section, acquired upon a dead-stop operation of a pilot scale extruder, was analysed using MRI and SAS techniques to quantify anisotropic structure formation at multiple length scales. This comprehensive study has answered **(RQ1)** and enabled coupling of the different structure formation length scales to regions in the extruder. The SANS nematic order, describing the alignment of protein fibrils at the 10^{-1} µm-scale, revealed that anisotropic structure formation already takes place in the extruder barrel section and continues to develop in the early sections of the cooling die. These protein fibrils are comprised of 10^{-2} µm-scale protein nano-aggregates. The size of these protein nano-aggregates remains roughly unchanged as the protein melt progresses through the extruder barrel and cooling die. MRI revealed that the alignment of protein fibrils in the barrel section and transition zone serves as an imprint of 10^{2} µm-scale lamellar phase separation. Thus, substantial lamellar alignment was already observed at the start of the cooling die and the height of the aligned lamellar region increased in the early sections of the cooling die

To answer **(RQ2)**, in **Chapter 5**, the mechanism behind structure formation during HME was explored further by using pH as a processing aid to alter protein-protein interactions. The combined analysis of the MRI, SAS and protein extractability data revealed that the dominant structuring mechanism in HME of SPC is dependent on electrostatic charge distribution of protein aggregates. The effect pH has on structure formation is non-monotonic. At pH $\sim$ pI, the absence of charge shielding between protein nano-aggregates leads to efficient cluster formation and a particulate protein network. At the 10^{2} µm-scale, an isotropic phase-separated structure is observed. At pH > pI, the formation of a fibrillar protein network occurs when a balance between electrostatic repulsion of nano-aggregates and fibrillar nano-aggregate clustering is achieved. This network is strongly aligned with the extruder flow direction, and an optimal lamellar phase-separated structure is observed at

the 10^2 µm-scale. However, at pH >> pI, excess charges lead to electrostatic repulsion between nano-aggregates. Resulting aggregates align into fibrils, but the lamellar structure is less aligned along the extruder flow direction due to interfibrillar electrostatic repulsion. The anisotropic lamellar structure at the 10^2 µm-scale decreases with respect to the optimal lamellar structure observed at lower pH.

To understand the structure formation mechanisms inside cooling die, comprehensive knowledge on the flow behaviour of the hot protein melt is required. As a result, many *in silico* models have been developed to investigate this behaviour. Yet, to describe such flow behaviour, models need to be parametrised for protein melt rheology. *Ex situ* rheological studies can only do this in part. Therefore, *in situ* methodologies are required that can directly measure the velocimetric profiles, that enable quantification of wall-slip and the yield stress of the protein melt. In **Chapter 6**, a flow-MRI platform was developed to study the flow of the protein melt through the cooling die *in situ*. The platform uses a commercially available benchtop high-moisture extruder and LF MRI spectrometer, in combination with an in house developed PEEK cooling die with a circular internal channel of 4 mm in diameter. MRI velocimetry data could identify different responses of pH-shifting on SPC extrusion. Fitting of this data enabled answering of **(RQ4)** through the characterisation of wall-slip and temperature-dependent yield stress of the protein melt inside the cooling die. The yield stress was found to decrease as the pH is shifted from the pI of the protein melt towards alkaline conditions and the quantification of wall-slip opened up the possibility to parameterise models thereof.

The remainder of this chapter consists of three sections. Firstly, the performance of MRI as a measurement tool to study anisotropic structure formation of SPC during HME is discussed. New technological MRI capabilities, *e.g.* based on cryo-probe MRI, are explored. Additionally, the expansion of measurements techniques developed in this thesis, to increase our understanding of extrudate structure, are discussed. Secondly, the role of carbohydrate fibres in SPC and the role of the two major soy proteins, namely glycinin and β-conglycinin, on hierarchical structure development are discussed. Open questions regarding the effect of extruder process conditions with respect to pH-shifting are discussed. Finally, the use of MRI to characterise cooling die flow *in situ* is discussed and perspectives on technical improvements of the flow-MRI platform are presented. Furthermore, the potential of the flow-MRI platform to enable the experimental parametrisation of *in silico* models and the ability to scale such parametrised models to industrially relevant conditions is discussed.

7.2 Perspectives on anisotropic structure quantification in HME by MRI

In this thesis, HF MRI methods have been developed and validated for use on HM extruded plant protein materials with anisotropic structure. In **Chapter 2**, we used a conventional MRI room temperature probe at high field (14 T) to assess anisotropic structure in SPC extrudates at high resolution (39x39x500µm^3). Nevertheless, swelling and freeze-thawing are required post-processing steps to sufficiently enhance the ^{1}H MRI contrast between the PR and WR phases. It should be noted that, after this contrast enhancement step, the slice thickness for these images is still ~13 times larger than the in-plane resolution to retain sufficient SNR, roughly 10, in the PR phase. The slice thickness is roughly 1-2 times the width of the WR phase in the image resulting in partial volume effects at the interface between PR and WR phases, which is estimated to be up to 50% of WR phase voxels depending on the width of the WR feature. To limit this, it is preferred to use isotropic voxel sizes. One alternative approach is to use ultra-high field microimaging systems yielding higher sensitivity. As demonstrated in **Chapter 3**, a slice thickness of 100 µm could be achieved at 28 T to acquire CEST data on the PR and WR phase in an SPC extrudate sample. This brought the estimated amount of voxels with partial volume effects down to 34%. Another approach is the use of cryo-probe MRI with a 10 mm probe diameter on the high field wide bore 14 T magnet used in this work. In cryo-probe MRI, the radio frequent (r.f.) coil and pre-amplifier are cooled to liquid nitrogen temperatures, decreasing the passive thermal noise therein [1]. Thus, an increase in SNR of 5x to 7x could be achieved for pH-shifted SPC extrudate samples (Fig 7.2A) as compared to similar measurements using the room-temperature probe with a 25 mm diameter. It is to note that the smaller probe diameter aided in additionally boosting the SNR. The increased SNR allows for imaging at smaller voxel sizes, which is required to discern the PR and WR phases in benchtop-scale extrusion samples. Furthermore, even fresh and non-swollen extrudate samples could be measured with sufficient signal intensity and imaging contrast between PR and WR phases. These samples have shorter ^{1}H T_2 relaxation times, close to the shortest echo times available for the MRI measurements, roughly between 6 and 18 ms. In Fig 7.2B, T_2-weighted MRI data and respective WOP(MRI) maps of two fresh, non-swollen, extrudate samples, respectively extruded at pH 7.1 (top) or at pH 8.6 (bottom), are shown using an MRI resolution of 20x20x500 µm^3. Aided by the increased SNR and imaging resolution, this revealed that a phase-separated lamellar structure is present prior to freeze-thawing of the material. Such lamellar structure was indiscernible by high-field MRI with room temperature probes. The slice thickness was calibrated to minimise the effective b-value during DT-MRI. DT-MRI measurements of these extrudates, displayed in Fig 7.2C, show that the 10^{-1} µm-scale lamellar phase separation, observed in **Chapter 3** for frozen-thawed and swollen SPC extrudates, can be discerned prior to freeze-thawing. Thus, the increased sensitivity of cryo-probe MRI or ultra-high field strengths open

up the possibility to quantify structures in samples with small feature sizes. These experimental capabilities will aid in fully characterising HME processing of plant proteins.

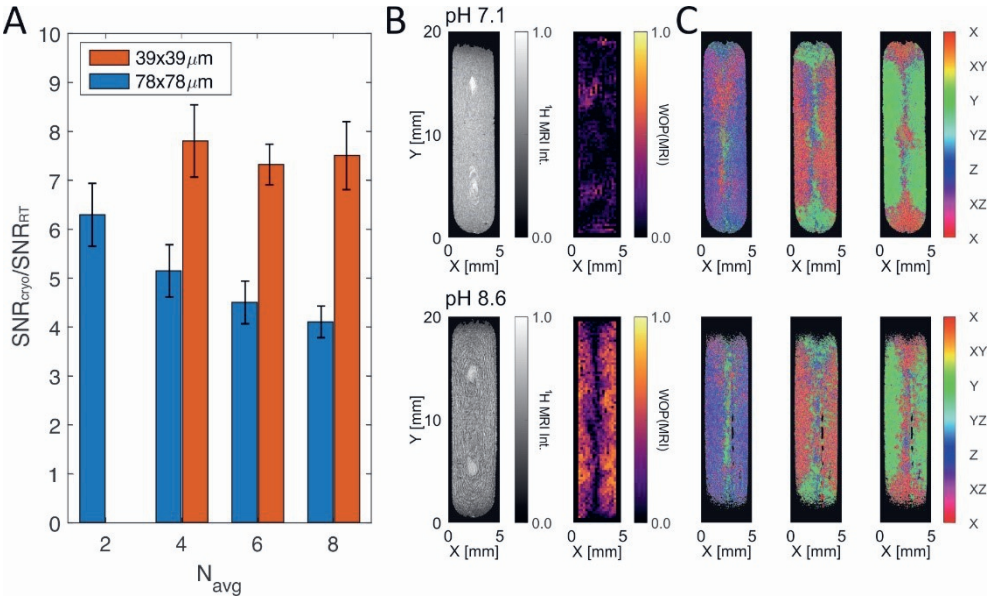

Fig. 7.2: *Cryo-probe MRI data acquired at 14 T for SPC extrudates obtained by benchtop-scale HME, and frozen-thawed and swollen in water. (A) For axial RARE MRI images with higher (39x39x500 µm³) or lower (78x78x500 µm³) spatial resolution, acquired with a T_E of, respectively, 8.2 ms or 6.4 ms: SNR enhancement between cryo- and RT probe MRI, SNR_{cryo}/SNR_{RT}, upon increasing number of signal averages, N_{avg}, from 2 to 8 (T_R = 1 s, RARE-factor = 2). The histogram shows an average value based on multiple SPC extrudate samples extruded between pH 5.9 and 8.6. The error bars represent the standard deviation. (B,C) Axial cryo-probe MRI results for a fresh and non-swollen SPC extrudate at pH 7.1 (top) and pH 8.6 (bottom), including (B) T_2-weighted image (left) and respective WOP(MRI) map (right), as well as (C) DT-MRI PDD maps of, from left to right, the first, second and third eigenvalue after post-processing by dyadic tensor sorting using a 7x7 voxel window size. The axial T_2-weighted image acquisition parameters were: T_E = 10 ms, T_R = 1 s, N_{avg} = 8, RARE-factor = 2, voxel size = 20x20x500 µm³ and FOV = 20x5 mm². DT-MRI images were recorded using an STE sequence with T_E = 12 ms, T_R = 1 s, N_{avg} = 6, voxel size = 40x40x1000 µm³, FOV = 20 x 5 mm², 8 images with a minimal b-value (~120 s/mm²) and 36 images at b = 1000 s/mm².*

7.2.1 Assessment of anisotropic structure quantification by MRI at low field strength

The powerful high-field MRI equipment used in this thesis, providing high-resolution spatial maps of sub-mm scale anisotropic structures, limits applications to a specialised facility. Yet, compact, lower-maintenance and cheaper low-field MRI equipment can be a suitable and accessible alternative approach for applications in less specialised laboratories. For instance in **Chapter 2**, the relative fraction of the PR and WR phases between HF imaging and LF TD-NMR are shown to be in mutual agreement. If a one-directional gradient system is present in a low-field MRI equipment, typically for self-diffusion measurements, some lower-

resolution information on structural heterogeneity can be achieved by one-dimensional MRI profiling. A classic example is the rotation of the sample relative to this gradient in between repeated measurements to generate a projection from different angles [2]. This gradient can also be used to encode diffusion and potentially allow the semi-quantitative assessment of diffusion anisotropy as function of the rotation angle. To validate such methodologies, however, high resolution (DT-)MRI data would be necessary.

Another benefit of low-field NMR/MRI equipment is the short pulse durations, down to the µs range, that can be utilised. This allows assessment of very short relaxation time components as demonstrated in **Chapter 2**. Data on these fast-relaxing components within plant-protein extrudates, namely the carbohydrate and protein polymers themselves, can aid in quantifying the diffusional [3] and chemical [4] exchange present between the gelled protein network and water in the PR phase. This could aid in validating the effects of exchange that were hypothesised in **Chapter 2** and **6**. Thorough understanding of the exchange effects can aid in the quantification of the cross-sectional temperature gradient present during *in situ* measurements. A qualitative relation between T_2 and the cross-sectional temperature profile in a dead-stop melt was observed in **Chapter 6**. Quantitative assessment of the exchange rates would require CPMG-based T_2 dispersion measurements at multiple echo times, including echo times much shorter than those available in MRI measurements [4, 5]. However, bulk TD-NMR measurement after a dead-stop would include spatially-varying temperature conditions with corresponding spatially-varying exchange conditions. To measure spatially-unvaried exchange conditions, a series of experiments will have to be conducted *ex situ* at different temperatures. This would require an MRI probe that can reach the 130 °C present directly after dead-stop operation of the extruder. Additionally, to prevent evaporation of water from the sample at such temperature, headspace should be avoided and tubes will have to be (flame) sealed. At temperatures above the boiling point of water, it might be required to use sapphire NMR tubes that can withstand high pressures. In such *ex situ* steady-state temperature measurements, information on the diffusive exchange processes could be obtained by correlated T_2-T_2 [6] or diffusion-diffusion [7] measurements. The former method has been demonstrated for measurement of exchange effects in muscle tissue of meat and seafood [8]. Due to the longer acquisition times of such measurements and the loss of the temperature profile in the sample due to cooling towards thermal equilibrium after dead-stop operation, such measurements are not possible inside the cooling die. Alternatively, chemical compounds with known temperature-dependent chemical shift differences could be utilised for temperature profile assessment, such as methanol or ethylene glycol [9–11]. Methanol has a boiling point of around 57 °C and is less well suited for use during extrusion. The temperature range of ethylene glycol spans up to roughly 140 °C [9, 11], which is higher than the expected cooling die temperatures but on the lower limit for typical temperatures in the barrel section. These substances require encapsulation into beads to prevent exchange with

the water and protein environment. Such beads will need to be small enough not to disrupt structure formation or break during extrusion. This temperature-probing method, however, relies on the chemical shift differences between the OH and CH_2 groups within a molecule. Such chemical shift difference, which is roughly in the order of 0.010 ppm/°C [11], is likely too small to be accurately determined at 0.5 T. The ability to distinguish these chemical shift differences is likely further hampered by the line broadening of peaks due to confinement of the molecules in a bead. A solution to this could be the use of fluorinated compounds [12]. Measurements using ^{19}F NMR could be more feasible as the range of chemical shift differences of fluorinated compounds is much larger (~300 ppm) compared to water (~14 ppm) [13]. Such approach would require an MRI system for *in situ* use that is able to both measure ^{1}H and ^{19}F nuclei. A different approach is the use of the proton resonance frequency method [14], which can be used to measure the temperature-dependent phase shift between two measurements [15], similar to the measurement of flow velocimetry in **Chapter 6**. The phase difference would have to be assessed for a sample both at an elevated temperature, e.g. immediately after dead-stop operation, and at thermal equilibrium conditions after cooling. However, in the latter process phase separation into PR and WR phases may occur, which in turn results in spatial heterogeneities beyond that of the cross-sectional extrusion temperature profile.

7.2.2 Assessment of 10^{-1} µm-scale anisotropic structure characterisation by DT-MRI

In **Chapter 3**, DT-MRI has been used to study the 10^{-1} µm-scale lamellar phase separation in the cross-sectional plane of frozen-thawed and water swollen SPC extrudates. The focus was to identify the dominant structuring direction by means of water self-diffusion. To enable a more direct comparison between the 10^{-1} µm-scale and 10^{2} µm-scale phase separation, it could be beneficial to apply the WOP(MRI) analysis to the eigenvector data of the diffusion tensor eigenvalues. Due to the sensitivity of the WOP(MRI) analysis to large deviations in angle of single vectors within one window region, it is recommended to apply this method on diffusion tensor data after post-processing using dyadic tensor sorting [16]. Additionally, in future work it could be of interest to acquire multiple imaging slices with minimal slice gap to generate continuous spatial data in the slice direction, *i.e.* extrusion flow direction. Such data can, after denoising of the data to generate smooth principal direction maps [17], be analysed using a technique called fibre tractography, which is routinely used in brain research to track the path and orientation of nerve fibres in the brain [18]. As briefly mentioned in **Chapter 3**, when the denoising window is similar in size to width of the PR and WR features in the image, the definition of these phases is lost. To alleviate this, cryo-probe or ultra-high field MRI can be employed, which enable using smaller voxel sizes whilst maintaining SNR. Fibre tractography of these denoised data enables assessing the 10^{-1} µm-scale structure over a larger volume. These measurements rely on a large number of

diffusion encoding directions to maintain accuracy. The disadvantage is that multiple orientations within one voxel are difficult to discern. By using a multiple tensor fit [19] and by taking into account diffusion kurtosis effects [20], multiple orientations can be discerned within one voxel, enabling the tracking of complex fibre pathways. Such measurements require multiple discrete b-values to be measured in multiple diffusion encoding directions which will significantly increase measurement time. Yet, the capability of analysing multiple diffusion orientations within one voxel can enable separating the contributions of the PR and WR phase in the presence of partial volume effects in voxels.

7.3 Perspectives on hierarchical structure development in high-moisture extrudates from plant proteins

In **Chapters 3, 4 and 5**, a multiscale characterisation of structure formation in high-moisture extrudates of soy protein has been presented. While these chapters have answered some of the open research questions in the field, several areas remain where the mechanistic multiscale understanding of structure formation is lacking. This section provides directions for future research to strengthen this understanding.

7.3.1 Influence of soy protein composition

The first direction is the further investigation of the multiscale impact of soy protein composition on structure formation during HME. In this thesis, SPCs from two manufacturers with similar composition and properties have been used. Yet, using other SPC sources, with different solubility or degree of denaturation, can affect structure formation [21]. Such differences can arise from botanical variety or from the use of different industrial separation processes [22–24]. A current hypothesis on the difference in structure formation is the different ratio between glycinin and β-conglycinin that make up the majority of proteins in soy, which can vary between soy cultivars and growth climate zones [25, 26]. Based on their sedimentation behaviour during ultracentrifugation, glycinin and β-conglycinin are commonly respectively referred to as 11S and 7S. Both 11S (~31–52 % of soy protein) and 7S (~25–37 % of soy protein) are large oligomeric proteins, with 11S being a hexamer and 7S a trimer [25–27]. Additionally, 11S proteins contain more cysteine residues compared to 7S proteins [24]. Apart from their structural differences, they have distinct physical properties such as different iso-electric points and denaturation temperatures [28, 29]. As a result, their gelation behaviour is different at different pH values [30]. HME of SPI with different ratios of 7S and 11S protein has shown that lower contents of 7S lead to irregular structure, whereas higher contents of 7S result in a more defined layered structure [25, 31]. This was explained by SANS results showing that the 7S addition weakens the protein gel structure, which has a positive effect on the extrusion process [30]. It was proposed that the optimal blend contains about 30% 7S [30], which is slightly lower from most commercially available sources [25, 27]. However, this study was performed on

largely native protein, which can influence the overall structure formation during HME [30, 32]. For example, it was shown for SPI that using native soluble protein does not necessarily increase structure formation. Optimal extrusion conditions are reached when a blend of native and denatured SPI is used [32]. Furthermore, pH can be used as a tool to tune the structuring capacity of different soy protein batches to specific product requirements [33]. This shows how a thorough understanding of the role of these protein fractions is vital for optimising the HME process of soy protein. In turn, this could aid in understanding the different extrusion characteristics of other legume proteins. These varieties natively can differ in ratio between 7S and 11S globulins, as well as their molecular structure, with cysteine content being most relevant for structure formation during HME.

7.3.2 Influence of carbohydrate fibres

The second direction of interest is the role of non-protein ingredients. The majority of this thesis focused on the use of SPC which consists of about 20% of insoluble carbohydrate fibres. A comprehensive understanding of the role of insoluble carbohydrate fibres on structure formation enables the optimisation thereof, and of the production of meat alternatives with high fibre contents. Our understanding of the role of fibre in our diet, and of the associated health benefits, has increased in recent years and lack of fibres in our diet has been linked to a number of pathologies [34]. Fibre-rich meat alternatives could play into this trend and influence consumers in choosing more fibrous food compared to meat which lacks fibre. Additionally, inclusion of higher concentrations of fibre is of industrial interest as less processing steps are required to convert dehulled soybeans to soy flour for extrusion compared to SPC, which is more cost-effective. While it was originally hypothesised that a second biopolymer phase, such as a fibre phase, was a requirement to result in a lamellar phase-separated structure [35], **Chapter 2**, and other works [32, 36, 37], show that such structure can be achieved with SPI. It should be noted, however, that SPI can still contain roughly 6% carbohydrate fibre, mainly originating from cell-wall fragments. The inclusion of larger fractions of carbohydrates has been shown to increase the fibrous structure formation by resulting in more abundant, smaller, lamellae at the sub-mm scale [37–40]. Carbohydrate-rich regions are formed at the µm-scale, which act as nucleation sites for initiating fractures that develop into the fibrous structure at larger length scales [40]. These carbohydrates have to be insoluble fibre as opposed to soluble fibres to improve fibrous structure in extrudates [38]. Generally, an optimum seems to be reached at around 20-25% fibre content, while extrudates with higher fibre contents exhibit decreased fibrousness [37, 39, 40]. CLSM images of SPI and insoluble carbohydrate fibre blends show that the continuous protein phase is broken up by the fibre phase resulting in a higher degree of protein fibrousness at the µm-scale [37, 39, 41]. At the nm-to-µm scale, these carbohydrate fibres are poly-dispersed in shape and size, and have been shown to align along the extrusion direction [42]. The strongest alignment of these fibres seems to be achieved in the

extruder transition zone, between the barrel section and cooling die, where tensile forces are highest [42, 43].

7.3.3 Effect of HME conditions: pH-shifting, extrusion parameters and extruder scale

The third direction of interest is the relation between pH-shifting and processing conditions used during extrusion. In **Chapter 5**, *ex situ* MRI measurements on SPC extrudates obtained at varying liquid-feed pH-shifting conditions are shown. Here, an increase in the optimal pH for structure formation was shown from lab- to pilot-scale HME. If such pH conditions are repeated at benchtop-scale, using similar temperature settings for the barrel and cooling die, the pH optimum increases further to the alkaline region as shown in Fig 7.3. This highlights how an increase in extrusion scale and corresponding changes in process conditions influence structure formation. The origin of these differences in optimal pH during extrusion are unknown but their understanding is vital for up-scaling the use of pH as an optimisation strategy for structure formation or tuning of structuring capacity between soy protein batches.

The processing parameters of the three extrusion scales used in this work, are shown in the table in Fig 7.3. The most notably parameters are the Length/Diameter (L/D) ratio, throughput, and screw speed which affect the residence time and specific mechanical energy (SME) during extrusion. As shown in the AI(DR) data in Fig 7.3, longer residence times move the optimum pH condition towards the alkaline region. One possible explanation relates to the L/D ratio of each extruder. The extruder barrel can effectively be divided in two regions. The first region, operating at lower temperatures, between 40-80 °C, serves as the mixing zone where hydration of the protein takes place. A high L/D ratio generally results in a longer residence time of the protein in the barrel, promoting hydration of the protein, which can be controlled by altering the throughput of the process. At the same time, a higher throughput will result in shorter residence times. In **Chapter 2** and **5** of this work, pH-shifting via the liquid feed is employed which may result in insufficient time for the pH to equilibrate within the protein dough. This can be circumvented by feeding hydrated and equilibrated protein doughs directly into the extruder [45], or feeding freeze-dried equilibrated protein doughs as powder into the feeder [44]. When pH is shifted via acidification or alkalinisation of the water feed, the length of the low-temperature mixing zone, and thus the residence time of the protein therein, has a strong effect on the level of protein hydration before the protein dough enters the high temperature kneading zone. A longer residence time may allow for a better hydration and longer equilibration time for the protein to adjust to the imposed pH condition.

The interplay between insufficient protein equilibration and the temperature conditions during thermo-mechanical treatment in the kneading section is intricate. This hampers

unravelling the effects of residence time in the mixing section and further thermo-mechanical treatment in the kneading section as captured in the SME parameter. One approach to investigate this effect would be to vary the length of the mixing section in the extruder barrel on hydration of the protein dough.

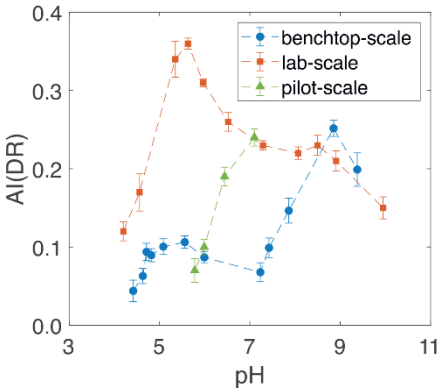

extruder scale	benchtop	lab	pilot
L/D ratio [-]	44	25	34
throughput [kg/h]	1.6	5	57.5
screw speed [RPM]	400	300	250
end plate pressure [bar]	2 - 12	4 - 15	20 - 25
SME [kJ/kg]	120 - 140	40 - 60	115 - 130
free barrel volume [L]	0.06	0.15	1.76
cooling die length [mm]	150	300	1200
cooling die volume [L]	0.008	0.036	0.50
t_{res} barrel [s]	175	120	144
t_{res} cooling die [s]	23	33	40

Fig 7.3: *Extrusion AI(DR) results for pH-shifted SPC extrudates, and processing parameters at benchtop- (blue), lab- (orange) or pilot-scale (green). Lab- and pilot-scale data are reproduced from Fig 5.6 in* ***chapter 5****. SPC extrudates were produced by liquid feed pH-shifting using different molarities of citric acid or trisodium phosphate.*

7.4 Perspectives on *in situ* quantification of cooling die flow by MRI velocimetry

A detailed understanding of the flow properties inside the cooling die and, thus, the corresponding mechanisms behind structure formation, will enable a more efficient prediction-based rational design of plant-based extrudate products from conventional and/or novel sources. The flow-MRI platform, developed for **Chapter 6**, enables measuring the velocity profiles in SPC protein melts *in situ* inside the extruder cooling die. Such measurements have assessed the dominant contribution of wall-slip to the observed velocity. The current setup enables using different protein melt inlet temperatures, as shown in Fig. 7.5. At pH 7.1, the temperature of the protein melt, upon entering the cooling die, does not noticeably influence the measured flow profile. As expected at pH 8.6, a reduced velocity is observed, within the core region of the protein melt inside the cooling die, for lower inlet temperatures. Additionally, at a barrel exit temperature of 130 °C, the slip velocity is ~1 mm/s higher at pH 8.6 compared to the higher barrel exit temperatures. Further investigation using a more detailed range of temperature and pH settings will enable determining the effect of melt viscosity on the wall-slip and yield stress.

As briefly discussed in **chapter 6** and fig S6.5 in the SI, this would enable the parametrisation of both wall-slip and yield stress from the MRI data alone, without having to rely on bulk CCR measurements on SPCs. It can be concluded that parametrisation of wall-slip and yield stress can be performed during extrusion of these or other protein ingredients, such as pea protein concentrate, and aid in understanding the rheology thereof.

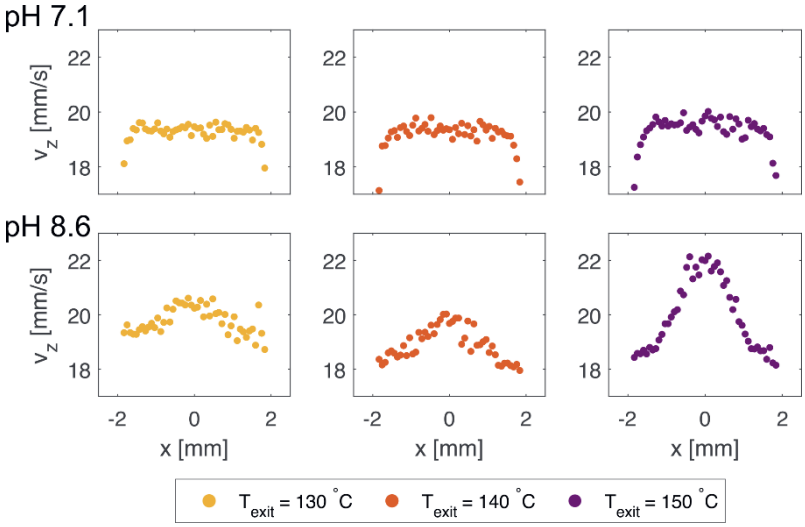

Fig 7.5: *In situ LF flow-MRI data for HME of SPC under pH-shifting to pH 7.1 (top) and 8.6 (bottom), acquired upon varying the barrel exit temperature between 130 °C and 150 °C to influence protein melt viscosity. Flow velocimetry acquisition parameters are identical to those employed in* ***Chapter 6****. The data at 150 °C is a reprint of the data shown in Fig. 6.3*

7.4.1 Perspectives on expanding the flow-MRI platform

The main current limitation of the *in situ* flow-MRI platform used in this thesis work is the fixed position at which flow velocity data can be measured, namely 150 mm after the protein melt has entered the 235 mm cooling die for the benchtop extruder. As discussed previously, by utilising a longer cooling die with a wider inner diameter, more information on the onset of wall-slip and resulting changes in the velocity profile shape along the cooling die could be acquired. The current design involves a coolant channel that flows around the cooling die, from the extruder side to the exit of the cooling die. The design utilises an inlet and an outlet which limit the flexibility in positioning the LF MRI magnet along the cooling die length. By placing both the inlet and outlet on the extruder side of the cooling die, the magnet could be moved closer to the end of the cooling die, enabling the acquisition of flow-MRI data along the cooling die. This could potentially yield information on the changes in the observed plug- or bell-shaped flow profiles along the cooling die as the hot protein melt

cools further. However, if a larger magnet bore would be available, a cooling die with a larger inner diameter could be used. Due to the larger protein volume, relative to the cooling surface area, more time would be required for the hot protein melt core to cool down. This condition could yield the persistence of a bell-shaped flow profile along the cooling die. Data from different locations at higher cooling temperatures could aid validating the modelled data by Högg *et al.* (2025) [52], which estimated that the flow velocity profile primarily changes early in the cooling die and becomes a plug-flow with constant velocity once the melt is sufficiently solidified. Alternatively, the cooling die could be altered to include two coolant channels, at the expenses of a more complex design and manufacturing process. The outer coolant channel could then be kept at the operating temperature of the magnet, whereas the inner coolant channel will cool the protein melt. This inner channel can then be operated at a different temperature from the operating temperature of the magnet, such as the 65°C used during HME in **chapters 2, 3, 4 and 5**. The additional benefit is that this system will enable parametrisation of the effect of cooling temperature on the flow of the protein melt, which has thus far only been modelled [53]. Such design could work using a bore size of just 15 mm, cooling die walls of 1 mm thickness, and keeping the inner diameter of the cooling die at 4 mm.

By using a wider-bore magnet, e.g. around 40 mm, the cooling die design outlined previously could be upscaled to fit a lab-scale extruder as used in **Chapters 2, 3 and 5**. At this condition, it would be possible to utilise rectangular cooling die designs, whose cross-sectional surface area and aspect ratio can be varied. Such flexibility in the design would enable parametrising the actual cooling die geometry on flow. The data could be used to validate some of the results in Hogg *et al.* (2025), where the effect of cross-sectional area and aspect ratio was modelled [52]. However, as briefly discussed in **chapter 6**, commercially available magnets at this bore size using H- or C-yoke permanent magnets or electromagnets are too large and heavy to operate *in situ* near an extruder [54]. This calls for the use of Halbach array magnets [55], which come at a low cost and can be scaled to different magnet bore sizes [56]. These Halbach arrays use a number of small cubic permanent magnets assembled in a ring at specific angles. The strength and homogeneity of the magnet depends on the permanent magnet strength itself as well as their orientation. The bore diameter of the magnet can be designed to match the required geometry. Additionally, the assembled magnet naturally has a very small stray magnetic field [55]. While not commercially available yet, several designs have been proposed in literature using bore sizes between 6 mm and 40 mm [57–60]. While these magnet designs mostly target portable NMR spectroscopy, there are groups scaling these magnets for use in MRI systems [61] with 3D imaging capability using magnetic field gradients [62]. One example uses an elliptically shaped Halbach array for MRI [63], which

shows how these Halbach arrays could be designed to more optimally fit a rectangular cooling die geometry. For such rectangular cooling die designs, it could be beneficial to investigate the use of surface r.f. coils, which have a better SNR ratio close to the sample surface compared to volume coils [64]. Such custom-optimised designs could enable positioning the magnet closer to the start of the cooling die and measure flow profiles at the entrance of the cooling die.

7.4.2 Scalability of parametrised models

Implementation of previously proposed technological expansions on the flow-MRI platform would strengthen our knowledge on the cooling die flow. However, in terms of practicality, the scope of application of such flow-MRI platforms will remain at benchtop- to lab-scale. Further increasing its size, to pilot- or industrial-scale, would give only limited new insights into the cooling die flow behaviour of plant-protein extrudates, while the manufacturing cost increases due to more challenging equipment dimensions and process conditions. Furthermore, while it could be feasible to enable *in situ* measurements of the barrel exit with a sufficiently large magnet bore and custom radiolucent barrel exit that extends past the extruder and barrel screws, measurements of the barrel itself will remain infeasible due to the necessity of the metal twin screws. For these zones one will need to rely on the use of *in silico* models to assess the local rheological properties.

As proposed in **Chapter 6**, detailed experimental data gathered at benchtop- or lab-scale, acquired at different process conditions, enables parametrising the rheological properties of the protein melt, such as the temperature-dependent yield stress, viscosity and wall-slip velocity. When these can be accurately predicted at benchtop- or lab-scale, the *in silico* model can be adapted to accommodate different extrusion scales and cooling die geometries. Such models could be validated with pressure and temperature data collected by an array of sensors attached to the barrel, barrel exit and cooling die. The model developed in **Chapter 6** to fit the velocity data, and to obtain estimates of wall-slip and yield stress, relies on constitutive relations derived from CCR data. The next step would be to instead use accurate predictions for the temperature gradient inside the protein melt and to derive these constitutive relations directly from the flow velocimetry data, as outlined in Fig. S6.5 in the SI of that chapter. The application of this method is not limited to the use of SPC, but can be expanded to the study of HME of other conventional or novel protein sources, as well as of non-protein food ingredients [65].

To place the flow-MRI system in a wider perspective, with this setup the constitutive relations can be quantified for any material with sufficient ^{1}H density and long enough relaxation times to enable MRI velocimetry measurements. The platform can be applied to any extruder that has the temperature range to be employed for the extrusion of plastic [66] or has small enough operating volumes to be of interest for 3D printing of food or medical purposes [67]. With sufficient experimental data, *in silico* models of these lab-scale processes could be scaled to industrial conditions.

References

[1] H. Kovacs, D. Moskau, and M. Spraul, “Cryogenically cooled probes - A leap in NMR technology,” *Prog. Nucl. Magn. Reson. Spectrosc.*, vol. 46, no. 2–3, pp. 131–155, 2005, doi: 10.1016/j.pnmrs.2005.03.001.

[2] “Lauterbur1973,” 1973.

[3] P. S. Belton and B. P. Hills, “The effects of diffusive exchange in heterogeneous systems on N.M.R. line shapes and relaxation processes,” *Mol. Phys.*, vol. 61, no. 4, pp. 999–1018, 1987.

[4] B. P. Hills, S. F. Takacs, and P. S. Belton, “The effects of proteins on the proton N.M.R. transverse relaxation time of water II. Protein aggregation,” *Mol. Phys.*, vol. 67, no. 4, pp. 919–937, 1989, doi: 10.1080/00268978900101541.

[5] A. Gottwald, L. K. Creamer, P. L. Hubbard, and P. T. Callaghan, “Diffusion, relaxation, and chemical exchange in casein gels: A nuclear magnetic resonance study,” *J. Chem. Phys.*, vol. 122, no. 3, 2005, doi: 10.1063/1.1825383.

[6] R. Song, Y. Q. Song, M. Vembusubramanian, and J. L. Paulsen, “The robust identification of exchange from T2-T2 time-domain features,” *J. Magn. Reson.*, vol. 265, pp. 164–171, 2016, doi: 10.1016/j.jmr.2016.02.001.

[7] O. Mankinen *et al.*, “Ultrafast diffusion exchange nuclear magnetic resonance,” *Nat. Commun.*, vol. 11, no. 1, pp. 1–8, 2020, doi: 10.1038/s41467-020-17079-7.

[8] K. E. Anderssen and E. R. McCarney, “Mechanisms of transverse relaxation of water in muscle tissue,” *Food Control*, vol. 132, no. April 2021, p. 108373, 2022, doi: 10.1016/j.foodcont.2021.108373.

[9] A. L. Van Geet, “Calibration of the Methanol and Glycol Nuclear Magnetic Resonance Thermometers with a Static Thermistor Probe,” *Anal. Chem.*, vol. 40, no. 14, pp. 2227–2229, 1968, doi: 10.1021/ac50158a064.

[10] N. Karschin, S. Krenek, D. Heyer, and C. Griesinger, “Extension and improvement of the methanol-d4 NMR thermometer calibration,” *Magn. Reson. Chem.*, vol. 60, no. 2, pp. 203–209, 2022, doi: 10.1002/mrc.5216.

[11] W. M. Spees, S. K. Song, J. R. Garbow, J. J. Neil, and J. J. H. Ackerman, “Use of ethylene glycol to evaluate gradient performance in gradient-intensive diffusion MR sequences,” *Magn. Reson. Med.*, vol. 68, no. 1, pp. 319–324, 2012, doi: 10.1002/mrm.23201.

[12] B. A. Berkowitz, J. T. Handa, and C. A. Wilson, “Perfluorocarbon temperature measurements using 19F NMR,” *NMR Biomed.*, vol. 5, no. 2, pp. 65–68, Mar. 1992, doi: https://doi.org/10.1002/nbm.1940050204.

[13] J. L. Kitevski-LeBlanc and R. S. Prosser, “Current applications of 19F NMR to studies of protein structure and dynamics,” *Prog. Nucl. Magn. Reson. Spectrosc.*, vol. 62, pp. 1–33, 2012, doi: https://doi.org/10.1016/j.pnmrs.2011.06.003.

[14] J. De Poorter, C. De Wagter, Y. De Deene, C. Thomsen, F. Ståhlberg, and E. Achten, “Noninvasive MRI Thermometry with the Proton Resonance Frequency (PRF) Method: In Vivo Results in Human Muscle,” *Magn. Reson. Med.*, vol. 33, no. 1, pp. 74–81, Jan. 1995, doi: https://doi.org/10.1002/mrm.1910330111.

[15] R. M. Botnar, P. Steiner, B. Dubno, P. Erhart, G. K. Von Schulthess, and J. F. Debatin, “Temperature quantification using the proton frequency shift technique: In vitro and in vivo validation in an open 0.5 Tesla interventional MR scanner during RF ablation,” *J. Magn. Reson. Imaging*, vol. 13, no. 3, pp. 437–444, 2001, doi: 10.1002/jmri.1063.

[16] P. J. Basser and S. Pajevic, “Statistical artifacts in diffusion tensor MRI (DT-MRI) caused by background noise,” *Magn. Reson. Med.*, vol. 44, no. 1, pp. 41–50, 2000, doi: 10.1002/1522-2594(200007)44:1<41::AID-MRM8>3.0.CO;2-O.

[17] J. L. Olesen, A. Ianus, L. Østergaard, N. Shemesh, and S. N. Jespersen, “Tensor denoising of multidimensional MRI data,” *Magn. Reson. Med.*, vol. 89, no. 3, pp. 1160–1172, 2023, doi: 10.1002/mrm.29478.

[18] P. Mukherjee, J. I. Berman, S. W. Chung, C. P. Hess, and R. G. Henry, “Diffusion tensor MR imaging and fiber tractography: Theoretic underpinnings,” *Am. J. Neuroradiol.*, vol. 29, no. 4, pp. 632–641, 2008, doi: 10.3174/ajnr.A1051.

[19] B. W. Kreher, J. F. Schneider, I. Mader, E. Martin, J. Hennig, and K. A. Il’Yasov, “Multitensor approach for analysis and tracking of complex fiber configurations,” *Magn. Reson. Med.*, vol. 54, no. 5, pp. 1216–1225, 2005, doi: 10.1002/mrm.20670.

[20] J. H. Jensen and J. A. Helpern, “MRI quantification of non-Gaussian water diffusion by kurtosis analysis,” *NMR Biomed.*, vol. 23, no. 7, pp. 698–710, 2010, doi: 10.1002/nbm.1518.

[21] K. Nishinari, Y. Fang, S. Guo, and G. O. Phillips, “Soy proteins: A review on composition, aggregation and emulsification,” *Food Hydrocoll.*, vol. 39, pp. 301–318, 2014, doi: 10.1016/j.foodhyd.2014.01.013.

[22] K. H. Lee, H. S. Ryu, and K. C. Rhee, “Protein solubility characteristics of commercial soy protein products,” *JAOCS, J. Am. Oil Chem. Soc.*, vol. 80, no. 1, pp. 85–90, 2003, doi: 10.1007/s11746-003-0656-6.

[23] D. Verfaillie, F. Janssen, G. Van Royen, and A. G. B. Wouters, “A systematic study of the impact of the isoelectric precipitation process on the physical properties and protein composition of soy protein isolates,” *Food Res. Int.*, vol. 163, no. November 2022, p. 112177, 2023, doi: 10.1016/j.foodres.2022.112177.

[24] J. Medic, C. Atkinson, and C. R. Hurburgh, “Current knowledge in soybean composition,” *JAOCS, J. Am. Oil Chem. Soc.*, vol. 91, no. 3, pp. 363–384, 2014, doi: 10.1007/s11746-013-2407-9.

[25] D. Verfaillie, J. Li, F. Janssen, E. Blontrock, G. Van Royen, and A. G. B. Wouters, “Structure formation in high moisture extrudates produced from soy protein fractions varying in 7S/11S globulin ratio,” *Int. J. Biol. Macromol.*, vol. 283, no. P1, p. 137369, 2024, doi: 10.1016/j.ijbiomac.2024.137369.

[26] E. N. C. Mills, L. Huang, T. R. Noel, A. P. Gunning, and V. J. Morris, “Formation of thermally induced aggregates of the soya globulin β-conglycinin,” *Biochim. Biophys. Acta - Protein Struct. Mol. Enzymol.*, vol. 1547, no. 2, pp. 339–350, 2001, doi: 10.1016/S0167-4838(01)00199-6.

[27] N. A. Deak, L. A. Johnson, E. W. Lusas, and K. C. Rhee, “Soy Protein Products, Processing, and Utilization,” *Soybeans Chem. Prod. Process. Util.*, pp. 661–724, 2008, doi: 10.1016/B978-1-893997-64-6.50022-6.

[28] I. Koshiyama, “Chromatographic and Sedimentation Behavior of a Purified 7S Protein in Soybean Globulins,” *Cereal Chem.*, vol. 45, pp. 405–412, 1968.

[29] I. Koshiyama, “Purification and Physico-chemical Properties of 11S Globulin in Soybean Seeds,” *Int. J. Pept. Protein Res.*, no. 4, pp. 167–176, 1972.

[30] E. D. Garina *et al.*, “From gels to high-moisture extrudates : pH and 11S : 7S globulin ratio govern multiscale structure formation,” *Food Hydrocoll.*, vol. 176, no. November 2025, p. 112567, 2026, doi: 10.1016/j.foodhyd.2026.112567.

[31] C. Fei *et al.*, “Texture and structure of high-moisture extrudates produced from soybean protein isolates with different 7S/11S globulin ratios,” *Food Hydrocoll.*, vol. 171, no. May 2025, p. 111771, 2026, doi: 10.1016/j.foodhyd.2025.111771.

[32] D. Verfaillie, J. Li, F. Janssen, E. Blontrock, G. Van Royen, and A. G. B. Wouters, “Relating the protein denaturation degree and solubility of soy protein isolates to the structure of high moisture extrudates,” *Food Hydrocoll.*, vol. 155, no. January, p. 110211, 2024, doi: 10.1016/j.foodhyd.2024.110211.

[33] M. I. Gobes, Y. Bugday, J. P. M. van Duynhoven, J. Hohlbein, and R. G. M. van der Sman, “Impact of pH, temperature, and moisture on the rheological behaviour of soy protein concentrate doughs,” *Food Hydrocoll.*, vol. 174, no. December 2025, p. 112316, 2025, doi: 10.1016/j.foodhyd.2025.112316.

[34] T. M. Barber, S. Kabisch, A. F. H. Pfeiffer, and M. O. Weickert, “The health benefits of dietary fibre,” *Nutrients*, vol. 12, no. 10, pp. 1–17, 2020, doi: 10.3390/nu12103209.

[35] V. B. Tolstoguzov, “Thermoplastic extrusion-the mechanism of the formation of extrudate structure and properties,” *J. Am. Oil Chem. Soc.*, vol. 70, no. 4, pp. 417–424, 1993, doi: 10.1007/BF02552717.

[36] P. Wittek, N. Zeiler, H. P. Karbstein, and M. A. Emin, “High moisture extrusion of soy protein: Investigations on the formation of anisotropic product structure,” *Foods*, vol. 10, no. 1, Jan. 2021, doi: 10.3390/foods10010102.

[37] J. Li *et al.*, “The interplay between soy proteins and dietary fiber in determining the structure and texture of high moisture extrudates,” *Food Hydrocoll.*, vol. 156, no. February, p. 110256, 2024, doi: 10.1016/j.foodhyd.2024.110256.

[38] M. Nieuwland, W. Heijnis, A. J. van der Goot, and R. Hamoen, “XRT for visualizing microstructure of extruded meat replacers,” *Curr. Res. Food Sci.*, vol. 6, p. 100457, 2023, doi: 10.1016/j.crfs.2023.100457.

[39] Q. Deng *et al.*, “High-moisture extrusion of soy protein: Effects of insoluble dietary fiber on anisotropic extrudates,” *Food Hydrocoll.*, vol. 141, no. March, p. 108688, 2023, doi: 10.1016/j.foodhyd.2023.108688.

[40] T. Guan *et al.*, “From nano to bite : Dietary fibers induce fracture mechanisms during high moisture extrusion of plant-based meat alternatives,” *Food Hydrocoll.*, vol. 173, no. November 2025, p. 112241, 2026, doi: 10.1016/j.foodhyd.2025.112241.

[41] J. Li *et al.*, “Understanding the effect of pH on structure formation in high moisture extrudates produced from soy protein-dietary fiber blends,” *Food Hydrocoll.*, vol. 170, no. June 2025, p. 111710, 2026, doi: 10.1016/j.foodhyd.2025.111710.

[42] E. D. Garina *et al.*, “SANS and SAXS : A Love Story to unravel structural evolution of soy proteins and

polysaccharide fibres during high moisture extrusion for meat alternatives," *Food Hydrocoll.*, vol. 155, no. January, p. 110121, 2024, doi: 10.1016/j.foodhyd.2024.110121.

[43] P. Wittek, F. Ellwanger, H. P. Karbstein, and M. A. Emin, "Morphology development and flow characteristics during high moisture extrusion of a plant-based meat analogue," *Foods*, vol. 10, no. 8, Aug. 2021, doi: 10.3390/foods10081753.

[44] A. Nisov, M. Nikinmaa, E. Nordlund, and N. Sozer, "Effect of pH and temperature on fibrous structure formation of plant proteins during high-moisture extrusion processing," *Food Res. Int.*, vol. 156, p. 111089, Jun. 2022, doi: 10.1016/j.foodres.2022.111089.

[45] B. J. Muhialdin and J. Ubbink, "Effects of pH and aging on the texture and physicochemical properties of extruded pea protein isolate," *Food Hydrocoll.*, vol. 140, no. November 2022, p. 108639, 2023, doi: 10.1016/j.foodhyd.2023.108639.

[46] V. L. Pietsch, J. M. Bühler, H. P. Karbstein, and M. A. Emin, "High moisture extrusion of soy protein concentrate: Influence of thermomechanical treatment on protein-protein interactions and rheological properties," *J. Food Eng.*, vol. 251, pp. 11–18, Jun. 2019, doi: 10.1016/j.jfoodeng.2019.01.001.

[47] T. E. Creighton, "Disulfide bond formation in proteins," *Methods Enzymol.*, vol. 107, no. C, pp. 305–329, 1984, doi: 10.1016/0076-6879(84)07021-X.

[48] I. Rombouts, B. Lagrain, K. Brijs, and J. A. Delcour, "β-Elimination reactions and formation of covalent cross-links in gliadin during heating at alkaline pH," *J. Cereal Sci.*, vol. 52, no. 3, pp. 362–367, 2010, doi: 10.1016/j.jcs.2010.06.006.

[49] Y. Gao *et al.*, "Mechanism of L-cysteine-induced fibrous structural changes of soybean protein at different high-moisture extrusion zones," *Int. J. Biol. Macromol.*, vol. 268, no. P1, p. 131621, 2024, doi: 10.1016/j.ijbiomac.2024.131621.

[50] H. Bader Ul Ain *et al.*, "Comparative study of chemical treatments in combination with extrusion for the partial conversion of wheat and sorghum insoluble fiber into soluble," *Food Sci. Nutr.*, vol. 7, no. 6, pp. 2059–2067, 2019, doi: 10.1002/fsn3.1041.

[51] S. H. V. Cornet, S. J. E. Snel, F. K. G. Schreuders, R. G. M. van der Sman, M. Beyrer, and A. J. van der Goot, "Thermo-mechanical processing of plant proteins using shear cell and high-moisture extrusion cooking," *Crit. Rev. Food Sci. Nutr.*, vol. 62, no. 12, pp. 3264–3280, 2022, doi: 10.1080/10408398.2020.1864618.

[52] E. Högg, T. Horneber, and C. Rauh, "Modeling and experimental analysis of protein matrix solidification in cooling dies during high-moisture extrusion," *Front. Food Sci. Technol.*, vol. 5, no. February, pp. 1–19, 2025, doi: 10.3389/frfst.2025.1443376.

[53] E. Kaunisto, C. Ohgren, N. Lor, and M. Stading, "A mean-field phase separation model enabling the coupling of non-isothermal flow phenomena with fibre formation in high-moisture extrusion of meat analogues," *J. Food Eng.*, vol. 412, p. 112972, 2026, doi: 10.1016/j.jfoodeng.2026.112972.

[54] J. P. Marques, F. F. J. Simonis, and A. G. Webb, "Low-Field MRI : An MR Physics Perspective," *J. Magn. Reson. Imaging*, vol. 49, no. 6, pp. 1528–1542, 2019, doi: 10.1002/jmri.26637.

[55] H. Raich and P. Blu, "Design and Construction of a Dipolar Halbach Array with a Homogeneous Field from Identical Bar Magnets : NMR Mandhalas," *Concepts Magn. Reson. Part B*, vol. 23B, no. 1, pp. 16–25, 2004, doi: 10.1002/cmr.b.20018.

[56] T. O'Reilly, W. M. Teeuwisse, D. de Gans, K. Koolstra, and A. G. Webb, "In vivo 3D brain and extremity MRI at 50 mT using a permanent magnet Halbach array," *Magn. Reson. Med.*, vol. 85, no. 1, pp. 495–505, 2021, doi: 10.1002/mrm.28396.

[57] A. Telfah, A. Bahti, K. Kaufmann, E. Ebel, R. Hergenröder, and D. Suter, "Low-field NMR with multilayer Halbach magnet and NMR selective excitation," *Sci. Rep.*, vol. 13, no. 1, pp. 1–14, 2023, doi: 10.1038/s41598-023-47689-2.

[58] M. C. D. Tayler and D. Sakellariou, "Low-cost, pseudo-Halbach dipole magnets for NMR," *J. Magn. Reson.*, vol. 277, pp. 143–148, 2017, doi: 10.1016/j.jmr.2017.03.001.

[59] P. Yu *et al.*, "Theoretical foundation for designing multilayer Halbach array magnets for benchtop NMR and MRI," *J. Magn. Reson.*, vol. 344, p. 107322, 2022, doi: 10.1016/j.jmr.2022.107322.

[60] M. Meribout and S. Sonowan, "Optimal Halbach Magnet Array Design for Portable NMR Targeting Multiphase Flow Metering Applications," *IEEE Trans. Magn.*, vol. 55, no. 1, pp. 1–7, 2019, doi: 10.1109/TMAG.2018.2877603.

[61] T. O'Reilly, W. M. Teeuwisse, and A. G. Webb, "Three-dimensional MRI in a homogenous 27 cm diameter bore Halbach array magnet," *J. Magn. Reson.*, vol. 307, p. 106578, 2019, doi: 10.1016/j.jmr.2019.106578.

[62] B. De Vos, P. Fuchs, T. O'Reilly, A. Webb, and R. Remis, "Gradient Coil Design and Realization for a Halbach-Based MRI System," *IEEE Trans. Magn.*, vol. 56, no. 3, pp. 1–8, 2020, doi:

10.1109/TMAG.2019.2958561.
[63] F. Galve *et al.*, "Elliptical Halbach magnet and gradient modules for low-field portable magnetic resonance imaging," *NMR Biomed.*, vol. 37, no. 12, pp. 1–19, 2024, doi: 10.1002/nbm.5258.
[64] C. E. Hayes and L. Axel, "Noise performance of surface coils for magnetic resonance imaging at 1.5 T," *Medical Physics*, vol. 12, no. 5. pp. 604–607, 1985. doi: 10.1118/1.595682.
[65] K. Prabha *et al.*, "Recent development, challenges, and prospects of extrusion technology," *Futur. Foods*, vol. 3, no. January, p. 100019, 2021, doi: 10.1016/j.fufo.2021.100019.
[66] R. Chokshi and H. Zia, "Hot-melt extrusion technique: A review," *Iran. J. Pharm. Res.*, vol. 3, no. 1, pp. 3–16, 2004, doi: 10.22037/IJPR.2010.290.
[67] G. Gillispie *et al.*, "Assessment Methodologies for Extrusion-Based Bioink Printability," *Biofabrication*, vol. 12, p. 022003, 2020, doi: 10.1088/1758-5090/ab6f0d.

Chapter

8

Summary

Transitioning to a diet more focused on plant-based food has the potential to reduce the environmental foodprint and promote the general health of the human population. However, a major barrier for this transition is changing consumer dietary habits. To facilitate this transition, plant-based meat alternative products need to be designed that resemble the texture of animal-meat. High-moisture extrusion (HME) is the current dominant industrial process to produce such textured plant-protein materials and involves the thermo-mechanical processing of a plant-protein dough. This dough is forced through a cooling die at high pressure and cooled under shear, resulting in a fibrous protein texture. Understanding the structuring mechanisms behind fibrous texture formation during HME is key to enabling the rational design and optimisation of meat alternative products

Departing from hypotheses on anisotropic structure formation during HME, this thesis addressed the following research questions (RQ): (**RQ1**) where inside the extruder, and at what length scale, does anisotropic structure formation occur; (**RQ2**) what is the role of electrostatic protein interactions during multiscale structure formation; (**RQ3**) at what length scales does phase-separated lamellar structure formation occur; (**RQ4**) what is the role of wall-slip during cooling die flow; and (**RQ5**) what is the effect of post-processing on the phase-separated extrudate structure? In the present work, MRI is explored as a technique that can non-invasively provide structural information at multiple length scales and is potentially applicable under *in situ* conditions. Small angle scattering and microscopy techniques provide complementary nm-to-µm scale structural information on soy protein extrudates.

In **chapter 2**, the ability of low-field TD-NMR and high-field MRI to quantify the phase-separated structure of SPC and SPI extrudates was assessed. TD-NMR revealed the presence of four distinct water populations assigned to immobile crystalline cellulose and protein cores, mobile gelled protein, and water inside the protein-rich (PR) and water-rich (WR) phases. The latter two domains could be spatially identified, at the 10^2 µm-scale, by MRI. Post-processing, by swelling of extrudates with water, enhanced the imaging contrast, whereas freeze-thawing enhanced the delamination of the PR phase into distinct protein- and water-rich regions, answering research question (v).

Chapter 3, expanded on this and utilised DT-MRI to probe the diffusion anisotropy of water inside the PR phase down to the µm-scale to answer research question (iii). DT-MRI revealed that this phase is comprised of 10^{-1} µm-scale lamellae with a primary diffusion direction oriented in the extruder flow direction. The secondary dominant diffusion direction is parallel to the phase-separated lamellae, irrespective of their orientation. Additionally, T_2-weighted MRI images were analysed by RFT to quantify the 10^2 µm-scale lamellae. DT-MRI results were underpinned by CLSM images. Furthermore, the effect of cooling die geometry on the orientation of lamellar phase separation was estimated using *in silico* generated images.

In **Chapter 4**, a comprehensive *ex situ* multiscale assessment of structure formation during HME at pilot-plant scale was performed. By extruder dead-stop operations, samples could be obtained from the extruder barrel section, transition zone and cooling die, which enabled answering research question (i). SANS results showed that nm-scale protein nano-aggregates cluster to form fibrils already within the extruder barrel. Yet, alignment of these fibrils primarily develops in the transition zone and in early sections of the cooling die. MRI revealed that the imprint of localised phase separation at the 10^2 µm-scale is already present in the transition zone. During passage of the melt through the cooling die, the lamellar phase-separated region increases in size.

Chapter 5 explored the effect of pH-shifting of the protein during extrusion on anisotropic structure formation. Multiscale analysis performed using MRI, SAS and protein extractability, revealed that the dominant structuring mechanism is based on electrostatic interactions between protein nano-aggregates, answering research question (ii). The effect was found to be non-monotonic, where at a pH close to the iso-electric point, absence of electrostatic charges led to formation of a particulate protein network and an isotropic phase-separated structure. When electrostatic charges are present, fibrillar aggregation of the nano-aggregates occurs, which align with the extruder flow direction and form a lamellar phase-separated structure at larger length scales. However, if excess charges are present, electrostatic repulsion between nano-aggregates decreases nematic order of protein fibrils, resulting in a decrease of the degree of aligned lamellar structure at the larger length scales.

In **Chapter 6**, a flow-MRI platform was developed that enabled the direct *in situ* measurement of flow in the cooling die required to answer research question (iv). Velocimetry profiles could be analysed using an adapted Herschel-Bulkley model that accounts for the temperature-dependent dynamic yield stress and presence of wall-slip. It was found that wall-slip has a dominant contribution to the velocity profiles in the cooling die. The quantitative characterisation of wall-slip allows for the parametrisation thereof for *in silico* models predicting flow in a cooling die.

Chapter 7, contains an overview of the main findings and conclusions, as well as a general discussion on (i) the further employment of MRI for characterising anisotropic structure formation during HME; (ii) the role of soy protein composition and (iii) carbohydrate fibres on anisotropic structure formation; (iv) the relation between extruder process conditions and the effect of pH-shifting on structure formation. Finally, perspectives are given to expand the developed flow-MRI platform to accommodate different cooling die geometries and extrusion scales. The ability of these platforms to measure data that enable the parametrisation of *in silico* models is discussed as well as their relevance to HME processing at industrially relevant scales and conditions.

List of publications

This thesis:

Kuijpers, S.A.; Goudappel, G.-J.; Huppertz, T.; Van Duynhoven, J.P.M. and Terenzi, C., Quantification of phase separation in high-moisture soy protein extrudates by NMR and MRI, *Food Res. Int.*, **2024**, *197*, 115225.

Kuijpers, S.A.[1]; Garina, E.D.[1]; Gobes, M.I.; Den Adel, R.; Smith, G.N.; Sztucki, M.; Hohlbein, J.; Bouwman, W.G.; Van Duynhoven, J.P.M. and Terenzi, C., Impact of pH-shifting on multiscale structural anisotropy of high-moisture extrudates of soy proteins, *Food Hydrocoll.*, **2025**, *168*, 111456.

Garina, E.D.[1]; **Kuijpers, S.A.[1]**; Gobes, M.I.[1]; Sein, A.; Den Adel, R.; Smith, G.N.; Sztucki, M.; Hohlbein, J.; Terenzi, C.; Van Duynhoven, J.P.M. and Bouwman, W.G., Mapping anisotropic structure formation of soy protein during high-moisture extrusion, *Food Hydrocoll.*, **2026**, *172*, 112037.

Kuijpers, S.A.; Gobes, M.I.; Mayar, M.; Vergeldt, F.J.; Hohlbein, J.; Huppertz, T.; Van Duynhoven, J.P.M.; Terenzi, C. Underpinning hierarchical anisotropic structure formation in soy protein high-moisture extrudates by magnetic resonance imaging, *Curr. Res. Food Sci.*, **2026**, 13, 101575

Kuijpers, S.A.; Vergeldt, F.J.; Gobes, M.I.; Philippi, J.; Hohlbein, J.; Van Duynhoven, J.P.M.; Terenzi, C. MRI velocimetry during high-moisture extrusion: probing wall-slip and yield stress of soy protein concentrate (to be submitted)

Other publications:

Gobes, M.I.; **Kuijpers, S.A.**; Terenzi, C.; Van der Sman, R.G.M.; Van Duynhoven, J.P.M. and Hohlbein J., Rotated Fourier transform (RFT) enables the quantification of anisotropic structure in high-moisture plant-protein extrudates, *Food Struct.*, **2025**, *44,* 100437.

Garina, E.D.; **Kuijpers, S.A.**; Gobes, M.I.; Smith, G.N.; Sztucki, M.; Wouters, A.G.B.; Van Duynhoven, J.P.M. and Bouwman, W.G., From gels to high-moisture extrudates: pH and 11S: 7S globulin ratio govern multiscale structure formation, *Food Hydrocoll.,* **2026***, 176*, 112567.

Garina, E.D.; Gobes, M.I.; **Kuijpers, S.A.**; Saavedra, G.I.; Kamman, K.; Dalgliesh, R.M.; Parnell, S.R.; Smith, G.N.; Van Duynhoven, J.P.M. and Bouwman, W.G. Inside the cooling die: in situ SANS to probe structure formation during high-moisture extrusion of soy protein concentrate. *Food Hydrocoll.*, **2027**, *183*, 113153.

Gobes, M.I.; **Kuijpers, S.A.**; Terenzi, C.; Van Duynhoven, J.P.M.; Hohlbein, J. and Van der Sman, R. G. M., Inside the cooling die : prediction of the flow profile of a high-moisture soy protein melt during extrusion. *Food Hydrocoll.*, **2027**, 185, 113436.

[1] Authors contributed equally.

Overview of completed training activities

Discipline specific activities	Organizing institute	Year
18th European School of Rheology	KU Leuven	2022
Zakopane School of NMR	Adam Mickiewicz University	2022
in vivo NMR	UMC Utrecht	2022
NMR-DG	Shell, Amsterdam	2022
NMR-DG[p]	Organon, Oss	2023
NMR-DG[o]	University of Twente	2024
NMR-DG[p]	Radboud University	2025
Advanced Food Analysis 2023[p]	VLAG	2023
ISFRS[p]	Wageningen University & Research	2023
Dutch Biophysics[p]	NWO	2023
Dutch Biophysics[o]	NWO	2024
Dutch Biophysics[p]	NWO	2025
MR Food[o]	ITAIPU	2024
MR Food[o]	CNR	2026
MRPM[o]	NoFima	2024
Edible Soft Matter in between Fluid and Solid States[o]	Wageningen University & Research	2024
ICMRM[o]	Wurzburg University	2025
FBNL MR[o]	LILLIAD	2026
General courses		
VLAG PhD week	VLAG	2021
Scientific Writing	WGS	2023
Philosophy and Ethics of Food Science and Technology	WGS	2023
Career Perspectives	WGS	2025
Optional activities		
Preparation of research proposal	VLAG	2022
VLAG PhD Council member	VLAG PhD Council	2022-2024
Bi-weekly NMR group meetings	BIP	2022-2026
Bi-weekly BIP colloquia	BIP	2022-2026
half-yearly MP3 OTP user meetings	NWO	2022-2026

[o] oral presentation [p] poster presentation

Authorship statement

Chapter 1, I wrote the first draft of the introduction. I revised the text after top-level comments from my supervisors.

Chapter 2, the original research question was formulated together with my supervisory team. I performed the measurements on lab-scale samples provided by Unilever and analysed the data. My supervisors provided guidance in the experimental design and in theoretical framework required for interpretation of results. I wrote the first complete draft of the manuscript, including the figures, and revised this in response to feedback from my supervisory team.

Chapter 3, I designed the methodology, performed the measurements on lab-scale samples provided by Unilever. CLSM measurements were performed by Martijn Gobes (MG), and I performed the data analysis. Validation experiments were formulated with input from Frank Vergeldt (FV). I wrote the first draft of the manuscript, made the figures and revised the manuscript in response to feedback from my supervisory team and co-authors.

Chapter 4, this chapter is published as a shared first authorship between Ekaterina Garina (EG), MG and me. I operated the pilot-scale extruder, while EG acquired and prepared the samples, and MG performed *at line* measurements. I performed the MRI and 2D AI(DR) measurements and analysed the data. SAS data was measured by EG and me, and data analysis was performed by EG. MG acquired CLSM data, improved an image analysis method and performed statistical analysis. The original draft was written by EG with review and editing performed by EG and me after critical feedback from co-authors and our supervisory teams.

Chapter 5, this chapter is published as a shared first authorship with EG. Lab-scale samples were provided by Unilever, MRI measurements were performed by Gert-Jan Goudappel, and I performed MRI data analysis. EG analysed the SAXS and SANS data. WAXD and DR measurements were performed by Ruud den Adel. I wrote the draft of the manuscript with input on SAXS and SANS results from EG. I reviewed and edited the manuscript after responses from EG, my supervisory team and other co-authors.

Chapter 6, initial designs for the custom parts were drafted by John Philippi; I managed design refinements and manufacturing by the technical facilities The flow MRI pulse sequence was written by FV and validated by me. I performed extrusion and *in situ* flow-MRI measurements as well as subsequent *ex situ* characterisation by MRI. I performed the data analysis and wrote the first complete draft. My supervisors contributed through discussion of the data and several rounds of revision of the text.

Chapter 7, I wrote the first draft and revised the text after comments from supervisors.

Acknowledgements

The astute among you might have noticed, a whole list of co-authors is mentioned for every research chapter, throughout this work. That is because none of this work could have arrived at its current state without the help of others. As it turns out, however, that to get through four years of PhD research, there are also many unofficial co-authors involved who contributed to parts of this journey that may have had nothing to do with the research itself. This section is to highlight all of these wonderful people that would otherwise go unnoticed. Some of you probably still went unnoticed, as with any man-made list, in case you can't find your name but do expect it, I am sorry! But thank you nonetheless ;)

First of all, my supervisors (that of course have also been actual co-authors), who have been key in my successful completion of my PhD. **Camilla**, I tried really hard to not make some kind of joke here, hopefully I succeeded. In the beginning I had to adjust a bit to our different approaches to research and meetings in general, yet it was instantly clear that you care a lot not only about the work itself but also about the person doing the work. At times you would nudge me (or push in the case of Zakopane) to broaden my narrow Dutch horizon or reflect on my position within situations, and as a result, I have learned a great deal more during this PhD than just academic skills. Although traveling and networking will never be my favourite occupation, my presentations have never looked so polished, and I have learned at conferences that this seems to be a critically undervalued skill in academia. Overall I look back on a great time being your PhD candidate. **John**, during the interview you recalled that you once was a reviewer for a mock PhD proposal I wrote during my studies and you asked if anything ever came out of that. While that proposal itself was never submitted, in the end I joined almost precisely the type of project I wrote about and I never regretted it. It has been great to have you as a supervisor during the past four years. While you were usually quite busy juggling between Unilever and WUR, you always found the time to review manuscripts or have a quick meeting for feedback. I am a great fan of your pragmatic approach and your deep interest as well as enthusiasm for the project. The latter which was always easy to spot when you would leap up from your seat every time new and interesting data was presented at meetings.

The overarching project of this work featured not one but two other PhD colleagues with whom I have shared much data and many memories. The first of these to mention is my self-appointed favourite colleague **Katja**. Of course we met at the best of circumstances on Utrecht Centraal during a nationwide train black-out without any way to get to Leuven, our conference destination (before I even started the PhD). This set us up to persevere through other trips to both Norway and the UK, with the one slightly more demanding than the

other. Here I learned, among things, that you are one of the few people I know that can get lost on a straight road, have a wildly different sense of fashion than I do, that we seek the same level of quality in the lab or data, and you actually enjoy videogames more than you initially led us to believe. While your attempts to teach me rudimentary Russian have failed miserably, I do now own a mono-colour green linen shirt! Тише едешь — дальше будешь. The second of these is **Martijn**. We are from the same study year, ended up at the same start-up for our internship but really only got to know each other at BIP. While we have differing ideas on when it is an appropriate moment to start preparing for a consortium meeting or what level of polish to put in such slides, I have learned much about the mathematics behind oven timings. It has been fun playing Arkham Horror with Jarne or Magic the Gathering on the train to the UK. You a (sometimes) great slightly-stronger-than-beer collection at Christmas dinners which really showed we have like-minded interest in craft beer and whisky. Yet when there is an actual tasting in Wageningen, you always seem to be abroad. I wish you luck on your next career step and may you at some point convince Katja that Magic is indeed a fun game.

The next group of wonderful people I have met at Biophysics, and who else to start with than my paranymph **Dana**. Need I say more than “drie uur?”, “half elf?” or “koffie?”, for while we worked on completely different projects, I don’t think there is someone I interacted more with at BIP. A kinship that started during the lab-uitje curling with the question “kom jij toevallig uit Oss?” to the great astonishment of our colleagues that I could city-specifically guess a regional accent. You always have great scouting stories, news articles about Helmond (and I about Oss). Nearly always busy and fully booked but you have an ability to reflect that I look up to. Hopefully your schedule allows some time to keep in contact when we don’t see each other five days a week anymore ;). **Morwarid** is my other paranymph but was also part of the NMR group and even co-author on one of my publications! I am very happy that you were the one to put my samples in a 5-mm tube, then again, you had me stuck in an MRI for well over an hour without the radio... Let’s call it a draw. I enjoyed working with you even and taking over your teaching duties on the PD (finally no more spectroscopy for me :)). I enjoyed our dinners and it is great to have found someone who also enjoys playing Wingspan, which we should do more often. Finally, I never expected to learn so much about the culinary application of giant red ants.

Next up in the NMR group is **Klaudia**, with whom I have enjoyed many walks around campus, teas after NMR meetings and even the occasional beer at Onder De Linden. It was great to discover that you also enjoy talking about music and aspired to learn an instrument beside doing a PhD. May we keep on occasionally jamming in the future! Then, not so quietly in the

background there is **Frank**, who has been a fantastic source of MRI, pulse sequence and diffusion tensor wisdom as well as the occasional sanity check. You are an all-round great character that can ask the sharpest of questions before, during or after meetings. I hope I will ever be able to come up with such questions and even dare ask them. **Dmytro**, you were only briefly at BIP, but I have never seen a room go silent so quickly. **Annelies**, it has been fun teaching the same courses and looking confused at each other during student presentations like "did you tell them this?". **Laura**, you are a kind soul that, usually to my amusement, startles incredibly easy. Hopefully my sharing of code, the occasional polymer opinion and critical eye at strain has allowed me to be as helpful to you as my predecessors were to me. Also, keep on improv baking! Finally, the newest addition, **Rajeev**, you have picked up MRI right fast without having had any prior experience. It is great to know that parts of my project live on and are being used to support your own project. Its good that you seem to vibe well with the extruder and its technician and without you I would never have known that Madras is in fact not known for curries. Of course, I also greatly appreciate your embracing of the cheese on bread lunch!

No facility will run smoothly without people managing all the technical aspects**. John** (Philippi), your designs and simulations for the PEEK cooling die were instrumental in kickstarting the *in situ* work and without your wealth of 3D-printed add-ons for MAGNEFY, my multi-sample measurement days wouldn't have been possible. **Yanzhang**, while I am a big fan of figuring things out myself, whenever I needed help in MAGNEFY you were quick to reply and resolve whatever curious issue I had come up with.

BIP is a very special group with multiple research lines present, so there are many people that were not involved in NMR or MRI related activities. First up, **Jarne**, whose impeccable timing I have only managed to best a handful of times, and to great comedic relief of the PhD office. It has been fun playing Arkham Horror with you, although it is a bit sad that you left me to float around in the space between dimensions forever. May your heartrate be stable and your holidays plentiful in your future. **Cleo**, you have been an excellent source on what goes and what goes not outside of 'de provincie' as well as excellent questions to certain colleagues. Your sense of rhythm and visualisation have been enlightening and I wish you a lot of hours spent behind your piano or with a good ~~Brandon Sanderson~~ fantasy novel. **Keshav**, it has been great conversing and joking around with you even though your soundwaves at times overruled my brainwaves. Also, I never knew salt could be smelled. **Peter**, I had a lot of fun sampling craft beers and whisky with you and I will never forget Reiny during my first Veluweloop at BIP. **Ludo**, you are the second Ludovico I know, but the first I have met and I admire your absolute relaxed approach to work and renovating a house.

Mariska, I was very surprised that after walking 20 km from Ede to Wageningen you just casually got up to run back to Ede. **Tinko**, I never did manage to join any of the climbing related activities of BIP, but I trust you that climbing is fun. **Erwin**, while only very briefly in the PhD office, rarely have I seen such thought out gift ideas. **Ian**, It's always great to look around in the lab and see a 3D printed tool in just the shape and size you need. Additionally, I sometimes actually wear a labcoat nowadays! **Cor**, when I am gone from BIP, finally you will have no one to clash with for bringing cake on your birthday! **Brenda**, most likely you have done more behind the scenes than I will ever know, but what I do know is that I always managed to be right on time for the reminder of the reminder to log my hours. I have managed to evade Diversity Travel for most of the PhD, but my laptop has never been cleaner than the one time I did use it. **Francesco**, **Lennart**, **Mohammad** and **Mateusz**, some of you I know from BIP longer, others shorter. Nevertheless, I have enjoyed hearing about your stories from during your own PhDs in other countries, which mostly made me realise that The Netherlands is a great place to be. **Johannes**, generally it is not appreciated if someone says 'please redo all figures' on the day of submission, but admittedly, it does look better now in the published work. **Arjen**, my affinity for magnets will always be bigger than lasers but I will promise to not stick one to a drone, not even an infra-red laser. **Emilie**, I appreciate your incredibly chill look at life and your occasionally joining me during my lonely breakfast in the coffee corner after I went for a morning swim. **Milda**, I have learned much about bears in Greenland. **Jeremy**, the purveyor of wonderful quotes and questions that are really more like comments. **Herbert**, thank you for finding the time to join my colloquia and apologising if you couldn't.

Jumping to the other side of the street in Axis we have **Marjanne** who I met through the coincidence of FQD purchasing a benchtop extruder. Initially my project probably cost you years of your life, since we kept on finding new things to do with your extruder-shaped baby that nobody has done before or would willingly subject such equipment to. Once both of us got the hang of it, it was great fun extruding and chatting with Q-music foute uur. After a day of extrusion, we always managed to let Martijn slip into a Limburg accent (beggars can't be choosers I guess). I wish you all the happiness with your first person-shaped baby! On the far side of campus sits a bustling Hive. **Gert-Jan**, I have enjoyed our chats over coffee about MRI, managing an automated low field setup, phase cycling and several other topics. It was great to have been able to learn the finer details of imaging soy extrudates from you. If a supporting position ever opens up, you know where to find me ;). **Ruud** (den Adel), you always seem busy but still find the time to make sure I have all the samples I need and understand the AI-box or Kramer-cell completely before you leave. When I pick up samples, I now always make sure I have an extra half hour spare to chat. Finally, occasionally on

campus but usually somewhere in the world is **Thom** Huppertz. You win the prize for best out-of-office email. I think we probably would have worked well together if the project would have leaned more towards cheese but I can greatly appreciate your choice to let go on being a co-promotor in a project instead of staying in name only.

Ruud van der Sman, **Atze Jan** van der Goot, **Jo** Janssen, **Klaartje** Houben, **Ariette** Matser **Laurice** Pouvreau, **Michael** Foucault, **Maxime** Touffet, **Ralf** Jakobi, **Wil** van Loon, **Isabel** Verhulst and **Liane** Boudestein, I keep hearing praise about our consortium about how rare it was that we got to results so quickly and that all partners were so involved during meetings. As a result, I actually enjoyed all our meetings and I think we got something valuable out of every meeting as well. **Gregory**, **Robert** and **Steven**, sorry for *almost* burning down LARMOR and the large chunk of extruder-shaped metal that was stuck just outside your door for a very long time. You have to admit though, those were some pretty guerilla SANS measurements and you guys run a pretty great and high-quality facility that made them possible. From the thesis students **Gijs** and **Julia** that I have worked with during my PhD, I have learned a great deal about how teaching and coaching can be quite different at times. While the data both of you acquired was never directly used in a publication, its wisdom is passed on to the next set of thesis students, **Robin** and **Femke**, who will continue the topic together with Rajeev. **Maaike** and **Lauren**, while you may not have been my thesis students, you have been great fun to hang around with after the NMR meetings or in MAGNEFY. **Sonja** Döller, **Jamila** Guichelaar, **Jeroen** de Groot, **Antonia** Wörtche, who I have met at one of the many conferences I have been to during this PhD, some of them as the sole representative of the MRI work done in Wageningen. It is great to have met like-minded people to spend the week with. This made those conference just that little bit nicer and more memorable. I hope you all complete your PhDs without too much turmoil and stress. The **VLAG PhD Council** of which I have been a part for two years, keep on doing what you are doing! It may not feel like it but if things are brought up often enough at the right places, you can change things. **Jenny**, I have enjoyed our occasional lunches and if ever I find myself in a terrible accommodation, I can always think “it could be worse, it could be Haarweg 333”.

Volledig losstaand van het PhD werk zelf, of de campus omgeving, zijn er natuurlijk ook nog mensen die bijgedragen hebben aan het mentale welzijn. **Robert** en **Zoë**, hoewel we niet vaak afspreken, zou ik zeggen dat we dan wel *goed* afspreken. Uiterst onduidelijke tijdsplanningen, lekker eten of drinken, en altijd diepgaande gesprekken die vanzelf lijken te gaan totdat het spontaan al tijd is voor de laatste bus tussen Wageningen en Arnhem. **Ayleen**, een vriendschap gebouwd op uitgebreid dineren met bier, waar we beide minder van zagen de afgelopen jaren. Wat niet is, kan nog komen!? **Kim**, **Jurre**, **Naty** en **Matteo**, het

is top dat we nogsteeds de tijd vinden om met elkaar af te spreken en dan chille proeverijen of uitgebreide etentjes weten te houden. Hopelijk gaat dit nog lang door. Al moet ik wel bekennen dat een van jullie vier betrekkelijk slecht is geweest voor mijn portemonnee de afgelopen vier jaar. Dit is wel afdoende verrekend met uitstekende taart en planten verzorging ;). **Justin** en **Remco**, eenieder gaat zijn eigen weg en zo spreek je elkaar toch ineens een stuk minder dan voorheen, maar als we de tijd gevonden krijgen dan voelt het altijd weer als vanouds en weet ik dat ik altijd terecht kan mocht er iets zijn.

Als laatste wil ik dan nog een paar familieleden benoemen. Opa **Frits** en oma **Diny**, toen ik de PhD begon had ik de hoop om jullie beide uit te nodigen voor het moment dat ik officieel, vooralsnog in elk geval het eerste kleinkind ben dat zichzelf Dr. Kuijpers mag noemen. Hoewel dat niet meer mogelijk is, wil ik nog wel even zeggen dat ik altijd met veel interesse naar verhalen over vroeger heb geluisterd, uit een tijd die soms moeilijk voor te stellen is, en ik vraag me nu toch steeds vaker af, waren sommige dingen vroeger niet toch beter? **Paps**, je had gelijk, hoe vaker je ergens presenteert, hoe makkelijker het wordt. Ik voorspel dat de PhD verdediging daar een uitzondering op is, maar ondertussen heb ik over de halve wereld praatjes gegeven voor steeds groter en meer expert publiek en het is toch echt waar. **Mams**, ik heb vermoedelijk zeker in mijn begin jaren vast de nodige stress en zorgen om later gegeven, maar ik denk dat we wel kunnen stellen dat het allemaal best goed heeft uitgepakt. Hoewel jullie beide waarschijnlijk maar een half idee hadden wat ik nu eigenlijk echt gedaan heb, waardeer ik toch de poging om in elk geval het abstract van mijn publicaties te lezen en begrijpen ;). **Kato** en **Lisa**, we zijn uiteindelijk opgegroeid met allemaal compleet andere interesse velden, hoe top is dat. Ik kan nu altijd iets nieuws leren over taal, kunst, literatuur, of dieren. Zou er een bordspel zijn waar dat allemaal samenkomt?

Als laatste is er dan **Madelief**, die denk ik als enige echt alle kanten van mij heeft meegemaakt tijdens de PhD. (en als resultaat hiervan ook graag wil opkomen voor de belangen van *partners van* PhD'ers.) Dat moet vast niet altijd makkelijk geweest zijn, zeker met een vriend die liever alles onder het tapijt schuift dan ergens echt goed op reflecteert (en het allerbelangrijkste, dat ook deelt). Sommige dingen zullen we het nooit over eens zijn, zoals metingen starten in het weekend, maar ik ben wel echt beter geworden in aangeven wat er allemaal omgaat (ik beroep mij op mijn zwijgrecht). Je was niet altijd even gelukkig met de souvenirs die ik meenam uit conferenties, zeker bij de allereerste conferentie alleen naar het buitenland, maar ik had hier geen betere steun kunnen hebben. Hopelijk, na vier jaar, ben ik nog altijd je favoriete nep-voedseltechnoloog ;)

Colophon

The research described in this thesis was performed at the Laboratory of Biophysics, Wageningen University & Research, The Netherlands. This work was part of the "Measurement and Modelling of Multiscale Processed Protein Products (MP3)" (with project number 18744) of the research programme OTP TTW financed by the Dutch Research Council and by the consortium partners Unilever, dsm-firmenich, FrieslandCampina, Cargill and Wageningen Food and Biobased Research. This project was also supported by the uNMR-NL Grid: A distributed, state-of-the-art magnetic resonance facility for the Netherlands (NWO grant 184.035.002).

Financial support from the Laboratory of Biophysics, Wageningen University & Research, for printing this thesis is gratefully acknowledged

Cover design by Madelief de Groot.

Printed by proefschriftmaken.nl on FSC-certified recycled paper

